Sawata, Tadashi (1998) A study of fault and generating operation of the switched reluctance machine. PhD thesis.

http://theses.gla.ac.uk/4881/

Copyright and moral rights for this thesis are retained by the author

A copy can be downloaded for personal non-commercial research or study, without prior permission or charge

This thesis cannot be reproduced or quoted extensively from without first obtaining permission in writing from the Author

The content must not be changed in any way or sold commercially in any format or medium without the formal permission of the Author

When referring to this work, full bibliographic details including the author, title, awarding institution and date of the thesis must be given.

Glasgow Theses Service
http://theses.gla.ac.uk/
theses@gla.ac.uk

A STUDY OF FAULT AND GENERATING OPERATION OF THE SWITCHED RELUCTANCE MACHINE

A THESIS

SUBMITTED TO

THE DEPARTMENT OF ELECTRONICS AND ELECTRICAL ENGINEERING

OF

THE UNIVERSITY OF GLASGOW

FOR THE DEGREE OF

DOCTOR OF PHILOSOPHY

By

Tadashi Sawata

December 1998

© Tadashi Sawata, 1999

Abstract

This thesis studies fault-tolerant operation and generating operation of switched reluctance (SR) machines, paying special attention to the single-phase (1-ph) machine.

Firstly, it is shown that the 1-ph SR machine can be designed to achieve higher efficiency over some poly-phase equivalents. Dynamic simulations and experiments showed that the efficiency of the 1-ph 8/8 prototype was 3 to 5% higher than that of a 4-ph 8/6 machine with the same rotor and stator volumes.

A SR generator controller which regulates the DC-bus voltage in proportion to the speed was proposed for the maximisation of the energy conversion effectiveness. Simulation results showed that the load voltage could be regulated at a constant value of 80 V for a speed range of 3,000 to 10,000 rpm, independently of the DC-bus voltage, with an addition of a simple step-down converter. The controller was implemented and confirmed by experiments with 1-ph 8/8 SR machine rated 0.8 kW at 2,000 rpm.

Fault-tolerant operation of the 1-ph SR generator was discussed. A split-winding converter which requires a few additional components was proposed. The circuit equations under faults were derived. Simulation and experiment confirmed the proposed system could separate faulty coils dynamically and keep generating half the normal power after coil faults.

Furthermore, winding and inverter faults in the 3-ph 6/4 SR motor were analysed by computer simulations. A new lumped-parameter, magnetic equivalent circuit was developed, taking full account of nonlinearity and mutual couplings. The model was

validated by time-stepping finite-element analysis. Many possible faults were analysed for different winding configurations and operating conditions.

Finite element analysis of the multi-teeth per pole SR motor is also included. The number of teeth per pole and tooth shape were analysed by finite-element analysis for a maximum output torque.

Contents

Acknowledgements

I would like to thank my supervisor Prof. T.J.E. Miller for his guidance and advice. Special thanks to P.C. Kjaer and C. Cossar for their useful suggestions and support.

I would like to acknowledge the support for the PhD study by my employer NSK Ltd., Tokyo, Japan. Thanks to the SPEED consortium for the support provided for experiments. Thanks to J.R. Hendershot and the Magna Physics Tridelta company for building the single-phase and four-phase prototype switched reluctance machines. Thanks to Large Electro-Mechanical Actuation Systems for Future Civil Aircraft (LEMAS) project and Lucas Varity plc. for providing simulation facilities and useful data for chapter 5. Thanks to Prof. Y. Hayashi for designing the single-phase switched reluctance machine and Prof. I. Boldea for his suggestion.

Thanks to J.J. Bremner for contribution especially to chapter 5. I would like to thank I. Young, P. Miller and J. Kelly for hardware and experimental set-up, and L. Kelly for advice on software implementation. Thanks to SPEED software team, M. McGilp, D. Ionel and P. Brown, for their support in software. I would like to acknowledge the administrative support provided by S. Alsford. Thanks to all former and present SPEED colleagues. I would like to thank G. Gallegos-López and M. Piron, who studied towards PhD together and shared difficulties, for encouragement and useful discussions.

Finally, I would like to thank my family and friends in Japan and my wife, Saeko for their support.

List of Figures

List of Tables

List of Symbols

AC	Alternating current
ADC	Analogue to digital converter
AEE	All electric accessory engine
BIEM	Boundary integral equation method
BLDCM	Permanent-magnet brushless DC motor
CAD	Computer-aided design
cmp	Comparator
CPU	Central processing unit
D/A	Digital/analogue
DC	Direct current
DD	Direct-drive
EMF	Electromotive force
FEA	Finite element analysis
FPGA	Field programmable gate array
IGBT	Insulated gate bipolar transistor
I/O	Input/output
MEC	Magnetic equivalent circuit
MMF	Magnetomotive force
o/c	Open-circuit
P	Proportional
PBW	Powered-by-wire
PC	Personal computer

PI	Proportional-integral	
PWM	Pulse width modulation	
ROM	Read only memory	
s/c	Short-circuit	
SR	Switched reluctance	
SRG	Switched reluctance generator	
SRM	Switched reluctance machine/motor	
SW	Switching	
TRV	Torque per unit rotor volume	
A_1	Integral of excitation current in one PWM period	[C]
A_2	Integral of generated current in one PWM period	[C]
A_{olp}	Pole overlap area	[m^2]
A_x	x-axis component of vector potential	[Wb/m]
A_y	y-axis component of vector potential	[Wb/m]
A_z	z-axis component of vector potential	[Wb/m]
$\boldsymbol{A}$	Vector potential	[Wb/m]
A, B, C, D	Coil banks	
A, B, C	Stator poles with north magnetic polarity	
A', B', C'	Stator poles with south magnetic polarity	
B_{olp}	Flux density in pole overlap area	[Wb/m^2]
$\boldsymbol{B}$	Flux density vector	[Wb/m^2]
C	Filter capacitor	[F]
C_{exc}	Excitation capacitor	[F]
d	Stator slot depth	[m]
d	Duty cycle	
D_1	Relative excitation period in one PWM period	
D_2	Relative generating period in one PWM period	

e	Back-EMF	[V]
E	Energy ratio	
f_{pwm}	PWM frequency	[Hz]
F_k	MMF in pole k	[A-turns]
F_o	MMF potential at stator yoke	[A-turns]
F_r	Radial force towards pole A	[N]
F_{rp}	Radial force at a pole	[N]
F_{sp}	Stator pole MMF	[A-turns]
$\boldsymbol{F_r}$	Total radial force vector	[N]
$Flux_1$	Flux in pole A	[Wb]
$Flux_f$	Fault flux	[Wb]
g	Air gap	[m]
h	Slot depth	
H	Magnetic field intensity	[A/m]
H_N	Normalised magnetic field intensity	
i	Current	[A]
i_1	Current in phase 1	[A]
i_2	Current in phase 2	[A]
i_3	Current in phase 3	[A]
i_{c1}	Current in coil 1 in phase 1	[A]
i_{c2}	Current in coil 2 in phase 1	[A]
i_{coil}	Coil current	[A]
i_{exc}	Excitation current	[A]
i_f	Fault current	[A]
i_{gen}	Generated current	[A]
i_{in}	Phase in-going (excitation) current	[A]

i_k	Current in coil k	[A]
i_N	Current in north magnetic polarity coil	[A]
i_{off}	Turn-off current level	[A]
i_{out}	Phase out-going (generated) current	[A]
i_{peak}	Peak current	[A]
i_p	Average peak value of PWM current	[A]
i_{ph}	Phase current	[A]
i_S	Current in south magnetic polarity coil	[A]
i_{supply}	Current from DC power supply	[A]
I_A	Current in coil bank A	[A]
I_{ave}	Average of generated current	[A]
I_B	Current in coil bank B	[A]
I_{Fault}	Current in a faulty coil	[A]
I_{HI}	Current set point	[A]
I_{in}	Average of i_{in}	[A]
I_L	Load current	[A]
I_{max}	Threshold current for fault detector	[A]
I_N	Current in north magnetic polarity coil	[A]
I_{NA}	Current in north magnetic polarity coil in bank A	[A]
I_{NB}	Current in north magnetic polarity coil in bank B	[A]
I_o	Average net generated current	[A]
I_o	Output current	[A]
I_o^*	Average net generated current reference	[A]
$I_{o,pwm}$	Average net generated current in one PWM period	[A]
$I_{o,total}$	Average net generated current in all phases in one PWM period	[A]
I_{out}	Average of i_{out}	[A]
I_{ph}	Average of i_{ph}	[A]
I_{phase}	Phase current	[A]
I_S	Current in south magnetic polarity coil	[A]

I_{SA}	Current in south magnetic polarity coil in bank A	[A]
I_{SB}	Current in south magnetic polarity coil in bank B	[A]
K_{sp}	Ratio of $N_{stk}N_{active}$ between single- and poly-phase SRMs	
L	Phase inductance	[H]
L	Coil inductance in 1-ph 8/8 SRM	[H]
L_a	Aligned inductance	[H]
L_c	Copper losses	[W]
L_{cnv}	Converter losses	[W]
L_i	Iron losses	[W]
L_m	Mechanical and windage losses	[W]
L_{off}	Phase inductance at turn-off angle	[H]
L_{peak}	Phase inductance when current reaches its maximum value	[H]
L_{stk}	Stack length	[m]
L_u	Unaligned inductance	[H]
L'	Inductance gradient	[H/rad or H/deg]
m	Number of phases	
M	Mutual inductance between coils	[H]
N	North magnetic polarisation	
n	Number of faulty coils	
N	Number of coils	
N_{active}	Number of active poles per stroke	
N_p	Number of turns per pole	
N_r	Number of rotor poles	
N_s	Number of stator poles	
N_ε	Number of strokes	
$N_{\varepsilon 5}$	Number of strokes of 5-teeth model	
$N_{\varepsilon 8}$	Number of strokes of 8-teeth model	

N_t	Number of teeth per pole	
O	Open-circuit coil	
P	Permeance	[Wb/A-turns]
P_{dc}	DC input power into converter	[W]
P_{exc}	Mean electrical excitation power	[W]
P_{fault}	Output power after fault	[W]
P_{in}	Input power into motor	[W]
P_m	Mechanical output power	[W]
P_{normal}	Normal output power	[W]
P_o	Generated power	[W]
P_{out}	Mean electrical output power	[W]
R	Coil resistance	[Ω]
R	Reactive energy returned to supply	[J]
R_0	Rotor slot bottom	[m]
R_1	Rotor radius	[m]
R_{1G}	Stator inner radius	[m]
R_2	Stator slot bottom	[m]
R_3	Stator radius	[m]
R_g	Gap reluctance	[A-turns/Wb]
R_{gap}	$= R_g + R_{rp} + R_{rt} + R_{sp} + R_{st}$	[A-turns/Wb]
R_k	Reluctance in pole k	[A-turns/Wb]
R_{rp}	Rotor pole reluctance	[A-turns/Wb]
R_{rt}	Rotor pole tip reluctance	[A-turns/Wb]
R_{ry}	Rotor yoke reluctance	[A-turns/Wb]
R_{sh}	Shaft radius	[m]
R_{sp}	Stator pole reluctance	[A-turns/Wb]
R_{st}	Stator pole tip reluctance	[A-turns/Wb]

R_{sy}	Stator yoke reluctance	[A-turns/Wb]
$\mathcal{R}$	Reluctance	[A-turns/Wb]
S	South magnetic polarisation	
S	Total slot area	[m^2]
S_t	Area of tooth surface per pole	[m^2]
t	Time	[sec]
t_w	Tooth width	
t_{pwm}	PWM period	[sec]
T	Total torque	[Nm]
T_1	Torque produced at pole 1	[Nm]
T_{ave}	Average torque	[Nm]
$T_{coil,k}$	Torque under fault for case k	[Nm]
T_{em}	Average electromagnetic torque	[Nm]
$\overline{T_{ls}}$	Specific torque	
U	Total energy supplied	[J]
v_{coil}	Coil voltage	[V]
v_k	Voltage in coil k	[V]
v_N	Voltage in north magnetic polarity coil	[V]
v_S	Voltage in south magnetic polarity coil	[V]
V_B	Voltage in coil bank B	[V]
V_{DC}	DC-bus voltage	[V]
V_{DC}^*	DC-bus voltage reference	[V]
V_{ext}	External voltage source for initial excitation	[V]
V_{exc}	Excitation voltage source	[V]
V_{iron}	Iron volume	[m^3]
V_L	Load voltage	[V]
V_L^*	Load voltage reference	[V]

V_o	Nominal DC-bus voltage	[V]
V_o	Output voltage	[V]
V_r	Active rotor volume	[m^3]
V_s	Supply voltage	[V]
W	Coenergy	[J]
W_m	Stored energy	[J]
W_{pole}	Energy converted in one revolution at one pole	[J]
W_{rev}	Energy converted in one revolution	[J]
W_ε	Energy conversion per stroke	[J]
$\hat{\boldsymbol{x}}$	Unit vector in x-axis	
$\hat{\boldsymbol{y}}$	Unit vector in y-axis	
$\hat{\boldsymbol{z}}$	Unit vector in z-axis	
β	Pole arc	[rad or deg]
β_N	Normalised pole arc	
β_r	Rotor pole arc	[rad or deg]
β_s	Stator pole arc	[rad or deg]
ε	Excitation penalty	
θ	Rotor position	[rad or deg]
θ_{1d}	Angle at which pole overlap ends	[rad or deg]
θ_{1u}	Angle at which pole overlap begins	[rad or deg]
θ_a	Aligned angle	[rad or deg]
θ_{dwell}	Dwell angle	[rad or deg]
θ_{ext}	Angle at which flux reaches zero	[rad or deg]
θ_{off}	Turn-off angle	[rad or deg]
θ_{on}	Turn-on angle	[rad or deg]
θ_{peak}	Angle at which current reaches its peak value	[rad or deg]

λ	Tooth pitch	
τ	Electromagnetic torque for each airgap	[Nm]
τ	Time	[sec]
τ_s	Pole pitch	
ϕ_k	Flux in pole k	[Wb]
ψ	Flux-linkage	[Vs]
ψ_{ph}	Phase flux-linkage	[Vs]
ω	Rotor speed	[rad/sec or rpm]
ω_B	Base speed	[rad/sec or rpm]
ξ	Ratio of net generated energy to excitation energy	
@	Short-circuit coil	

Chapter 1

Introduction

In this section, firstly, published papers on switched reluctance (SR) machines are reviewed and works done are summarised. Secondly, important technologies in the SR machine are pointed out, and problems to be investigated are defined, which include fault-tolerant operation, maximisation of energy conversion effectiveness, single-phase SR machine for high efficiency operation, and multi-tooth per pole design for robotics applications. Thirdly, the structure of the thesis is presented, including a description of original contributions.

1.1 SR technology: Advantages, disadvantages and improvements

Since the potential of the SR machine was indicated by Byrne [1] and Lawrenson [2], many works have been done on SR machines and their controllers since the late 1970's. The advance in SR technology coincides with that in the semiconductor switch and microprocessor technologies. The increasing number of commercial applications seems to indicate that SR technology is ready to expand its potential and to compete with other types of electric drives including those based on induction and permanent magnet machines. Examples of commercial SR machine applications include mining and

other heavy-duty applications by British Jeffrey Diamond; automatic door openers by Besam; fan motors by Emotron; and washing-machine drives by Emerson for Maytag. Apart from commercial applications, prototype SR machine applications include electric vehicle traction motors developed by Aisin Cosmos [3] and Bausch et al. [4]; and a starter/generator system for an aircraft engine application by Ferreira et al. [5].

Evaluations of the capabilities of the SR drive system for rail traction of several hundred kilowatts were published by French [6] and Ray et al. [7]. While French concluded that the total system including converter of the SR drive did not appear to have clear advantages over the induction motor system, Ray et al. indicated the benefit of cost savings with the SR system for a comparable performance. Harris et al. provided a comparable assessment of the SR drive of tens of kilowatts [8]. They concluded that SR motors could be designed to equal the overall performance of the induction motor drive and in the torque/inertia ratio SR motors could be two to three times larger. Miller presented an analysis to determine the converter kVA requirements of the SR drive and compared it with that of the induction motor drive [9].

The features of the SR machine are generally described as:

- Simple and robust construction
  - Absence of permanent magnet
  - Absence of winding on rotor
  - Low material and manufacturing cost
  - Low rotor losses
  - Suitable for high-speed, high-temperature applications
- Simpler converter
  - Unipolar current
  - Fewer switches than in AC drives
  - Low converter cost

- Fault-tolerance
  - No shoot-through fault
  - Independence between phases
  - No high open-circuit voltage or short-circuit current.

On the other hand, the disadvantages are also described as:

- Higher torque ripple
- Higher noise level
- Requirement of rotor position sensor
- Higher number of connections between motor and converter
- Difficult to design good machine and controller.

Improvements in SR technology

To overcome the above weaknesses, many researchers have been working. The number of publications on the SR machine is very large. Review papers of those publications have also been published [10, 11, 12]. In the following, a brief review of published works on the SR machine are presented to show how the weaknesses listed above have been improved.

Low torque ripple control

Normally, SR motors are operated with the flat-topped current, voltage PWM, or single-pulse control. With these traditional controls, only the average torque is controlled and torque ripples can be significant because of the variation of torque/ampere as the rotor rotates. The limitations of the traditional control make the SR motor difficult to use for servo applications.

There have been several publications on controlling the instantaneous torque of the SR motor since Ilic-Spong et al. proposed a concept of the instantaneous torque control of the SR drive [13].

Filicori et al. presented a detailed modelling of a SR motor and proposed a cascade controller consisting of a feedforward nonlinear torque compensator and flux or current closed-loop controller.

Husain and Ehsani proposed a torque sharing function between phases using a sinusoidal function for low torque ripple operation when two phases were conducting [14]. Stankovic et al. proposed a torque sharing method for a minimum voltage requirement [15].

Wallace et al. studied SR motors with multiple teeth per pole for direct-drive robot applications [16]. They proposed another torque sharing method. In the method, the phase with the largest torque-per-amp ratio produces the bulk of the total torque, providing low copper loss as well as low torque ripple [17].

Kjaer et al. studied a low torque ripple control method achieving low copper loss at low speeds and low voltage requirement at high speeds [18].

Although those methods will require a higher computing power and a larger memory size for the controller resulting in higher cost, it does not seem to be impractical to achieve low torque ripple operation with the SR drive system for servo applications.

Noise and vibration

Higher noise level and vibration are considered to be the main drawbacks of the SR drive. Cameron et al. experimentally studied the sources of acoustic noise in a 4-ph 8/6 SR motor and identified that the main source was the radial deformation of the stator due to its radial magnetic attraction to the rotor [19].

Colby et al. also studied the vibration and acoustic noise in a 4-ph 8/6 SR motor and

derived an approximate formula to predict the frequency of the fundamental vibration mode [20]. Design considerations to reduce vibration and noise level were also provided.

Wu and Pollock presented a time domain analysis of vibration and acoustic noise in the SR motor [21, 22, 23]. It was shown that most of the vibration and noise were produced at the current commutation point. A switching technique to reduce vibration and noise was proposed and studied. In the technique, a two-stage commutation process is employed. In the first stage, at the current commutation point, one of the switches of the energised phase is opened (zero voltage loop). In the second stage, half a resonant cycle after the first switching, the other switch is opened (negative voltage loop). By doing this, the vibration in the stator cancels out. Experimental data showed a dramatic reduction in the vibration and acoustic noise. The technique was further studied and improvements were reported [24].

The technology to reduce the noise and vibration in the SR drive have been improved. One of the examples of commercial SR drives which is claimed to be quiet is the Maytag washing-machine drive by Emerson. This is an indication that careful design and control could make the SR drive quieter.

Sensorless control

In SR motor drives, rotor position sensors are essential since the phase current must be commutated in synchronism with the rotor position. The encoder and resolver are most commonly used, and the Hall sensor and slotted disk may be used for low-cost applications. However, sensors are undesirable because of their cost, size, weight, inertia, number of connections and potential unreliability. In other electric motor drive systems, like DC brushless drive systems or induction motor vector control systems, sensorless drive systems have been becoming common technologies. Such a technology is also required for the SR drive system.

Several methods to eliminate the sensors in the SR drive have been reported. Bass

et al. studied a stabilising technique without the position sensor by modulating the conduction angle in response to the DC supply current [25, 26].

One way to detect the rotor position is to measure the phase inductance since the inductance is a function of the position in the SR machine. Gallegos-Lopez et al. proposed a technique to detect the position where the rotor and stator poles start overlapping [27]. Acarnley et al. detected the rate of change of current in an energised phase to obtain the rotor position [28]. Harris and Lang used a method to inject short voltage pulses into an unenergised phase [29]. Ehsani et al. studied a method using a linear frequency modulation (FM) injecting into unenergised phase [30]. More sophisticated techniques using state observers were also reported [31, 32].

The advance in the sensorless drive technology will expand applications of the SR drive.

Finite element analysis

Finite element analysis (FEA) is essential for detailed electromagnetic analysis and design of the SR machine. Several analyses of the SR machine by FEA have been reported and the results were well validated by measurements [33, 34, 35].

Moallem et al. studied the effects of the rotor geometry on the torque by FEA [36]. It was pointed out that the most effective way to increase the average torque was to reduce the air gap length. Two advantages of skewing the rotor were also pointed out: One was that the phase inductance was its maximum positive slope (hence, maximum torque) when the phase was energized. Second, the flatter inductance profile near the aligned position when the phase current was to be commutated allowed a faster drop off of the current.

Jack et al. developed an automated method to produce a set of magnetisation curves using FEA [37]. The method drives FEA including mesh generation, adaptive solution and postprocessing.

While above mentioned works were on two-dimensional FEA, for more accurate prediction of the performance of the SR machine, three-dimensional FEA may be required.

Williamson and Shaikh compared magnetisation curves calculated by two- and three-dimensional FEA [38]. Three-dimensional FEA results showed a good agreement with experimental results, although the computation time was excessive.

Michaelides and Pollock studied the effect of end core flux on the performance of the SR motor using two- and three-dimensional FEA [39]. They proposed a correction method of two-dimensional FEA results to take into account three-dimensional effects of the end core flux.

Modelling of SR machine

Because of the nonlinear nature of the SR machine, modelling of electromagnetic characteristics and numerical simulations are important for an accurate performance prediction. Several attempts to model the magnetisation curves of the SR machine using mathematical functions have been made.

Byrne and O'Dwyer proposed the use of exponential functions [40]. Torrey and Lang used a different type of exponential functions [41]. Stephenson and Corda utilised a quadratic interpolation method to derive intermediate values from stored discrete magnetisation data [42]. Fulton described a CAD program developed for designing SR machines in [43]. The use of customised cubic splines was proposed by Pulle [44].

While all the methods described above use functions of flux linkage against current with rotor position as a parameter, Miller and McGilp proposed to use functions of flux linkage against rotor position with current as a parameter [45], which was claimed to be more efficient.

1.2 Single-phase SR machines: high-efficiency multi-pole machine

Most of the SR machines studied, including ones described above, have three or more phases. This is due to the fact that single-phase and two-phase motors require some starting assistant because of the existence of torque dead zones. The torque dead zones may also lead to discontinuous torque, possibly producing large ripples. These disadvantages make the motors difficult to use in applications that require constant torque or speed, for example in computer disk drive, video, or audio equipment. On the other hand, single-phase and two-phase SR motors are advantageous because of the following points:

- Fewer connections between motor and converter
- Fewer switching devices
- Higher inductance ratio between the aligned and unaligned positions.

In the following, firstly, traditional types of *low-cost* single-phase SR machines are reviewed. Secondly, *multi-pole* single-phase SR machines for *high-efficiency* operation, which are the subjects studied in the thesis, are introduced and described.

Traditional low-cost single-phase SR motors

Traditionally, single-phase SR machines have been studied and developed as low-cost motors. Several single-phase SR motor designs have been reported. Early work on the single-phase SR motor was presented by Nasar [46]. He studied a uniformly tapered disk rotor type motor with output power of tens of watts.

An outer rotor, single-coil, radial-axial flux motor was proposed and studied by Bolton et al. for low-power, low-speed and low-cost applications [47, 48]. Further study and modifications of the single-phase motor were reported by Chan [49]. In

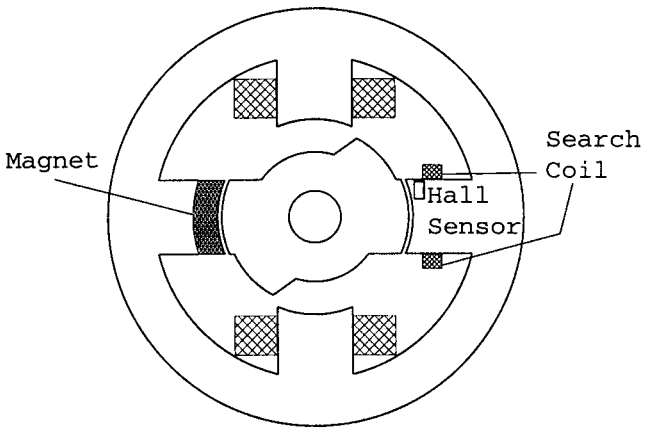

Figure 1.1: Horst's single-phase SR motor with one magnet

the motor, a parking magnet was considered for starting for low starting and friction torque applications. An analysis of a single-phase SR motor which has similar construction but fewer poles was given by Chan and Bolton for sub-kW, wide speed range applications [50].

Compter studied a microprocessor control system of a single-phase SR motor with parking magnets for starting [51]. Two magnets were used to hold the rotor at standstill in the position where sufficient starting torque was obtained. The study aimed to replace the AC series motor in domestic appliances with the SR motor.

Horst developed a single-phase stepped-gap SR motor with one parking magnet [52]. Fig. 1.1 shows the cross-section of the motor. The stator has four poles and windings are wound on two poles. The other two stator poles have the magnet and a Hall sensor or a search coil for rotor position detection, respectively. The magnet and stepped-gap rotor ensure the rotor position to be in the torque producing zone at standstill.

DC-bus voltage boost converters for single-phase SR motors have been studied [53, 54, 55]. The DC-bus voltage is boosted by means of capacitor boost circuits when the phase current builds up and down. The reduced rise and fall time of the motor current leads to a higher output power at a given speed. The simplicity of the single-phase SR motor contributes to the requirement of fewer additional components for the

implementation of the boosting circuits.

High-efficiency multi-pole single-phase SR machine

Most publications on the SR machine are on poly-phase machines and only limited numbers are on single-phase machines. Furthermore, the properties of single-phase machines with equal numbers of stator and rotor poles appear to have been largely overlooked — even for generators, where self-starting is not required. It is probable that an excessive preoccupation with torque ripple has discouraged the development of these machines, even though torque ripple is not a serious issue in many applications.

Harris et al. introduced a design procedure in which running torque of the SR machine is expressed as a fraction of torque produced by ideal "basic machine" with given tooth/gap geometry and rotor and stator volumes. "The basic machine" is a single-phase machine with equal numbers of stator and rotor poles ($N_s = N_r$). Four factors which limit the ideal torque to an actual value produced by a vernier type SR machine were introduced. The factors are: magnetic saturation; availability of excitation MMF; stator current waveform; and the fraction of the rotor that is interactive on average with the stator. Since these factors are less than one, it indicates that output power of a single-phase SR machine with $N_s = N_r$ will be larger than that of a vernier type machine. They also analysed SR machines with multiple teeth per stator pole. It was shown that those machines have a fundamental advantage over normal single-tooth designs, in that total slot MMF for given torque is substantially reduced [1]. The multiple teeth per pole design is discussed later in this chapter.

Hayashi and Miller described a multi-pole single-phase SR machine for a solar-powered vehicle application, where *higher efficiency* over a wide speed and torque range was required and some auxiliary starting method may be used [56]. The multi-pole single-phase SR machine was claimed to have higher efficiency because the larger slot area and shorter flux paths led to lower copper and iron losses. They examined

[1] M. R. Harris et al., private communication

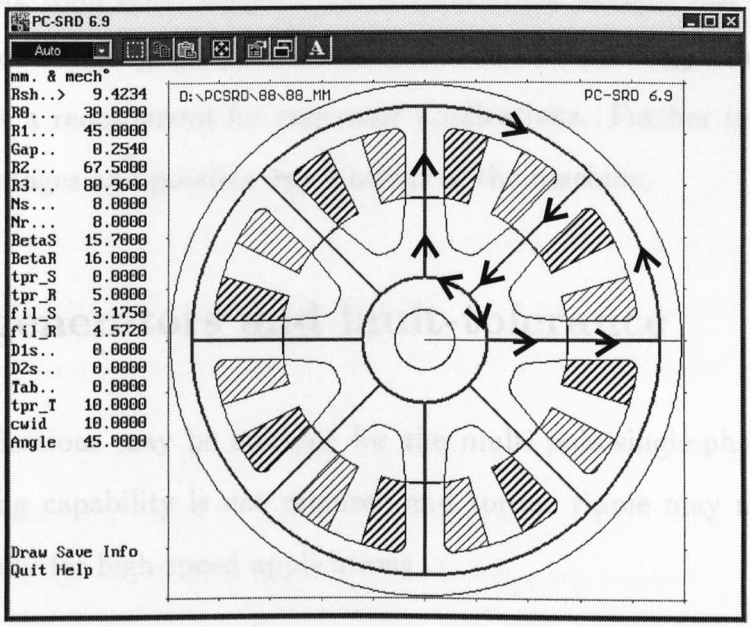

Figure 1.2: Single-phase 8/8-pole SR machine proposed by Hayashi and Miller

two single-phase SR machines, 6/6-pole and 8/8-pole, by computer simulation using the PC-SRD CAD program developed by SPEED laboratory at the University of Glasgow [57]. They also built a prototype single-phase 8/8-pole SR machine rated 0.8 kW at 2,000 rpm. The cross-section and flux paths of the single-phase 8/8-pole SR machine are shown in Fig. 1.2.

They made a comparison of the single-phase and equivalent poly-phase motors. The comparison was based on designs with identical stator outer diameters and stack lengths and the same air gap. Other parameters were determined for maximum performance for each machine. The result of the comparison of the single-phase 6/6 and 3-phase 6/4 SR motors was that the copper losses of the 6/6 SR motor were 60% and the iron losses were 71% of the 6/4 SR motor. Furthermore, the estimated efficiency of a prototype single-phase 8/8-pole based on measured magnetisation curves was over 90% over a wide speed and torque range.

The results by Hayashi and Miller suggest that the multi-pole single-phase SR machine can be used for high-power, high-efficiency applications, with the feature of

low-cost resulting from fewer connections and switching devices still remaining. Although multi-pole single-phase SR machines are not self-starting machines, starting capability is not a requirement for generator applications. Further investigation will reveal the advantages and possible applications of the machine.

1.3 SR generators and fault-tolerance

Generator applications may be suitable for the multi-pole single-phase SR machine since the starting capability is not required and torque ripple may not be a serious problem especially for high-speed applications.

In recent years, the concepts of all electric accessory engine (AEE) [58, 59] and power-by-wire (PBW) [60] for aircraft have been receiving considerable attention. In AEE, an electrical machine is integrated on an engine main shaft and acts as a starter/generator, eliminating mechanical gearboxes, and providing simplicity and design flexibility [59]. In PBW, electric actuators replace the hydraulic and pneumatic actuators currently used in aircraft, providing improved reliability and efficiency, and reduced maintenance [60].

The SR machine is a candidate for these applications because of its simplicity, ruggedness, high-speed capability, and efficiency. The application of the SR machine to the starter/generator system is presented in [61, 62, 63, 64, 5, 65] and seems successful.

Many applications like the aircraft ones require fault-tolerance. Reported studies on the fault-tolerant operation of the SR machine include the experimental work by Stephens [66], unbalanced force analysis by Miller [66], and dual-channel systems by Ferreira and Richter [67] and by Radun et al. [65].

The wind-driven generation of electric power is an important issue in the conservation of fossil fuels and the reduction of pollution. Furthermore, wind is widely available and perhaps the most predictable of natural energy sources [68]. Control methods of

electric generators for wind generation have been studied [69, 70]. In wind generation, variable speed operation is required for an optimum turbine tip-speed ratio, and the turbine spends much of its time in the lower part of its speed range. Therefore, a high efficiency at low speed is required for the electric machine. Fulton and Randall pointed out that the SR machine was advantageous for such applications [71]. Torrey and Hassanin designed a SR generator having 60 rotor poles, which is directly coupled to a wind turbine and is designed to produce 20 kW at a rotor speed of 120 rpm [72].

Although several papers have been published, the control of SR generators is not yet well established compared to that of SR motors. Further research is required to improve performance of SR generators. Detailed studies on faults in SR machines are also needed to reveal fault-tolerance of the machine in generating and motoring operations.

1.4 Multi-tooth per pole SR machine

The SR machine can be designed to have multiple teeth per stator pole and it has an advantage as mentioned before. Two-tooth per pole SR machines were studied by Finch et al. [73] and Lindsay et al. [74]. Hedlund proposed two- and three-tooth per pole designs [75]. Wallace and Taylor designed a multi-tooth SR motor for direct-drive robotics [16]. The number of teeth on the stator and rotor was increased to achieve an electromagnetic gearing and to eliminate a mechanical gear box which increases positioning error and losses.

The Megatorque motor is one of the multi-tooth per pole SR motors commercially available, which is currently manufactured by NSK Ltd., Tokyo, Japan [76, 77]. The motor is designed for low-speed high-torque applications typically for robotics, and was originally developed by Motornetics Corp., California, USA [78]. The motor has a ring shape rotor with 150 teeth and two stators both inside and outside the rotor. It is remarkable that the Megatorque motor is one of the most commercially successful

SR motors in history in spite of its unique design. The number of the Megatorque systems which have been sold is more than 90,000 since 1985 mainly in Japan, USA and Europe.

A few publications on the Megatorque motor are found. Wagner et al. analysed the slot shape of the motor by finite element analysis [79, 80]. A modelling and controller design for the motor were studied by Filicori et al. [81].

Although it is commercially successful and a few publications exist, the design method of the multi-tooth per pole SR motor is not well established. This is because of the existence of many geometrical parameters to be designed. The complexity of the motor geometry and nonlinearity make the use of analytical methods very difficult. A design guidance for such motors is required for certain criteria, e.g. for a maximum output torque.

1.5 Thesis objectives

In this section, the objectives of the thesis are defined.

Required SR technology, regarding especially single-phase machines and multi-teeth per pole machines can be summarised as follows.

The multi-pole single-phase SR machine has a potential for high-efficiency operation with lower cost resulting from fewer connections and switching devices. Further investigation is required to evaluate its advantages.

The multi-pole single-phase SR machine can possibly be applied to generator applications, where starting is not a requirement and the effect of higher torque ripple may be less significant especially at high speed. However, generating operation of the SR machine has not been established compared to motoring operation and research on generating operation is required.

Detailed analysis on faults in SR machines, including motoring and generating

operations, is needed because many applications require fault-tolerance.

Another requirement in SR technology is the establishment of design method of the multi-tooth per pole SR motor.

Therefore, the main objectives of the thesis are defined as follows:

- To investigate the performances of the multi-pole single-phase SR machine compared to poly-phase equivalents.
- To investigate the fault-tolerance of the SR machine.
- To investigate the SR machine, and particularly the single-phase machine, as a generator.
- To analyse an optimum geometry of multi-tooth per pole SR motors for maximum output torque.

The thesis thus includes two extreme examples of the design and application of the SR machine: a simple, high-speed, low-torque *single-phase SR generator*, and a complex, low-speed, high-torque *multi-tooth per pole poly-phase motor.*

1.6 Thesis structure

The overall structure of the thesis is described in this section. Fig. 1.3 shows the outline of the thesis structure. The literature related to each one of the topics is reviewed individually in each chapter. The list of the author's publications is given on page 252.

In chapter 2, advantages of multi-pole single-phase SR machines are investigated. The design and test results of prototype 8/8-pole single-phase and 8/6-pole 4-phase SR machines are also included.

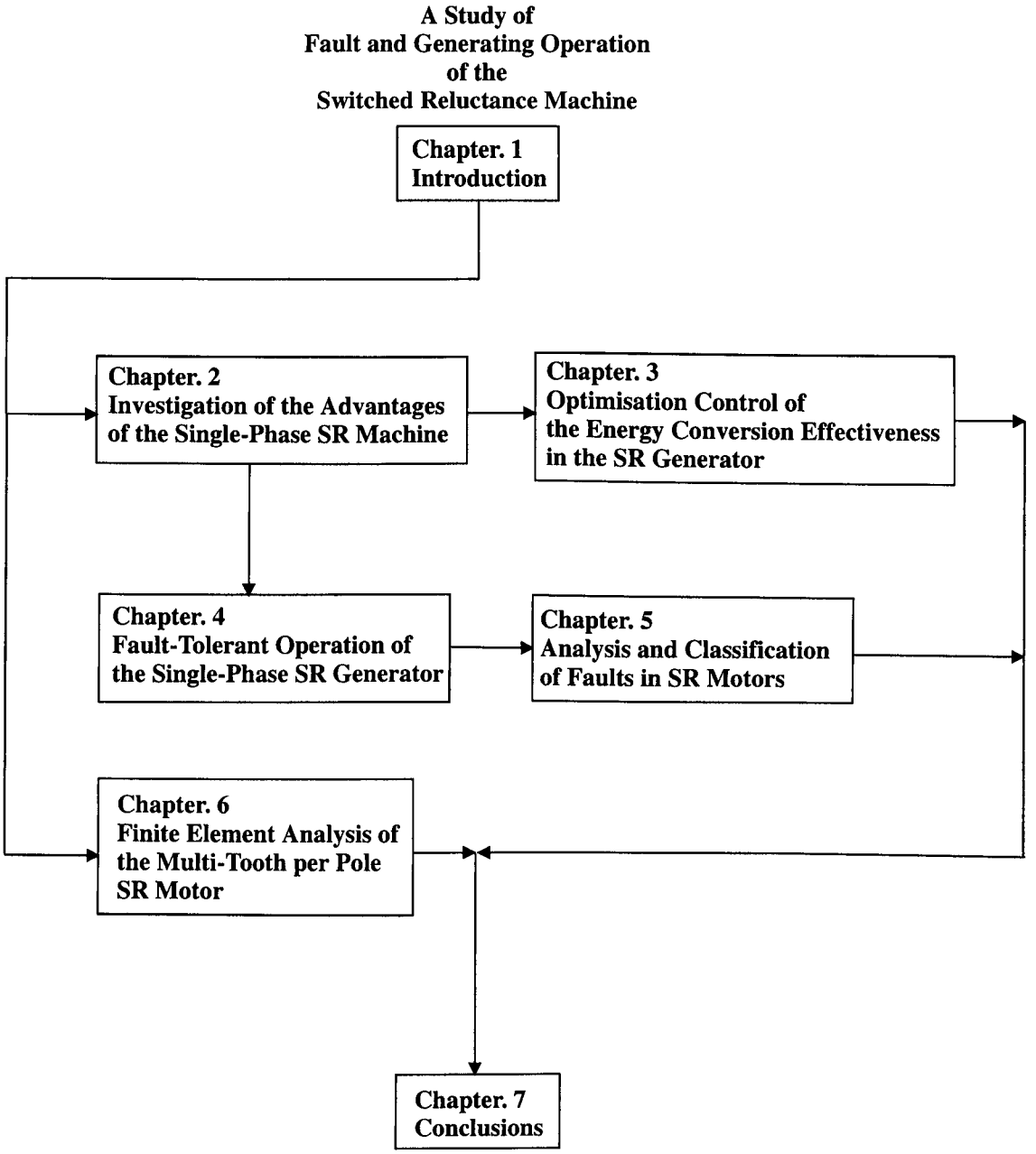

Figure 1.3: Thesis structure

Chapter 3 concerns the SR generator control. A control strategy which maximises the energy conversion effectiveness of SR generators is proposed and investigated. Simulation, experimental results, and implementation of the proposed system are included.

Chapters 4 and 5 concern faults in SR machines.

In chapter 4, fault-tolerant operation of the single-phase SR generator is discussed. A fault tolerant converter topology is proposed and operation under coil faults with the converter is analysed. The analysis is validated by experimental results.

In chapter 5, coil and converter faults in SR motors are analysed in detail by simulation. A new lumped parameter, magnetic equivalent circuit is described. A 3-ph 6/4 SR motor model implemented in Saber™ simulation package is used for the analysis.

In chapter 6, multi-tooth per pole SR motors are analysed by finite element analysis. Firstly, an existing commercial machine *the Megatorque motor* is analysed and problems in the design are pointed out. Then, an optimum design for the multi-tooth per pole structure is analysed.

Finally, overall conclusions are drawn and some possible future works are discussed in chapter 7.

1.7 Original contributions

The original contributions of the work are listed for each chapter.

Chapter 2 Comparison of single- and poly-phase SR machines

- It describes analytically why the single-phase SR machine can be designed to achieve higher efficiency over poly-phase equivalents.
- It shows using finite element analysis that the poly-phase equivalents have to have wider pole width for a comparable output with the single-phase

machine. This leads to a higher copper loss per output.

- It performs dynamic simulations to confirm the prediction.
- Prototype single-phase 8/8-pole and 4-phase 8/6 SR machines which have comparable geometry are built. Test results using the prototypes validated analysis and simulation results. It shows the single-phase prototype is 5% higher in efficiency.

Chapter 3 Optimisation control of the energy conversion effectiveness in the SR generator

- It points out how the DC-bus voltage and rotor speed affects the energy conversion effectiveness of SR generators by simulations.
- It proposes a control scheme which regulates the DC-bus voltage proportionally to the rotor speed for a maximum energy conversion effectiveness.
- It proposes a converter topology which regulates the load voltage at a constant value with only one additional switch required.
- It validates functionality of the proposed method by nonlinear computer simulations.
- It implements the proposed SR generator system for a single-phase 8/8-pole SR machine rated at 800W at 2,000 rpm using a microprocessor MC68332.
- It shows a good agreement between the experimental and simulation results.

Chapter 4 Fault-tolerant operation of the single-phase SR generator

- It proposes a fault tolerant converter topology for the single-phase 8/8-pole SR generator with a mimimum number of additional components.
- It shows the reduction in output power for the same coil current when some of the coils are disconnected for several winding configurations analytically and experimentally.

- Circuit equations under coil faults are derived and digital simulations are performed for a dynamic operation analysis under faults.
- The analytical and simulation results are validated by experiments using the SR generator system developed in chapter 3.
- The results show that the proposed SR generator system can separate faulty coils dynamically and keep generating half the normal power after coil faults.

Chapter 5 Analysis and classification of faults in SR motors

- A new magnetic equivalent circuit of the SR machine [2] is implemented in Saber™ simulation package.
- The model is validated by comparing with time-stepping finite element analysis.
- Possible winding and converter faults are listed and simulated for a 3-phase 6/4-pole SR motor for series and parallel connected phase coils, two pole magnetic configurations, and different operating conditions.
- A detailed analysis of the simulated results are given and the faults are classified in terms of impacts on operation.

Chapter 6 Finite element analysis of the multi-tooth per pole SR motor

- An optimum ratio of tooth width/tooth pitch for a maximum output is analysed by finite element analysis and it confirms previously published results.
- Output torque with different number of teeth per pole is analysed by half pole finite element models. It is found that the optimum number of teeth for a maximum torque varies with saturation level and the number of teeth should be chosen according to a given MMF value.

[2]This was originally proposed by Dr. P. C. Kjaer formerly with SPEED Laboratory and presently with ABB Corporate Research, Sweden.

- Practical 5- and 8-teeth per pole models are analysed by finite element analysis. It shows that increasing the number of teeth can be beneficial for increasing the average torque, however, the cost of higher losses and device ratings must be paid.

The work in chapter 3 is published in the paper No. 3 in the list of author's publications in appendix A on page 252. The work in chapter 4 is published in the papers No. 1, 2 and 5. The work in chapter 5 is published in the paper No. 4.

The thesis contributes an advance in SR technology through the findings above.

Chapter 2

Investigation of the advantages of the single-phase SR machine

This chapter investigates the advantages of single-phase switched reluctance machines (SRMs). The analyses demonstrate the potential of single-phase SRMs for a higher efficiency resulting from the larger slot area, lower iron volume and short flux paths. Computer simulations were performed using a CAD program PC-SRD and finite-element analysis. The simulation results agreed with the analytical ones and the efficiency of the single-phase 8/8-pole SRM was 3 to 5% higher than a comparable 4-phase 8/6 SRM. Prototype machines of 8/8 and 8/6 SRMs were built. Dynamic tests of the prototype machines verified the analytical and simulation results. It is concluded that the multi-pole single-phase SRM could be designed for higher performance over poly-phase machines for certain applications where the lack of starting capability is not a serious issue, like generator applications. It contributes a better understanding of single-phase SRMs by following a systematic approach.

2.1 Introduction

The single-phase SRM has been studied for low cost applications. The attractiveness of the single-phase SRM over poly-phase drives is the small number of semiconductor

switches and wires required, which is typically 2. This leads to a simpler system structure which results in lower cost and higher reliability. Simple outer-rotor type single-phase SRMs were investigated for applications in domestic appliances, where the SRM may be a reasonably strong competitor of the universal motor [49, 51].

Harris et al. proposed a method to assess the output power of normal poly-phase vernier type SRMs by comparing them with "the basic machine". The basic machine has the same number of rotor and stator poles ($N_r = N_s$), and the same N_r as the actual machine [82]. The multi-pole single-phase SRM discussed in the present paper is practically the same as the basic machine.

Hayashi et al. compared single-phase and poly-phase SRMs by computer simulations using a CAD software PC-SRD [56] and built a prototype 8/8-pole single-phase SRM for a solar car racing application.

One of the main disadvantages of the single-phase SRM is the lack of starting capability. Several starting methods have been reported [51, 52]. These methods require extra parts and may lead to a higher cost, and sacrifice some degree of output power for starting. Furthermore, the methods are only applicable where the required starting torque is relatively small. The starting issue is considered outside the scope of the thesis. For generators which are possible applications of the SRM [72, 71], starting capability is not a requirement.

The large torque ripple is also a potential drawback of single-phase SRMs. However, high speed makes the influence of torque ripple less significant.

Features of single-phase multi-pole SRMs are discussed in detail through analyses together with computer simulations using PC-SRD and finite-element analysis (FEA). The results are verified by measuring the performance of prototype machines of single-phase 8/8 and 4-phase 8/6 SRMs.

2.2 Analysis of the advantages of the single-phase SRM

In this section, it is shown why the single-phase multi-pole SRM could achieve a higher efficiency over the poly-phase SRM for the same output power.

2.2.1 Output power

For the SRM, the number of strokes per revolution N_ε is defined as

$$N_\varepsilon = mN_r \tag{2.1}$$

where m is the number of phases [83].

The number of active poles per stroke N_{active} is the number of poles which are excited at the same time in one stroke. N_{active} is equal to $N_s = N_r$ for the multi-pole single-phase SRM because all the stator poles are excited simultaneously, while $N_{active} = N_s/m$ for poly-phase ones

The energy conversion in one revolution W_{rev} is

$$W_{rev} = N_\varepsilon \times N_{active} \times W_{pole}. \tag{2.2}$$

where W_{pole} is the energy conversion in one stroke at one pole. The ratio of $N_\varepsilon N_{active}$ between the single- and poly-phase SRMs is calculated below. For the single-phase SRM

$$N_\varepsilon N_{active} = {N_s}^2. \tag{2.3}$$

For the poly-phase SRM, substituting $N_\varepsilon = mN_r$ and $N_{active} = N_s/m$ gives

$$N_\varepsilon N_{active} = mN_r\frac{N_s}{m} \tag{2.4}$$

$$= N_r N_s. \tag{2.5}$$

Here, possible N_r is

$$\begin{aligned} N_r &= N_s \pm (N_{active} \times k) && (2.6)\\ &= N_s \pm \left(\frac{N_s}{m} \times k\right) && (2.7)\\ &= \left(1 \pm \frac{1}{m} \times k\right) N_s && (2.8)\\ & \quad k = 1, 2, 3, ... \end{aligned}$$

For simplicity, only $k = 1$ is considered here, which covers most of possible designs, and $N_r = (1 \pm 1/m)N_s$. Here, negative sign is for SR machines with $N_s > N_r$ and positive sign is for ones with $N_s < N_r$. However, having a higher number of rotor poles than that of stator poles will result in a lower inductance ratio which may increase the converter volt-ampere requirement and decrease W_{pole}, although N_ε is increased. Therefore, only machines with $N_s > N_r$ are considered here. This gives that:

$$\begin{aligned} N_\varepsilon N_{active} &= N_r N_s && (2.9)\\ &= \left(1 - \frac{1}{m}\right) N_s^2. && (2.10) \end{aligned}$$

Therefore, the ratio of $N_\varepsilon N_{active}$ in the poly-phase SRM to the single-phase SRM K_{sp} is

$$K_{sp} = \frac{N_\varepsilon N_{active} \text{ of poly-ph SRMs}}{N_\varepsilon N_{active} \text{ of single-ph SRMs}} = 1 - \frac{1}{m}. \qquad (2.11)$$

K_{sp} is shown in Table 2.1 for different SRMs. The difference in K_{sp} shows that a vernier poly-phase SRM could produce only a fraction of output power which a single-phase SRM with the same N_s could, provided that W_{pole} is the same for both SRMs. An analysis on W_{pole} is presented in a later section using finite element analysis. K_{sp} represents the sacrifice in vernier motors for a continuous and starting torque which is normally required [82]. However, for certain applications where the torque ripple and the starting are not critical, e.g. generator applications, the single-phase multi-pole SRM has the potential to be a serious candidate.

The equation (2.11) and Table 2.1 show that the advantage in K_{sp} of the single-phase SRM over the poly-phase one decreases with the increase in the number of

Type	SRMs	K_{sp}
$N_s = N_r$	Single-phase	1
Vernier	3-phase	0.667
	4-phase	0.750
	5-phase	0.800
	6-phase	0.833
	7-phase	0.857

Table 2.1: K_{sp} for different SRMs

phases. For example, K_{sp} of the single-phase 6/6-pole SRM is 1.5 times as large as that of 3-phase 6/4 SRM while that of a single-phase 14/14 SRM is only 1.17 times of that of a 7-phase 14/12 one. The single-phase SRM may be more advantageous for higher speed applications where a lower number of poles is normally chosen.

2.2.2 Pole width

The single-phase SRM is larger in K_{sp} than poly-phase SRMs and the output power is expressed by equation (2.2). Thus, the single-phase SRM could produce a certain amount of output power with smaller W_{pole} than the poly-phase equivalent. Since W_{pole} is a function of the pole arcs the single-phase SRM could have narrower pole arcs when other dimensions are fixed. For the poly-phase machines, the pole arc has to be wider for a higher aligned inductance to compete with the single-phase ones. The single-phase SRM could reduce the losses with the narrower pole arcs.

Fig. 2.1 shows the magnetisation curves calculated by FEA in the aligned and unaligned positions for the single-phase 8/8 and 4-ph 8/6 SRMs whose geometry is identical except for the pole width. For the 8/8 SRM, curves for a pole arc of $\beta = 15.75°$ are shown, which is identical to the prototype single-phase machine described later. For the 8/6 SRM, curves for two cases are shown, one is $\beta = 15.75°$ and the other one is $\beta = 22.40°$ which is also identical to the prototype 4-phase machine described later. Cross-sections of the three SRMs are shown in Fig. 2.2. There is little difference

SRMs	MMF per pole	
	800 AT	1400 AT
8/8 ($\beta = 15.75°$)	1.21 (100%)	2.24 (100%)
8/6 ($\beta = 22.40°$)	1.73 (143%)	3.27 (146%)
8/6 ($\beta = 15.75°$)	1.25 (103%)	2.36 (106%)

Table 2.2: Energy conversion per stroke per pole [J] (Relative values to the 8/8 SRM with $\beta = 15.75°$ are also shown.)

between the magnetisation curves in the aligned position of the 8/6 and 8/8 SRMs with $\beta = 15.75°$. The unaligned inductance of the 8/6 SRM is approximately 30% lower than that of the 8/8 SRM because of the difference in N_r. The energy conversion at a pole per turn with MMF of 1400 AT is 2.24 and 2.36 J for the 8/8 and 8/6 SRMs respectively. The 8/6 SRM is about 6% higher than the 8/8 SRM. This observation proves that the single-phase SRM could produce more output by the ratio of K_{sp} than a poly-phase SRM with an identical pole geometry.

The poly-phase SRM requires wider poles in order to produce a comparable output power with a comparable single-phase SRM. Fig. 2.3 shows the energy conversion/pole/turn with the change in pole arc β for the 1-ph 8/8 and 4-ph 8/6 SRMs calculated by FEA. The range of β varied was determined for *reasonable* designs in which the pole width was not too narrow or too wide by the PC-SRD cross-section editor. For both machines, the energy increases proportionally to β. This is an indication that the increase in the flux-linkage in the aligned position dominates the increase in the amount of energy conversion.

From Fig. 2.3 for the 4-ph 8/6 SRM to have the same output compensating the difference in K_{sp} it may require β of 20.6° which is 1.30 times of that of the 1-ph 8/8 with $\beta = 15.75°$. The slot area of the 4-ph 8/6 SRM will be smaller resulting in higher copper losses for the same output power.

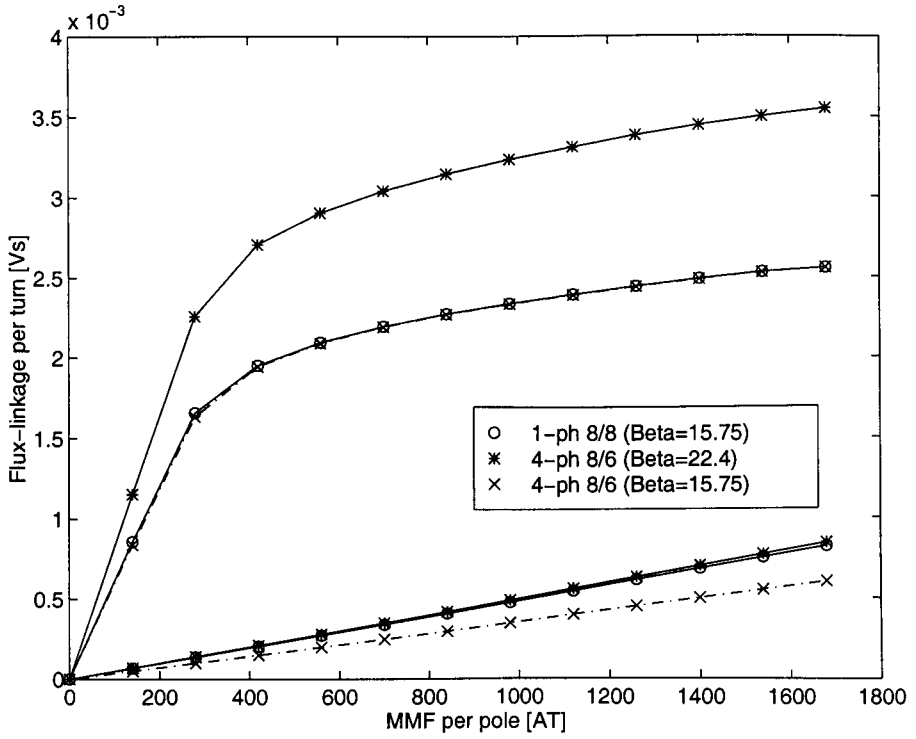

Figure 2.1: Magnetisation curves of 8/8 and 8/6 SRMs

2.2.3 The copper loss

The narrower poles increase the slot area and result in lower copper losses. The total slot area S can be calculated from the geometry:

$$S = (2\pi - \beta_s N_s) R_{1G} d + \pi d^2 \tag{2.12}$$

where β_s is the stator pole arc, N_s is the number of stator poles, d is the stator slot depth $d = R_2 - R_{1G}$, R_{1G} is the stator inner radius and R_2 is the stator slot bottom. For the same number of turns per pole, slot fill factor and current, the copper loss is proportional to the inverse of S. The change in the copper loss with pole arc β_s was calculated and shown in Fig. 2.4. The pole arc is normalised to $\beta_N = \pi/N_s$ and the copper loss is normalised to the loss with β_N. The dimensions of the prototype single-phase SRM discussed in the later section were used for R_{1G} and d. The normalised copper loss vs. normalised stator pole arc is independent of N_s and the result shown is applicable to SRMs with different N_s. The normalised copper losses for the single-phase

SRMs are also shown when the pole width is $K_{sp}\beta_N$ of the corresponding poly-phase SRMs. The curve predicts that the copper losses in the single-phase 8/8 SRM is 86% of those of the comparable 8/6 SRM.

2.2.4 Iron losses

The iron losses are proportional to the iron volume V_{iron}. V_{iron} is expressed as

$$V_{iron} = \{A + (BN_s + CN_r)\beta\} L_{stk} \tag{2.13}$$

where $A = \pi(R_3^2 - R_2^2) + \pi(R_0^2 - R_{sh}^2)$, $B = (R_2^2 - R_{1G}^2)/2$, $C = (R_1^2 - R_0^2)/2$, β is the stator and rotor pole arc, R_{sh} is the shaft radius, R_0 is the rotor slot bottom, R_1 is the rotor radius, R_{1G} is the stator inner radius, R_2 is the stator slot bottom and R_3 is the stator radius. When the pole width of a poly-phase machine is $1/K_{sp}$ times wider that of a single-phase one, the equation above always gives larger V_{iron} for the poly-phase machine. Lower iron volume will contribute to lower weight and material cost of iron and maybe to lower copper losses.

Fig. 2.5 shows typical flux waveforms in different parts of 4-ph 8/6 and 1-ph 8/8 SRMs [2, 84, 85]. The waveforms in the 1-ph SRM are simpler than those of the 4-ph one although this does not give a clear understanding of the amount of iron losses. The iron losses in the single- and poly-phase machines are calculated by a computer simulation in the later section.

Fig. 2.6 shows the flux paths for both machines (Dimensions are those of prototypes described later.). The 1-ph 8/8 SRM is assumed to have short flux paths. This can be achieved by connecting the coils such that adjacent poles have opposite magnetic polarity. The short flux paths help to reduce the iron losses [86].

The effects of iron losses on overall performance of the 8/8 and 8/6 SRMs may not be clear from the comparison in this thesis as the comparison is restricted at low speeds (under 4,000 rpm).

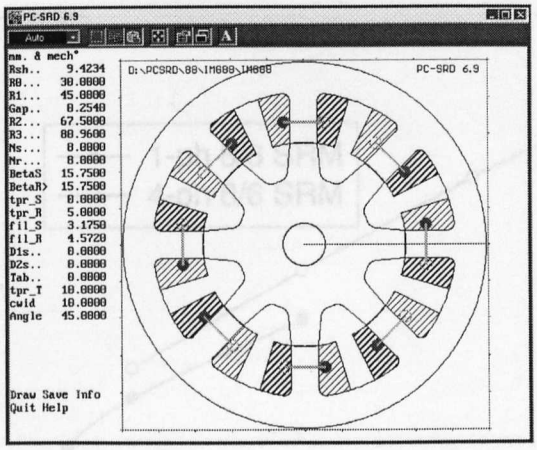

(a) single-phase 8/8 SRM with $\beta = 15.75°$

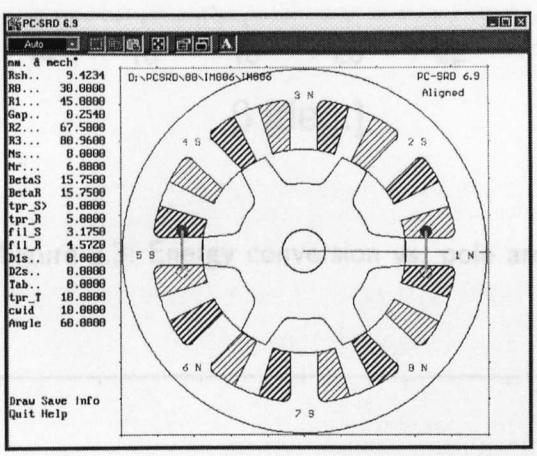

(b) 4-phase 8/6 SRM with $\beta = 15.75°$

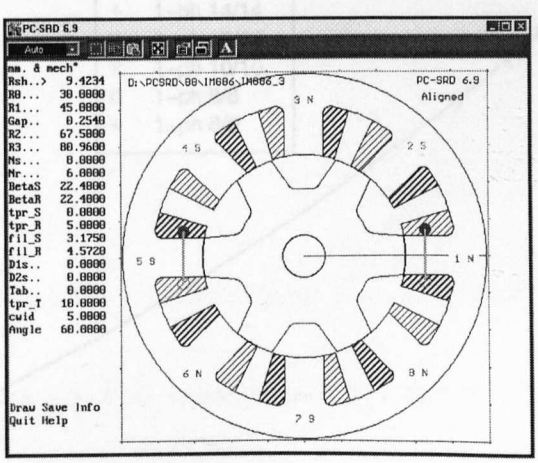

(c) 4-phase 8/6 SRM with $\beta = 22.4°$

Figure 2.2: Cross-sections of the 8/8 SRM with $\beta = 15.75°$ and 8/6 SRMs $\beta = 15.75°$ and $22.40°$

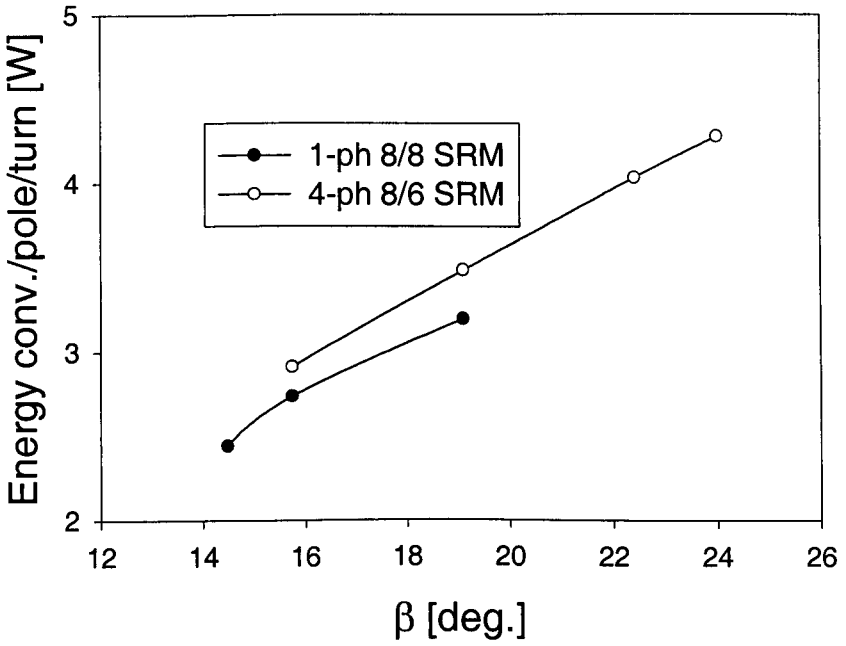

Figure 2.3: Energy conversion vs. pole arc

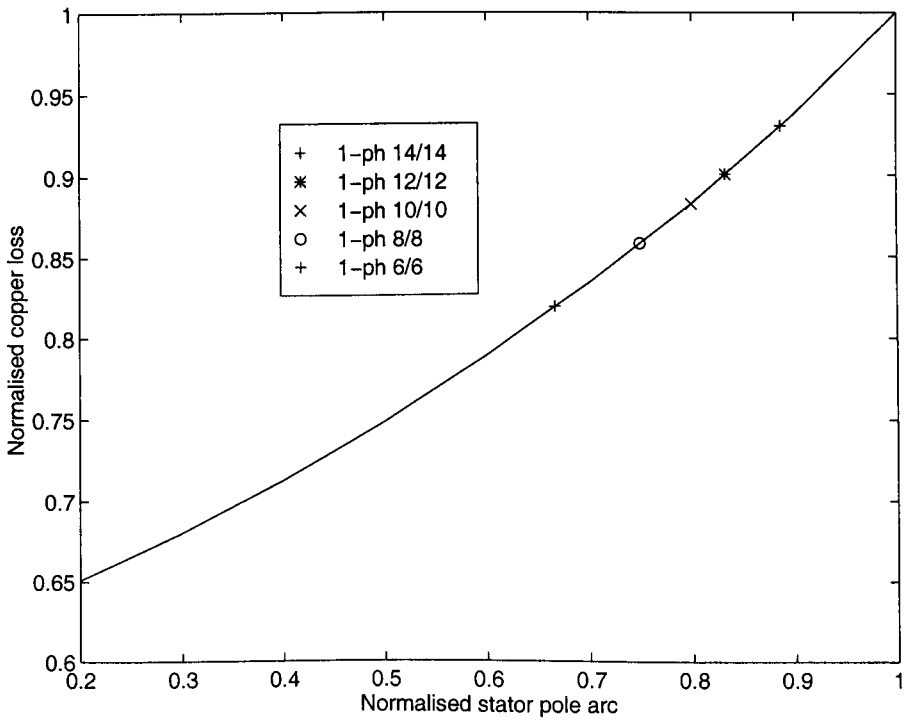

Figure 2.4: Pole arc vs. copper losses

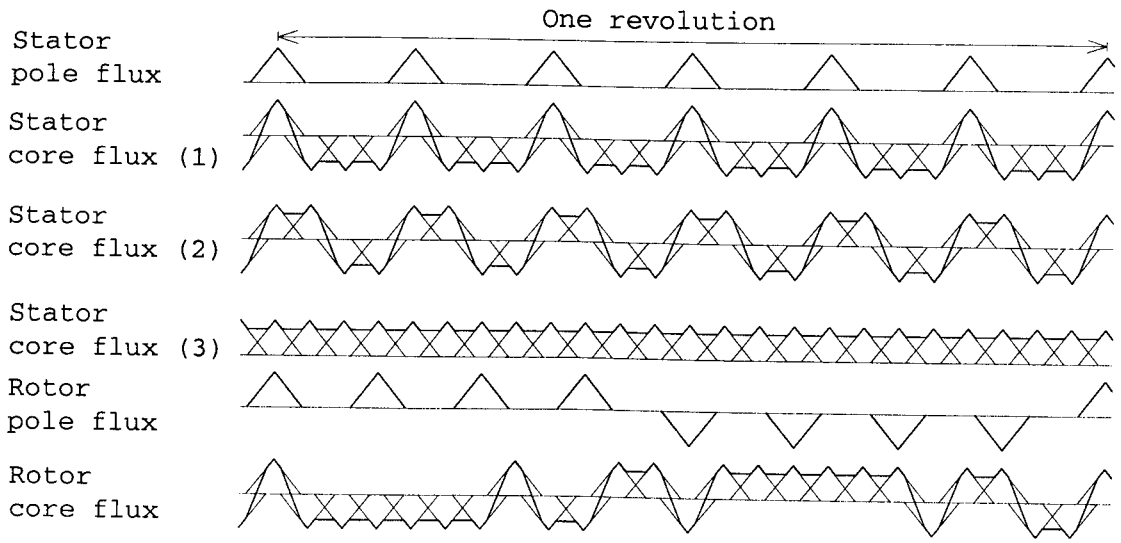

(a) Flux waveforms in 4-ph 8/6 SRM

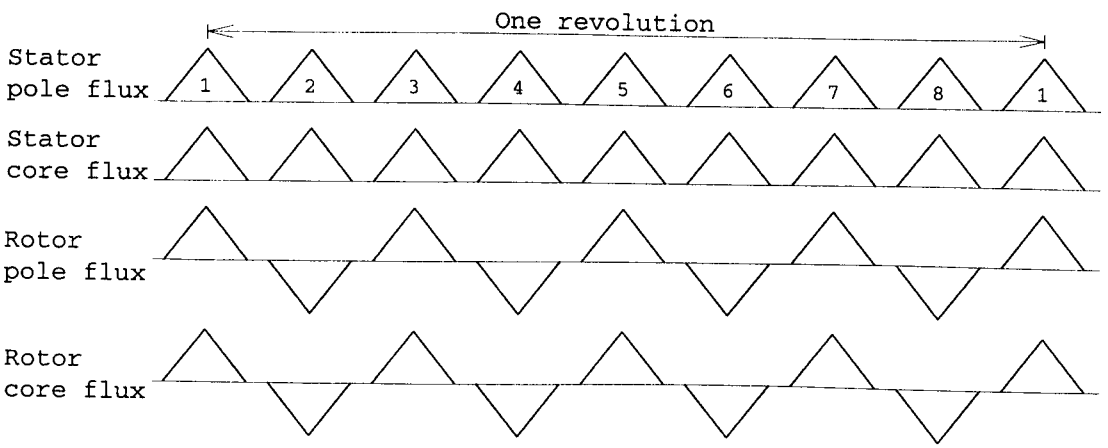

(b) Flux waveforms in 1-ph 8/8 SRM

Figure 2.5: Flux waveforms in 8/6 and 8/8 SRMs

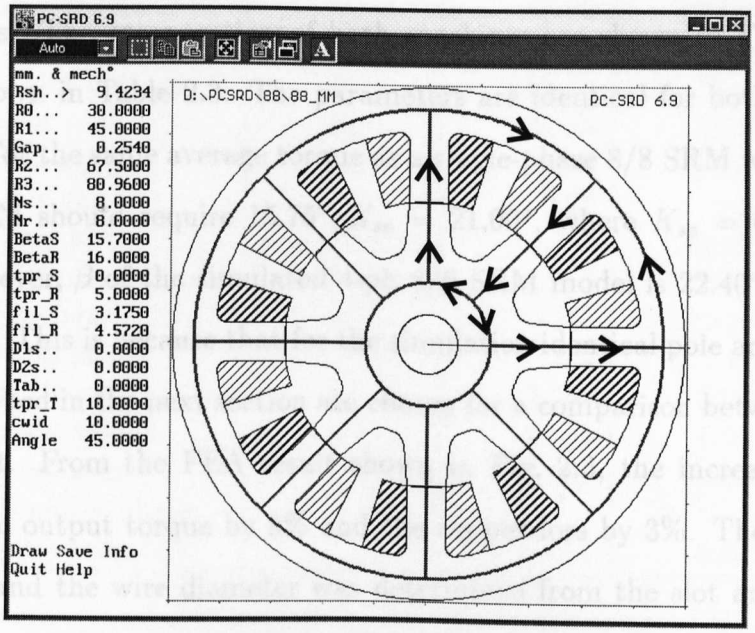

(a) 1-ph 8/8 SRM

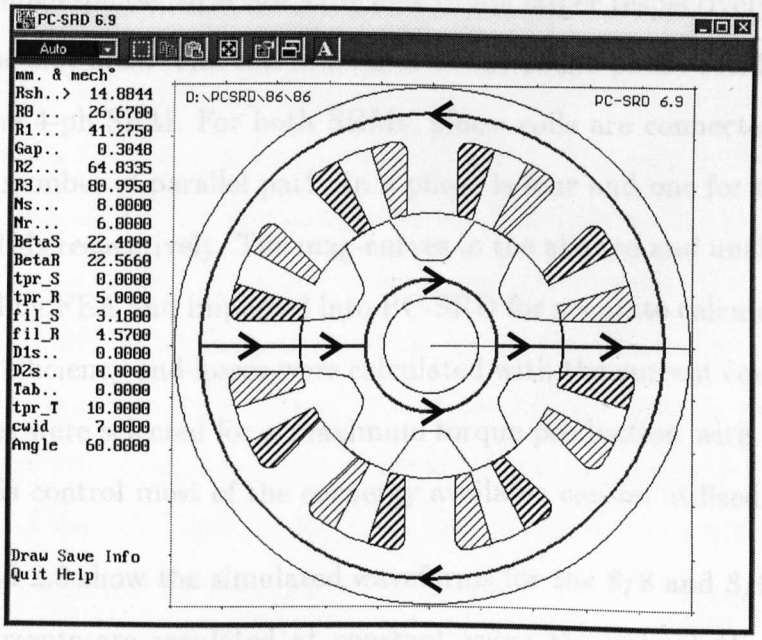

(b) 4-ph 8/6 SRM

Figure 2.6: Cross-sections and flux-paths of the SRMs

2.3 Computer simulations

The dynamic performances were simulated by PC-SRD for the single-phase 8/8 and 4-ph 8/6 SRMs. The cross-section of both machines are shown in Fig. 2.6 and the geometry is shown in Table 2.3. The parameters are identical for both SRMs except for N_r and β. For the same average torque as a single-phase 8/8 SRM with $\beta = 15.75°$, a 4-ph 8/6 SRM should require $15.75°/K_{sp} = 21.00°$, where $K_{sp} = 0.75$ for a 4-ph 8/6 SRM. However, β of the simulated 4-ph 8/6 SRM model is 22.40° and 7% wider than this value. This is because that for the simulation identical pole arcs to prototype machines described in the next section are chosen for a comparison between simulation and experiment. From the FEA result shown in Fig. 2.3, the increase in β by 7% will increase the output torque by 8% and the copper loss by 3%. The slot fill factor was set at 0.4 and the wire diameter was determined from the slot area, the slot fill factor and the number of turns per pole. The calculated wire diameter and the copper weight for the single-phase SRM are 9.5% and 18.5% larger respectively because of the difference in the slot area. The coil resistance of the single-phase SRM is 16.4% lower than that of the 4-ph SRM. For both SRMs, phase coils are connected two in series. Therefore, the number of parallel paths in a phase is four and one for the single-phase and 4-phase SRMs respectively. The mag-curves in the aligned and unaligned positions were calculated by FEA and imported into PC-SRD for accurate calculations [45]. The output torque, efficiency and losses were calculated with the current control drive. The switching angles were selected for a maximum torque production with a given current value. With this control most of the coenergy available can be utilised.

Figs. 2.7 and 2.8 show the simulated waveforms for the 8/8 and 8/6 SRMs respectively. The currents are regulated at constant value throughout the stroke. Thus, most of $i - \psi$ loops are utilised and the difference in the amount of energy conversion available in both SRMs will directly affect the performance calculated.

The performance calculated by simulation are shown in Figs. 2.9, 2.10 and 2.11. The simulations were carried out with coil currents of 20 and 40A which correspond

Geometry	Symbol	8/8 SRM	8/6 SRM	Unit
Shaft radius	R_{sh}	9.42	9.42	mm
Rotor slot bottom	R_0	30.00	30.00	mm
Rotor radius	R_1	45.00	45.00	mm
Stator inner radius	R_{1G}	45.25	45.25	mm
Stator slot bottom	R_2	67.50	67.50	mm
Stator radius	R_3	80.96	80.96	mm
Stack length	L_{stk}	50.04	50.04	mm
Air gap	g	0.25	0.25	mm
Pole arc	$\beta = \beta_s = \beta_r$	15.75°	22.40°	deg
Number of turns per pole	N_p	35	35	turns
Slot area	S	5.623×10^3	4.689×10^3	mm^2
Slot fill factor		0.4	0.4	
Wire diameter		2.263	2.065	mm
Copper weight		1.803	1.521	kg
Coil resistance		0.028	0.0335	Ω
Parallel paths/phase		4	1	
Phase resistance		0.014	0.067	Ω

Table 2.3: Geometry of simulated SRMs

to MMFs per pole of 700 and 1,400AT in Fig. 2.1. The currents did not reach the regulation set point over 3,000rpm. The average torques for both SRMs are comparable and the difference is less than 6% for the range of speed. The data in Tables 2.1 and 2.2 predicts approximately 10% higher output for the 8/6 SRM with 40A of coil current. The dynamic simulation and the static analysis agree with each other. The efficiency of the 8/8 SRM is 3% to 5% higher than that of the 8/6 SRM. The copper losses of the 8/8 SRM are approximately 85% of that of the 8/6 one because of the lower coil resistance. The reduction in the copper losses is close to the predicted one in Fig. 2.4. The iron losses of the 8/8 SRM are less than half of those of the 8/6 one. The short flux paths can be effective for reducing the iron losses.

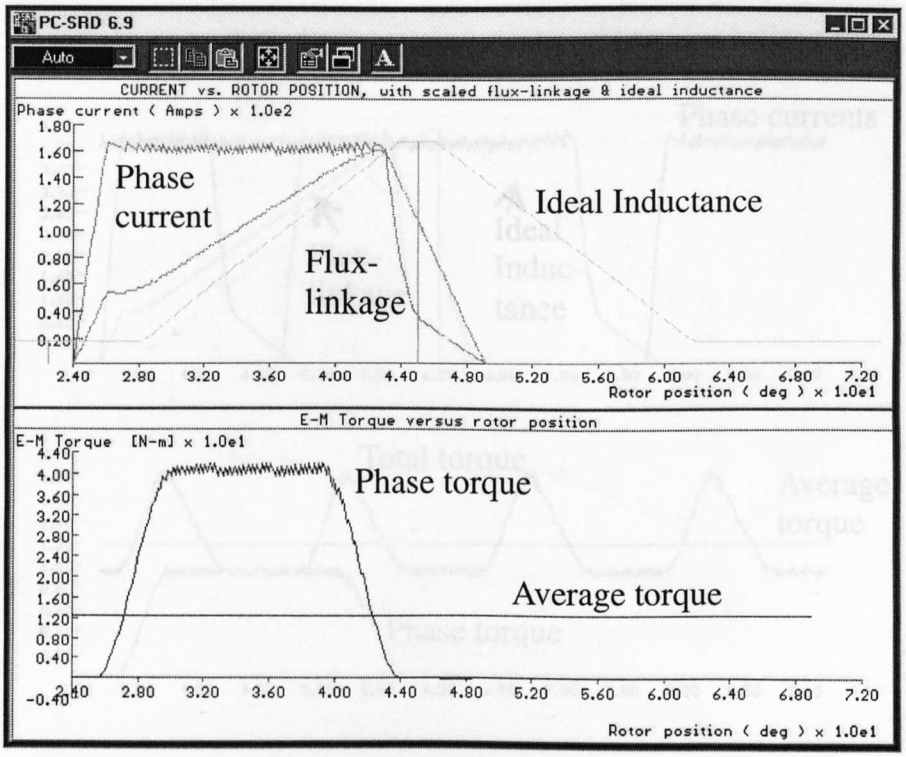

(a) Current and torque waveforms

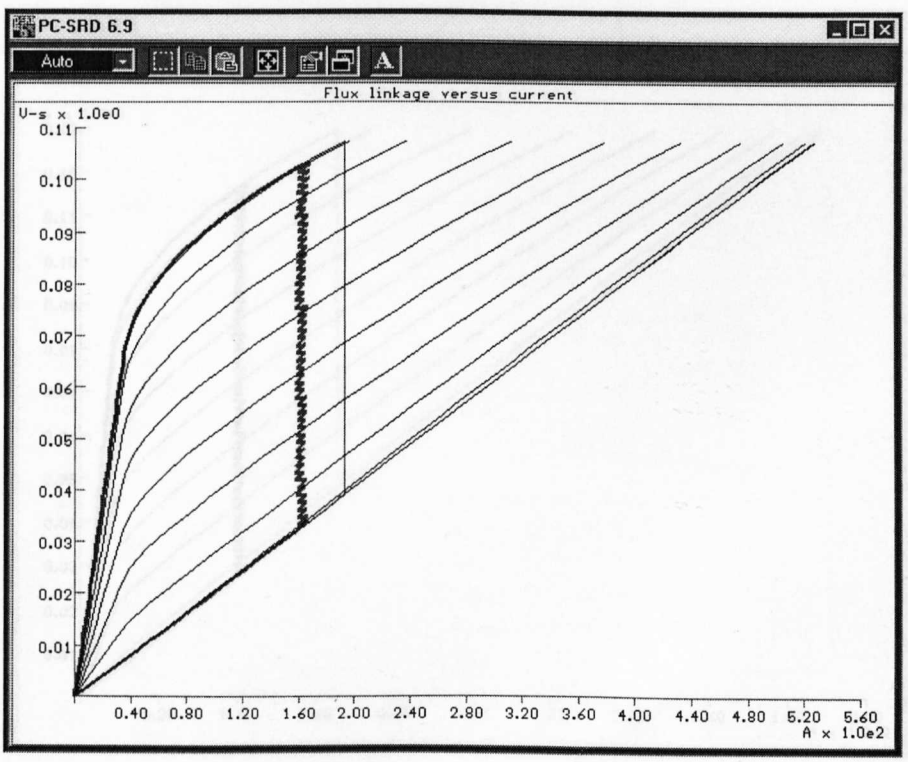

(b) $i - \psi$ loop

Figure 2.7: Simulated waveforms of the single-phase 8/8 SRM

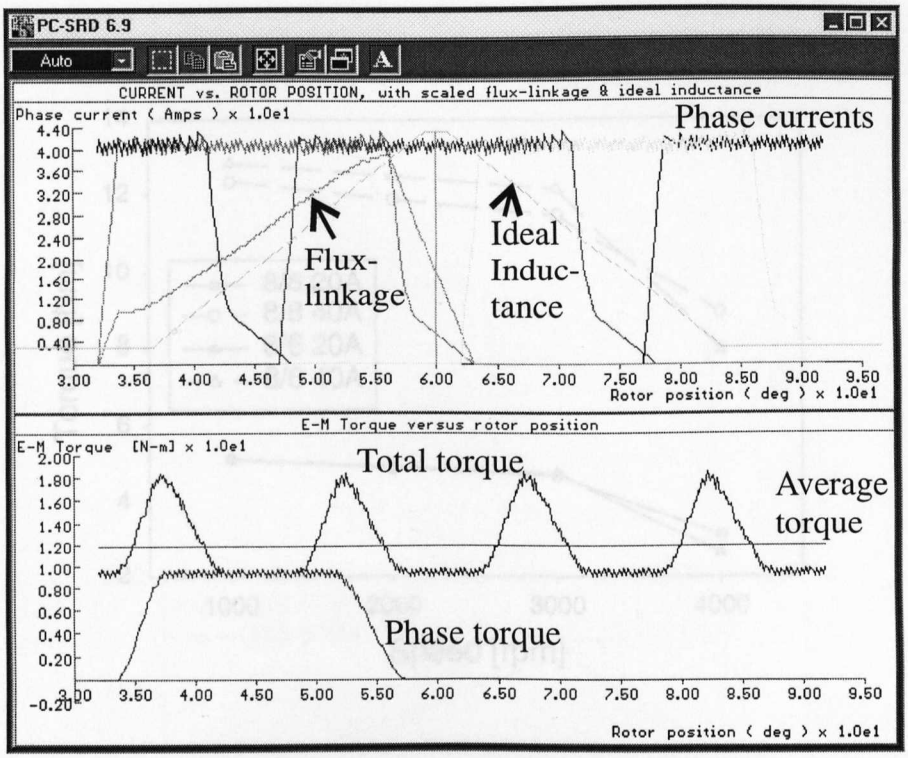

(a) Current and torque waveforms

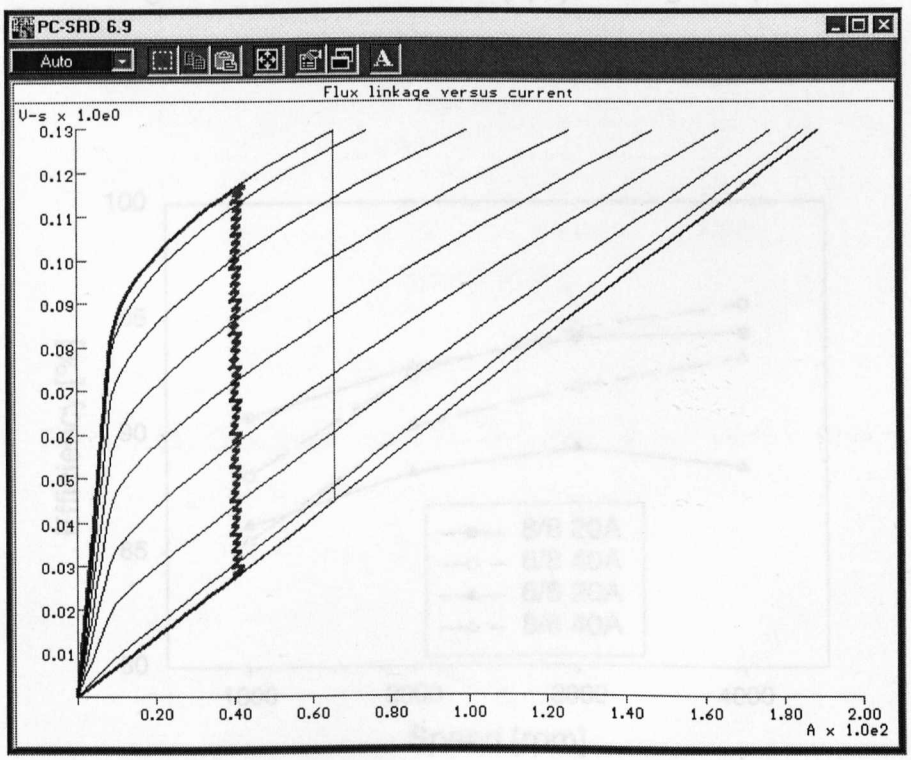

(b) $i - \psi$ loop

Figure 2.8: Simulated waveforms of the 4-phase 8/6 SRM

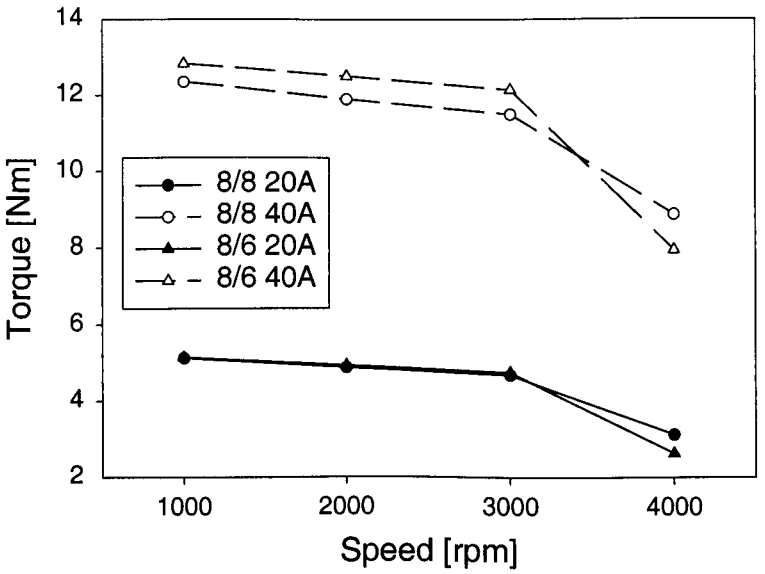

Figure 2.9: Simulation result (1/3), Average torque

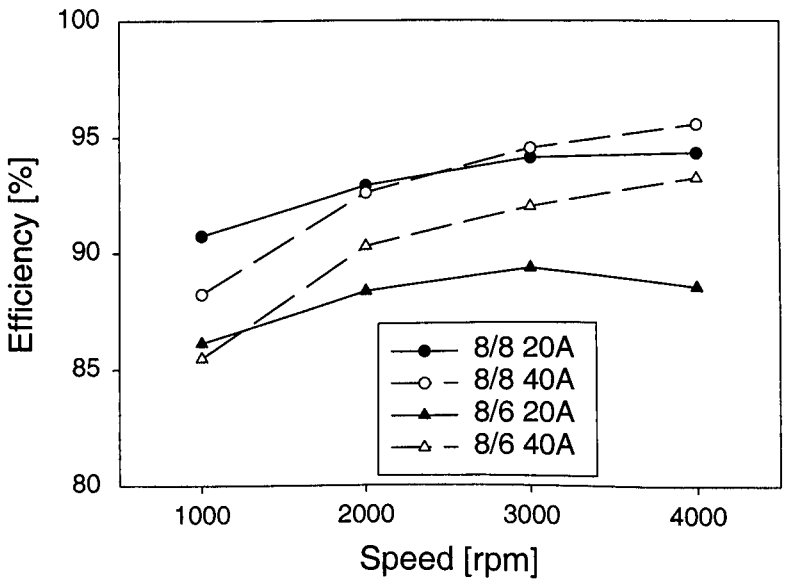

Figure 2.10: Simulation result (2/3), Efficiency

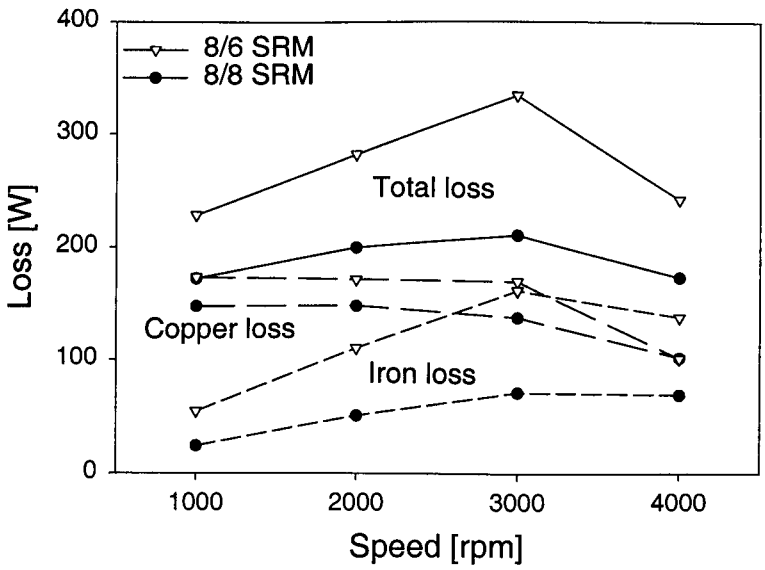

Figure 2.11: Simulation result (3/3), Losses at coil current=40A

2.4 Validation with prototype machines

Dynamic tests were carried out for the validation of the analyses and simulations using prototype machines.

2.4.1 The prototype machines

Prototype machines of the 8/8 and 8/6 SRMs were built [56]. The design of the 8/8 SRM is identical to that in the simulation while the design of the 8/6 SRM is slightly different. This was because commercially available laminations were used from a cost point of view. The design of the 8/6 SRM together with that of the 8/8 SRM is shown in Table 2.4. The cross-sections are identical to those in Fig. 2.6. One of the main differences in the designs is that the airgap g of the 8/6 SRM is 1.20 times larger than that of the 8/8 SRM. The smaller rotor radius makes the rotor volume smaller. The rotor volume of the 8/6 SRM is 0.84 times of that of the 8/8 SRM. These give the 8/6 SRM a slight disadvantage for the amount of output power. The ratios of stator yoke thickness to the stator pole width are 1.086 and 0.995 for the 8/8 and 8/6 SRMs respectively. The ratios of rotor yoke thickness to the rotor pole width are 1.660 and 0.725 for the 8/8 and 8/6 SRMs respectively. The rotor yoke thickness of the 8/8 is 1.75 times wider because a thinner shaft is used. The saturation level in the stator and rotor yoke sections in both SRMs should be lower compared to that in poles as the yoke thickness is more than half the pole width. Since the number of turns per pole of the 8/6 SRM is 1.486 times of that of the 8/8, a current required for the same pole MMF for the 8/6 SRM is 0.673 times for the 8/8 SRM. On the other hand, the coil resistance of the 8/6 SRM is 2.235 times of that of the 8/8. Therefore, an estimated ratio of copper loss of the 8/6 SRM to the 8/8 SRM is roughly $0.673^2 \times 2.235 = 1.012$ for the same pole MMF. It is expected that copper losses in both SRMs are approximately the same for the same pole MMF.

Fig. 2.12 shows photographs of the rotors and stators of the prototypes. Differences

Dimensions	4-ph 8/6	1-ph 8/8	Ratio of 8/6 to 8/8
R_{sh}	14.89 mm	9.42 mm	1.581
R_0	26.67 mm	30.00 mm	0.889
R_1	41.28 mm	45.00 mm	0.917
R_{1G}	41.58 mm	45.25 mm	0.919
R_2	64.84 mm	67.50 mm	0.961
R_3	81.00 mm	80.96 mm	1.000
L_{stk}	50.04 mm	50.04 mm	1.000
g	0.305	0.254 mm	1.201
β_s	22.40°	15.75°	1.422
β_r	22.57°	16.00°	1.411
N_p	52	35	1.486
Slot fill factor	0.368	0.330	1.115
Slot area	4.706×10^3 mm^2	5.622×10^3 mm^2	0.837
Wire diameter	1.628 mm	2.053 mm	0.793
Copper weight	1.355 kg	1.485 kg	0.912
Coil resistance	0.076 Ω	0.034 Ω	2.235
Parallel paths/phase	1	4	0.250
Phase resistance	0.152 Ω	0.017 Ω	8.941

Table 2.4: Design of prototype 4-ph 8/6 SRM

in the stator diameter, bore and pole width may be seen in Fig. 2.12 (a). The identical stack length and a slight difference in diameters of the rotors may also be seen in Fig. 2.12 (b).

Fig. 2.13 shows the measured magnetisation curves of the prototype machines. The curves match with the FEA results in Fig. 2.1 well. The magnetisation curves suggest the difference in design between the simulation and prototype is negligible.

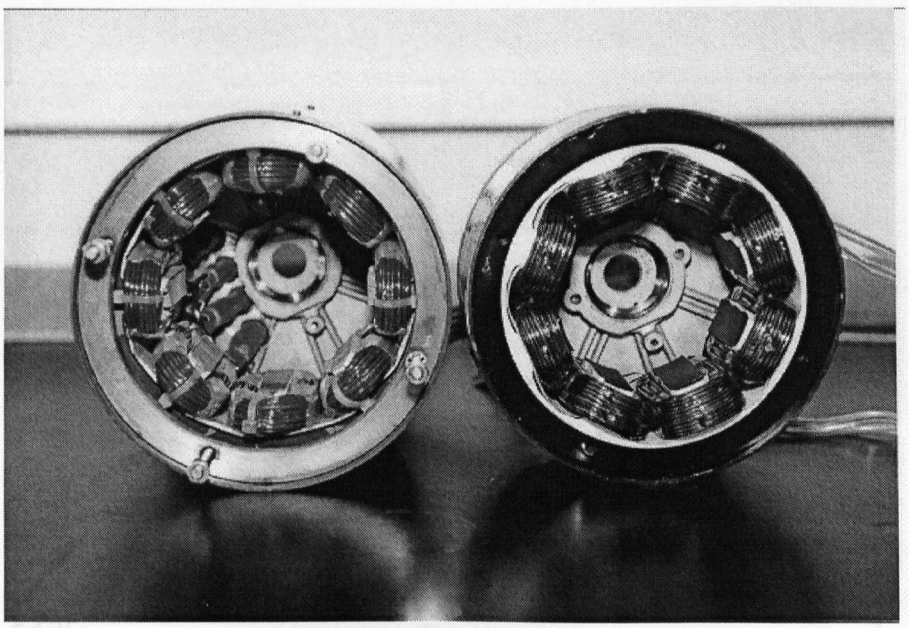

(a) Stators (left: 1-ph 8/8, right: 4-ph 8/6)

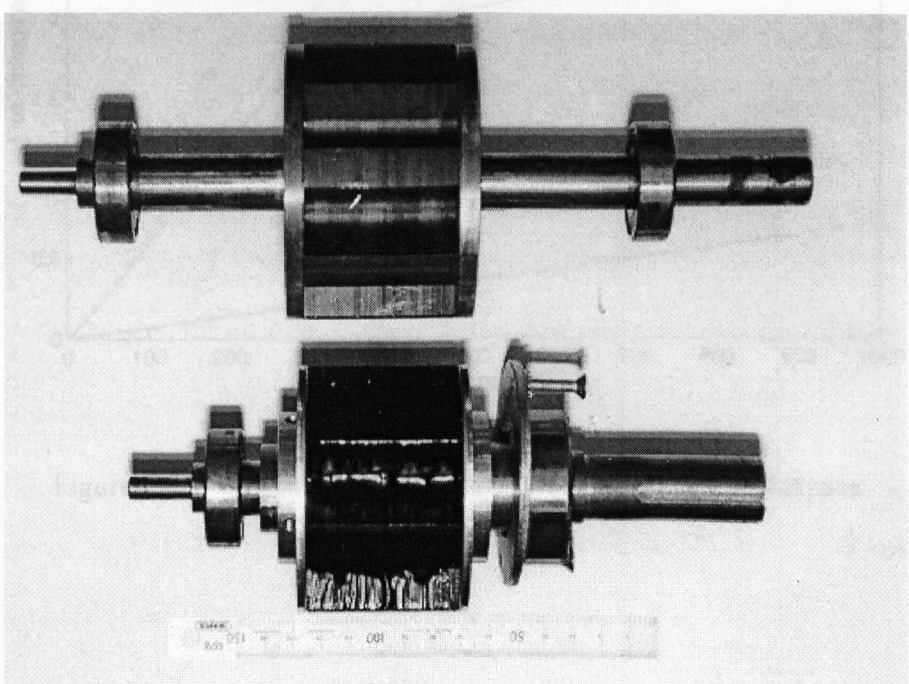

(b) Rotors (top: 1-ph 8/8, bottom: 4-ph 8/6)

Figure 2.12: Photographs of the prototypes

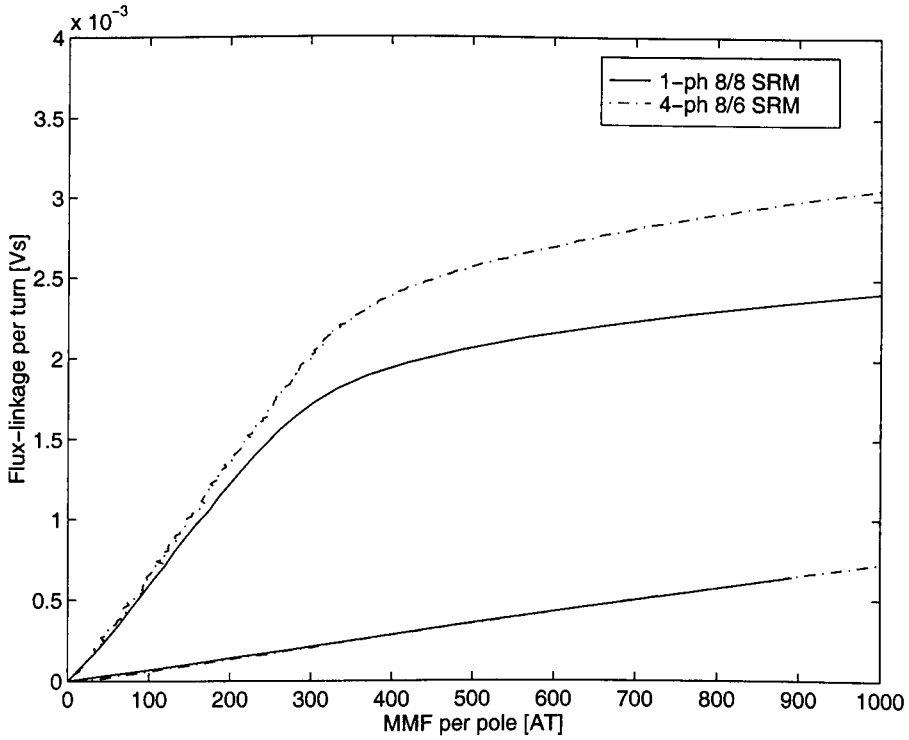

Figure 2.13: Measured magnetisation curves of the prototypes

2.4.2 Experimental setup and results

Fig. 2.14 shows the dynamometer used for the measurement of the performance of the prototypes. The test machines were mechanically coupled with a vector controlled induction motor. While the switching angles and current level were controlled in the test machines, the speed was maintained at constant values by the speed controller in the vector controller which controls the breaking torque produced by the induction motor. The DC input power to the converter P_{dc} was measured by DC voltmeter and ammeter. The converter losses L_{cnv} were estimated from the datasheet of the IGBTs and power diodes for the test conditions. The input power to the test SRMs P_{in} is calculated as

$$P_{in} = P_{dc} - L_{cnv}. \tag{2.14}$$

The mechanical output power P_m was calculated by measuring the mean output torque of the SRMs with a torque transducer. The mechanical and windage losses L_m were calculated from the torque when the system runs at constant speeds with the SRM converter switched off. The copper losses L_c were calculated from the winding resistances and the current waveforms measured with a digital storage oscilloscope. The iron losses L_i were calculated as

$$L_i = P_{dc} - P_m - L_{cnv} - L_c - L_m. \tag{2.15}$$

An example of the current waveform under the measurement is shown in Fig. 2.15. The current is regulated at a reference value of 20 A corresponding to a pole MMF of 700 AT by the PWM current regulator.

Fig. 2.16 (a) shows the measured output torque with a pole MMF of 700 AT. The value is shown on a torque per pole pair basis. The torques produced by both SRMs are comparable over the range of speed under 2,500 rpm. The cause of the drop in torque of the 8/8 SRM at 3,000 rpm was that the supply voltage was insufficient to overcome the back-EMF.

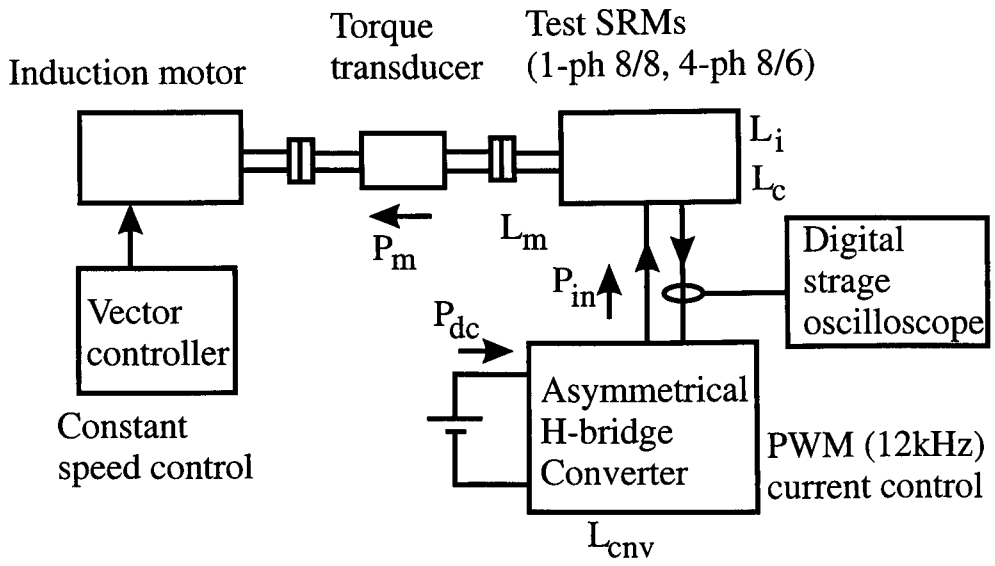

Figure 2.14: Dynamometer

The measured motor efficiencies are shown in Fig. 2.16 (b). The 8/8 SRM is higher in efficiency by 3% than the 8/6 one, which is close to the PC-SRD simulation results.

Fig. 2.17 (a) and (b) shows the measured motor losses per pole pair in the 8/8 and 8/6 SRMs respectively. The copper losses are at the same level for the both SRMs as expected. The difference in the iron losses leads to the difference in the total losses. The short flux paths and simpler flux shape lead to smaller iron losses. The slot fill factor of the 8/8 SRM is 0.329 which is 89% of that of the 8/6 SRM. The 8/8 SRM is able to reduce its copper losses by about 10% and achieve higher efficiency than the experimental result by achieving the same slot fill factor as the 8/6 SRM.

The iron loss of the 8/8 SRM was expected to decrease at 3,000 rpm as the current does not reach its set point because of a high back-EMF. However, Fig. 2.17 (a) shows that the total loss of the 8/8 SRM suddenly increases at 3,000 rpm resulting in the calculated iron loss also increasing. For torque and speed measurement a Vibro-meter TM207 torque transducer was used, whose rated torque was 10 Nm, accuracy was 0.1 Nm and speed resolution was 4 rpm. While the error in speed measurement should be less than 0.2% at 3,000 rpm, the error in torque measurement is about 15% as torque

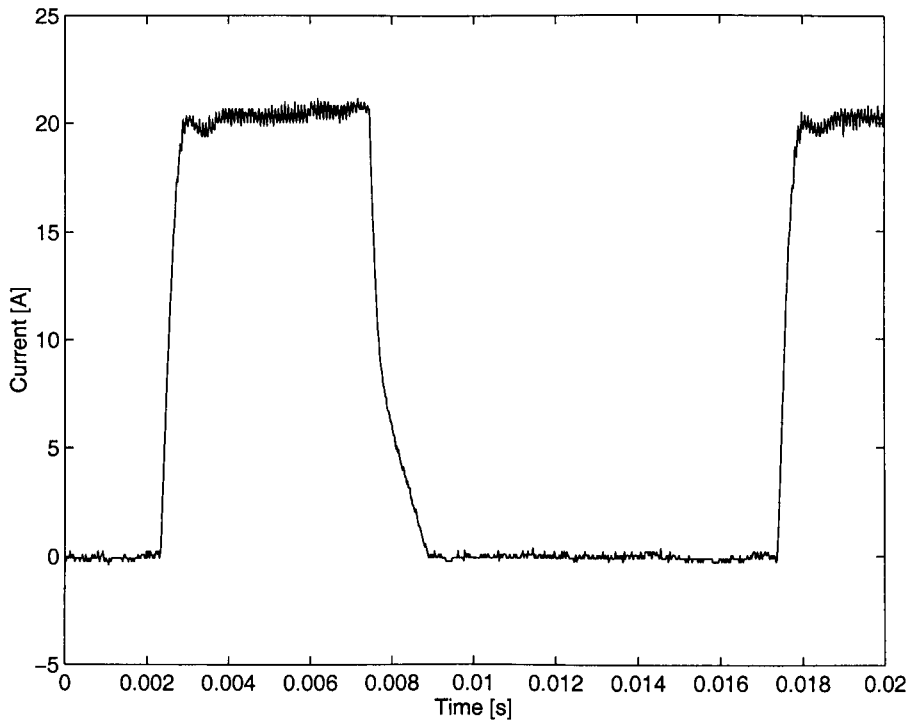

Figure 2.15: Example of current waveform under the measurement

drops at 3,000 rpm. The error in torque may have contributed the increased total and iron losses obtained in Fig. 2.17 (a). This is a limitation of the laboratory equipment available, although the error may be reduced by using a torque transducer with lower rated torque. Larger torque ripple of the 8/8 SRM may be one of the possible sources of the error.

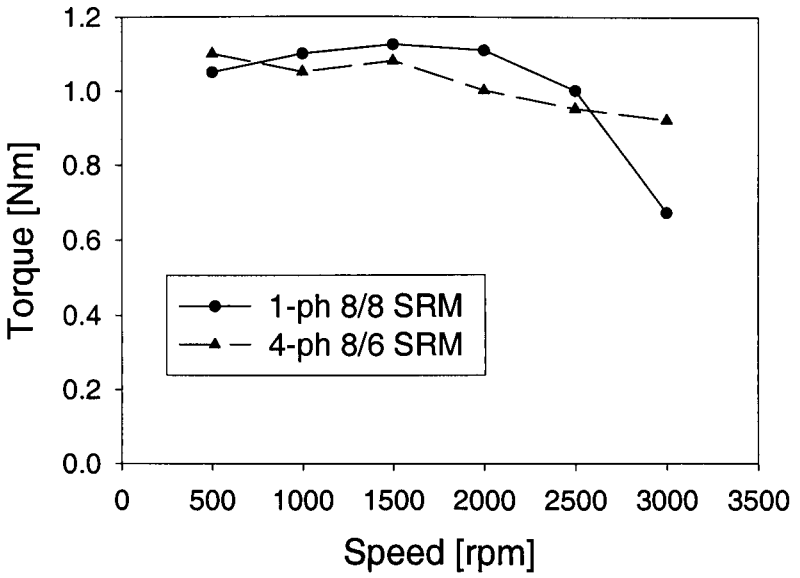

(a) Torque/pole pair

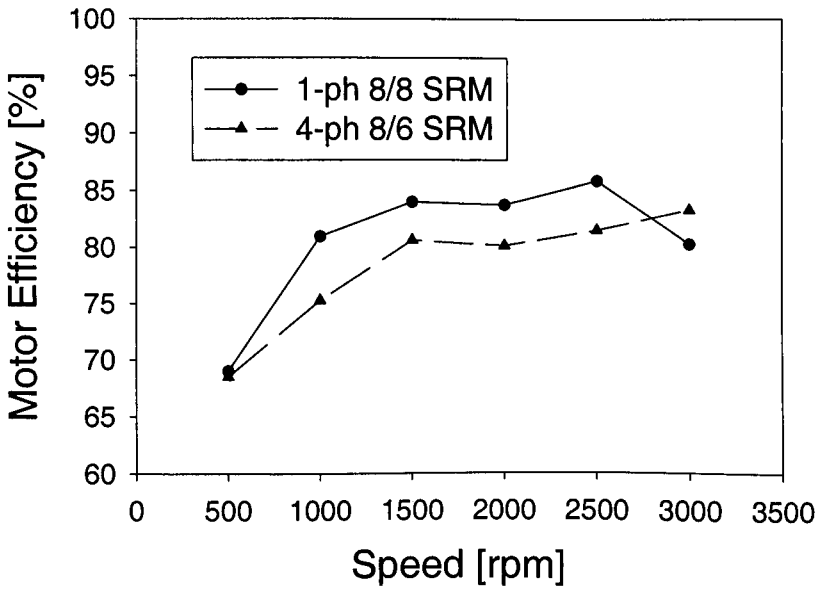

(b) Motor efficiency

Figure 2.16: Measured torque and efficiency

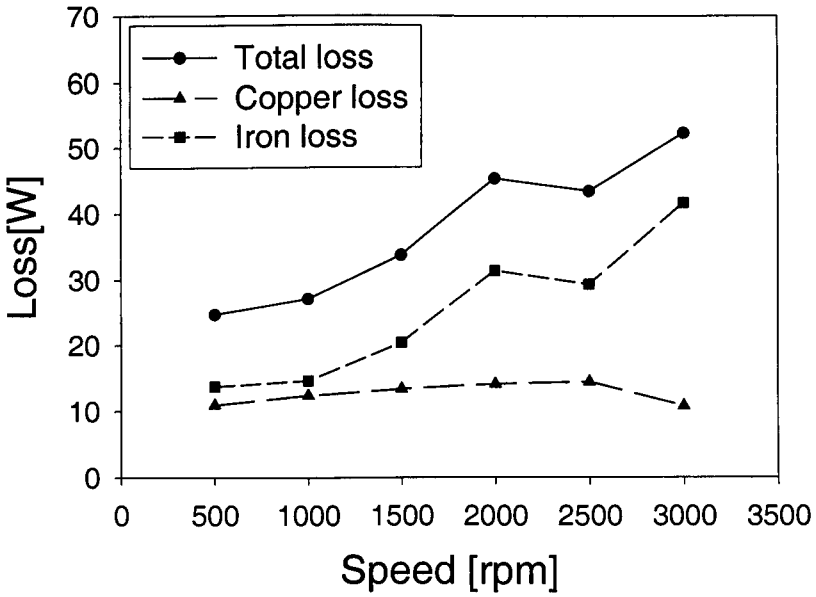

(a) 1-ph 8/8 SRM

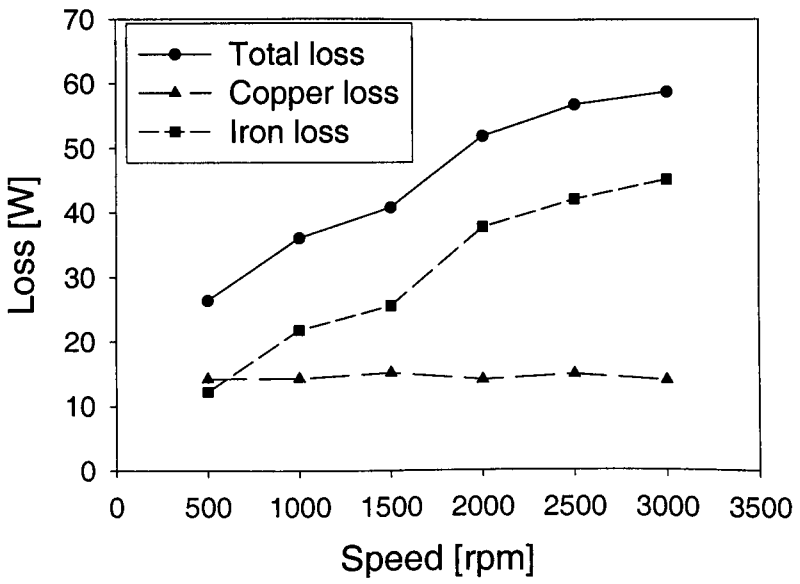

(b) 4-ph 8/6 SRM

Figure 2.17: Measured losses/pole pair

2.5 Conclusion

This chapter has investigated the advantages of the single-phase multi-pole SRM over poly-phase equivalents. The single-phase SRM can achieve a higher efficiency over poly-phase SRMs. The main reason for this is that the dynamic rotor utilisation factor is larger; hence, the pole width can be designed narrower for a given output; which in turn leads to a wider slot area and a smaller amount of iron, resulting in lower copper and iron losses. The analytical and simulation results agreed with each other and the efficiency of the single-phase 8/8-pole SRM was 3 to 5% higher than a comparable 4-phase 8/6 SRM. The dynamic and static tests of the prototype machines confirmed the analyses and simulations.

The analysis in the chapter does not include 2-phase SRMs and poly-phase SRMs with $N_r > N_s$. The 2-phase SRM does not have starting capability with the regular pole design, although it is possible to design self starting 2-phase SRMs with irregular designs such as the stepped gap and snail-cam. The irregular 2-phase SRM was not discussed as it may sacrifice the inductance ratio [83] resulting in a poor energy conversion capability. The regular 2-phase SRM may have either $N_s = 2N_r$ or $N_s = N_r$. The short flux paths configuration can be obtained with $N_s = N_r$. For both cases, the number of active poles per stroke N_{active} is $N_s/2$ and the number of strokes per revolution N_ε is N_s. Therefore, $N_\varepsilon N_{active}$ of the regular 2-phase SRM is always half that of the multi-pole single-phase SRM. This results in the regular 2-phase SRM having a significant disadvantage where energy conversion is concerned, although the energy conversion per stroke at a pole W_{pole} may be larger. Careful design of poly-phase SRMs with $N_r > N_s$ may provide good performance as N_ε can be increased although this in turn may increase the unaligned inductance. Further research on poly-phase SRMs with $N_r > N_s$ may be required.

It can be concluded that the multi-pole single-phase SRMs could be designed for higher performances over some poly-phase machines for certain applications where the lack of starting capability and the high torque ripple are not serious issues, like

generator applications. The study contributes a better understanding of the single-phase SRMs by following a systematic approach.

Chapter 3

Optimisation Control of Energy Conversion Effectiveness in the Switched Reluctance Generator

This chapter describes a method for controlling the switched reluctance generator (SRG) in order to maintain its current waveform close to the ideal "flat-top" shape, even when the speed of the prime mover varies over a wide range. This strategy maximises the energy conversion effectiveness of the SRG. Because the generated current waveform can not be controlled by chopping, it is necessary to vary the DC-bus voltage in proportion to the speed. In order to achieve a constant output voltage, it may be necessary to add a DC/DC converter at the output. The chapter includes simulation results and details of the design and test of a controller for a single-phase 8/8 SRG rated 0.8 kW at 2,000 rpm.

3.1 Introduction

The switched reluctance (SR) machine has been studied for generator applications especially where robustness, high speed and fault tolerance are important [5, 63, 87, 64, 62]. It has also been studied for wind energy generation [71, 72], in which the speed

range is wide and the operating speed is in the lower part of it for the majority of the time [68, 69].

The objective of the SRG control is normally to keep the DC-bus voltage at a desired value with the maximum efficiency. Several control methods of the SRG have been reported [5, 87, 88, 89, 61, 90, 91, 92]. A method for improving the overall drive efficiency of the SR motor with a variable supply voltage was reported in [93].

This chapter describes a control scheme of the SRG in which the DC-bus voltage is controlled with the rotor speed. With the SRG the current after turning-off the switches can not be controlled and is determined by the relationship between DC-bus voltage and back-EMF, which is a function of speed, current and machine parameters. The energy conversion by the SR machine is expressed by the current locus on the i-ψ plain. The ideal "flat-top" current which keeps a constant value from aligned to unaligned position maximises the energy conversion effectiveness with a given current whose amplitude is usually limited by converter ratings. It discusses a method to control the current waveform in order to suppress the peak current and maximise the energy conversion by controlling the DC-bus voltage of the SRG. The single-pulse control is used here. The switching angles are controlled in order to keep the DC-bus voltage at a command value. The angles are determined from the requirement of generating power by an analytical model called "the inverse machine model" proposed in [91].

A DC/DC converter may be necessary between the proposed SRG system and a load, which requires a constant voltage supply in many cases, since the DC-bus voltage changes with speed.

The effectiveness of the proposed method is first shown by simulation including the DC/DC converter stage. The proposed controller is implemented using a micro-controller "Motorola MC68332". The experimental results confirm the validity of the control scheme in transient states as well as steady state.

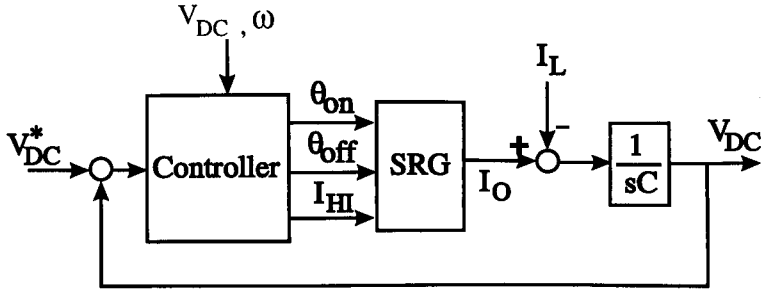

Figure 3.1: SRG controller

3.2 Review of SRG control

This section reviews literature on the SRG control. The control objective of the SRG is normally to control the DC-bus voltage at a desired value with the maximum efficiency. Fig. 3.1 shows a typical SRG control system. The DC-bus voltage V_{DC} is fedback and compared to its reference value V^*_{DC}. The controller regulates control variables such as the turn-on/off angles θ_{on}/θ_{off} and current set point I_{HI}. The controller may use V_{DC} and the rotor speed ω as input parameters. The SRG, which represents a converter and a SR machine in Fig. 3.1, generates current I_o. The difference between I_o and the load current I_L charges the filter capacitor C, the charge of which determines V_{DC}.

The necessity for a controller for the SRG was shown by Radun. He showed in [87] analytically that the SRG with fixed firing angles was unstable and the DC-bus voltage may increase or decrease exponentially depending on the load.

Relatively little has been reported on the design of the SRG controller. MacMinn [61] proposed a control scheme in which the turn-off occurs when the phase current reaches a "reference turn-off value" and the turn-on angle is controlled linearly with the difference between the reference value and actual value of the DC-bus voltage (Fig. 3.2 (a)). He showed the linearity between the turn-on angle and generated current by simulation and experiment. When the requirement of generating power is low another mode of control is introduced. This is because that the scheme keeps the current high even when the generating current required is small and this leads to reduced efficiency. In

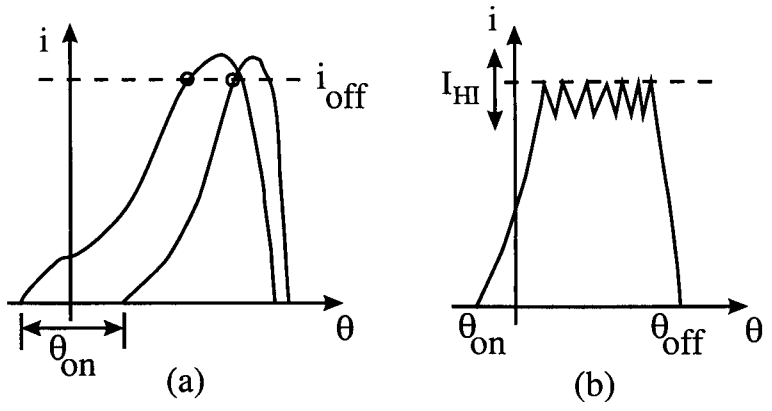

Figure 3.2: SRG controls

the low-power mode, the turn-on angle is fixed and dwell angle is controlled for the required output. The system efficiency of over 80 % was reported at a speed of 47,000 rpm and generating power of over 20 kW. Experimental results of the regulator's response to step changes in load were also reported. A good linear relationship seems to be achieved with the scheme. However, no explanation was given for determining the turn-off current level and turn-on angle and this may be the key element of the scheme.

Ferreira et al. controlled the output power by regulating the phase current level with fixed turn-on and turn-off angles [5]. The control is similar to the current chopping control in motoring mode; both power switches are on when the current is below the threshold and the switches are off when the current is above the threshold (Fig. 3.2 (b)). The threshold is the output of PI controller of the DC-bus voltage. They reported that if only the angle control was used, the output current is very sensitive to small changes in the turn-on and turn-off angles and poor voltage control would result in practice. A good linear relationship between the current command and the output power was shown. The system efficiency of over 85 % was reported at 41,000 rpm for the load of 20 to 30 kW. This scheme is simple to implement but the relationship between the threshold of the phase current and the output power must be obtained by experiment or simulation prior to implementation.

Cameron et al. [89] studied the control of an SRG system in electric power systems

by simulation. The power system includes the SRG and inverter, a filtering capacitor, a distribution network and a load. The network comprises a series resistor and inductor, while the load comprises a parallel resistor, capacitor and power sink. The average output current as a function of the turn-on and turn-off (dwell) angles was computed and mapped for the DC-bus voltage by simulation. For the DC-bus controller the turn-on angle is fixed and the turn-off angle is chosen to produce a desired current. The key feature here is that the DC-bus voltage controller which is designed to include the dynamics of the power system network.

Radun [90] proposed a scheme to linearise the relationship between the switching angles and the average generated current. When the DC-bus voltage V_{DC} increases the average generated current increases with constant switching angles. This nonlinearity is compensated for by introducing the quantity of V_{DC}/V_0, where V_0 represents the nominal DC-bus voltage. The turn-on and turn-off angles, that are determined from the function $F(\theta_{on}, \theta_{off})$, are multiplied by V_{DC}/V_0:

$$I_{ave} = \frac{V_{DC}}{V_0} F(\theta_{on}, \theta_{off}). \tag{3.1}$$

With this scheme, it was claimed that a linearised relationship between the switching angles and the average generated current was obtained over a wide range of the DC-bus voltage.

The use of the soft-chopping was proposed by Stephens et al. to control the current of the SRG at relatively low and medium speed where the current decreases with the application of the negative DC voltage [88]. Both switches are turned on at the turn-on angle and remain on until the current reaches the upper hysteresis level. When the current reaches the upper hysteresis level both switches are turned off and the current decreases. One switch is turned on when the current reaches the lower hysteresis level and the current freewheels through that device and the corresponding freewheeling diode. The process repeats until the turn-off angle is reached. This scheme is expected to reduce chopping frequency and hence reduce switching losses and result in lower current ripple.

Kjaer et al. derived an "inverse model" of the SRG which gives an analytical expression for the generated power. It was shown that the amount of energy generated with the SRG is determined only by the turn-off angle and the turn-off current level at a given speed and DC-link voltage and chopping is not necessary [91]. The limitation here is that the analysis assumed linear magnetic characteristics in the SR machine.

A technique to improve the efficiency of the SRG by on-line reduction of the reactive power flow was discussed by Kjaer et al. in [92]. In steady state, the turn-off angle is used to seek an optimum operating point while the DC-link voltage is regulated at a reference value by changing the turn-on angle.

All work described here assumes to control V_{DC} at a constant value. However, a constant V_{DC} will limit the speed range of the generating operation since the back-EMF is a function of speed. Some method of control which enables wide speed range operation is required especially for applications where the speed of prime mover varies over a wide range, like wind turbine generations.

3.3 Control of the current

3.3.1 Current waveform of SRG

An example of idealised current waveforms of the SRG with the single pulse control is shown in Fig. 3.3. The angles used are defined in Table 3.1. The peak occurs either at θ_{off} or θ_{1d}. Fig. 3.3 (a) shows the case where the current increases after turn-off the switches at θ_{off}, when the back-EMF in the coil is larger than the DC-bus voltage V_{DC}. In (b), the back-EMF and V_{DC} balance and the current stays constant until the pole overlap ends at θ_{1d}. In (c) the back-EMF is smaller than V_{DC} and the current decreases after θ_{off}.

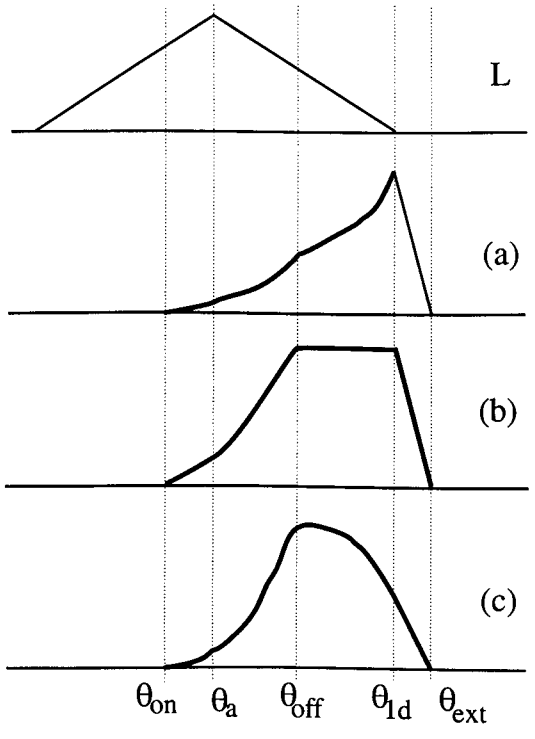

Figure 3.3: Energy conversion and current waveforms

The excitation penalty ε is defined as [83]

$$\varepsilon = \frac{P_{exc}}{P_{out}} \tag{3.2}$$

where P_{exc} is the mean electrical excitation power and P_{out} is the mean electrical output power. The waveform of (a) has the smallest ε and (c) has the largest. If the net generated current is the same in all the three cases, the current waveform of (a) is preferred since smaller excitation penalty reduces losses.

Fig. 3.4 shows the loci of the currents on the i-ψ plain when the peak values are the same. The energy converted by the SRG is proportional to the area enclosed by the loci. When the peak value of the current is limited, (b) is expected to generate the most energy.

θ_{on}	Turn-on angle
θ_a	Aligned position
θ_{off}	Turn-off angle
θ_{1d}	Angle at which pole over-lap ends
θ_{ext}	Angle at which the flux reaches zero

Table 3.1: Definition of the angles

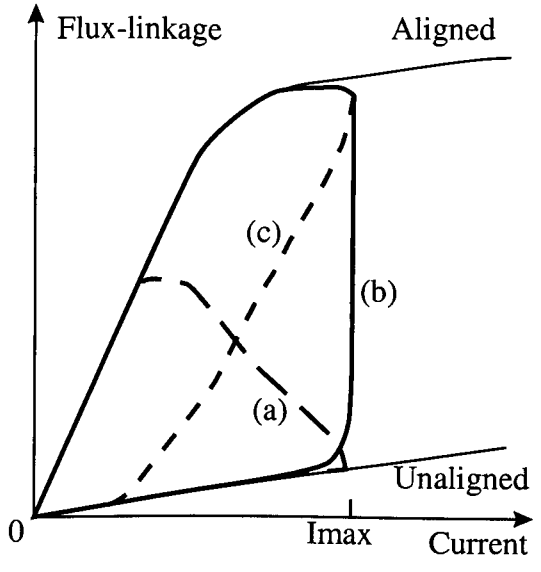

Figure 3.4: Energy conversion loop

3.3.2 Conditions for the current waveforms

In the idealised non-saturable machine the voltage equation of SRG is

$$V_{DC} = L\frac{di}{dt} + e \tag{3.3}$$

$$e = k\omega \tag{3.4}$$

$$k = i\frac{dL}{d\theta} \tag{3.5}$$

where e is the back-EMF. The speed at which $e = V_{DC}$ with rated current is called the base speed [83].

If V_{DC} is controlled as $V_{DC} = e$ the current keeps a constant value from the period from θ_{off} to θ_{1d} provided $\theta_{off} > \theta_a$. The thesis proposes to control V_{DC} with speed

in order to maximise the energy conversion effectiveness by keeping the condition of $V_{DC} = e$.

3.3.3 Peak value of the current

For case (a) in Fig. 3.3, the peak occurs at $\theta_{peak} = \theta_{1d}$ and expressed as:

$$\begin{aligned} i_{peak} &= \frac{\psi_{peak}}{L_u} \\ &= \frac{1}{L_u}\frac{V_{DC}}{\omega}(\theta_{ext} - \theta_{1d}) \\ &= \frac{1}{L_u}\frac{V_{DC}}{\omega}(2\theta_{off} - \theta_{on} - \theta_{1d}) \\ &= \frac{1}{L_u}\frac{V_{DC}}{\omega}\{\theta_{dwell} + (\theta_{off} - \theta_{1d})\} \end{aligned} \tag{3.6}$$

where L_u is the unaligned inductance and θ_{dwell} is the dwell angle ($\theta_{dwell} = \theta_{off} - \theta_{on}$). This equation shows that an earlier turn-off angle gives a smaller peak current for a fixed dwell angle (excitation period).

For case (b) the peak occurs at $\theta_{peak} = \theta_{off}$:

$$\begin{aligned} i_{peak} &= \frac{\psi_{peak}}{L_{peak}} \\ &= \frac{1}{L_{peak}}\frac{V_{DC}}{\omega}\theta_{dwell} \\ &= \frac{1}{L'}\frac{V_{DC}}{\omega}\frac{\theta_{dwell}}{\theta_{1d} - \theta_{off}} \end{aligned} \tag{3.7}$$

where L_{peak} is the phase inductance at θ_{off}:

$$L_{peak} = L'(\theta_{1d} - \theta_{off}). \tag{3.8}$$

This also shows that an earlier turn-off angle gives a smaller peak current for a fixed excitation period.

3.3.4 Proposed control of the SRG

The current waveform of SRG may be controlled as follows:

- The current waveform should resemble (a) in Fig. 3.3 when the generating current is small and the peak current, which is limited by the system, is less than its maximum value in order to minimise the losses. V_{DC} may be maintained at a nominal value.

- The current waveform should resemble (b) after the peak current reaches its maximum value in order to utilise the maximum energy available for a given maximum current. V_{DC} should be regulated to keep $V_{DC} = e$.

The drawback of the scheme is the necessity of an extra voltage regulator or DC/DC converter between the proposed SRG system and a constant voltage load. However, a simple step-down converter may be sufficient as shown in the following section. The thesis' limitation is that it does not try to reduce ε but to achieve the flat-top current for a maximum energy conversion. The method of controlling output power used here (the single-pulse switching angle control) may not be optimum. For better control further studies may be required.

3.3.5 Current waveform and generating energy

Fig. 3.5 shows an example of the current waveforms of the SRG as calculated by PC-SRD [57] for a speed of 10,000 rpm. A prototype 0.8 kW single-phase 8/8-pole SR machine was used for the simulation, with phase resistance = 0.016 Ω and aligned/unaligned inductance = 1.94/0.21 mH. Fig. 3.6 shows the loci of the currents on the $i-\psi$ plain together with measured magnetisation curves. Three cases are shown with V_{DC} =100, 270 and 350 V. The turn-off angles were adjusted to limit the peak value of the current around 65 A while the turn-on angles were kept almost constant. The conditions and data calculated are summarised in Table 3.2, where I_o is the net generated current, and P_o is the power generated. The switching angles are shown in electrical degrees.

The current at V_{DC}=100 V corresponds to (a), 270 V to (b) and 350 V to (c) in

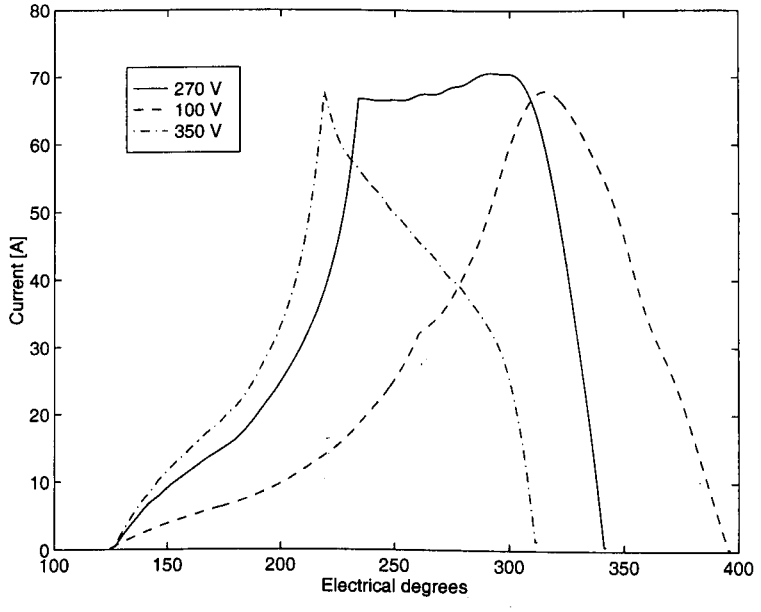

Figure 3.5: Example of current waveforms

V_{DC}	100 V	270 V	350 V
ε	0.256	0.350	0.525
I_o	12.0 A	11.5 A	5.2 A
P_o	1.20 kW	3.11 kW	1.81 kW
θ_{on}	124.0°	126.0°	126.0°
θ_{off}	260.0°	233.5°	218.5°

Table 3.2: Comparison of waveforms

Fig. 3.3. The excitation penalty with V_{DC}=100 V is 0.256 and approximately half that with 350 V. The power generated with V_{DC}=270 V is 3.11 kW, which is 2.6 times that with 100 V and 1.7 times that with 350 V. This is apparent from Fig. 3.6. The case of V_{DC}=270 V utilises most of the possible energy conversion with the given current (65 A), while the others do only part of that.

This observation supports the necessity of the DC-bus voltage control for a maximum energy conversion with the SRG system.

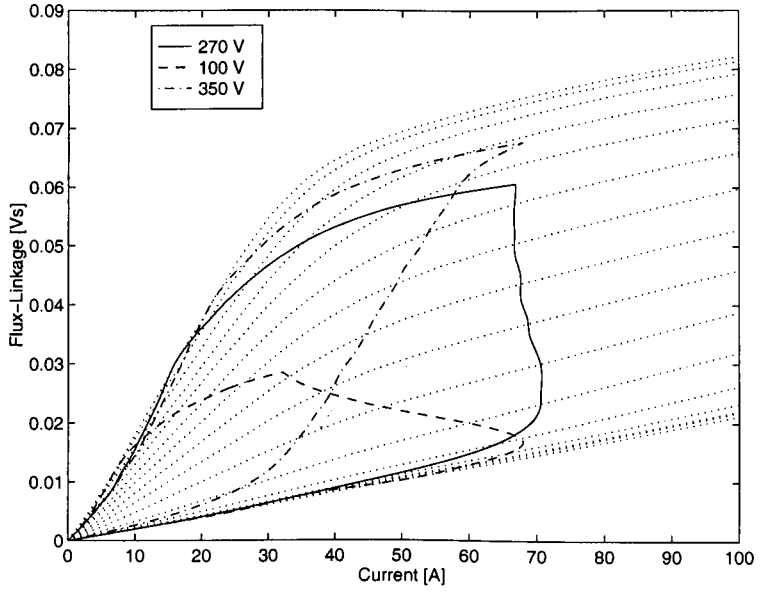

Figure 3.6: Example of energy conversion loops

3.3.6 Consideration on PWM control

The voltage PWM control can be used to regulate the current at a desired value by varying the average applied voltage in the SRG. However, many applications the SRG is likely to be used operate at very high speed which may make the application of PWM difficult. Another disadvantage of using PWM is that the excitation penalty is higher and operational speed range is narrow. This is analysed in the following. In the analysis the semiconductor switches and diodes are assumed to be ideal and voltage drops in those devices are neglected. The inductance profile is assumed to be linear. It is assumed that the turn-on is just before the aligned position and the current reaches its set point in the aligned position. The turn-off angle is assumed to be the position where the inductance reaches its minimum value.

In one PWM period the excitation current corresponds to the area A_1 and the generated current corresponds to A_2 in Fig. 3.7. Assuming that the duty cycle d is constant over a commutation period and the current ripple due to PWM is negligible

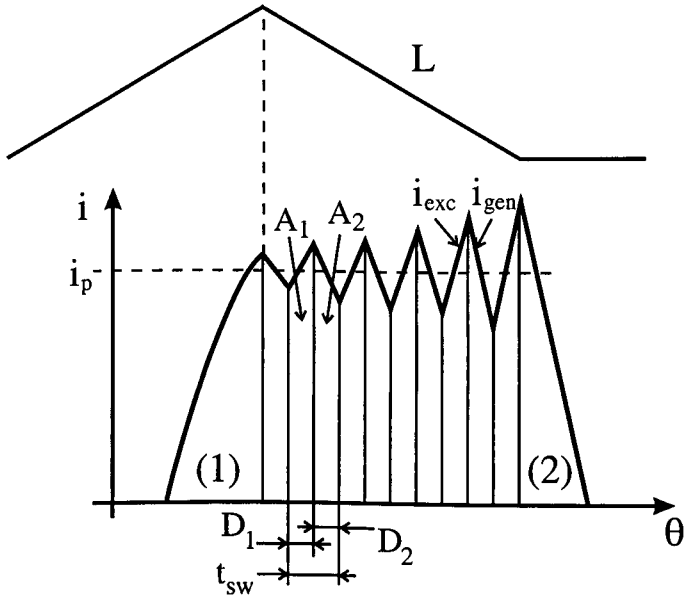

Figure 3.7: PWM control

compared to its average peak value i_p,

$$\begin{aligned} A_1 &= D_1 t_{pwm} i_p \\ A_2 &= D_2 t_{pwm} i_p \end{aligned} \tag{3.9}$$

where $D_1 = d$, $D_2 = 1 - d$ and t_{pwm} is the inverse of PWM frequency $t_{pwm} = 1/f_{pwm}$. The net generated current in one PWM period $I_{o,pwm}$ is:

$$\begin{aligned} I_{o,pwm} &= A_2 - A_1 \\ &= (D_2 - D_1)\, t_{pwm} i_p \end{aligned} \tag{3.10}$$

In the analysis, the initial excitation current (area indicated as (1) in Fig. 3.7) and the generated current after the turn-off angle (area indicated as (2)) are neglected. The ratio between the excitation energy and net generated energy ξ for the flat-top current with PWM is defined as:

$$\xi = \frac{D_1}{D_2 - D_1} \tag{3.11}$$

$$= \frac{d}{1 - 2d}. \tag{3.12}$$

During the excitation period, the circuit equation for a phase is expressed as follows:

$$V_{DC} = L\frac{di_{exc}}{dt} - e \tag{3.13}$$

where the resistance of coil is neglected and the back-EMF e is

$$e = i\left|\frac{dL}{d\theta}\right|\omega$$

where ω is the rotor speed. For generating operation $dL/d\theta$ is always negative and for clarity the negative sign is placed outside e. It should be noted that for the PWM control the condition of $|V_{DC}| > |e|$ must be always true otherwise the generated current is uncontrollable and increases during the freewheeling period. Since the current increases during the excitation period,

$$L\frac{di_{exc}}{dt} = V_{DC} + e > 0. \tag{3.14}$$

During the generating period, the equation is:

$$-V_{DC} = L\frac{di_{gen}}{dt} - e \tag{3.15}$$

and

$$L\frac{di_{gen}}{dt} = -V_{DC} + e < 0. \tag{3.16}$$

Assuming that the change in L in a PWM period is small and neglected, in order to keep the average current constant over a PWM period,

$$\begin{aligned}\left|\frac{di_{exc}}{dt} \times D_1 t_{pwm}\right| &= \left|\frac{di_{gen}}{dt} \times D_2 t_{pwm}\right| \\ |V_{DC} + e|\, D_1 &= |-V_{DC} + e|\, D_2 \\ (V_{DC} + e)\, D_1 &= (V_{DC} - e)\, D_2.\end{aligned}$$

By rearranging the equation above we obtain:

$$d = \frac{1}{2}\left(1 - \frac{e}{V_{DC}}\right). \tag{3.17}$$

From equation (3.12) if $d \geq 0.333$ then $\xi \geq 1$. In order to generate net energy which is greater than the excitation energy the condition of $d < 0.333$ must be satisfied.

Substituting this condition into equation (3.17) gives the condition of $e > 0.333V_{DC}$. Therefore, the condition to generate net power more than the power used for excitation with the PWM control is:

$$0.333\ V_{DC} < e < V_{DC}$$

and

$$0.333\ \omega_B < \omega < \omega_B \tag{3.18}$$

where ω_B is the base speed.

The result indicates that to generate net power more than the excitation power with PWM control the rotor speed must be higher than a third of the base speed and less than the base speed (speed range of 1:3). For applications which require wider operating speed range PWM control does not appear to be suitable.

I_o	Net generated current in one phase during a stroke
θ_{on}	turn-on angle
θ_{off}	turn-off angle
θ_a	aligned angle
θ_{1d}	angle at which overlap between poles finishes
L_a	aligned inductance
L_u	unaligned inductance
L'	inductance gradient with angle
L_{off}	inductance at turn-off angle

Table 3.3: List of principal symbols

3.4 Inverse machine model of SRG

For the simulation and implementation of the SRG system described in the following sections, the inverse machine model originally proposed by Kjaer et al. in [91] was used as the control low to determine the switching angles from generating current requirement. The scheme was chosen because it provides an analytical expression of generated power as a function of the switching angles, while other schemes described before all require simulations or experiments to determine the switching angles and/or current set point for required generating power prior to the implementation of the system.

In this section, the theory of the control using the inverse machine model is briefly reviewed. The detailed theory and derivation of the model are described in [91]. The symbols used are listed in Table 3.3.

3.4.1 Derivation of the inverse machine model

Fig. 3.8 shows the SRG circuit showing one phase-leg and Fig. 3.9 shows the phase currents, flux-linkage and idealised inductance. Both the converter and load are connected to the same DC-bus. The bus can be separated into two: one for the excitation and the other for the load for higher fault-tolerances [87]. However, the discussion here does not include such a converter configuration.

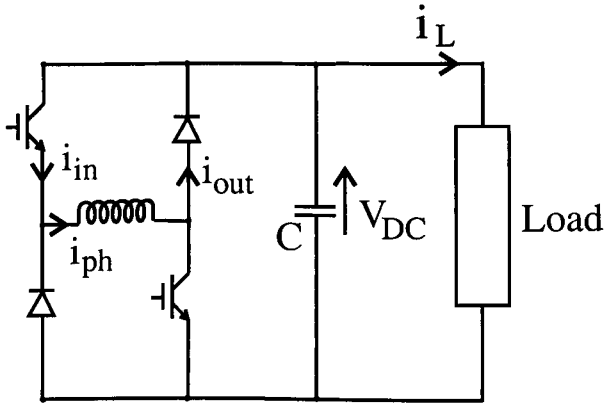

Figure 3.8: SRG circuit for a phase

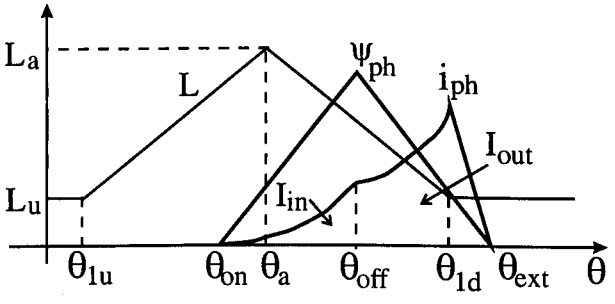

Figure 3.9: SRG phase currents, flux-linkage and idealised inductance

If the inverse machine model is derived the SRG circuit may be reduced to that of Fig. 3.10. The integral of the currents in Fig. 3.10 can be defined referring to Fig. 3.8 and 3.9 as:

$$I_{in} = \int_{\theta_{on}}^{\theta_{off}} i_{ph} d\theta$$

$$I_{out} = \int_{\theta_{off}}^{\theta_{ext}} i_{ph} d\theta$$

$$I_o = I_{out} - I_{in}$$

$$I_{ph} = \int_{\theta_{on}}^{\theta_{ext}} i_{ph} d\theta \tag{3.19}$$

where I_o is the net generated current. Excitation penalty ε is defined as follows:

$$\varepsilon = \frac{I_{in}}{I_{out}} = \frac{I_{in}}{I_o + I_{in}}. \tag{3.20}$$

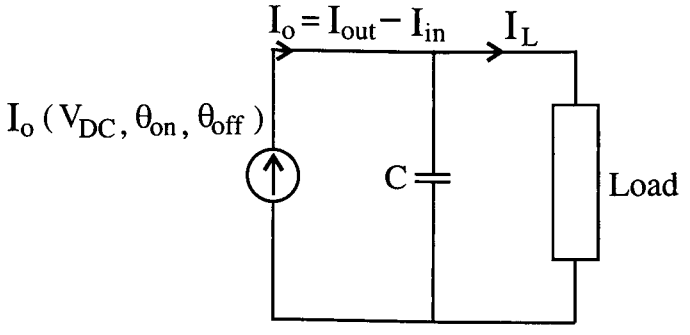

Figure 3.10: Simplified SRG diagram showing energy flow

The average net generated current $I_{o,total}$ in all phases during a stroke is:

$$\begin{aligned} I_{o,total} &= \frac{N_s}{2}\frac{1}{T}\int_0^T i_{ph}\mathrm{d}t \\ &= \frac{N_s}{2}\frac{1}{\frac{2\pi}{N_r}}\int_0^{\frac{2\pi}{N_r}} i_{ph}\mathrm{d}\theta \\ &= \frac{N_r N_s}{4\pi} I_o \end{aligned} \tag{3.21}$$

The DC-bus voltage is expressed by the following equation:

$$\begin{aligned} V_{DC}(t) &= V_{DC}(t_0) + \frac{1}{C}\int_{t_0}^{t} i\mathrm{d}\tau \\ &= V_{DC}(t_0) + \frac{1}{C}\int_{t_0}^{t}\left\{\frac{N_r N_s}{4\pi} I_o - I_L\right\}\mathrm{d}\tau \end{aligned} \tag{3.22}$$

where C is the filter capacitor. It is clear that the DC-link voltage is controlled by controlling the net generated current I_o. The inverse machine model can be obtained with the following assumptions:

1. A linear phase inductance, neglecting saturation and fringing.
2. Turn-on always takes place before aligned position.
3. The phase inductance must be regarded as constant and equal to L_a for positions $\theta_{on} < \theta < \theta_a$.

The derived model expresses I_o as a second order function of the turn-on angle.

$$I_o = k\left(A\theta^2 + B\theta + C\right) \tag{3.23}$$

where the coefficients are:

$$k = \frac{V_{DC}}{\omega} \tag{3.24}$$

$$A = \frac{1}{2}\left(\frac{1}{L_u} - \frac{1}{L_a}\right)$$

$$B = \frac{\theta_a}{L_a} - \frac{2\theta_{off} - \theta_{1d}}{L_u} + \frac{1}{L'}\left\{ln\left(\frac{L_u}{L_{off}}\right) - ln\left(\frac{L_{off}}{L_a}\right)\right\}$$

$$\begin{aligned} C = {} & \frac{(2\theta_{off} - \theta_{1d})^2}{2L_u} + \frac{(\theta_{1d} - \theta_a)}{L'} - \frac{\theta_a^2}{2L_a} \\ & + \frac{1}{L'}\left\{\theta_a + \frac{L_a}{L'}\right\} ln\left(\frac{L_{off}}{L_a}\right) \\ & + \frac{1}{L'}\left\{\frac{L_{off}}{L'} - \theta_{off}\right\} ln\left(\frac{L_u}{L_{off}}\right) \end{aligned} \tag{3.25}$$

The second order equation (3.23) can be solved real-time by a microprocessor. However, for the implementation of the SRG system, the relationship between I_o and the switching angles was pre-calculated off-line and stored in memory as look-up table for the reduction of calculation time and program size. The pre-calculated I_o and ε for the 1-ph 8/8 SRM are shown in Figs. 3.11 and 3.12 respectively.

Fig. 3.11 indicates the trend that I_o increases by advancing the turn-on angle and delaying the turn-off angle. The figure also indicates that I_o also increases by delaying the turn-on angle close to the aligned position and advancing the turn-off angle. The latter trend does not represent the actual characteristics of the SRG but is an error as a result of the assumptions for the simplification and the use of logarithm functions to derive the inverse machine model. The switching angles in those region were not used in the implemented system.

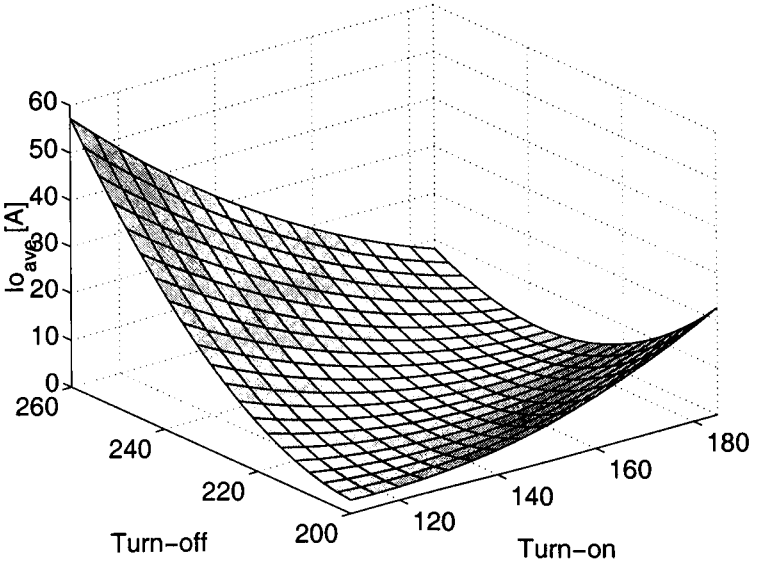

Figure 3.11: I_o vs. switching angles (angles in electrical degrees)

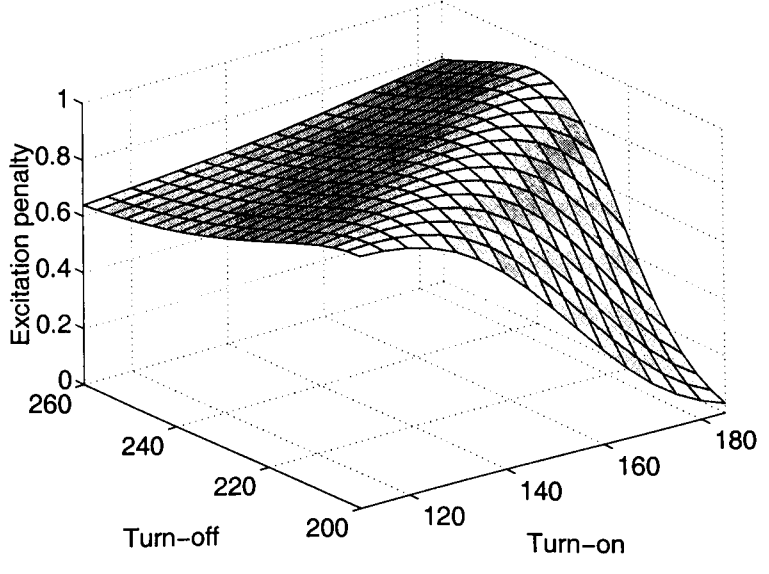

Figure 3.12: Excitation penalty vs. switching angles (angles in electrical degrees)

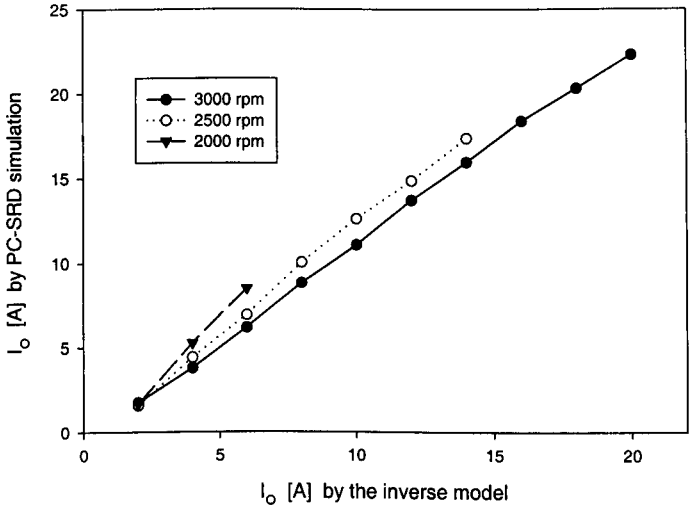

Figure 3.13: Comparison of generating current calculated by the inverse machine model and PC-SRD

3.4.2 Linearity of the inverse machine model

One of the limitations of the method is the assumption of a linear magnetic model in the derivation. In order to investigate the effect of nonlinearity the generating current calculated by the inverse model is compared with that of a nonlinear simulation. The simulation is done by PC-SRD [45] for the prototype single-phase 8/8-pole SR machine [56]. For the PC-SRD simulation measured magnetisation curve data of the machine was used and an accurate result was expected [57]. Fig. 3.13 shows the average generated current I_o by both methods. The relationship is fairly linear although the values are slightly different. In the implemented system described in the following section the error is expected to be compensated for by the PI controller for the purpose of the DC-bus voltage control.

Although the value of the generating current calculated by the inverse machine model is close to the simulation result, this does not approve the assumption of the linear magnetic characteristics in the SRG control. Fig. 3.14 shows current waveforms

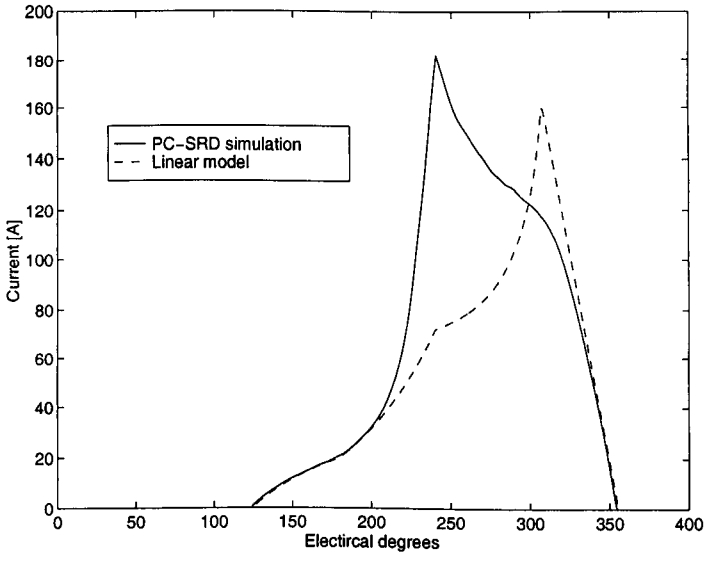

Figure 3.14: Current waveforms with linear and nonlinear magnetic characteristics

with the linear model and the nonlinear simulation. The operating conditions are identical for both cases: 3000 rpm, 100 V, turn-on at 124 and turn-of at 240 electrical degrees. The current waveforms over 40 A, where the effect of the saturation is significant, are very different each other. The current generated in the nonlinear simulation decreases after turn-off while the current generated in the linear model increases until the overlapping of the poles ends.

This limitation must be noted when the inverse machine model is employed. However, the primary objective of using the inverse machine model is to linearise the system and the model may be sufficient for this purpose.

3.5 Simulation study

Computer simulations were carried out in order to validate the proposed scheme. The system was modelled in SIMULINK® [94]. The top level schematic is shown in Fig. 3.15. In the SRM model block, measured magnetisation curves were used as look-up table for the calculation of instantaneous current taking the nonlinearity of the SR machine into account. The same single-phase SR machine was used for the PC-SRD simulation in the previous section.

Fig. 3.16 shows the SRG converter with an additional step-down converter used in the simulation. The excitation energy is supplied to the SRG from the capacitor C during the excitation period. During the generation period the generated energy is stored in C. When the generator starts operation with the capacitor discharged the excitation energy may be supplied from an external voltage source V_{ext} until the DC-bus voltage is established. The DC-bus voltage V_{DC} across C is regulated with speed for the ideal "flat-top" shape by a DC-bus voltage controller. The load voltage V_L is regulated at a constant value by chopping Q_3 by a load voltage controller. In the simulation, a chopping frequency of 5 kHz for Q_3, $C = 4,500\mu$F, $L = 10$ mH and a resistive load of 20 Ω were chosen.

Fig. 3.17 shows the block diagram of the DC-bus voltage controller. The DC-bus voltage command V_{DC}^* is calculated from the speed and then compared with its actual value. The PI controller outputs the reference value of the net generating current I_o^* from the DC-bus voltage error. The turn-off angle θ_{off} is controlled linearly with I_o. The turn-on angle θ_{on} is determined by the inverse model using θ_{off} and I_o.

Figs. 3.18 and 3.19 show the phase current and voltage waveforms at speeds of 2,000 and 4,500 rpm. The DC-bus voltage is regulated at 59 and 133 V respectively. In these simulations, the step-down DC/DC converter was disconnected and a constant resistor was directly connected to the SRG converter as load for a comparison to the experimental results described later. The load was adjusted so that the peak current

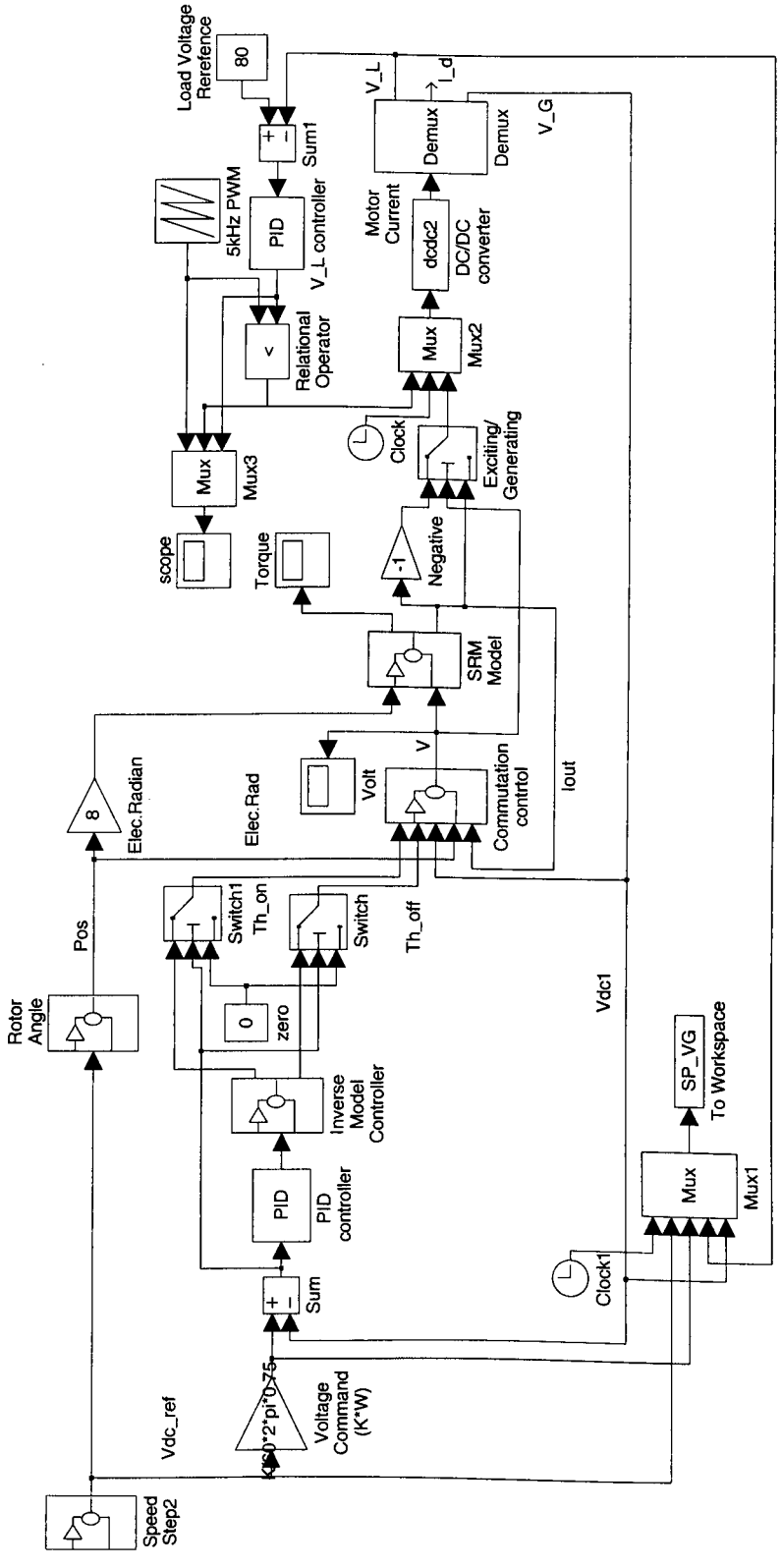

Figure 3.15: SIMULINK model

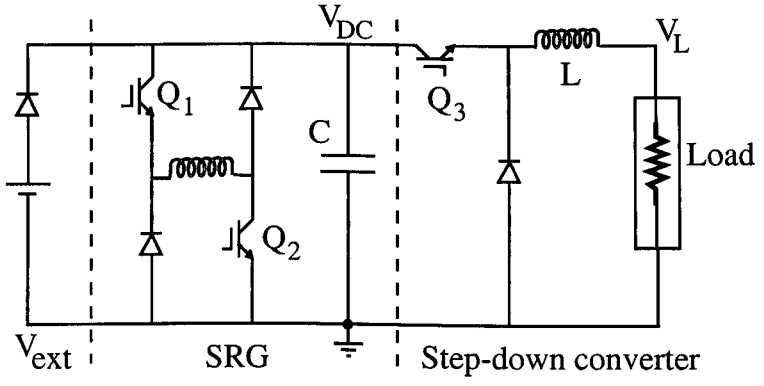

Figure 3.16: SRG converter with an additional step-down converter

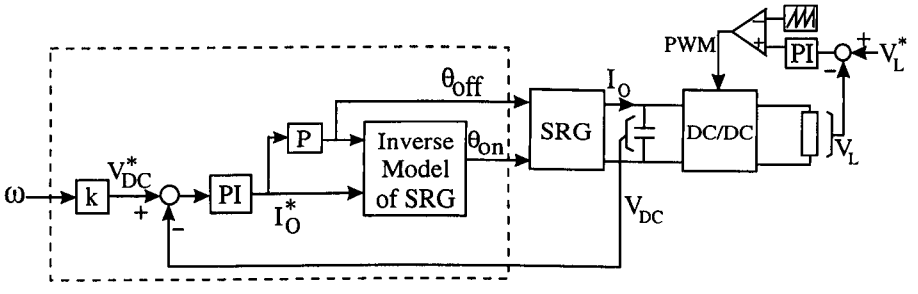

Figure 3.17: Proposed SRG controller

became approximately the rated value of 60 A. Both currents have more or less the "flat-top" shape. The DC-bus voltage command calculated was multiplied by a factor of 0.75 in order to compensate for the effect of saturation since the bulk saturation starts at about 40 A of phase current in this machine.

Fig. 3.20 shows how the DC-bus voltage changes with the rotor speed. The rotor speed was changed from 3,000 rpm to 10,000 rpm. The DC-bus voltage changes proportionally to the speed from 89 to 297 V while the load voltage is kept constant at 80 V by the step-down DC/DC converter connected between the SRG converter and the load. This shows that the DC-bus voltage can be controlled dynamically and independently of the load voltage with the proposed system. The current waveform at 10,000 rpm is shown in Fig. 3.21.

A simple step-down DC/DC converter is sufficient for the proposed system provided

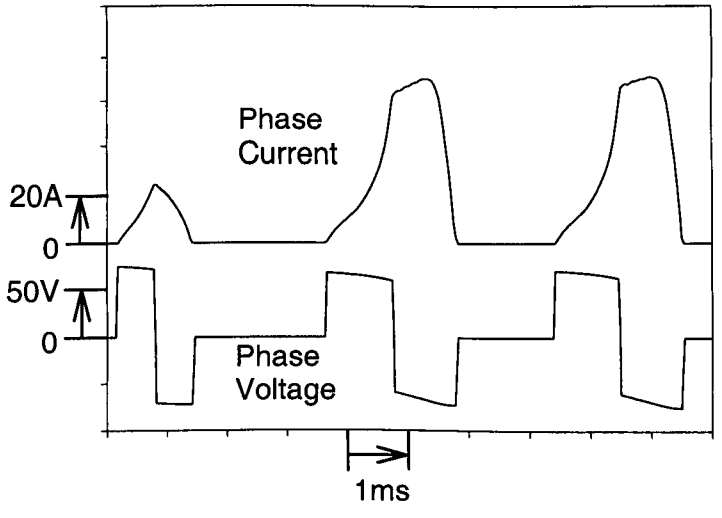

Figure 3.18: Current and voltage waveforms at 2,000 rpm (simulation)

that the minimum DC-bus voltage is higher than the load voltage over the range of operating speed.

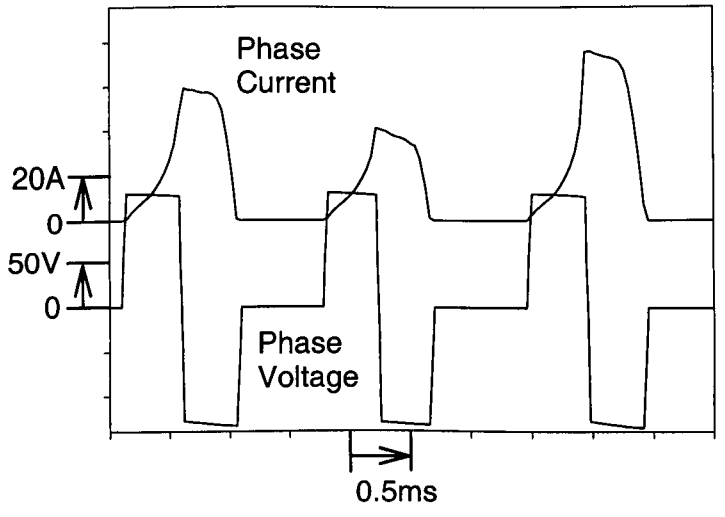

Figure 3.19: Current and voltage waveforms at 4,500 rpm (simulation)

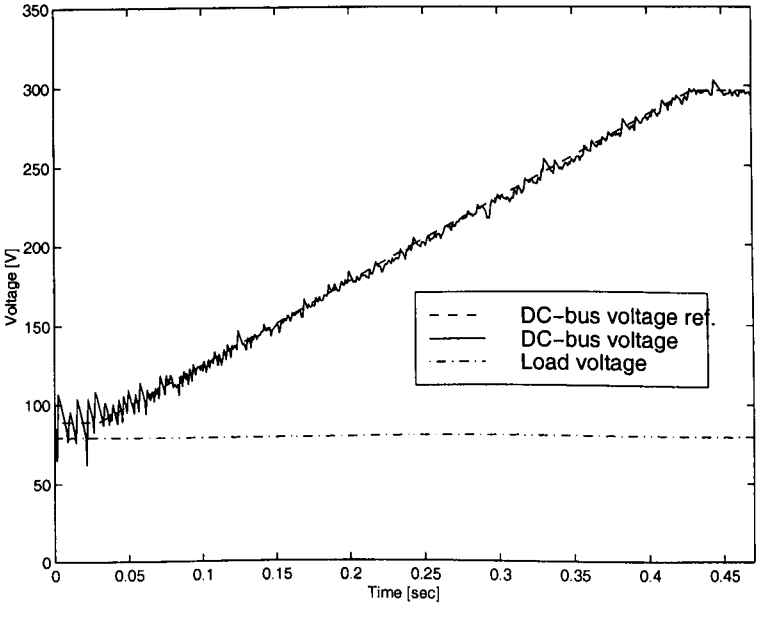

Figure 3.20: Change of the DC-bus voltage with speed (simulation)

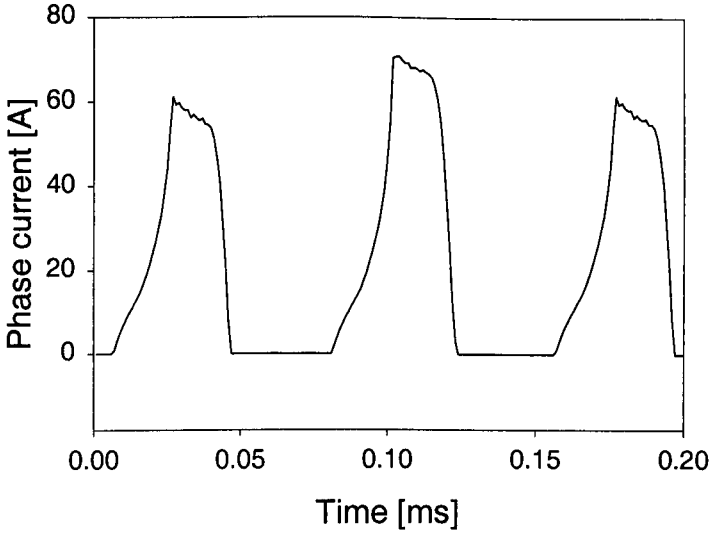

Figure 3.21: Current waveform at 10,000 rpm (simulation)

3.6 Experimental validation

3.6.1 Implementation of the controller

The system has been implemented using a Motorola MC68332 microcontroller [95]. The dotted part in Fig. 3.17 was implemented by software.

Fig. 3.22 shows the controller hardware and Fig. 3.23 highlights their functions. The controller consists of three circuit boards: microcontroller board, commutation board and I/O board. The main part of the microcontroller board are MC68332 microcontroller, external memory and an RS232 serial interface. The ROM on the microcontroller board holds a background program which provides interface between the microcontroller and PC and allows the SRG control software to be downloaded from the PC. The serial interface is used as a user interface for setting parameters of the SRG controller. The commutation board includes an FPGA (field programable gate array), encoder signal receiver and D/A converter. The commutator implemented in the FPGA determines the switching states of converter from the incoming encoder signals and commutation angles information from the microcontroller. The commutation signals are sent to the I/O board. The D/A converter is used for the current regulation and over current detection. The I/O board outputs the commutation signals through optical transmitters to the converter. The DC-bus voltage is fedback through an isolation amplifier and an A/D converter. The voltage information is processed for the generation power control. Photographs of the implemented controller are shown in Fig. 3.24.

The sampling time for the voltage controller was set at 1 ms. The same single-phase 8/8-pole SR machine as used for the simulation was used. A resistor was connected directly to the SRG converter as load and the DC/DC converter stage was omitted in the experiment.

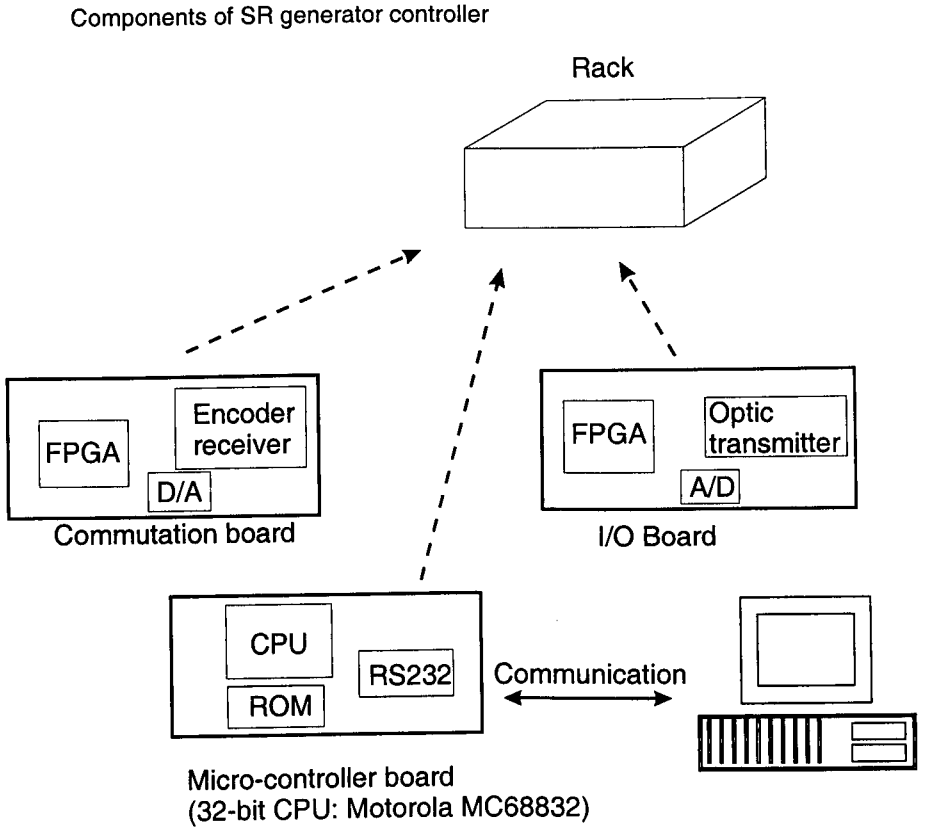

Figure 3.22: SRG controller boards

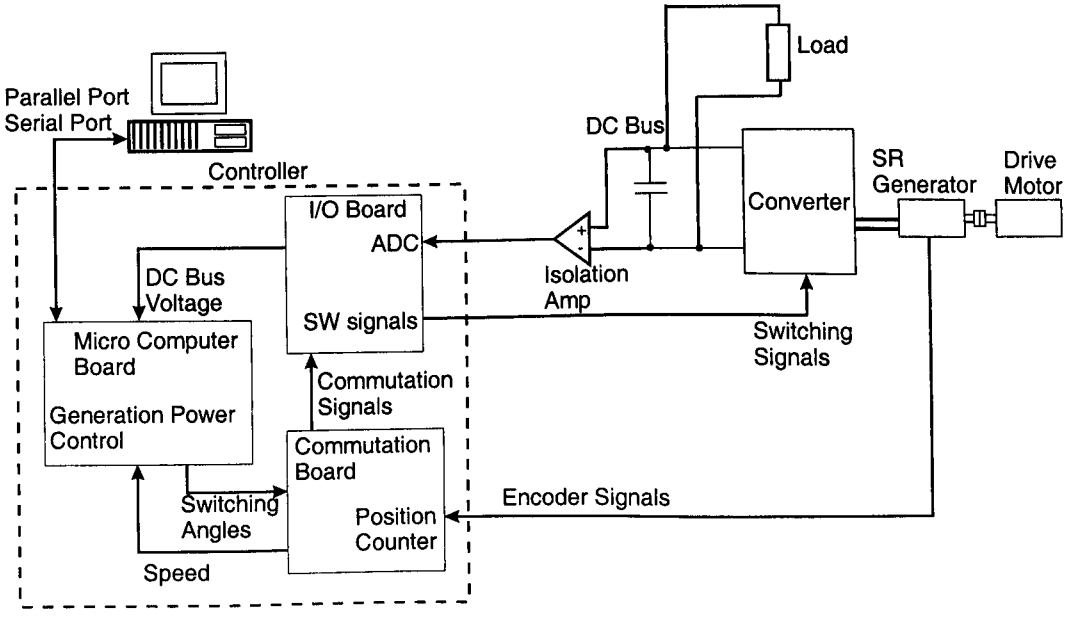

Figure 3.23: Implementation of the SRG controller

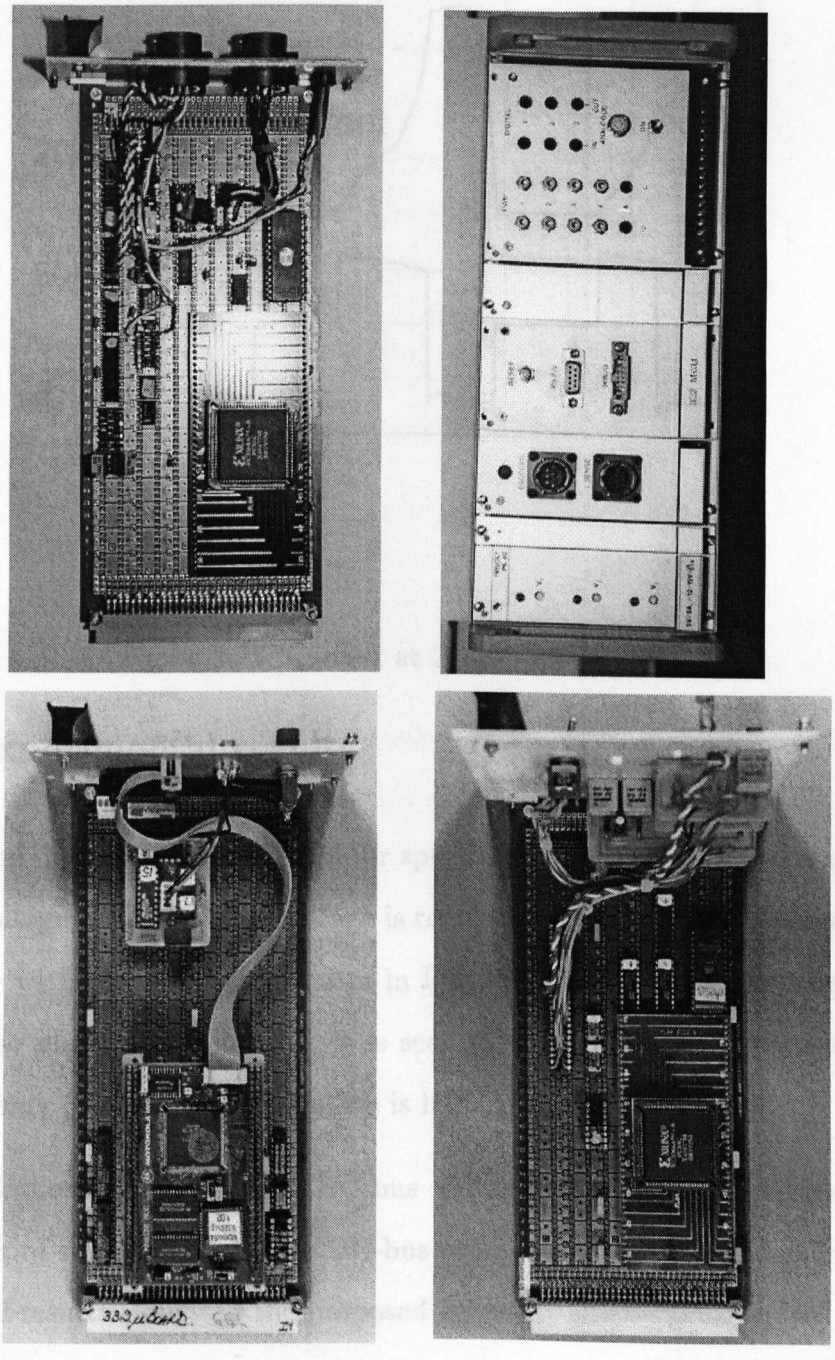

Figure 3.24: Photographs of implemented SRG controller (top right: rack, top left: commutation board, bottom right: I/O board, bottom left: microcontroller board)

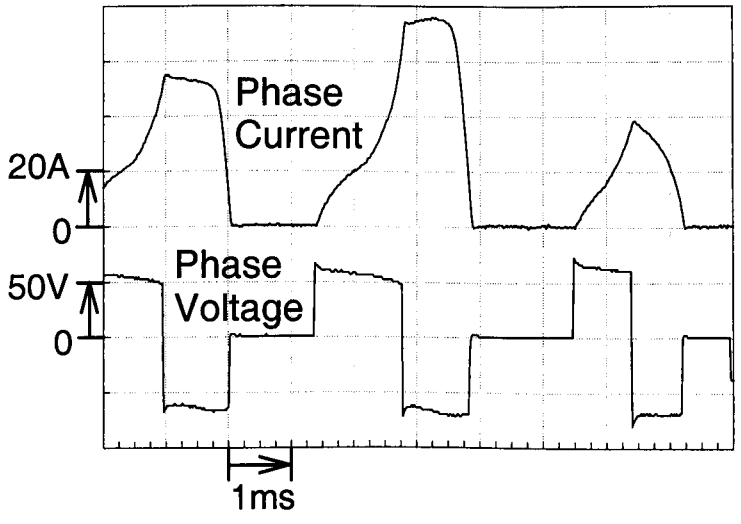

Figure 3.25: Current at 2,000 rpm (measured)

3.6.2 Experimental results

Figs. 3.25 and 3.26 show the currents for speeds of 2,000 and 4,500 rpm together with the phase voltages. The DC-bus voltage is regulated at 59 and 133 V respectively. The results agree with the simulation shown in Figs. 3.18 and 3.19. The energy conversion loops are also plotted in Fig. 3.27. It is seen that the "flat-top" shape was achieved and that energy conversion effectiveness is high for both cases.

Fig. 3.28 shows the change in DC-bus voltage when the rotor speed was varied from 2,000 rpm to 3,000 rpm. The DC-bus voltage follows the change in speed. The experimental results validated the proposed scheme.

The DC-bus voltage is shown in Fig. 3.29 for a speed of 3,000 rpm. It can be seen that the DC-bus voltage is regulated at the command value of 89 V by varying the generating current. It shows that the current waveform variation is relatively large resulting in the DC-bus voltage fluctuation even with a constant resistive load. This is

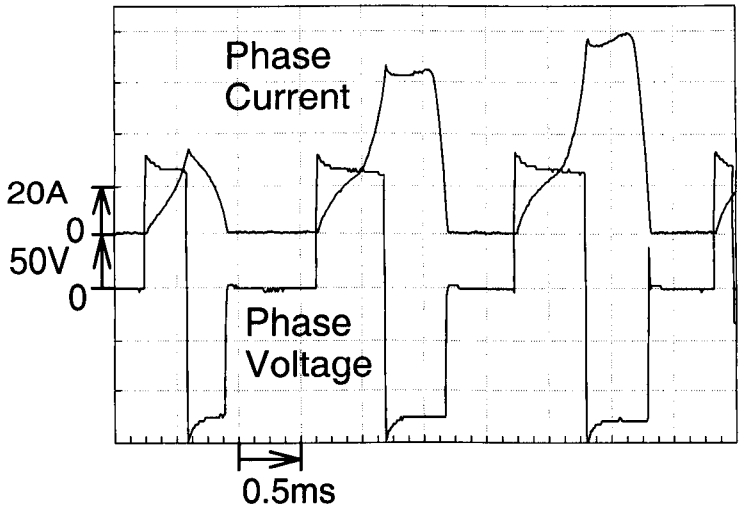

Figure 3.26: Current at 4,500 rpm (measured)

due to the fact that the switching angles calculated by the inverse machine model tend to vary sharply with the generating energy requirement. This is one of the limitations of using the linear magnetic model used. The ripple in the DC-bus voltage is less than 10 % of its reference value. The ripple can be reduced with a larger filter capacitor at the expense of lower dynamic response and higher cost. The use of poly-phase machines is also effective in reducing the ripple.

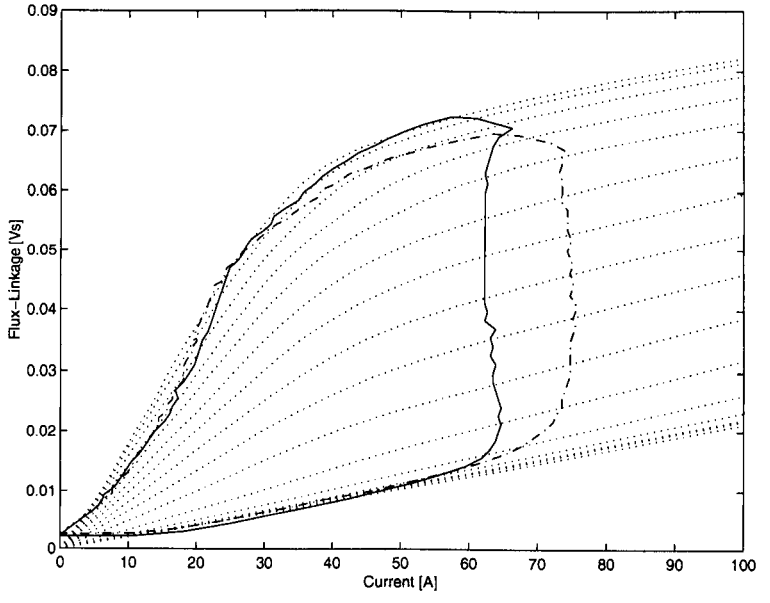

Figure 3.27: Measured energy conversion loops (dotted: 2,000 rpm, solid: 4,500 rpm)

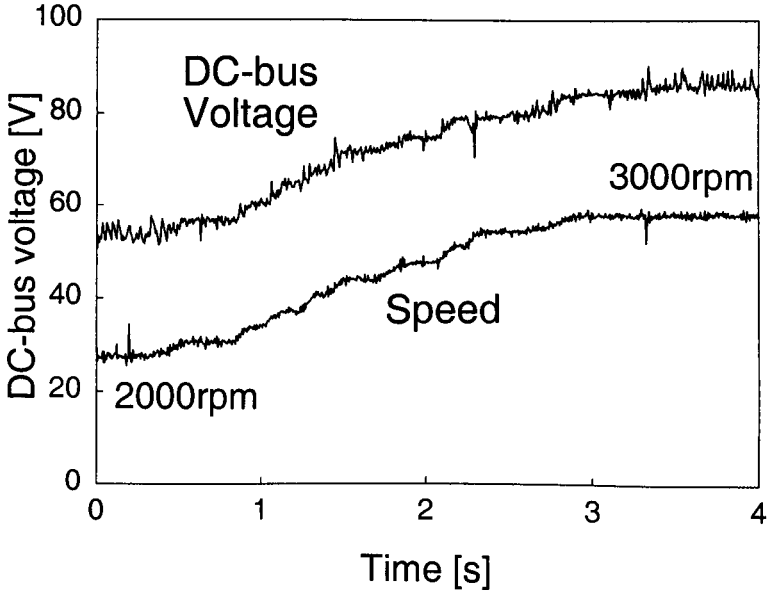

Figure 3.28: Change of the DC-bus voltage with speed (measured)

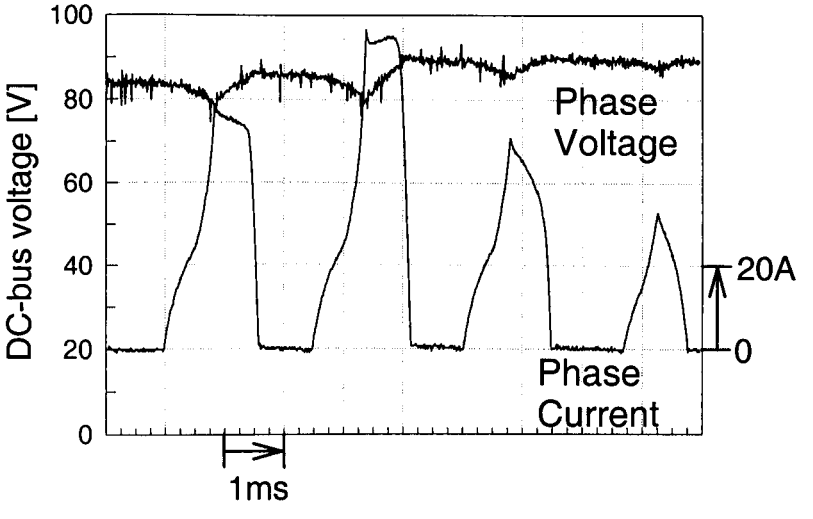

Figure 3.29: Ripple in DC-bus voltage (measured)

3.7 Conclusions

This chapter has described the DC-bus voltage controller for the SRG to achieve maximum energy conversion effectiveness. The limitation of PWM control to achieve a lower excitation penalty was shown analytically. For the implementation of the SRG controller in simulation and experiment, the inverse machine model was chosen as the control low to determine the switching angles from generating current requirement. The computer simulations using SIMULINK® were carried out and the results confirmed that the "flat-top" current can be achieved by controlling the DC-bus voltage with rotor speed and it can be controlled dynamically. It was also shown that the load voltage can be regulated at a constant value of 80 V for a speed range of 3,000 to 10,000 rpm independently of the DC-bus voltage by an addition of a step-down DC/DC converter. The controller was implemented using a microcontroller for the 0.8 kW single-phase 8/8-pole SR machine. The experimental results validated the proposed control scheme. The scheme is applicable to applications where the speed of the prime mover changes with conditions, such as wind generators and jet turbine generators.

Chapter 4

Fault-tolerant operation of single-phase switched reluctance generators

This chapter studies operation of the multi-pole single-phase Switched Reluctance Generator (SRG) under faults, in particular an 8/8-pole SR machine described in chapter 2.

A new converter topology is proposed which connects two banks of coils in parallel. The combination of multiple coils per phase and the converter circuit suggests improved operation under faults compared with conventional topologies.

Output power per coil current under faults is studied. Open- and short-circuit coils are studied through linear analysis, finite-element analysis and static torque measurement. Generated currents under faults with the proposed converter are measured.

Dynamic operation under faults with the single-pulse control mode is also analysed, while the DC-bus voltage is regulated at a constant value by a controller. The circuit equations under faults are derived and the operation is evaluated by simulation. The SRG system is implemented with a microcontroller and the operation under faults is tested.

4.1 Introduction

The switched reluctance generator (SRG) has been receiving an increasing attention for aircraft applications where robustness, high speed and fault tolerance are of major importance [5, 63, 87, 64, 62]. The classic converter topology [83] avoids the problem of shoot-through faults found in AC inverter technology. Furthermore, the short-pitched windings exhibit a large amount of electromagnetic independence, which may be exploited by appropriate converter as well as machine topologies.

Much interest has been paid to the possibility of replacing the 400 Hz AC power distribution found on many aircraft with a DC system at 270 V. The switched reluctance machine has been identified as a potential candidate for the generator in such systems, [87].

Relatively little has been reported on switched reluctance machines operating under fault conditions. Stephens suggested that switched reluctance motors could operate by disconnecting faulty windings with use of special fault detectors [7]. Miller reported an analysis of operation under faults and compared several winding configurations [8]. SRG converter topologies for improved fault-tolerance have been studied by Richter and Ferreira [4]. Radun suggested a dual-converter topology which has separate excitation and load buses [3], and MacMinn studied the design of the power stage for SRGs [2]. Various methods for closed-loop control of the DC-link voltage were described in [9]-[11], and Kjaer attempted to reduce the reactive power flow by on-line optimisation [12].

In this chapter the fault-tolerant operation of SRG is studied, in particular an 8/8-pole single-phase switched reluctance machine. The chapter focuses on faults in coils. A new "split winding" converter topology which separates the coils into two coil banks is proposed. The coil banks are connected in parallel and this increases the fault-tolerance of the single-phase SRG.

For open- and short-circuit coil faults, output power per coil current is studied

through linear analysis, finite-element analysis and measurements.

Dynamic operation under faults is also analysed, while the DC-bus voltage is controlled at a desired value. Although, various methods of the SRG control were reported in [89, 90, 91, 92], the single-pulse control described in Chapter 3 is chosen in this study. This is because it was shown by Kjaer et al. in [91] that the amount of energy generated with the SRG is determined only by the turn-off angle and the turn-off current level at a given speed and DC-bus voltage and chopping is not necessary for medium and high speeds. It focuses on operation with the proposed split winding converter under open- and short-circuit coil faults including transient states. The following topics are described:

- How to employ a multi-pole single-phase switched reluctance machine for maximum fault-tolerance
- Expected performance under faults
- Winding configurations for minimised impact from faults.
- Capability of the split winding converter to isolate faulty coils
- Modelling and analysis of fault impact on system
- Evaluation of fault-tolerance by simulation and experiments.

4.2 The single-phase SRG

The cross-section of the prototype single-phase 8/8-pole SR machine described in chapter 2 is again shown in Fig. 4.1. The machine is wound with one coil per pole and the number of turns per pole is 35. The design and construction of this machine are reported in Chapter 2 and Ref. [56], and briefly reviewed here. The 8 coils were initially connected such that adjacent poles have opposite magnetic polarity, producing so-called short flux paths. This has been reported to result in lower iron losses [86], which

is of importance especially in high-speed applications. The 8/8 machine has narrower stator pole-arcs than the equivalent 8/6 machine, hence a wider slot area is available, resulting in lower copper losses. On the other hand, a narrower pole-arc may also reduce the aligned inductance and increase the pole flux density. For a more detailed discussion on the choice of pole numbers, see [96]. Apart from a high efficiency, the 8/8 machine appears attractive as its coils may be connected to minimise the impact of faults. In the following sections, several winding configurations are studied.

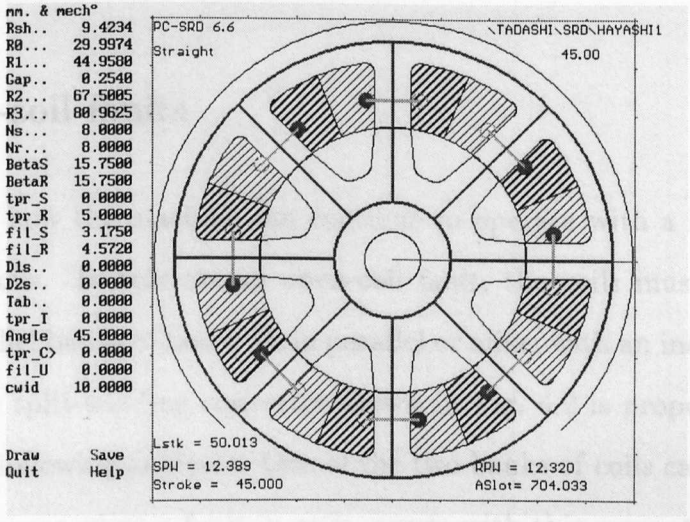

Figure 4.1: Cross-section of the prototype single-phase 8/8 SR machine

4.3 Output power under coil faults with constant currents

In this section, output power per coil current under coil faults is studied. A fault-tolerant converter for the single-phase SR machine is proposed. Open-coil faults are analysed by linear analysis. The analytical results are validated by finite element analysis, static torque measurement and generating test. The generating test includes short-coil faults as well as open-coil faults.

4.3.1 Open-coil faults

First, it is shown how the machine can continue to operate with a loss (open-circuit) of one or more coils. To tolerate an open-coil fault, the coils must be connected in parallel (two parallel banks of four coils in parallel or alike, with an increase in converter complexity). The split-winding converter shown in Fig. 4.2 is proposed and assumed to be used in the following analyses. One of the two banks of coils can be disconnected from the power source when a fault in coils occurs with this converter. Under normal condition S1, S2 and S3 receive identical switching signals. The excitation current flows from the positive DC-bus through S1, coils, S2 and S3 to the negative bus. The generated current flows from the negative bus through D1, coils, D2 and D3 to the positive bus, then charges the capacitor. In order to disconnect coil bank B, S3 is switched off and the generator is operated by controlling S1 and S2. If coil bank B does not share flux paths with bank A, the operation of coil bank B could be shut off completely. However, during the shut off process, uncontrollable transient current could flow through diode D3.

Other single-phase SRG topologies can be connected in a similar fashion, but the converter in Fig. 4.2 has the drawback of disconnecting half the total number of coils even if just one coil is faulty. To separate a smaller number of coils, increased circuit complexity is required. Fig. 4.3 shows one such example.

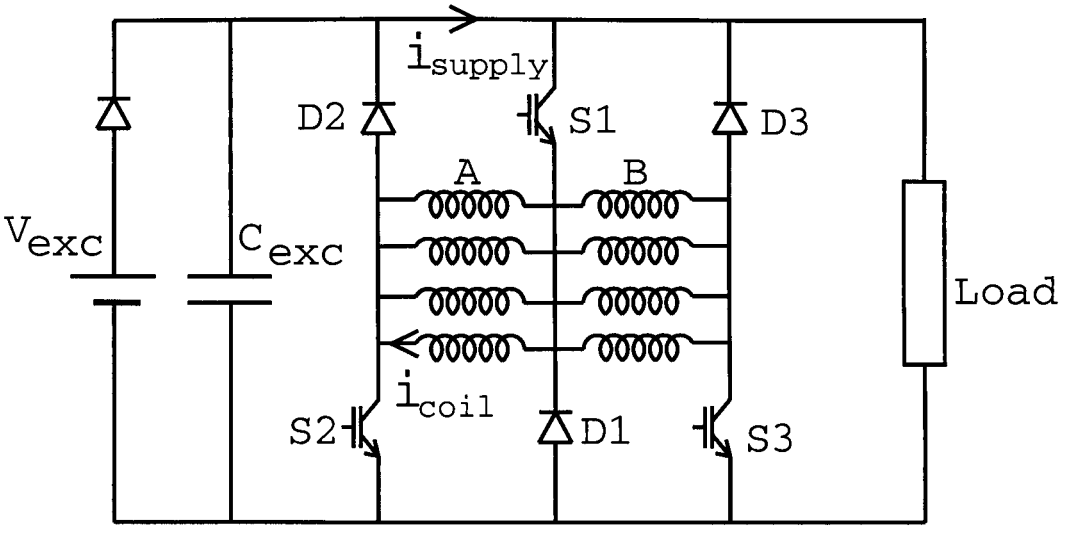

Figure 4.2: Fault-tolerant single-bus converter circuit for split winding single-phase SRG

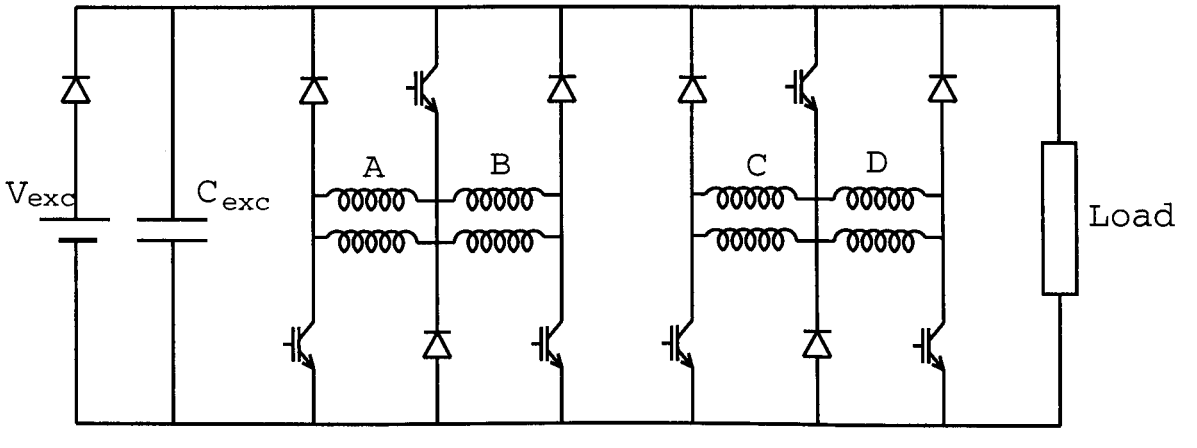

Figure 4.3: Fault-tolerant single-bus converter circuit for split winding with 4 banks for the single-phase SRG

Case I	Normal condition	(NSNSNSNS)
Case II	4-coil open	(NONOSOSO)
Case III	4-coil open	(NOSONOSO)
Case IV	4-coil open	(NONONONO)
Case V	1-coil open	

O refers to an open-circuit coil

Table 4.1: Definition of Open-Coil Faults

There are several ways to configure the magnetic polarity of the coils with the converter in Fig. 4.2. For normal operation the 8/8 SR machine should have 4 pairs of N and S coils. For a fault operation in which half the coils are disconnected (open-circuited), the polarity of remaining coils could be either 2 pairs of N and S or 4 of either polarity from a symmetrical point of view. Here, the five cases in Table 4.1 are examined. The study of 1-coil open-circuit fault is a good example to show how the magnetic unbalance affects the operation. The 1-coil short-circuit fault is also discussed in the later sections although it is not listed here.

Figs. 4.4, 4.5 and 4.6 show the flux paths of the machine when the healthy coils are excited by a coil current of 10 A, calculated using finite element analysis (FEA). Fig. 4.4(a) shows the short flux paths of Case I, corresponding to the rated phase current of 80 A with the converter of Fig. 4.2. Fig. 4.4(b) and Fig. 4.5(a) show the flux-paths of Case II and III respectively. For Case II and III, the flux in open-circuit coil poles is cancelled by the MMF of the conducting coils under linear conditions. Flux concentration in stator and rotor yoke sections is higher for Case II than for Case III. For Case IV shown in Fig. 4.5(b), the flux paths remain unchanged from Case I although the flux density decreases with decreased MMF-level. When one coil is unexcited (Case V) the distribution of flux is not symmetrical any more, as shown in Fig. 4.6. This may result in unbalanced lateral forces [97] and lead to mechanical failure. Therefore, this fault should be cleared as soon as possible. With the single-phase SRG system, the magnetic balance can be maintained and the problem of lateral forces can be avoided by disconnecting a coil bank when one of the coils is faulty.

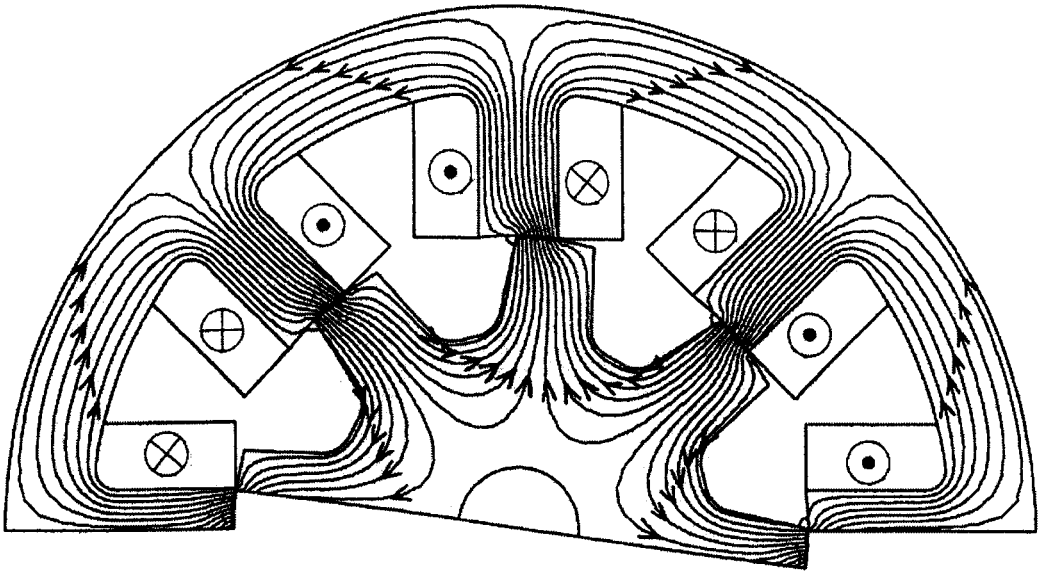

(a) Case I

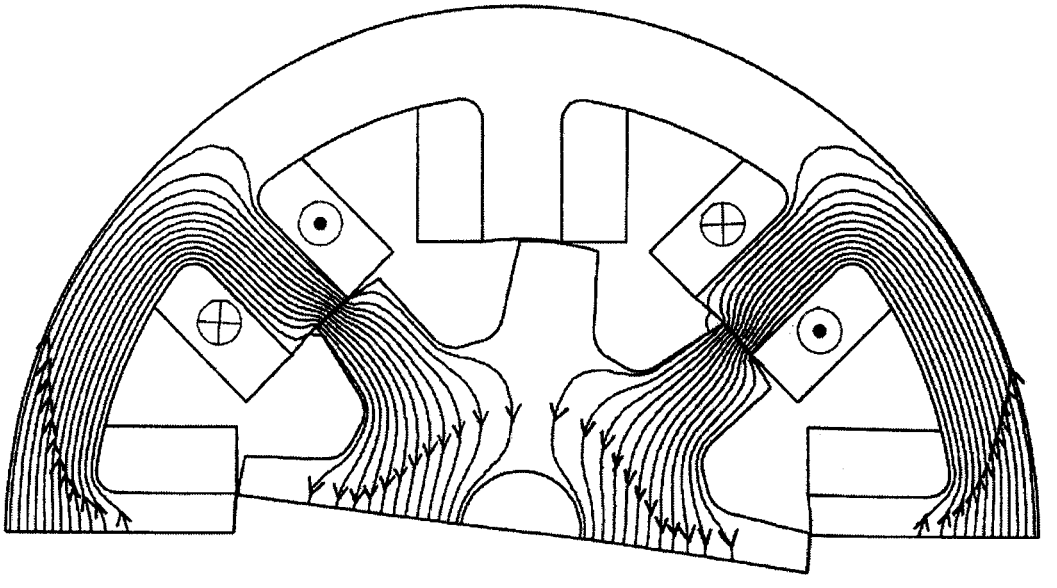

(b) Case II

Figure 4.4: Flux plots calculated by FEA (1/3)

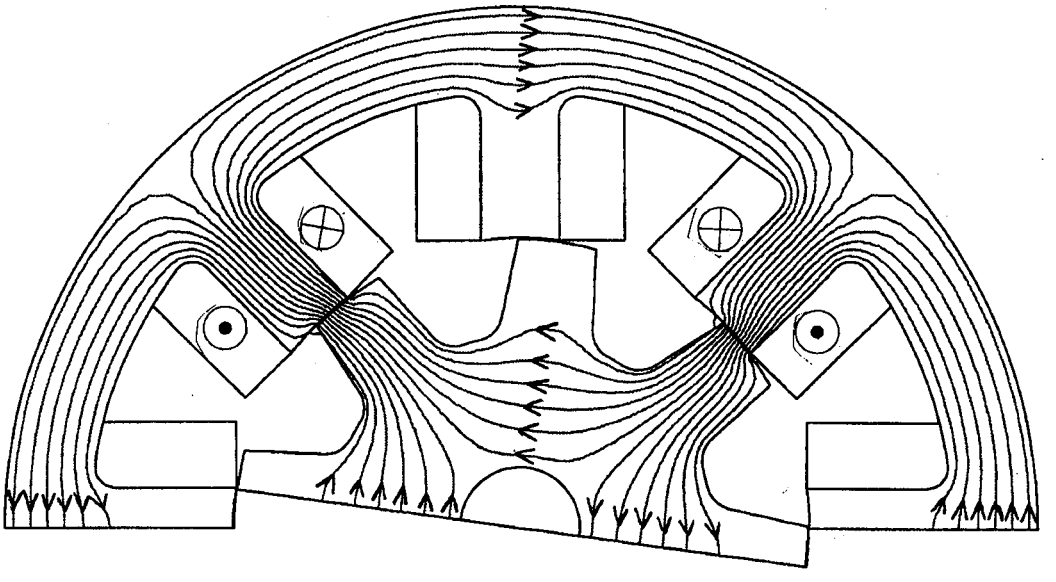

(a) Case III

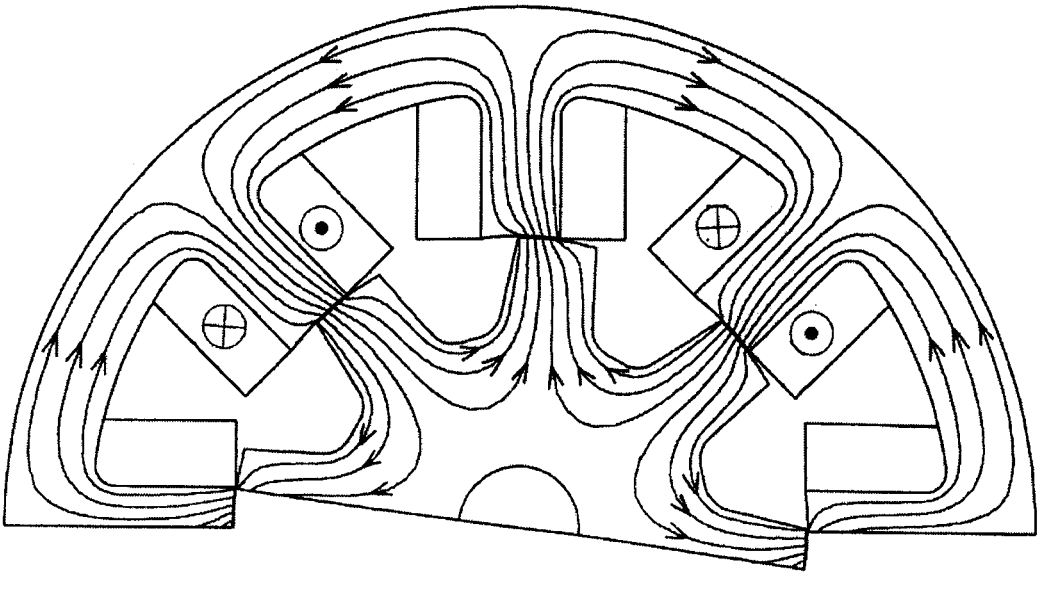

(b) Case IV

Figure 4.5: Flux plots calculated by FEA (2/3)

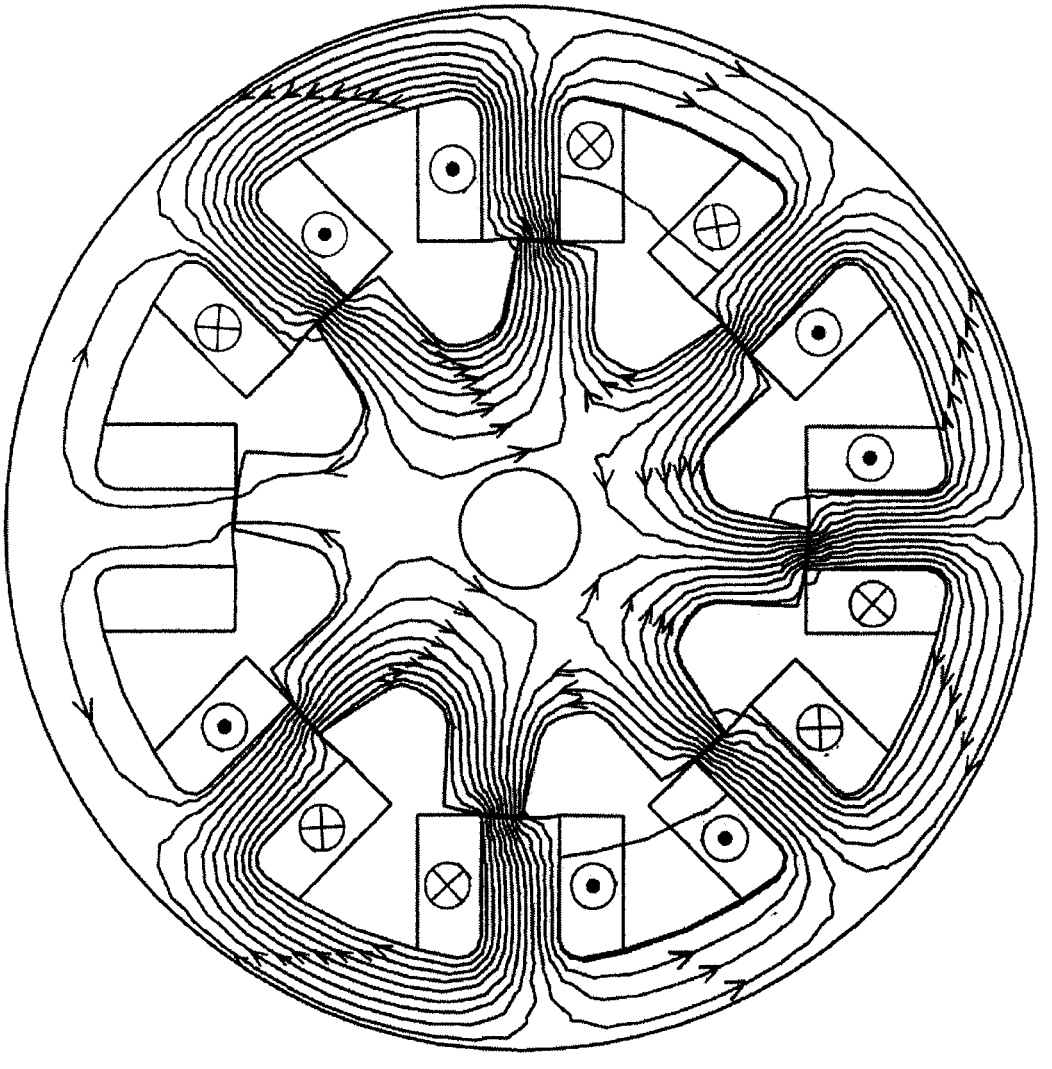

Case V

Figure 4.6: Flux plots calculated by FEA (3/3)

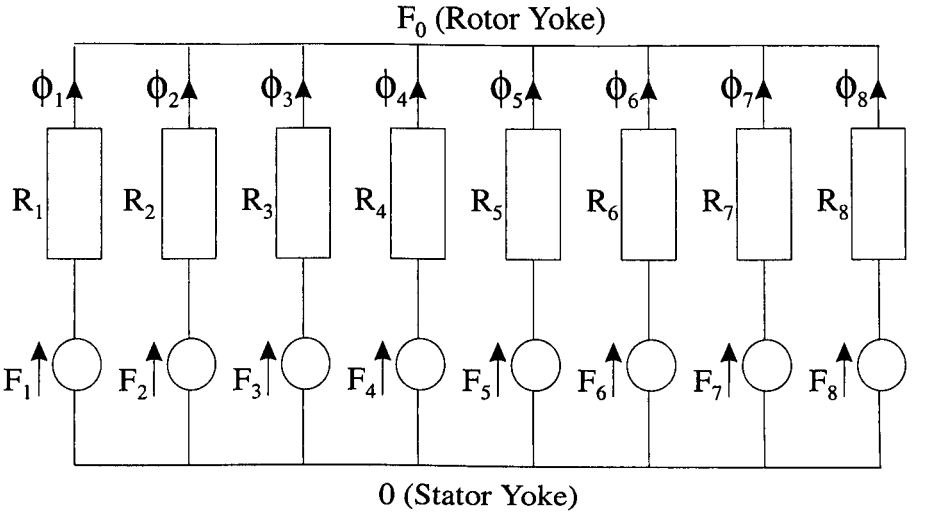

Figure 4.7: Equivalent magnetic circuit of the single-phase switched reluctance machine

4.3.2 Open-coil fault analysis

In this section the performance of the single-phase SR machine under faults is calculated by linear analysis.

The equivalent magnetic circuit of the machine is shown in Fig. 4.7. The MMF potential is defined 0 at the stator yoke and F_0 at the rotor yoke. F_k represents the MMF of coil 'k', R_k represents the airgap reluctance and ϕ_k represents the flux through pole. F_0 and ϕ_k are expressed by the following equation:

$$F_0 = \frac{\sum_k \frac{F_k}{R_k}}{\sum_k \frac{1}{R_k}} \tag{4.1}$$

$$\phi_k = \frac{F_k - F_0}{R_k} \tag{4.2}$$

Since all airgap reluctances are the same for the single-phase machine, it follows that:

$$F_0 = \frac{\sum_k F_k}{8} \tag{4.3}$$

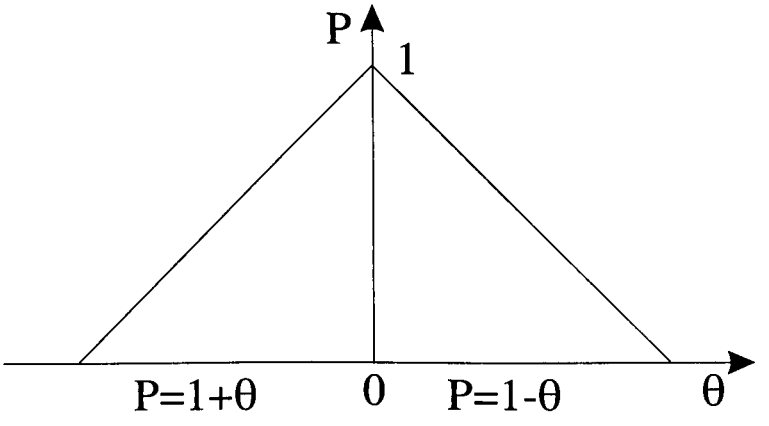

Figure 4.8: Normalised permeance profile

For a simple comparison between normal and faulted conditions, a normalised permeance profile shown in Fig. 4.8 is assumed.

Using this permeance profile, torque produced on each pole is expressed as follows:

$$T = \frac{1}{2}(F_k - F_0)^2 \frac{dP}{d\theta} = \frac{1}{2}(F_k - F_0)^2 \tag{4.4}$$

Case I

The MMF in each pole is such that:

$$F_1 = F_3 = F_5 = F_7 = N_p i \tag{4.5}$$

$$F_2 = F_4 = F_6 = F_8 = -F_1 \tag{4.6}$$

where N_p is the number of turns per pole. This gives total torque T_I for Case I:

$$T_I = 8T_k = 4N_p^2 i^2 \tag{4.7}$$

This torque will be compared with the torque produced during faults.

Case II and III

Cases II and III give the same result with linear analysis. The configuration of the MMF is as follows:

$$F_1 = F_5 = -F_3 = -F_7 = N_p i \tag{4.8}$$

$$F_2 = F_4 = F_6 = F_8 = 0. \tag{4.9}$$

Then the total torque $T_{II,III}$ for Cases II and III is:

$$T_{II,III} = 2N_p^2 i^2 = 0.5T_I. \tag{4.10}$$

Case IV

The MMF in each pole is such that:

$$F_1 = F_3 = F_5 = F_7 = N_p i \tag{4.11}$$

$$F_2 = F_4 = F_6 = F_8 = 0. \tag{4.12}$$

The total torque T_{IV} for Case VI is:

$$T_{IV} = N_p^2 i^2 = 0.25T_I. \tag{4.13}$$

Case V

The MMF of each coil is as follows:

$$F_1 = F_3 = F_5 = F_7 = N_p i \tag{4.14}$$

$$F_4 = F_6 = F_8 = -N_p i \tag{4.15}$$

$$F_2 = 0 \tag{4.16}$$

Faults	Torque (vs. Case I)
Case II,III	50%
Case IV	25%
Case V	86%

Table 4.2: Torque Production Analysis under Open-coil Faults

Then the total torque T_V for Case V is:

$$T_V \approx 3.44 N_p^2 i^2 = 0.86 T_I. \tag{4.17}$$

Table 4.2 summarises the analysis. It shows that the single-phase SRG could generate half the normal power when 4 of 8 coils are conducting, with winding configuration of either Case II or III.

4.3.3 2-D finite element analysis and static torque measurement

In this section, the previous analysis is confirmed through comparison with finite element analysis and static torque measurement.

Fig. 4.9 shows the magnetisation curves for the experimental machine for two rotor positions (maximum and minimum inductances). Measurements with all 8 coils connected and finite-element analysis (FEA) predictions for Cases I, II and IV are shown, all for identical coil current levels. The magnetisation curves of Case III may be expected to be similar to those of Case II. The flux linkage for Case II is at the same level as that of Case I and for Case IV half that of Case I, with the same coil current. With the connection shown in Fig. 4.2, the supply current for Cases II and IV is half that of Case I. Assuming that energy converted is proportional to the product of flux linkage and supply current, Fig. 4.9 gives the same output torque prediction as in Table 4.2.

Static torque curves of the prototype single-phase SRG were measured and are shown in Fig. 4.10 for a coil current of 15 A. The static torque of the machine for

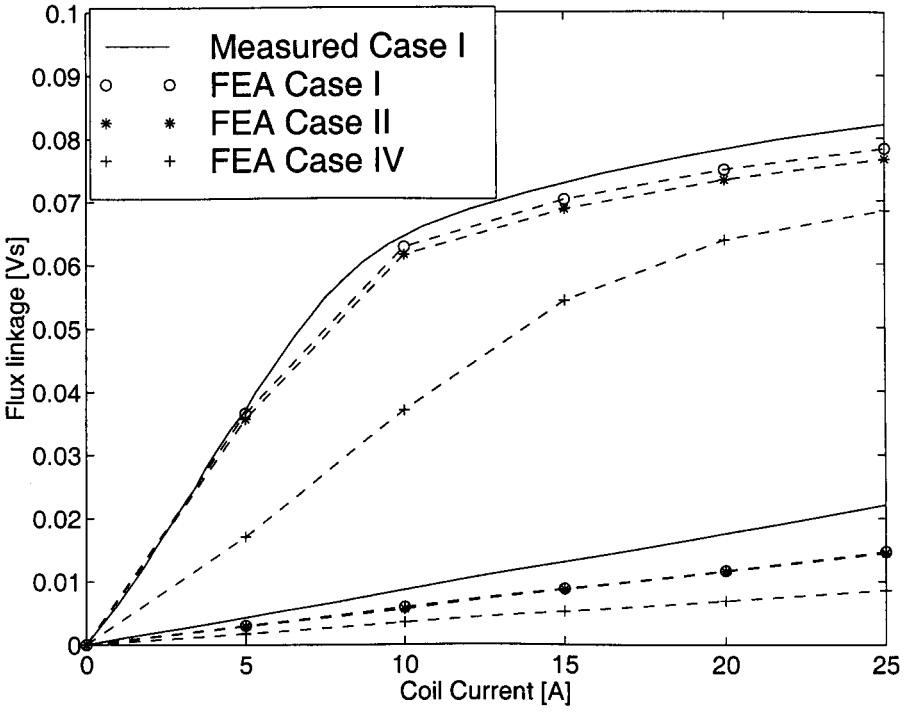

Figure 4.9: Magnetisation curves under normal operation and open circuit of 4 coils

Case II is 50% of Case I. The same measurement was carried out for Case III and it gave the same result as Case II although this is not shown in Fig. 4.10. The static torque for Case IV is 25% of that of Case I. When one of the eight coils is open-circuited (Case V) the static torque is 86% of Case I. When the coils are split into two banks, the magnetic polarity of Case II should be configured. The measurement results support the analytical predictions well.

The result confirms that the available power per coil current during faults is:

$$P_{fault} = P_{normal}\frac{N-n}{N} \tag{4.18}$$

where N is the number of coils and n the number of faulted coils. The single-phase SRG could generate half its normal energy when half the coils are disconnected and currents in the remaining coils are normal.

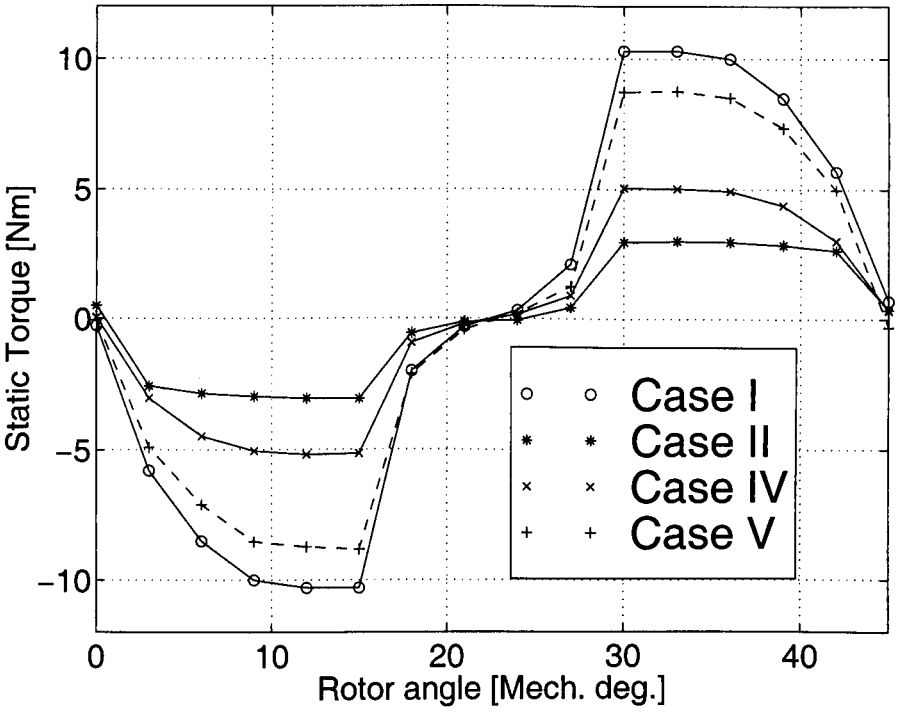

Figure 4.10: Measured static torque curves

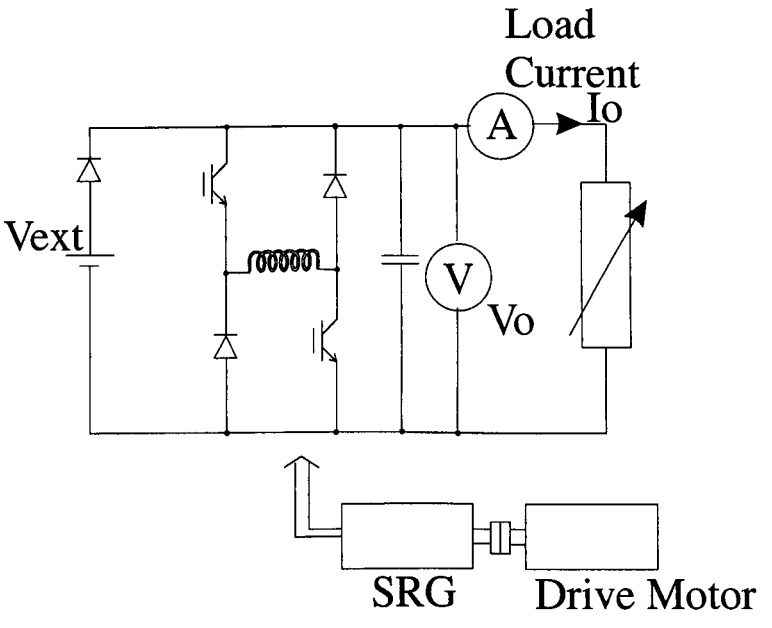

Figure 4.11: Experimental SRG setup

4.3.4 Generating test

Steady-state generating tests were performed and the load currents were measured. The measurement system is shown in Fig. 4.11. The SRG was turned by a motor at a constant speed. An external supply V_{ext} was used to charge the capacitor banks initially and used as back-up if the voltage could not be sustained. The SRG is inherently unstable when operated with the single-pulse excitation and requires the firing angles to be adjusted to match the load exactly [87]. For a set of firing angles the load was adjusted to assure equilibrium (constant V_o) and the load current I_o was measured. The same procedure was applied for normal operation as well as short- and open-circuit tests.

Open-circuit coil faults

The generated currents were measured for the winding configurations of Cases I, II and V.

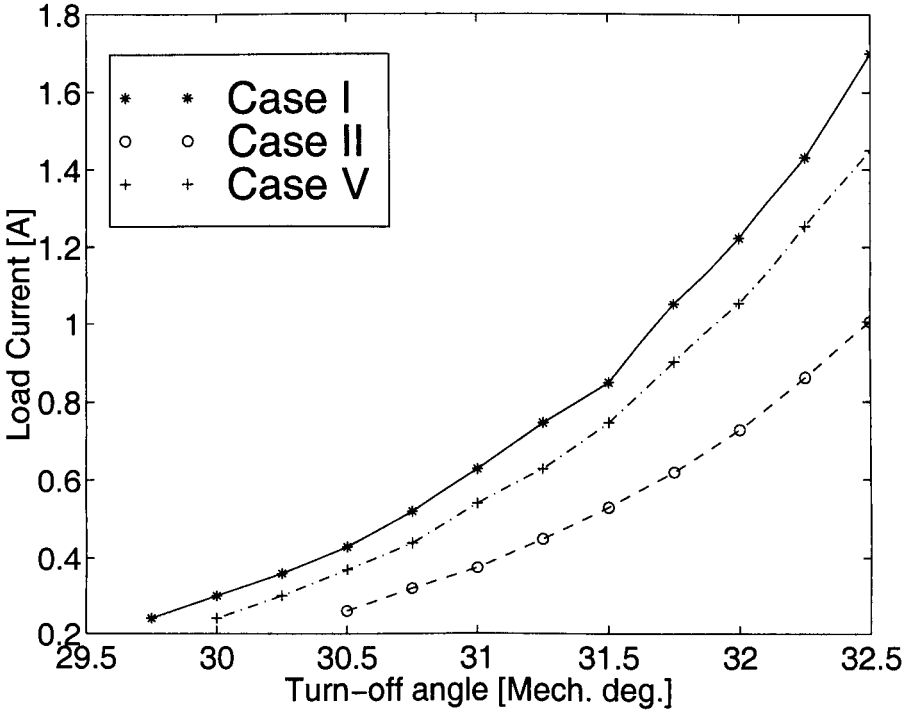

Figure 4.12: Load current under normal and open-coil fault conditions (1,500 rpm, V_o=30 V)

Fig. 4.12 shows the load current measured at 1,500 rpm with $V_o = 30$ V, and a fixed turn-on angle of 20.8 mechanical degrees relative to unaligned position. Fig. 4.13 shows the load current of Cases II and V normalised with Case I. For Case II the load current is approximately 60 % of that under normal condition at the same switching angles. This is approximately 10 % larger than the analytical result. This may be because constant currents are assumed in the linear analysis. In practice the current levels for Cases I and II may differ as a result of the single-pulse control and the difference in impedance on opening 4 coils. For Case V, the load current is approximately 86 % which agrees with the analytical prediction.

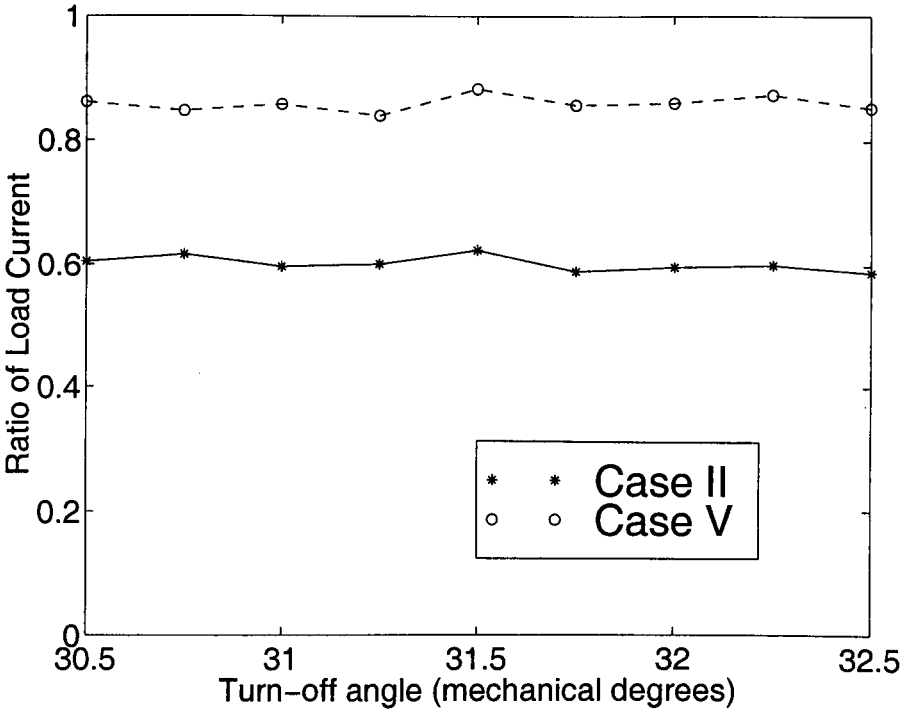

Figure 4.13: Ratio of load current under open-coil faults (load current for case I = 1)

Case I	Normal condition	(NSNSNSNS)
Case II'	4-coil short	(N@N@S@S@)
Case III'	4-coil short	(N@S@N@S@)
Case IV'	4-coil short	(N@N@N@N@)

@ refers to a short-circuit coil

Table 4.3: Definition of Short-Circuit Coil Faults

Short-circuit coil faults

The generating tests were also carried out with some of the coils were short-circuited instead of open-circuited. The fault conditions are listed in Table 4.3.

Fig. 4.14 shows the load current measured for the same conditions as for the open-circuit faults. Fig. 4.15 shows the ratio of the load current. For Cases II' and III' the load current is around 10 % smaller than the open- circuit faults. Induced current in the short-circuit coils may reduce the output of the SRG. The induced current was observed and its amplitude was around 10 % of that of the healthy current. Case II' generates slightly larger energy than Case III' does. The flux paths of Case II' may reduce the amount of flux which goes through the short-circuited coils. For Case IV' no output was measured and a very large current flowed from the external power supply. Short circuit of coils for this configuration is equivalent to a transformer whose secondary coil is short-circuited because the same amount of flux goes through the short-circuited coils as healthy coils.

The analyses and experimental results are summarised in Table 4.4. It may be concluded that for management of faults in coils with the converter in Fig. 4.2, the winding configuration of Case II has the highest fault-tolerance.

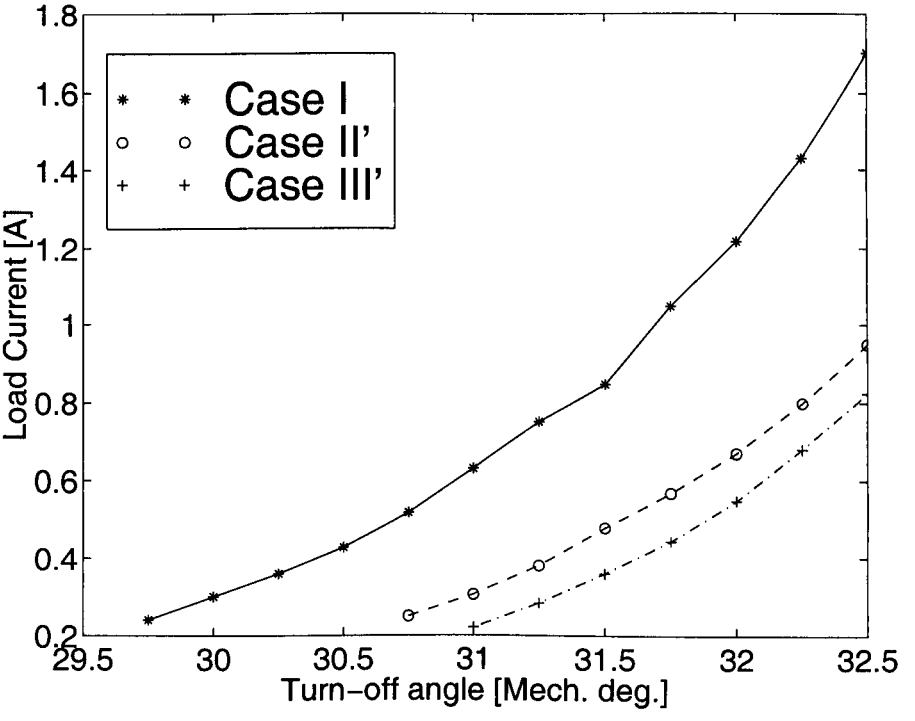

Figure 4.14: Load current under normal and short-circuited coil fault conditions (1,500 rpm, V_o=30 V)

Coil open-circuit faults	Output (vs. normal)
Case II	50 %
Case III	50 %
Case IV	25 %
Case V	86 %
Coil short-circuit faults	
Case II'	50 %
Case III'	40 %
Case IV	0 %

Table 4.4: Performances under Faults

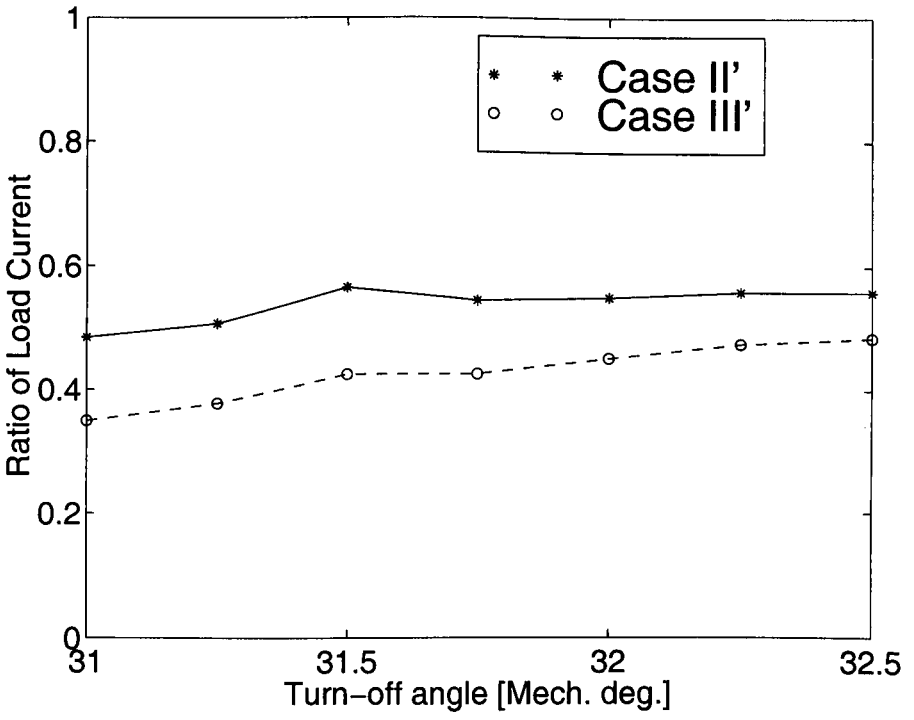

Figure 4.15: Ratio of generated current under short-circuited coil faults(generated current for case I = 1)

4.4 Dynamic operation analysis

In this section, dynamic operation of the proposed fault-tolerant single-phase SRG system is studied. Analytical models of the system under faults are derived and computer simulations are performed. Furthermore, the analysis is validated by experiments.

4.4.1 Modelling of faults

In order to investigate the dynamic operation under the faults, circuit equations of the single-phase SRG are derived. Conditions when one coil bank is disconnected and one coil is open-circuited are considered. For simplicity linear magnetic characteristics are assumed and fringing and leakage-flux are neglected.

Fig. 4.16 shows the model and defines the parameters which are used in the analysis. Coils 1, 2, 5 and 6 are in coil bank A and coils 3, 4, 7 and 8 bank B. The position of N- and S-coils does not affect the linear analysis and is chosen here from the symmetrical point of view. The reluctance is seen by a coil as shown in Fig. 4.17 where $\mathcal{R}$ is a gap reluctance. From Fig. 4.17 the total reluctance of coil 1 is $\mathcal{R}_1 = 8/7\mathcal{R}$ and the mutual inductance between any pair of coils is $M = 1/7L$, where $L = N_p^2/\mathcal{R}$ and N_p is the number of turns per pole. In the linear case $\mathcal{R}$ is the same for all coils, and varies only with rotor position[1].

The circuit equation for coil 1 is expressed as follows:

$$\begin{aligned} v_1 &= Ri_1 + \frac{d}{dt}(Li_1) \\ &\quad + \frac{d}{dt}(Mi_2) - \frac{d}{dt}(Mi_3) + \frac{d}{dt}(Mi_4) - \frac{d}{dt}(Mi_5) \\ &\quad + \frac{d}{dt}(Mi_6) - \frac{d}{dt}(Mi_7) + \frac{d}{dt}(Mi_8). \end{aligned} \tag{4.19}$$

[1]This is a remarkable simplification relative to a "vernier" type SR machine.

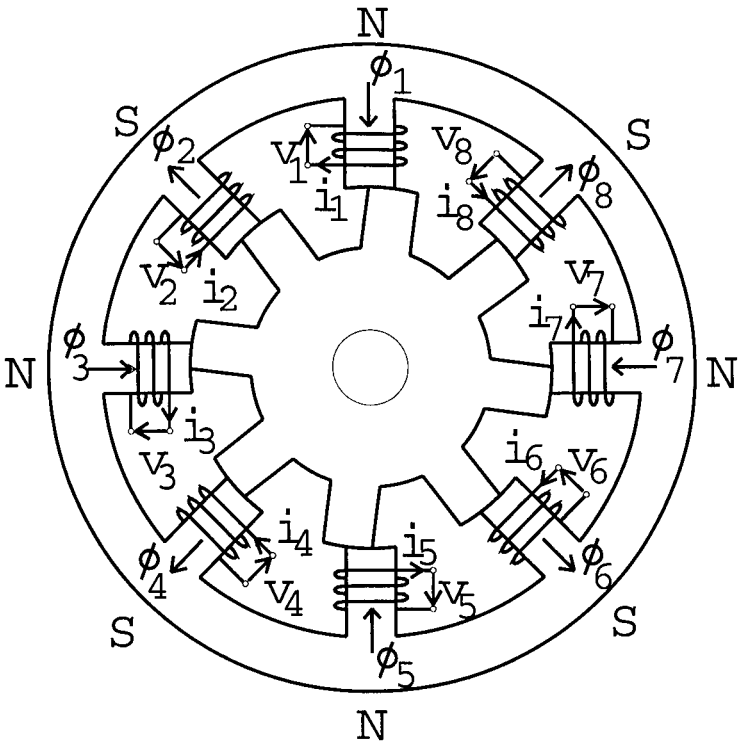

Figure 4.16: Model for the analysis of the 1-ph 8/8 SRM

The torque produced at the pole of coil 1 is

$$\begin{aligned} T_1 &= \frac{1}{2}i_1^2\frac{dL}{d\theta} \\ &+\frac{1}{2}i_1 i_2\frac{dM}{d\theta} - \frac{1}{2}i_1 i_3\frac{dM}{d\theta} + \frac{1}{2}i_1 i_4\frac{dM}{d\theta} - \frac{1}{2}i_1 i_5\frac{dM}{d\theta} \\ &+\frac{1}{2}i_1 i_6\frac{dM}{d\theta} - \frac{1}{2}i_1 i_7\frac{dM}{d\theta} + \frac{1}{2}i_1 i_8\frac{dM}{d\theta}. \end{aligned} \tag{4.20}$$

For the single-phase SRG currents and voltages of all the coils should be identical under the normal condition (Case I). This gives that:

$$v_{coil} = Ri_{coil} + \frac{d}{dt}(Li_{coil}) + \frac{d}{dt}(Mi_{coil}). \tag{4.21}$$

Substituting $M = 1/7L$ gives that:

$$v_{coil} = Ri_{coil} + \frac{8}{7}\frac{d}{dt}(Li_{coil}) \tag{4.22}$$

$$\begin{aligned} T_{coil,I} &= \frac{1}{2}i_{coil}^2\frac{dL}{d\theta} + \frac{1}{2}i_{coil}^2\frac{dM}{d\theta} \\ &= \frac{4}{7}i_{coil}^2\frac{dL}{d\theta} \end{aligned} \tag{4.23}$$

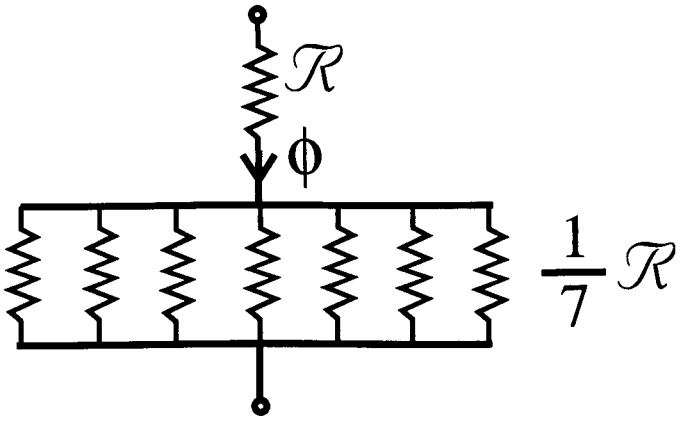

Figure 4.17: Reluctance seen by a coil

$$T_{total,I} = T_{coil,I} \times 8 \tag{4.24}$$

$$= \frac{32}{7} i_{coil}^2 \frac{dL}{d\theta}. \tag{4.25}$$

Disconnection of half the coils

Here, the operation when coil bank B is disconnected is analysed.

Case II and III

The analysis gives the same results for Case II and III. The voltage and current are as follows:

$$v_3 = v_4 = v_7 = v_8 = 0$$

$$i_3 = i_4 = i_7 = i_8 = 0.$$

The equations for a coil do not change from those of the normal condition. Therefore, if the switching angles are kept the values of the normal operation, the currents in operating coils should not change from the normal operation and the phase current is halved. The total torque is reduced to half its normal value since the number of active

poles is reduced to half.

$$T_{total,II} = T_{total,III} = T_{coil,I} \times 4 \tag{4.26}$$

$$= \frac{16}{7} i_{coil}^2 \frac{dL}{d\theta} \tag{4.27}$$

Case IV

For this condition the voltage and current are as follows:

$$v_2 = v_4 = v_6 = v_8 = 0$$

$$i_2 = i_4 = i_6 = i_8 = 0.$$

This gives that:

$$v_{coil} = Ri_{coil} + \frac{4}{7}\frac{d}{dt}(Li_{coil}) \tag{4.28}$$

$$T_{coil,IV} = \frac{1}{2} i_{coil}^2 \frac{dL}{d\theta} - \frac{3}{2} i_{coil}^2 \frac{dM}{d\theta}$$

$$= \frac{2}{7} i_{coil}^2 \frac{dL}{d\theta} \tag{4.29}$$

$$T_{total,IV} = T_{coil,III} \times 4 \tag{4.30}$$

$$= \frac{8}{7} i_{coil}^2 \frac{dL}{d\theta}. \tag{4.31}$$

With this configuration the total torque is reduced to a quarter of its normal value with the same coil currents. However, with fixed firing angles (single-pulse mode) the coil current is twice its normal value and the phase current is as normal since the flux-linkage and the back-EMF are halved, while the average torque is not changed.

This configuration features "self-regulation" of the output when half the coils are disconnected. This may be useful for applications in which output power must not be changed even following a fault provided that the thermal limitations are not exceeded when the coil current is twice its normal value for a certain period.

One coil open-circuit fault (Case V)

When one of the S-coils is open-circuited, the circuit equations for N- and S-coils are as follows:

$$v_N = Ri_N + \frac{d}{dt}(Li_N) + 3\frac{d}{dt}(Mi_S) - 3\frac{d}{dt}(Mi_N)$$

$$v_S = Ri_S + \frac{d}{dt}(Li_S) + 4\frac{d}{dt}(Mi_N) - 2\frac{d}{dt}(Mi_S).$$

Substituting $M = 1/7L$ into the equations above gives the following state-space equations:

$$\dot{x} = Ax + Bu. \tag{4.32}$$

$$x = \begin{bmatrix} i_N \\ i_S \end{bmatrix} \quad \dot{x} = \begin{bmatrix} \dot{i}_N \\ \dot{i}_S \end{bmatrix} \quad u = \begin{bmatrix} v_N \\ v_S \end{bmatrix}$$

$$A = \frac{1}{L}\begin{bmatrix} -4.375R - dL/dt & 2.625R \\ 3.5R & -3.5R - dL/dt \end{bmatrix}$$

$$B = \frac{1}{L}\begin{bmatrix} 4.375 & 2.625 \\ -3.5 & 3.5 \end{bmatrix}$$

Matrix B of equation (4.32) suggests that the rate of change of the current in S-coils i_S is independent of the applied voltage if $v_N = v_S$.

Coil short-circuit fault

With this fault the DC-bus is short-circuited when the switches are on and a large current may flow. In order to prevent the failure of the semiconductor switches and loss of winding insulation, the over-current should be detected by fault detectors and the faulty bank should be disconnected as soon as possible.

Apart from the DC-bus short-circuit, an induced current in the short-circuited coil could be a problem when the faulty coil is magnetically coupled with the healthy coils.

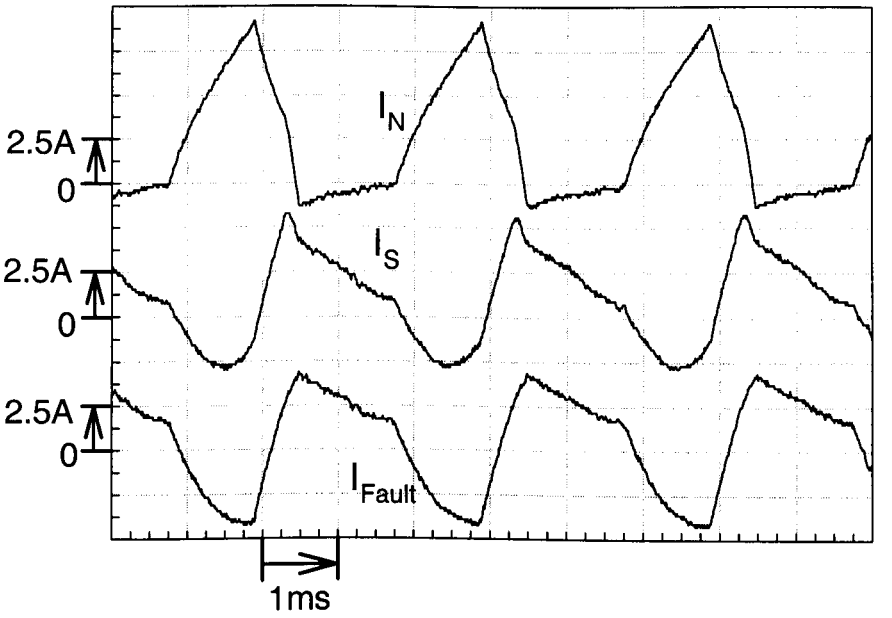

Figure 4.18: Current waveforms when one coil is short-circuited

An example of the induced current is shown in Fig. 4.18. It shows the measured current in the faulty coil when one of the S-coils is short-circuited and physically disconnected from the converter. The current in S-coils I_S differs very much from the normal one and the induced current in the faulty coil I_{Fault} has a comparable shape and amplitude to I_S. Under this condition the generating operation may not be sustained.

The operation after disconnection of the short-circuited bank is investigated by experiment and presented in the later section.

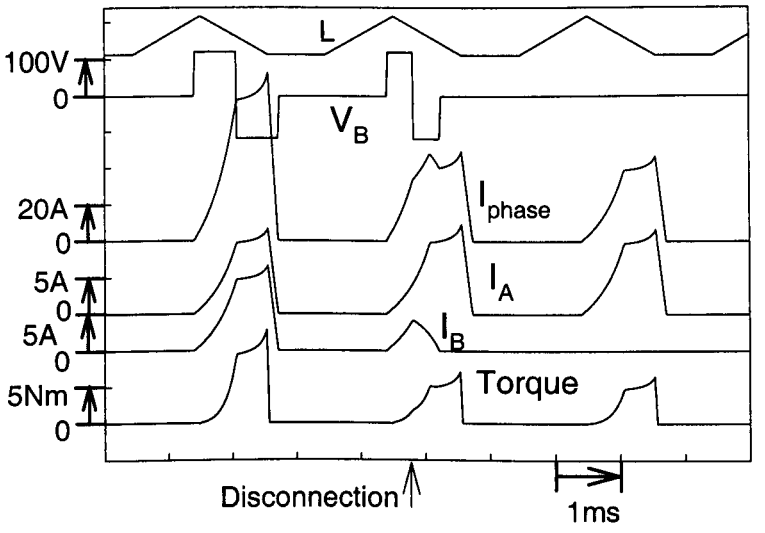

Figure 4.19: Disconnecting a coil bank with Case II and III (simulation)

4.4.2 Simulation study of faults

In this section coil faults are studied by computer simulation with the model derived in the previous section.

Disconnection of a coil bank

Fig. 4.19 shows the simulation result when coil bank B is disconnected while the SRG is generating its power with fixed firing angles (Case II and III). After the turning-off, the current in the disconnected coils I_B is reduced and consequently becomes zero since $-V_{DC}$ is applied through the diodes. The current in the working coil I_A is not changed because of the magnetic independence. The total (phase) current I_{phase} is reduced to half its original value, and the torque as well. During the transition period no impulsive torque was predicted. The proposed SRG system seems to be stable.

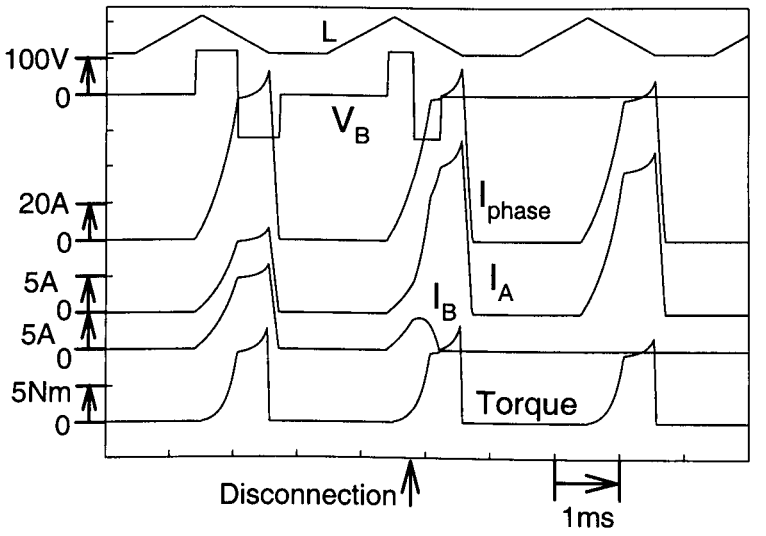

Figure 4.20: Disconnecting a coil bank with Case IV (simulation)

Fig. 4.20 shows the case which is similar to the previous simulation but the remaining coils and disconnecting coils share the flux-paths (Case IV), and are not magnetically independent. The current in the remaining coils increases and reaches twice its original value after the disconnection occurs. The phase current and torque keep their original values, confirming the earlier analysis.

One coil open-circuit fault

The state-space equation (4.32) was evaluated by MATLAB® [98] and the calculated currents in S- (I_S) and N-coils (I_N) are shown in Fig. 4.21 as well as the normal current. When one of the S-coils is open-circuited the current in the remaining S-coils becomes very small and that in N-coils becomes twice its normal value. Even a fault in one of 8 coils affects the operation of all the other coils with the single-phase SRG.

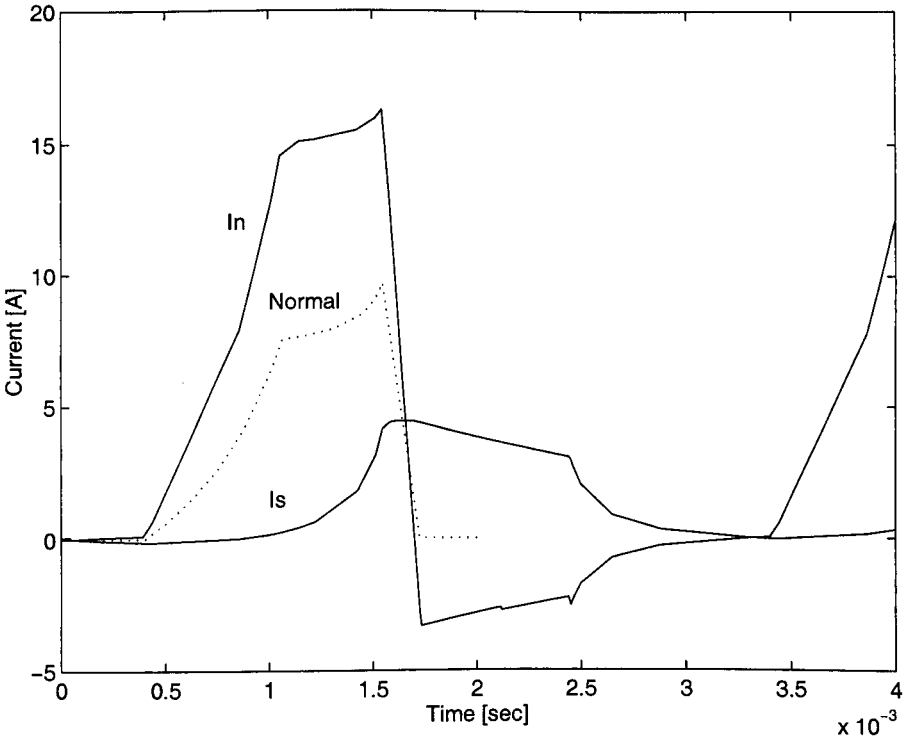

Figure 4.21: One coil open-circuited fault (simulation)

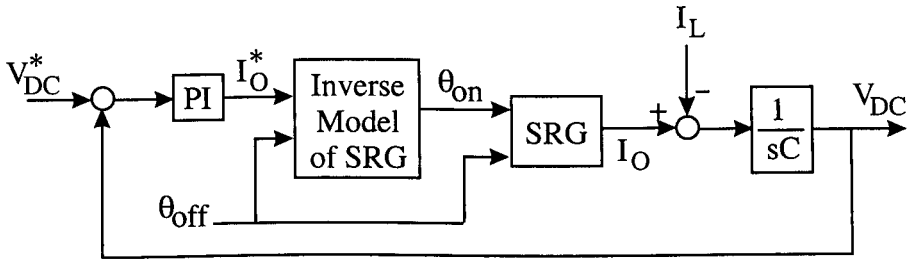

Figure 4.22: DC-bus voltage controller

4.4.3 Experimental validation

DC-bus voltage controller

It was reported in [87] that the SR generator system is inherently unstable with fixed firing angles. In the experiments, a linearised controller which uses an inverse model of the SR generator was used to control the DC-bus voltage [91]. The theory and implementation of the controller are described in detail in chapter 3 and described briefly here. Fig. 4.22 shows the block diagram of the controller. The DC-bus voltage V_{DC} is compared with its reference value and the difference is input to the PI controller. The PI controller outputs the reference value of the net generating current I_O^*. The inverse model of the SRG is used to calculate the switching angles from I_O^* at a V_{DC} and speed. In this experiment the turn-off angle θ_{off} was kept constant, but could also be varied for a dynamic compensation.

Turning off half the coil bank

Fig. 4.23 shows the current waveforms when one of the lower switch (IGBT) is turned off in order to disconnect coil bank B while currents are conducting. The magnetic polarity was configured as Case II. The current in the disconnected coils I_B was reduced since negative bus voltage was applied through the diodes. The current in the conducting coils I_A becomes approximately twice its normal value because the DC-bus voltage controller changes the turn-on angle.

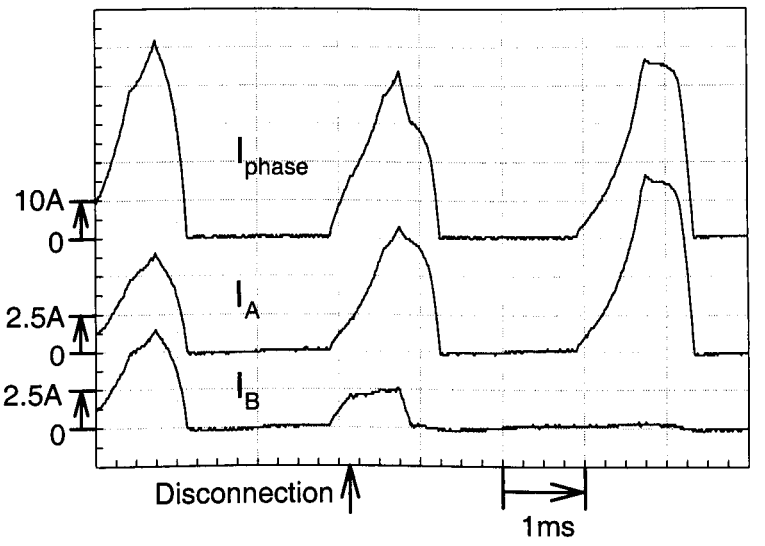

Figure 4.23: Current waveforms when a coil bank is disconnected

Current waveforms when 1 coil is open-circuited

Fig. 4.24 shows the current waveforms when one of the S-coils is open-circuited with the converter shown in Fig. 4.2. The balance between N- and S- coils does not exist any more and the current in S-coils I_S is forced to be small by the mutual coupling between the coils as shown by the simulation in the previous section. Circulating currents through parallel connected coils are also induced which will increase copper and iron losses. Fig. 4.25 shows the current waveforms when one of the S-coils is being open-circuited. The energy stored in the faulty coil is transferred to the other coils at the instance of the open-circuit fault.

Fig. 4.26 shows current waveforms when the faulty bank is disconnected by turning off the semiconductor switch which corresponds to the faulty bank. The currents in the disconnected coils I_{NB} and I_{SB} decrease with time while the current in S-coils in the healthy bank I_{SA} recovers and becomes the same level as that in the N-coils I_{NA}.

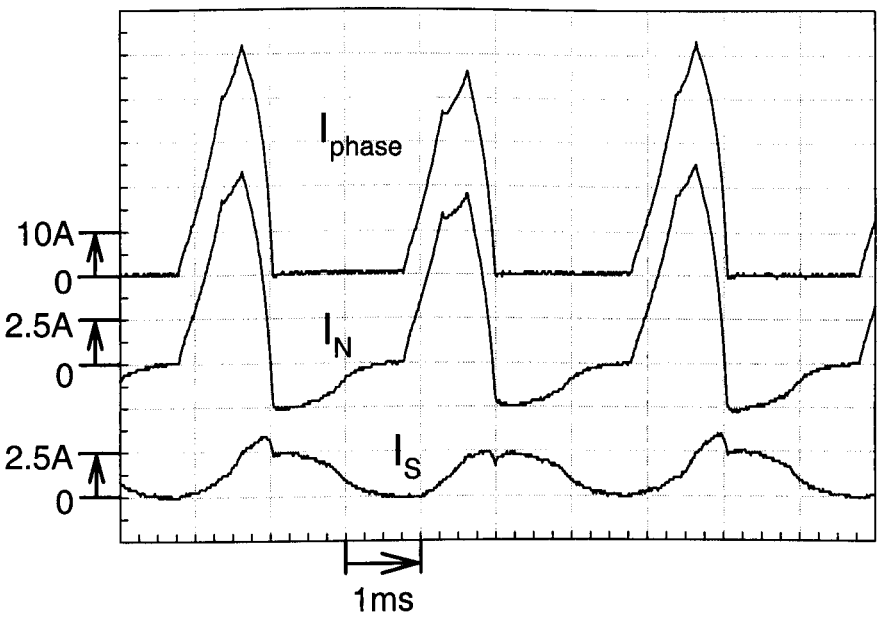

Figure 4.24: Current waveforms when one coil is open-circuited

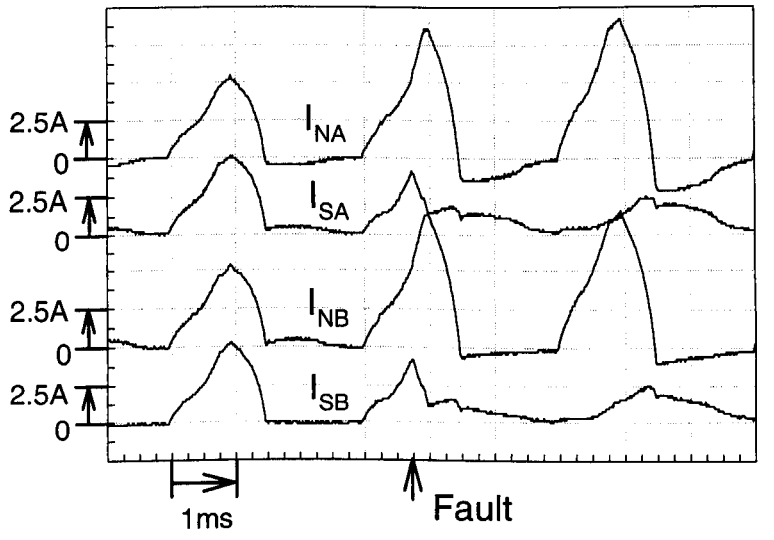

Figure 4.25: Current waveforms when one coil open-circuit fault occurs

The circulating currents in the healthy bank decrease but do not become zero. The reason may be that a perfect balance in the healthy coils is not obtained because of the leakage inductance and the partial saturation of the steel in the prototype machine.

Short-circuit coil fault

Fig. 4.27 shows the current waveforms when one coil is short-circuited by a fault and the faulty bank is disconnected by turning off the corresponding lower semiconductor switch. The current in the short-circuited coil is very small since the magnetic coupling between the banks is very small when one bank is turned off.

This result suggests that the proposed converter manages coil short-circuit fault with proper fault detectors. Detailed discussion on the fault detectors for SRMs is seen in [99]. This is not discussed here in detail but shows a simple example for the split-winding converter. An example of simple implementations of the detector is

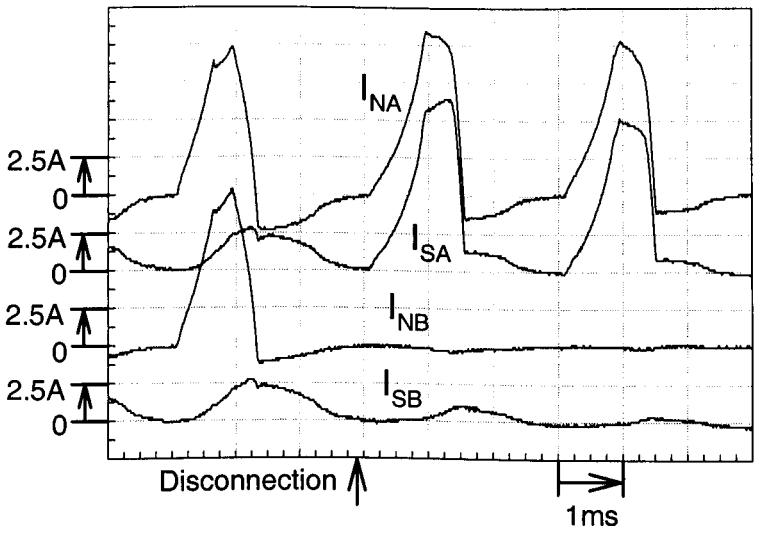

Figure 4.26: Current waveforms when disconnecting the faulty bank

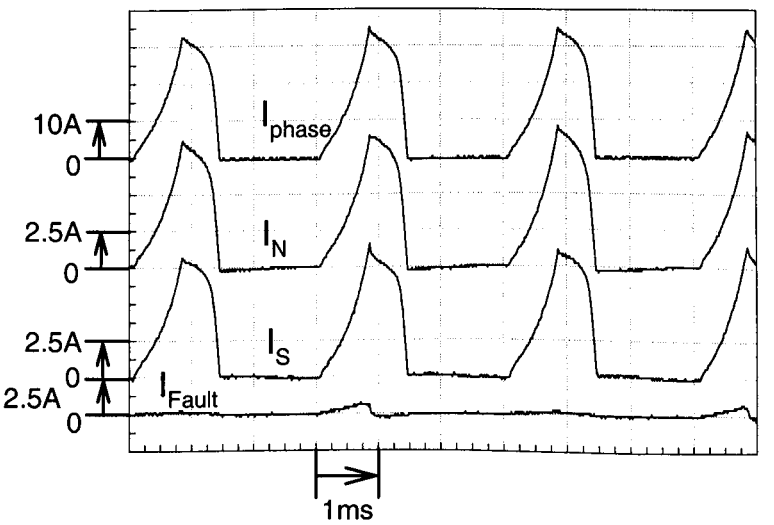

Figure 4.27: One coil short-circuit fault

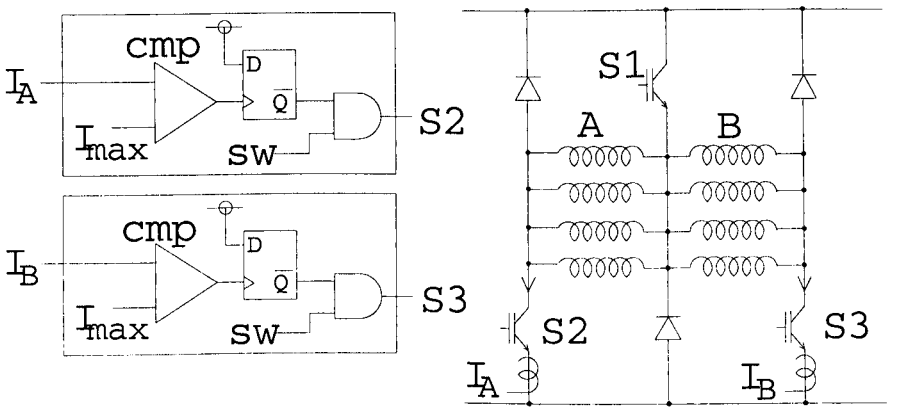

Figure 4.28: Example of fault detector

shown in Fig. 4.28. One current sensor may be used for the each leg to detect over currents. When the current in a leg exceeds the threshold I_{max} the fault is detected and the flip-flop hold the signal. The output of the flip-flop blocks the switching signal SW to the semiconductor switch in the faulty leg. It is an advantage of the proposed converter that only two current detectors are required.

4.5 Conclusions

This chapter has discussed fault-tolerant operation of switched reluctance generators, in particular the the single-phase 8/8-pole machine. It has studied the operation with the split-winding converter under open- and short-circuit coil faults.

The linear analysis and finite-element analysis reveals that with 4 of 8 coils open, the SRG is still capable of generating half its normal power for the same coil current. This was confirmed by static torque measurement and generating tests. It is concluded that the winding configuration which gives NNSSNNSS magnetic polarity may be the best when the windings of the single-phase SRG are split into two banks in parallel.

The transient states on disconnecting faulted coils with the proposed system have also been studied. The circuit equations under faults were derived and the operations under faults were simulated. The capability of the converter to disconnect a faulty bank was confirmed. It was shown that output power with the fixed-angle single-pulse control is normal value or half its normal value depending on the winding configuration when half the coils is disconnected. It was also shown that a fault in one of 8 coils affects all the coils significantly. Experiments were performed with the SRG controller using an inverse model to control the DC-bus voltage. The experimental results proved stable operation of the SRG under the coil faults with proper fault detectors.

Chapter 5

Analysis and classification of winding and inverter faults in the switched reluctance machine

In this chapter, an in-depth study of winding and inverter faults in switched reluctance machines (SRMs) is presented. The analysis is based on a new lumped parameter magnetic equivalent circuit (MEC).

It is commonly assumed that the SRM drive is fault tolerant because of the independence between phases. However, when shared magnetic paths saturate or when individual pole coils no longer exhibit identical properties, the per-phase modelling approach loses its accuracy. Winding and inverter faults in the SRM are analysed using a new lumped parameter MEC taking full account of the mutual coupling between phases. Faults are categorised in terms of the effects on the SRM drive system.

The study in the chapter was conducted as part of the Large Electro-Mechanical Actuation Systems for Future Civil Transport Aircraft (LEMAS) project.

5.1 Introduction

The SRM is considered for applications where a certain degree of fault tolerance is required, especially those for aircraft. However, very severe conditions can occur with certain faults although it is widely assumed to be fault tolerant. This chapter studies a variety of winding and inverter faults and aims to classify them in terms of their severity. The analysis is based on a new lumped parameter MEC. The method is able to model the airgap and rotor/stator pole-tip permeances independently of each other, and takes full account of the mutual coupling between phases. It also avoids the difficultly of representing the permeances analytically.

One of the earliest works on faults in the SRM is Stephens' work [66]. Various faults in a 4-ph 8/6 SRM were tested with a laboratory drive. The phase windings were assumed to be connected in series. It included phase open- and short-circuit, a coil short-circuit, midphase short to ground and phase to phase short-circuit faults. Fault detection circuits were also proposed and studied. The study included experimental results, but no detailed analysis of operation under faults was given.

The problem of lateral forces produced by winding failures and mechanical imbalances was discussed in [97]. Simulation results of open- and short-circuit coil faults were included. It also discussed the relative merits of different winding configurations. However, it did not include simulation or experimental results with different winding configurations.

The interaction between channels in dual-channel 3-ph 12/8 and 18/12 SRMs is discussed in [67]. It was reported that the control of each channel appears to be stable and the disturbance of the other channel seems to be small, even though the two channels share the flux paths.

An iterative approach for the dynamic simulation of the SRM system including fault conditions was discussed in [100, 101]. For the simulation, a state space model was solved, where the model parameters were determined from a series of finite element

analysis solutions. Open-circuit inverter switch failure and one coil short-circuit faults were analysed and verified by experimental results. The analysis was carried out at no load and full load conditions using single-pulse mode. However, neither induced currents in the short-circuit coil nor lateral forces were discussed.

Ref. [102] compared the SRM and the permanent magnet motor for high-performance fault-tolerant applications and proposed a new design of permanent magnet motors. Ref. [103] pointed out the significance of the induced current in the shorted turns when part of a coil is short-circuited in the permanent magnet motor.

Although several works have been reported as described above, the analysis on faults in the SRM does not seem to be complete. The objective of the study in the chapter is to provide an in-depth analysis of winding and inverter faults in the SRM.

5.2 The lumped parameter MEC

In this section, it describes the new lumped MEC used for the analysis, which was originally proposed by Kjaer in [104].

5.2.1 Method of the MEC

Several methods for analysing the SRM including the mutual-coupling between phases have been published. In [105, 106, 107] lumped parameter magnetic equivalent circuits were used to analyse mutual coupling and multi-phase operation of the SRM. The pole-tip and gap permeances were expressed analytically as functions of the flux level and rotor position. The network of [107] proposed by Preston is shown in Fig. 5.1 for a 4-ph 8/6 motor (leakage components omitted for clarity). However, difficulty in obtaining an accurate analytical expression of the pole-tip (R_{st}, R_{rt}) and gap permeances (R_g) remains.

Ref. [108, 109] discussed a different approach to model multi-phase operation, where

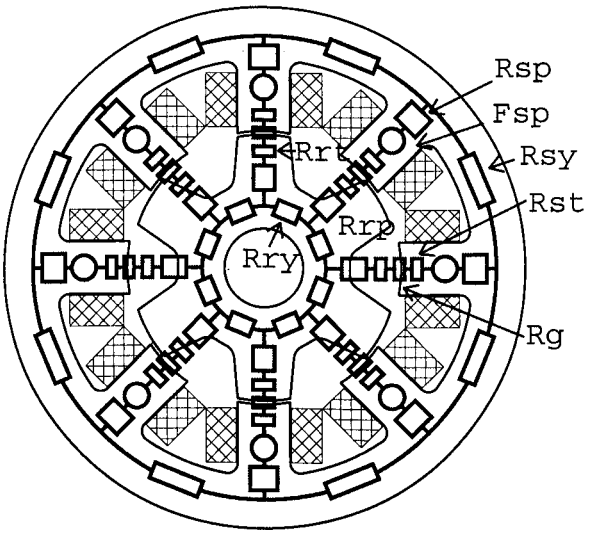

Figure 5.1: Magnetic equivalent circuit proposed by Preston

the magnetisation curves were expressed as functions of more than one phase current. However, this may not be suitable for dynamic simulations as it requires excessive magnetisation data and as it does not allow winding fault analyses.

The time-stepping finite element analysis is another option for dynamic simulation of the SRM [110] including faulty conditions. Although it provides a good accuracy, calculation time and limited flexibility to include converters and controllers are the drawbacks.

The MEC used here has advantages over previously published methods [104]. The features of the MEC are:

- An accurate and generic electromagnetic model.
- It allows multi-phase operation including faulty conditions.
- It avoids the problems of analytical expression of the pole-tip and gap permeances.
- It is easy to implement into commercial software packages that can simulate converters and controllers.

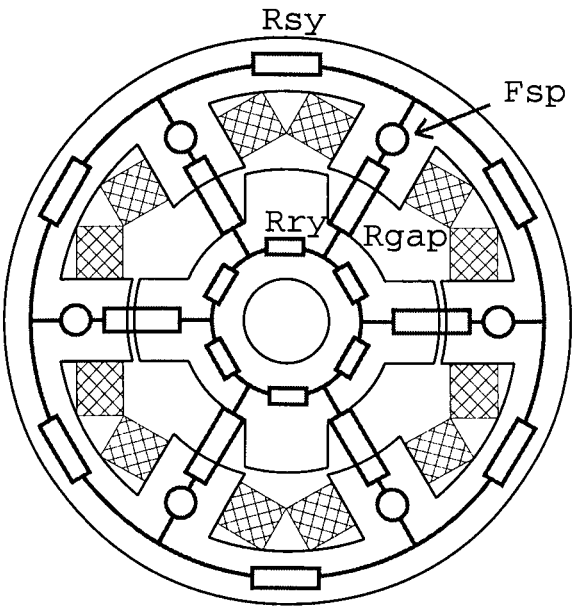

Figure 5.2: Magnetic equivalent circuit of a 3-ph 6/4 SRM

Fig. 5.2 shows the MEC of a 3-ph 6/4 SRM proposed and used in the analysis. The stator and rotor yokes are divided into N_s regions between stator poles, where N_s is the number of stator poles. The permeance in a segment of the stator yoke is represented as R_{sy}, and that of the rotor yoke is represented as R_{ry}. R_{sy} and R_{ry} are calculated from the geometry and steel B-H data, therefore, the nonlinearlity is taken into account. The stator and rotor poles, pole-tips and airgap permeances are included in R_{gap}. The method to calculated R_{gap} is described later. MMF produced by a pole coil is represented as $F_{sp} = N_p \cdot i(\psi, \theta)$, where N_p is the number of turns per pole and i is the coil current which is functions of the flux-linkage ψ and rotor position θ.

The way to derive R_{gap} is described in the following. Fig. 5.3 shows the magnetic equivalent circuit when only one phase is energised. The flux paths are assumed as shown in Fig. 5.3. This assumption gives that the pole-pole leakage is ignored and all the flux passes through the gaps. For a given flux level, the MEC equation is:

$$F_{ph}(\phi, \theta) = F_{sy}(\phi) + F_{ry}(\phi) + 2F_{gap}(\phi, \theta) \tag{5.1}$$

where F_{ph} is the phase MMF $F_{ph} = 2F_{sp}$, F_{sy} is the MMF drop in the stator yoke

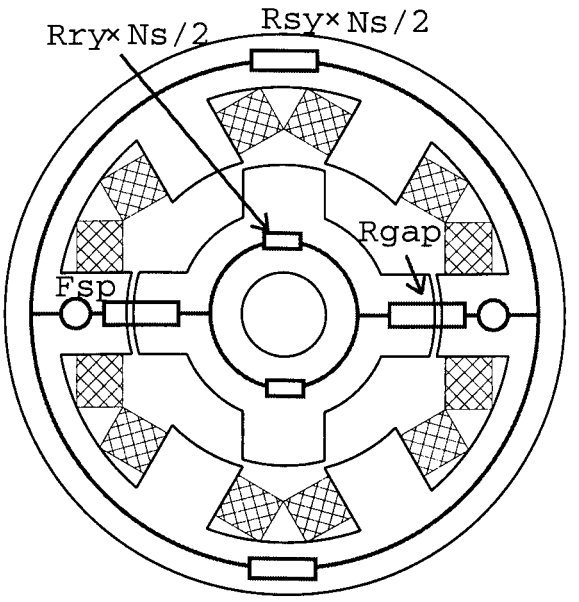

Figure 5.3: Magnetic equivalent circuit when one phase is energised

$F_{sy} = \left\{\frac{1}{2}\frac{N_s}{2}R_{sy}(\phi)\right\}\phi$, F_{ry} is the MMF drop in the rotor yoke $F_{ry} = \left\{\frac{1}{2}\frac{N_s}{2}R_{ry}(\phi)\right\}\phi$, and F_{gap} is the MMF drop in the gap including stator and rotor poles. By rearranging equation (5.1), F_{gap} is expressed as:

$$\begin{aligned} F_{gap}(\phi,\theta) &= F_{sp}(\phi,\theta) - \frac{1}{2}\{F_{sy}(\phi) + F_{ry}(\phi)\} \\ &= N_p i(\phi,\theta) - \frac{1}{2}\frac{N_s}{2}\left\{\frac{R_{sy}(\phi)}{2} + \frac{R_{ry}(\phi)}{2}\right\}\phi \end{aligned} \tag{5.2}$$

where N_p is the number of turns per pole. F_{gap} can be calculated from a set of magnetisation curves for one phase excitation which may be measured or FEA calculated, R_{sy} and R_{ry} can be derived from the geometry and steel B-H data.

Fig. 5.4 shows the magnetisation curves for a gap $F_{gap}(\phi,\theta)$ used for the analysis together with measured magnetisation curves for a coil from which $F_{gap}(\phi,\theta)$ was calculated.

The electromagnetic torque is calculated for each airgap as

$$\tau(F,\theta) = \frac{\partial}{\partial\theta}\int_0^F \phi\, dF \tag{5.3}$$

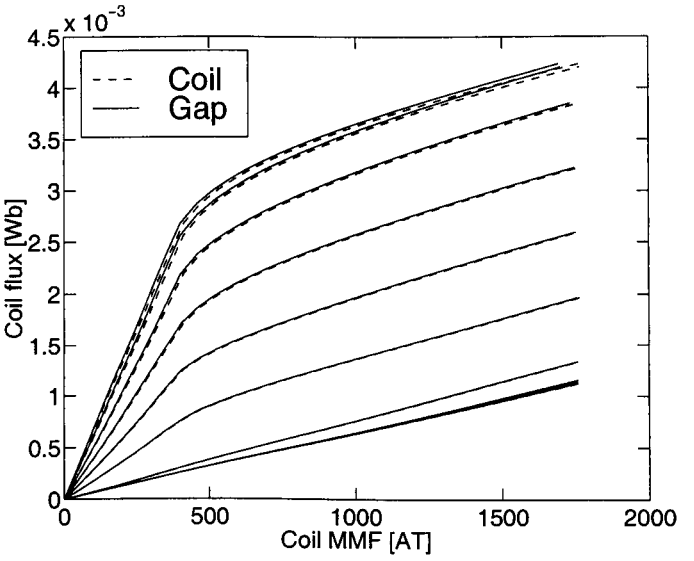

Figure 5.4: Measured magnetisation curves for a coil and calculated ones for a gap

and may be evaluated numerically from the look-up table. The total shaft torque is then formed by summation of each gap-torque.

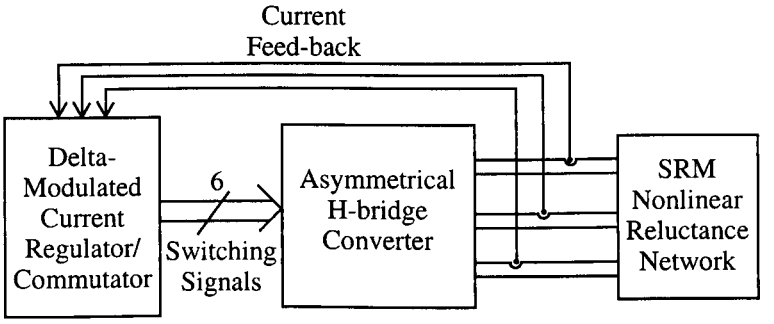

Figure 5.5: SRM drive model

5.3 Implementation of the MEC in Saber simulator

The network has been implemented in the Saber™ simulation package [111] which is a fast and powerful network solver highly suited for simulation of both the equivalent magnetic circuit and the power electronic converter including all commutation and current regulation elements.

Fig. 5.5 shows the block diagram of simulation model implemented in the Saber™. The SRM nonlinear reluctance network block consists of the MEC described in the previous section. The components in the asymmetrical H-bridge converter like power transistors, diodes, capacitors etc are simply picked from Saber™'s library. The phase currents are regulated by a delta-modulated regulator. The SRM is fed by the classical asymmetrical half-bridge inverter (Fig. 5.6). The static torque curves vs. gap flux data is calculated from measured magnetisation curves and stored as a look-up table. The radial force at a pole F_{rp} is simply estimated as:

$$F_{rp} = \frac{B_{olp}^2}{2\mu_0} A_{olp} \tag{5.4}$$

where A_{olp} is the overlap area of stator and rotor poles, B_{olp} is the flux density in the overlapped area and μ_0 is the vacuum permeance. The total radial force vector $\boldsymbol{F}_{rp}$ is calculated as vector sum of F_{rp}:

$$\boldsymbol{F}_r = \sum_{j=1}^{N_s} \boldsymbol{F}_{rp} \tag{5.5}$$

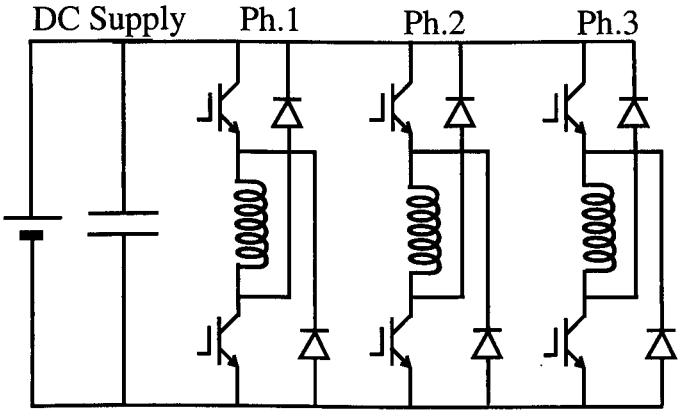

Figure 5.6: Classical asymmetrical half-bridge inverter

where N_s is the number of stator poles.

Number of phases	4
Number of stator/rotor poles	8/6
Rated power	5 KW
Number of turns per pole	70
Number of faulty turns	10
Phase coil connection	Series
Pole magnetic polarities	NSNSSNSN
Voltage	270 V
Current set point	10 A
θ_{on}/θ_{off}	26°/48°
Speed	5,000 rpm

Table 5.1: Conditions for turns short-circuit fault simulations

5.4 Validation with time-stepping FEA

For the validation of the proposed method, simulation results are compared with the time-stepping finite element analyses (FEA).

A 4-ph 8/6 motor was simulated running at a constant speed of 5,000 rpm and a reference current of 10 A was specified. The commutation angles were $\theta_{on} = 26°$ and $\theta_{off} = 48°$, i.e. most of the time two phases excited. The pole magnetic polarities were configured as NSNSSNSN which yields a higher average torque than NNNNSSSS (A comparison will be shown later.). 10 out of 70 turns on one coil were shorted in phase 1 after 5 msec, while all phases were excited as normal. The conditions are summarised in Table 5.1

For the validation of the proposed method, results of time-stepping FEA on the identical fault condition, which were supplied by Lucas Varity plc., were used. The current regulators were modelled by ideal current sources in the FEA. Although the analytical model was two-dimensional, the effect of end-winding flux was taken into account by adding extra resistance and leakage inductance components to the external circuit. In the FEA model the airgap length was set at 0.17 mm by accident, although the airgap was 0.26 mm for the prototype machine from which the electromagnetic data was measured for the simulation with the proposed method. Other parameters

were identical to the simulation.

The results are shown in Fig. 5.7, where solid lines show results by the proposed method and dotted lines show ones by the time-stepping FEA. The current in the faulty turns i_f is approximately 5 times the phase current i_1, yet the effect of the fault is barely visible in the phase current. If it is not detected and cleared, such a fault could propagate to other turns or coils in a short time. The total torque T is also affected by the very large current in the shorted turns. The phase and faulty currents predicted by both methods agree very well. However, the torque levels by the two methods differ by more than 20 % although the general trends are similar. The main source of the difference can be considered as the difference in the airgap length as mentioned above. $|F_r|$ shows the amplitude of radial force vector. Both methods predicted a considerable production of radial forces as a result of the fault.

For the particular simulation shown in Fig. 5.7, the proposed method took a few minutes (once static FEA data or measurements are available) while the time-stepping FEA took more than 7 hours with 9,000 elements and 500 timesteps on comparable Unix workstations. This indicates the advantage of shorter computing time of the proposed method over the time-stepping FEA.

As an example, torque output of the 8/6 motor with different pole magnetic polarities were simulated. The conditions were identical to those in Table 5.1 except for the switching angles θ_{on}/θ_{off} which were $20°/50°$ giving two phase excitation all the time. Fig. 5.8 shows the total electromagnetic torque for operation with phase interaction for an excitation sequence of (NSNSSNSN) and of (NNNNSSSS) together with the contribution of one phase. The straight lines show the average values of the torque. The first sequence yields 4% higher average torque than the latter because of shorter shared flux paths and hence lower yoke mmf-drops. Fig. 5.9 shows pole and yoke-segment fluxes for both cases. The yoke-segment fluxes differ because of the difference in flux distribution in the machine although the pole fluxes are similar for both cases.

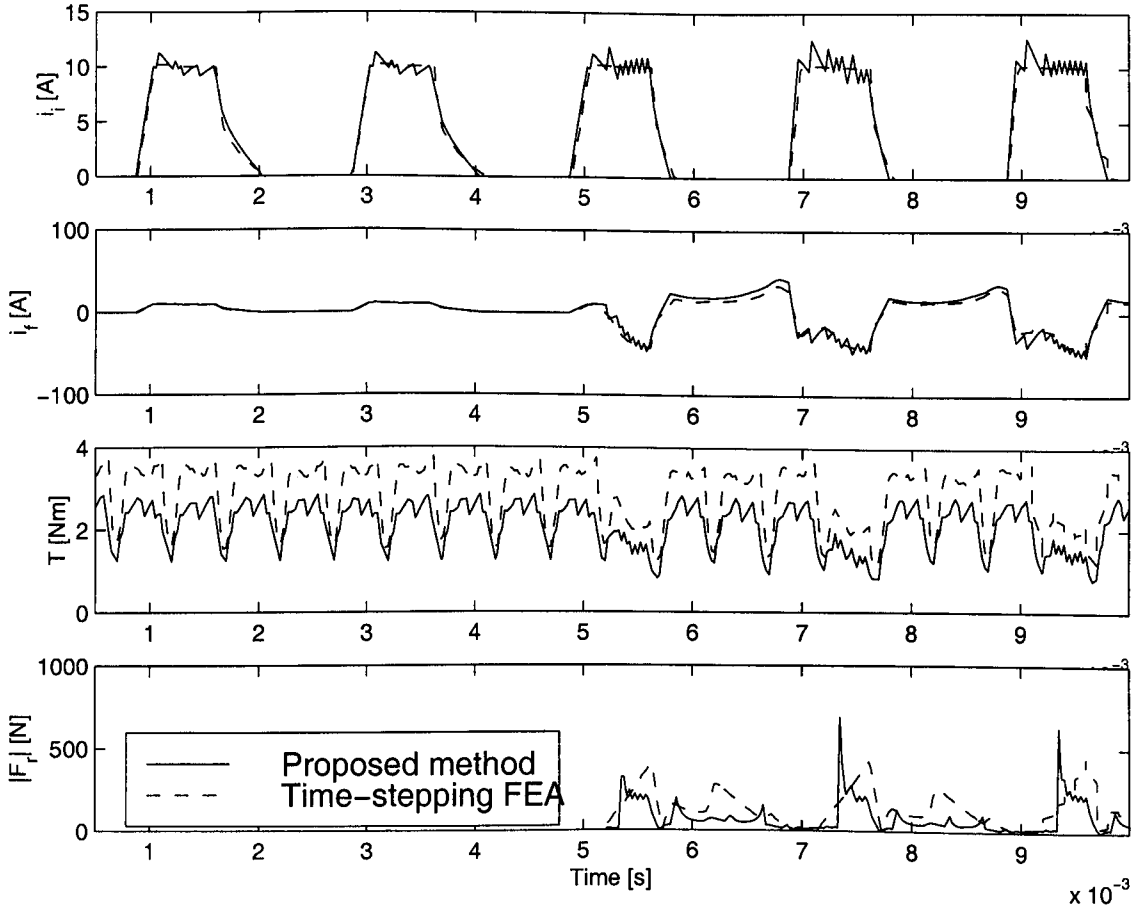

Figure 5.7: Comparison of proposed equivalent circuit method with time-stepping FEA results

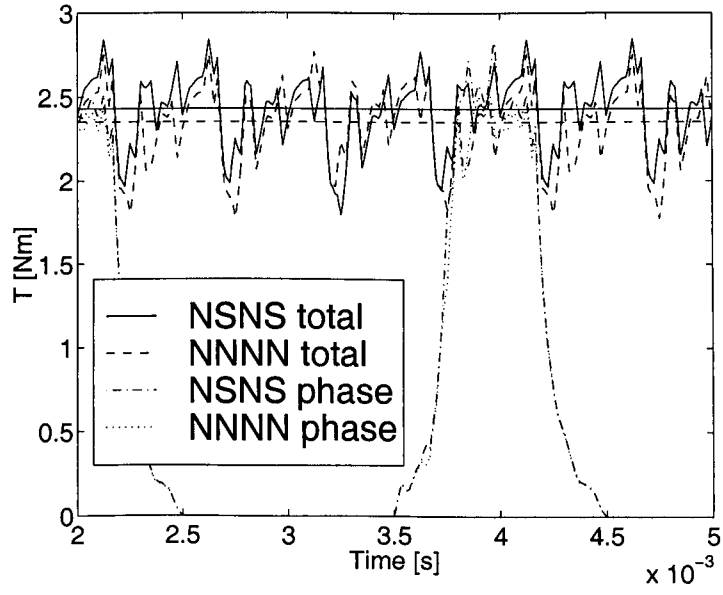

Figure 5.8: Torque output with NSNSSNSN and NNNNSSSS configurations

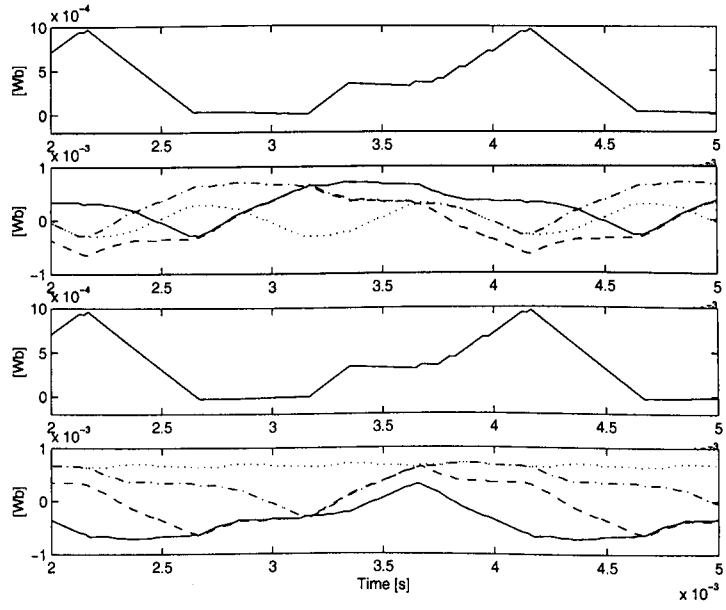

Figure 5.9: Flux waveforms in pole and yoke-segments (top: pole flux with NSNS, second top: yoke-segment fluxes with NSNS, second bottom: pole flux with NNNN, bottom: yoke-segment fluxes with NNNN)

5.5 Winding configurations and analysed faults

The windings of the SRM can come in several different configurations depending on the application. Fig. 5.10 illustrates some of the possible configurations. The single coil/pole series connection is the most commonly used (a). For high speed applications, it would be required to have more turns per pole. The parallel connection has the advantage of lower copper diameter thereby providing space for the additional turns (b) [97]. Multi-channel applications would use either of the two remaining configurations (Fig. 5.10 (c)(d)), again the parallel version being more applicable in high speed applications. Other winding configurations including the fully pitched winding [112] are possible. However, the analysis in this chapter includes the single-channel configurations shown in Fig. 5.10 (a) and (b) only.

All the faults studied assume a 3-phase 6/4 SRM. With current control mode, it is assumed that the upper leg transistors ($Q1$, $Q3$, $Q5$ in Fig. 5.11) are chopped. Table 5.2 shows the fault conditions analysed in this chapter. Three main categories of faults include:

1. Coil faults with series connected phase coils
2. Coil faults with parallel connected phase coils
3. Inverter faults.

Each coil fault includes coil open-circuit, full coil short-circuit, partial coil short-circuit, phase to phase short-circuit and coil to ground short-circuit. The studied faults are listed in Table 5.2. Fig. 5.11 shows the definition of the faults graphically, indicating (a) and (b) for series and parallel connected phase coils respectively. In Fig. 5.11 (a), closing switch a represents the bus short-circuit fault, closing switch b represents the transistor short, opening switch c represents the coil open, closing switch d represents the full and/or partial coil short, closing switch e to L or C represents the phase to phase either low to low or low to centre terminal short and closing switch f represents

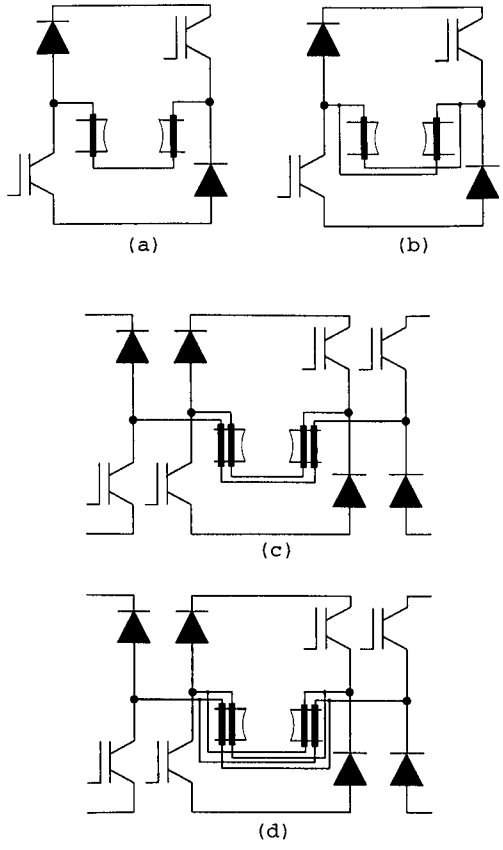

Figure 5.10: Winding configurations ((a) 1 coil/pole series, (b) 1 coil/pole parallel, (c) 2 coils/pole series, (d) 2 coils/pole parallel)

coil to ground short. Fig. 5.11 (b) indicates the similar ones for the parallel connection. For each faults, two cases of magnetic polarity of poles are considered. One case is that adjacent poles have opposite polarities and is expressed here as NSNSNS configuration as shown in Fig. 5.12. The other one is that the magnetic polarity of one of the phases is altered and expressed as NNNSSS. These conditions are considered since the mutual coupling is expected to perform significant role to the operation under faults.

Investigating the likehood of occurrence of faults in the SRM is of importance. However, it does not seem to have been published. The analysis in the chapter concentrates on the impacts of faults and the investigation of the likehood of occurrence of them is left for other work. For 3-phase permanent magnet motors, ref. [103] presented a list of failure rates.

Categories	Faults	Definition
Series connected coil faults	Coil open-circuit	Fig.5.11 (a)-c
	Full coil short-circuit	Fig.5.11 (a)-d
	Partial coil short-circuit	Fig.5.11 (a)-d
	Phase to phase short-circuit	Fig.5.11 (a)-e
	Coil to ground short-circuit	Fig.5.11 (a)-f
Parallel connected coil faults	Coil open-circuit	Fig.5.11 (b)-c
	Full coil short-circuit	Fig.5.11 (b)-d
	Partial coil short-circuit	Fig.5.11 (b)-d
	Phase to phase short-circuit	Fig.5.11 (b)-e
	Coil to ground short-circuit	Fig.5.11 (b)-f
Inverter faults	Transistor short-circuit	Fig.5.11 (a)-b
	Bus short-circuit	Fig.5.11 (a)-a

(Two cases of magnetic polarity of poles: NNNSSS & NSNSNS for each case.)

Table 5.2: List of analysed faults

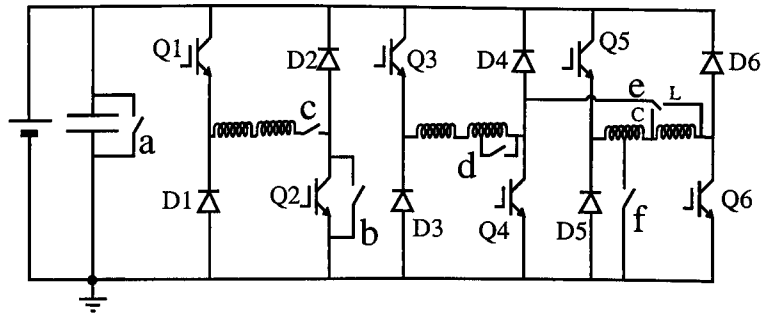

(a) series connected coils

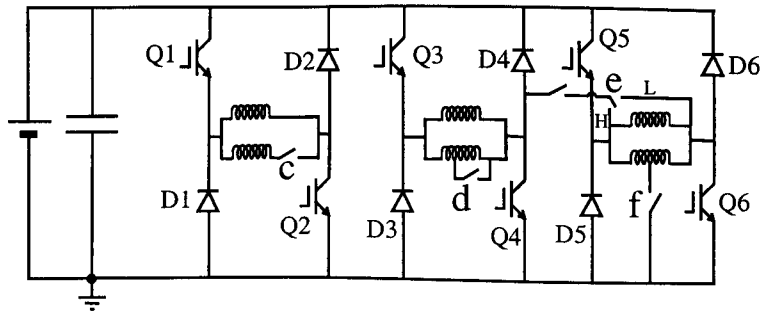

(b) parallel connected coils

Figure 5.11: 3-phase SRM circuit with series and parallel connected coils

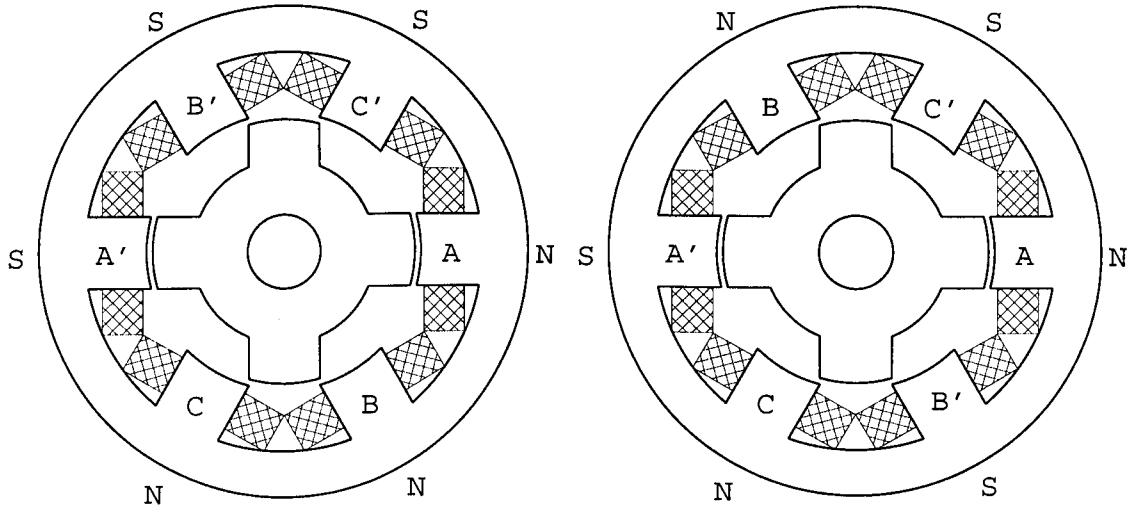

Figure 5.12: Two cases of magnetic polarity of poles

Output torque	T
Phase one current	i_1
Phase two current	i_2
Phase three current	i_3
Coil 1 current in phase 1	i_{c1}
Coil 2 current in phase 1	i_{c2}
Fault current	i_f
Radial force towards pole A	F_r
Flux in pole A	$Flux_1$
Fault flux	$Flux_f$

Table 5.3: Notation in figures

5.6 Series connected coils

In this section, coil faults with series connected phase coil configuration, which is commonly used in the SRM are studied.

5.6.1 Open-circuit phase coil

With series connected coils, the phase current in the faulty phase becomes zero after the fault and the total torque becomes 1/3 of its normal value. The fault does not affect the operation of the remaining healthy phases. The character of this fault is not affected by the saturation, or by the magnetic configuration of the machine. Because both coils of the faulty phase carry no current, there are no unbalanced radial forces. An example of waveforms of the fault is shown in Fig. 5.13, where one of the phases is open-circuited after 0.05 sec.

In the following figures, the notation shown in Table 5.3 is used otherwise stated.

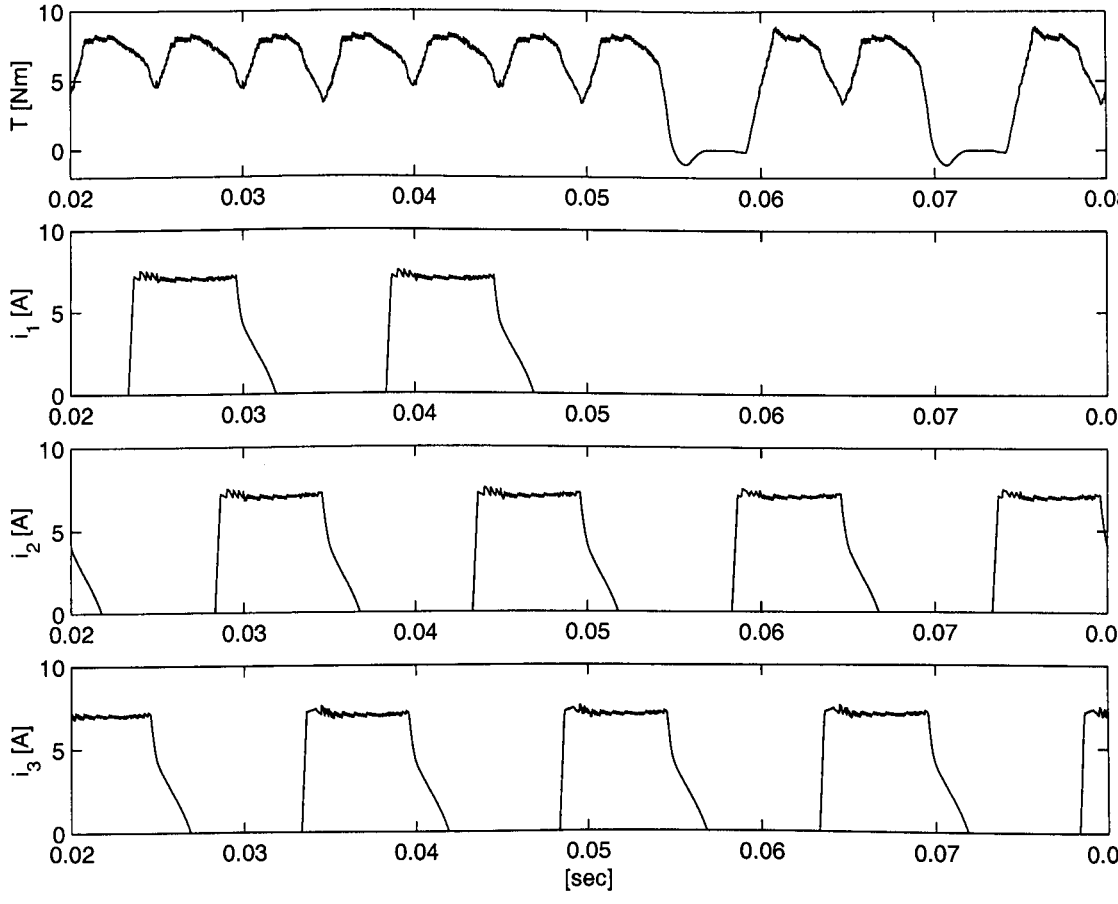

Figure 5.13: Coil open-circuit fault

5.6.2 Short-circuit coil

The short-circuited coil, whether being the full coil or only a fraction of, is perhaps the most likely fault to occur with the SRM. The character of the fault depends to a large degree on the number of turns shorted and on the operating point. Several configurations of this fault have been studied. All the faults are assumed to occur in phase 1.

When one of phase 1 coils is short-circuited with the current chopping operation, the most significant impacts to drive performance are the reduction in torque and unbalanced radial forces. The phase current in the faulty phase still can be regulated at a reference value. Since the phase inductance is reduced by the fault with loss of half the phase turns and change in flux paths, di/dt of the faulty phase increases. With the simulated machine, di/dt increased by a factor of 2 after the fault. The flux produced by the healthy coil does not flow into the faulty coil because the induced current opposes. The main paths of the flux are diverted through the phase 3 poles with the switching sequence being assumed Ph1-Ph2-Ph3. This results in larger mutual coupling between Phase 1 and other phases. However, the effect to the operation of the healthy phases does not seem to be significant (Fig. 5.14). The total output torque will have a large dip during Phase 1 exciting period. Excessive unbalanced radial force towards the phase 1 healthy coil is produced.

When only a fractional part of coil is short-circuited, temperature rise in the shorted turns produced by an excessively high induced current will become the main concern. Because the resistance of the shorted part of the coil is very low, the simulation results with 1% of a coil turns being short-circuited predicted induced current in excess of 30 times the phase current and will inevitably lead to insulation breakdown and a progressive shorting of adjacent turns. Since the number of turns being shorted is much smaller compared to the healthy part and the fault current flows through only a fractional turns, the reduction in the output torque is not significant. Because the effect on the flux through the faulted pole is also not significant, the amount of unbalanced

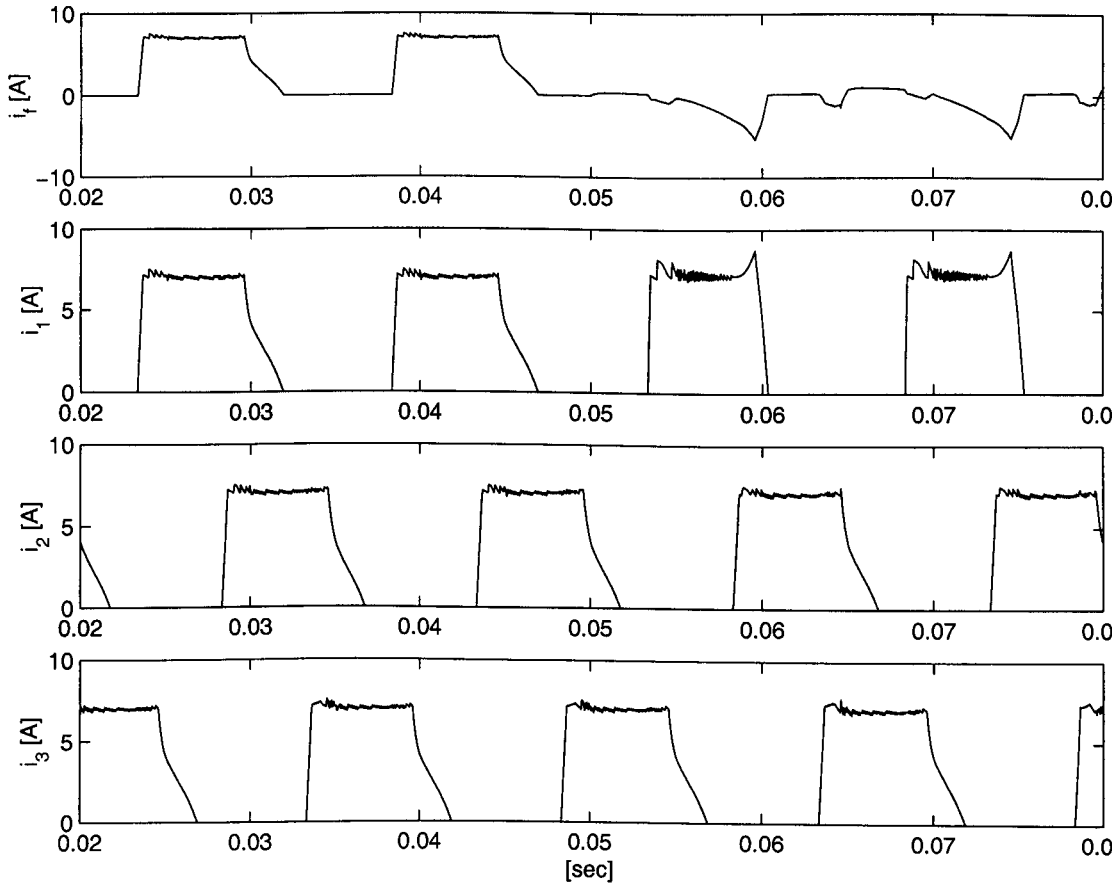

Figure 5.14: One coil short-circuit fault

radial forces are much smaller than those in one coil short-circuit fault.

Simulation results in Fig. 5.15 shows the faulty currents induced in the shorted turns i_f, total output torque T and radial force towards the phase 1 healthy coil F_r for 1-turn, 20-turns and full coil (98 turns) short-circuit faults. The amplitude of i_f of 1-turn short fault is more than 50 times the normal value of the phase current which is set at 7 A in the simulation while those of 20-turns and full coil short are much smaller and the amplitude of i_f of the full coil short is less than 7 A. Torque production T during the faulty phase excitation is reduced by approximately 20% for 1-turn and 60% for 20-turns and full coil short-circuit faults. Although not shown, radial forces towards other directions also exist even the amplitude is of fraction of F_r shown in Fig. 5.15.

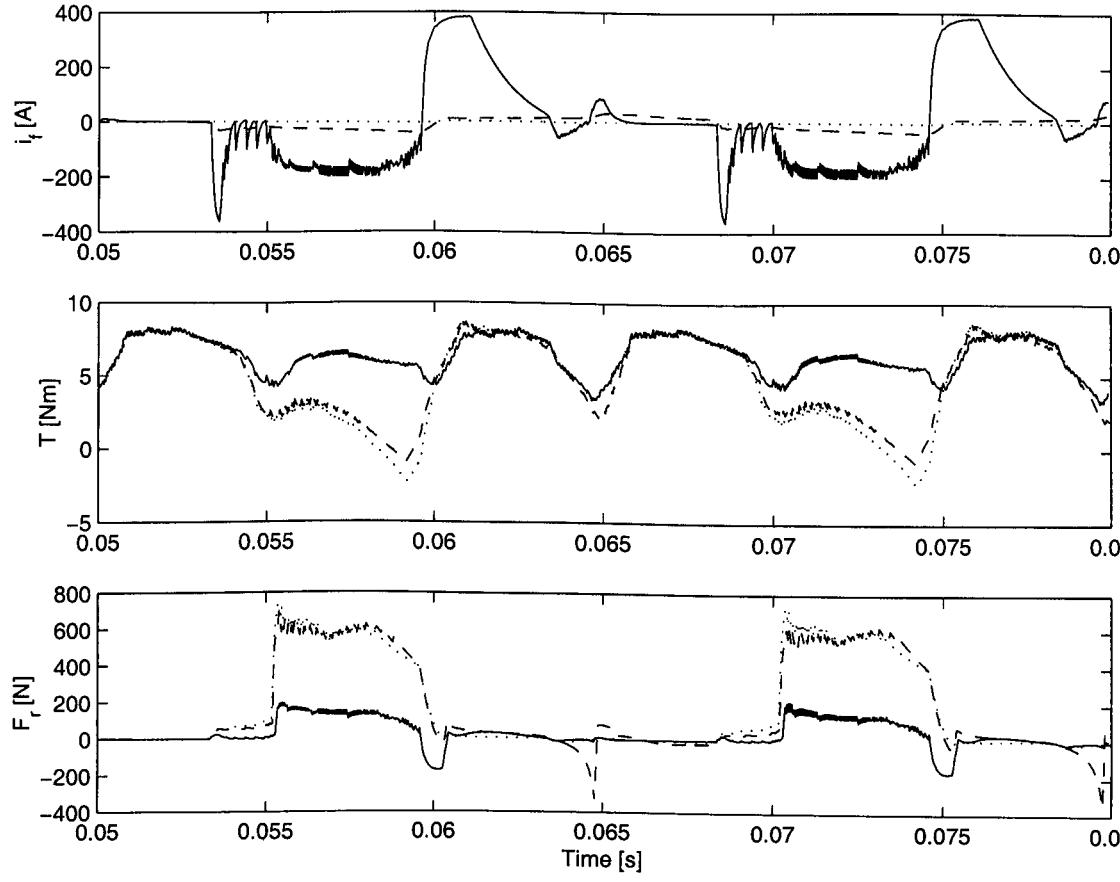

Figure 5.15: Short-turn faults (solid: 1 turn, dashed: 20 turns, dotted: full coil)

Differences between machines of different magnetic configurations are slight. The only noticeable difference is that the currents induced to flow in the shorted turns are of opposite polarity. Saturation of the stator yoke sections does not introduce any further abnormalities.

The operation with the single-pulse control under the faults has different characteristics from that with the constant current control discussed above. Fig. 5.16 shows the simulation result of 20-turns short-circuit. The phase current in the faulty phase i_1 increases after the fault at 0.05 sec as the inductance decreases with the loss of turns and change in flux paths. The increased phase current actually increases the torque output T during phase 1 excitation period. The induced current and radial forces are also increased.

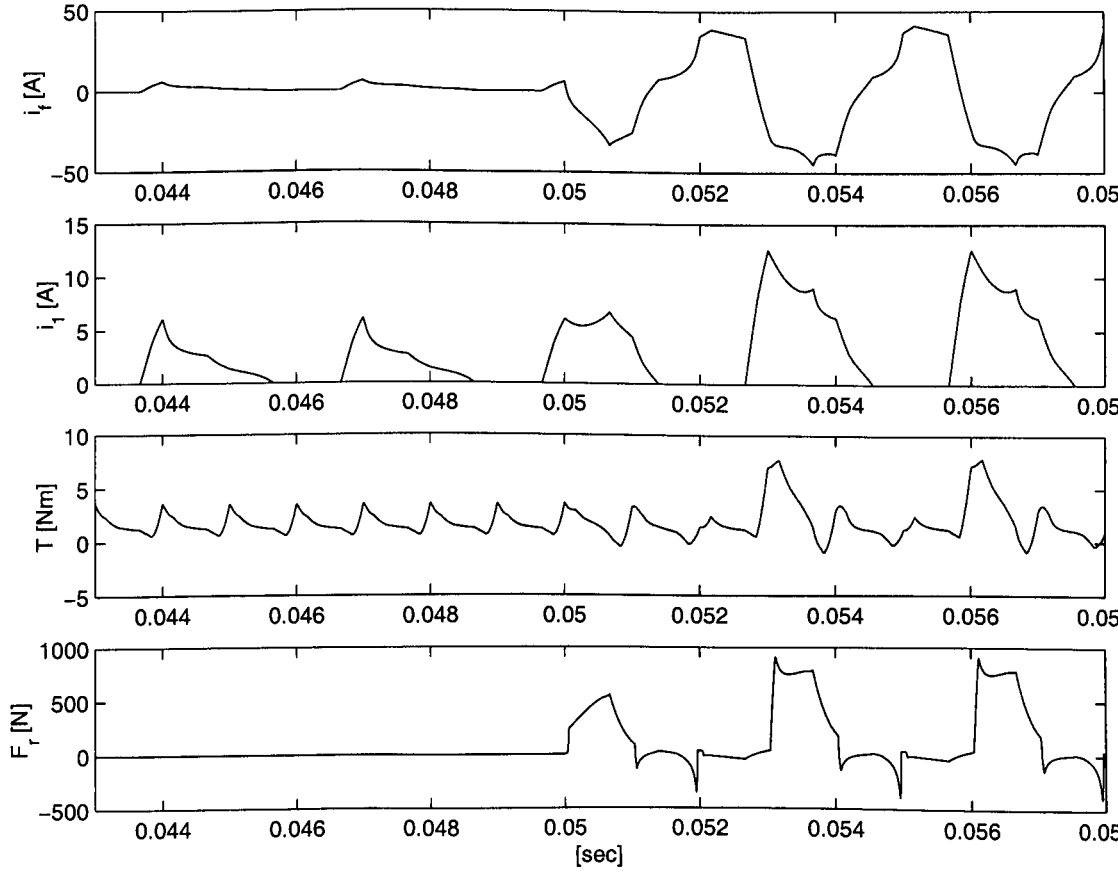

Figure 5.16: 20-turns short-circuit fault (the single pulse operation)

5.6.3 Coil to coil short-circuit fault

The short-circuit between adjacent coils could occur at the coil terminals or part of the way through each coil. In this section, the former is studied. The severity of the fault varies greatly depending on which coil terminals are shorted and on the magnetic configuration of the machine. All the simulations assume the fault occurs between the terminals of coils of phase 1 and 2.

Low terminal to low terminal

With this fault, during the excitation period of phase 1, no fault current flows through the short circuit since no current path through the phase 2 phaseleg exists. When the phase 1 conduction period ends and transistor $Q2$ turns off, the short circuit maintains diode $D2$ reverse biased. The freewheeling current from phase 1 will flow through the short-circuit to ground via transistor $Q4$. This is a zero voltage loop and the back-emf induced in the phase 1 winding will drive the current to excessive values. Commutation of phase 2 with phase 3 extinguishes both the fault current and the phase 2 freewheeling current.

Fig. 5.17 indicates the current waveforms for this case, showing the high peak current in phase 1. The influence of the fault current on torque production is also shown. It indicates the effect to produce a large braking torque component throughout the phase 2 conduction period. The flux crossing at opposite poles is balanced, so no unbalanced radial forces are present.

Low terminal to centre terminal

During the phase 2 conducting period and while transistor $Q2$ is still conducting, the phase 2 current will flow through the short circuit and back to the negative supply via $Q2$ bypassing the B' coil. No flux will flow through this pole since the flux from coil A2 returns through C and C'. However, when transistor $Q2$ turns off, diode $D2$ is

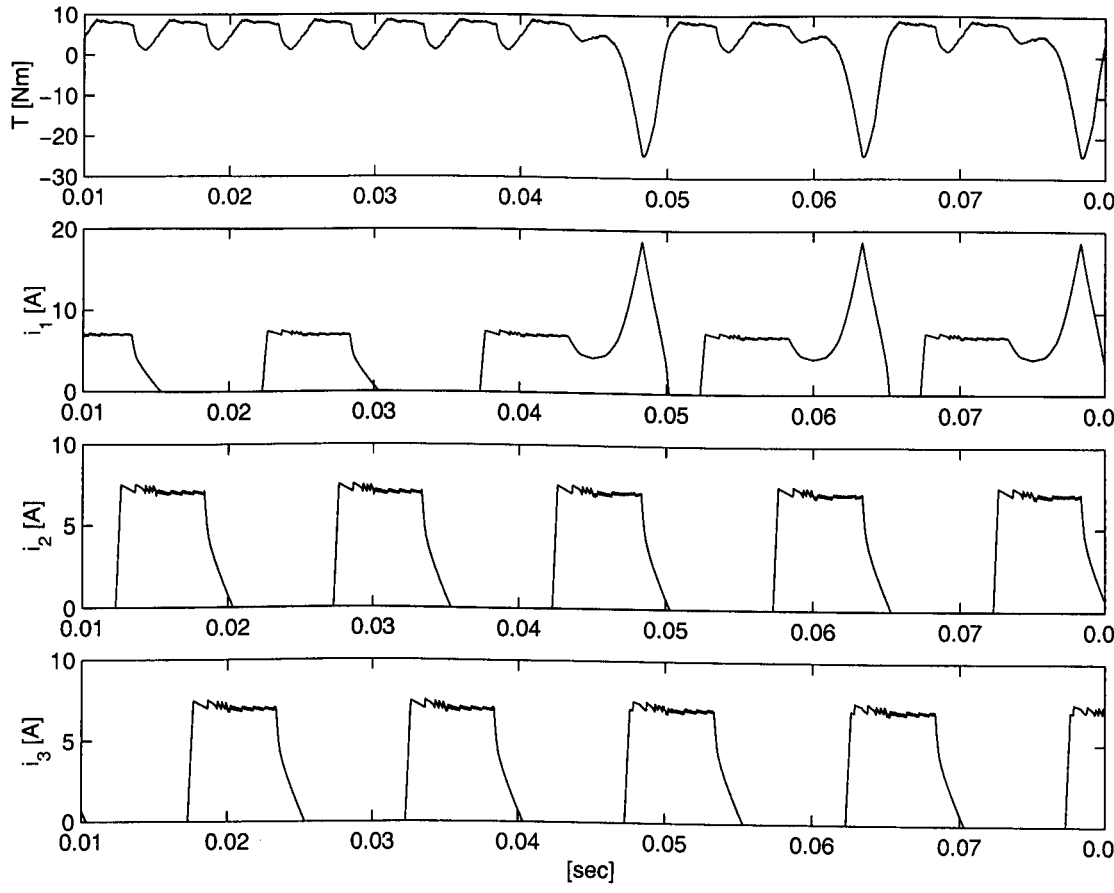

Figure 5.17: Coil to coil short-circuit fault (low terminal to low terminal)

momentarily forward biased and conducts both the phase 1 freewheeling current and the phase 2 current, driving the current through the short to zero. At this point, diode *D2* becomes reverse biased and both current components must now flow through coil B' to the negative of the supply. Pole B' is carrying a greater percentage of the return flux. The phase 1 freewheeling current is limited by the chopped supply voltage via the phase 2 phaseleg. As in the previous cases, the fault current is extinguished when phase 2 commutates with phase 3. Because the fault current is limited, the effect of the fault on the torque production is very slight, causing only a small reduction in the peak torque during the phase 2 conduction period, and a negligible reduction in average torque. Fig. 5.18 shows phase 1 currents, total torque and radial forces for both low to low and low to centre short circuit faults.

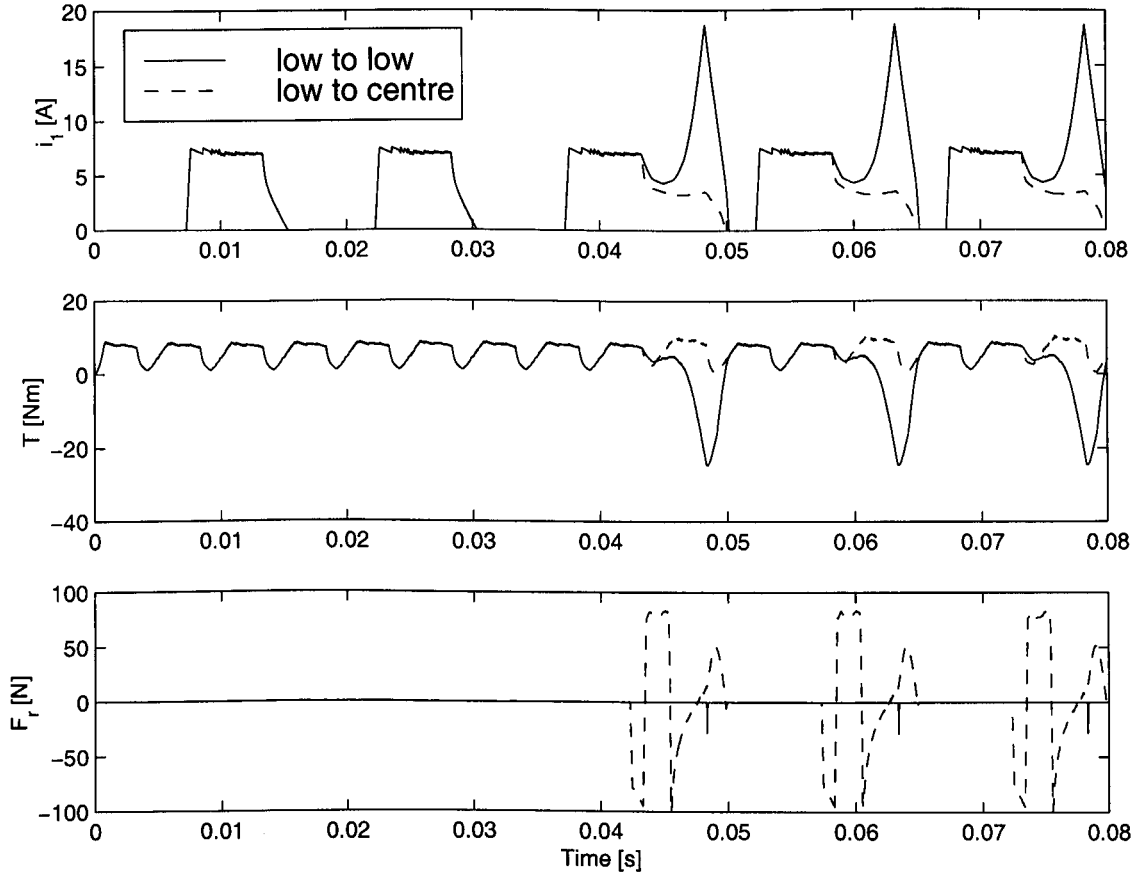

Figure 5.18: Coil to coil short-circuit fault (2 cases)

As with the low to low terminal fault, the basic characteristic of the fault does not change if the magnetic configuration is changed to NNNSSS. However, when the machine is saturated, the fault current with NNNSSS configuration is suppressed because of the difference in the flux distribution in the yoke segments.

Because of the imbalance in current carried by opposite poles in phases 1 and 2 during the phase 2 excitation period, unbalanced radial forces for both magnetic configurations will be present. During phase 1 and phase 3 excitation, no unbalanced forces exist.

5.6.4 Coil to ground fault

With this fault with the current control mode, during the phase 1 conduction period, the phase current is regulated at a reference value. However, since the phase current is diverted to the short circuit and no current flows through part of the coils, the output torque during the phase 1 conduction is reduced. Since the imbalance in the flux exists unbalanced radial forces are produced.

More serious situation can occur a few cycle after the fault. After the commutation of phase 1 with phase 2, the freewheeling current of phase 1 flows through $D1$ and the coil to the ground. Because this is a zero voltage loop, the flux may not vanish before the next phase 1 excitation period starts. This results in a excessive current in phase 1 and the amplitude of the faulty current could increase in time producing abnormal output torque and unbalanced radial forces.

The negative bus is assumed to be connected to ground in this analysis although this is not the case in some commercial applications. Analysis of those cases are left for future investigation.

5.7 Parallel connection

The same faults as in the series connection case are studied including coil open-circuit, full coil short-circuit, partial coil short-circuit, coil-to-coil short-circuit and coil to ground. All the faults are again assumed to occur in phase 1 and phase 1 and 2 for the coil-to-coil faults.

5.7.1 Open-circuit fault

With parallel connected coils, the remaining coil in the faulty phase will carry current of twice the normal value with the current control operation. As a result, torque production is not affected by the loss of the coil, although large radial forces are produced because of the imbalance in MMF and excessive heating may be apparent. Effect of different magnetic polarities is negligible.

The effect of the fault is also common for the single-pulse control operation. The simulation result with the single-pulse control operation is shown in Fig. 5.19 where i_1 is the phase 1 current, i_{c1} is the current in the faulty coil and i_{c2} is the current in the healthy coil of the phase 1. The reason why the remaining coil carries current of twice the normal value with the single-pulse control operation can be explained as follows. Circuit equation of a coil under normal condition is

$$v = i_{c2}\frac{dL}{dt} + L\frac{di_{c2}}{dt} + i_{c1}\frac{dM}{dt} + M\frac{di_{c1}}{dt} \tag{5.6}$$

where L is the coil inductance and M is the mutual inductance between coils in a phase. Under normal condition with no leakage flux assumed, $i_{c2} = i_{c1}$ and $L = M$. Then,

$$v = 2\left(i_{c2}\frac{dL}{dt} + L\frac{di_{c2}}{dt}\right). \tag{5.7}$$

For the faulty condition,

$$v = i_{c2}\frac{dL}{dt} + L\frac{di_{c2}}{dt}. \tag{5.8}$$

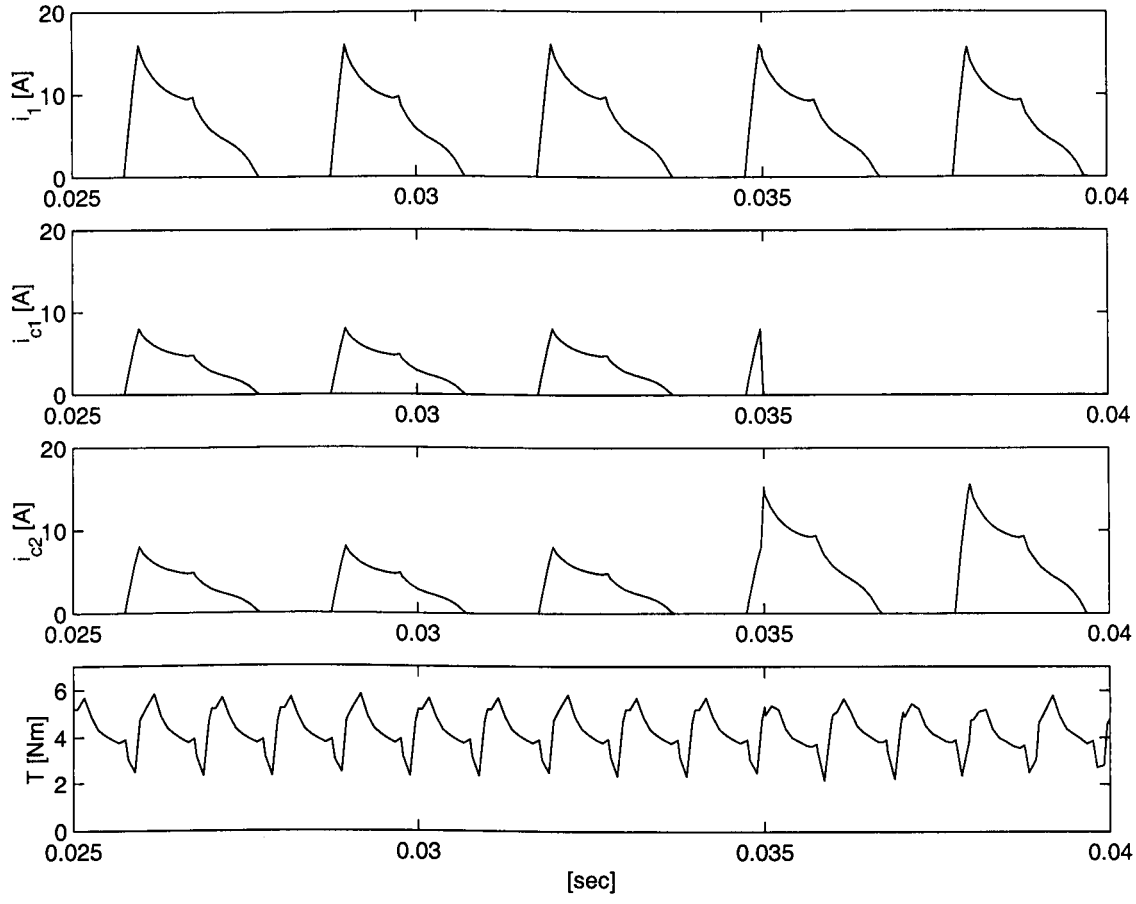

Figure 5.19: Coil open-circuit fault with parallel connection

Since v is constant, the coil current under the faulty condition becomes twice the normal value.

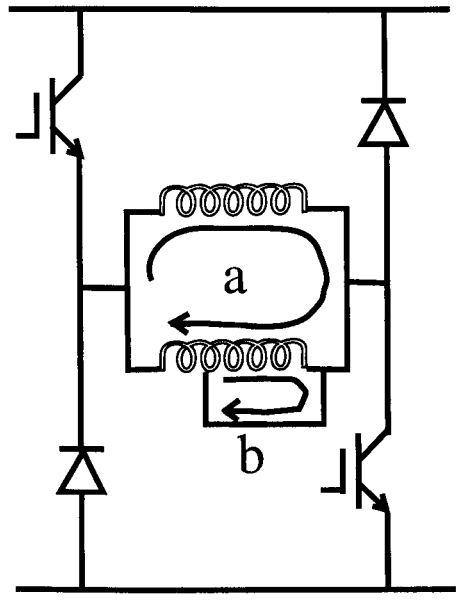

Figure 5.20: Short circuit current paths

5.7.2 Short-circuit coil

When the phase 1 excitation period ends, diodes $D1$ and $D2$ do not conduct the free-wheeling current. Rather, the decreasing flux passing through the A' pole induces a large fault current to circulate around two paths within the phase as illustrated in Fig. 5.20. The first path (b), circulating the shorted turns, carries a current which could be at least 100 times the normal peak phase current. This may lead to insulation breakdown and further shorted turns. The second path (a), flowing through both the remaining part of the faulty coil and the healthy coil within the phase, carries a fault current which peaks at approximately 100% of normal peak phase current.

With high frequency PWM chopping, the presence of the fault could cause di/dt in the faulty phase to become much higher than normal. This puts the devices in the converter at risk.

With the single-turn fault, torque production in the faulty phase is not adversely affected. Because the magnetic circuit is not unbalanced, no unbalanced radial forces are present. The simulation result is shown in Fig. 5.21.

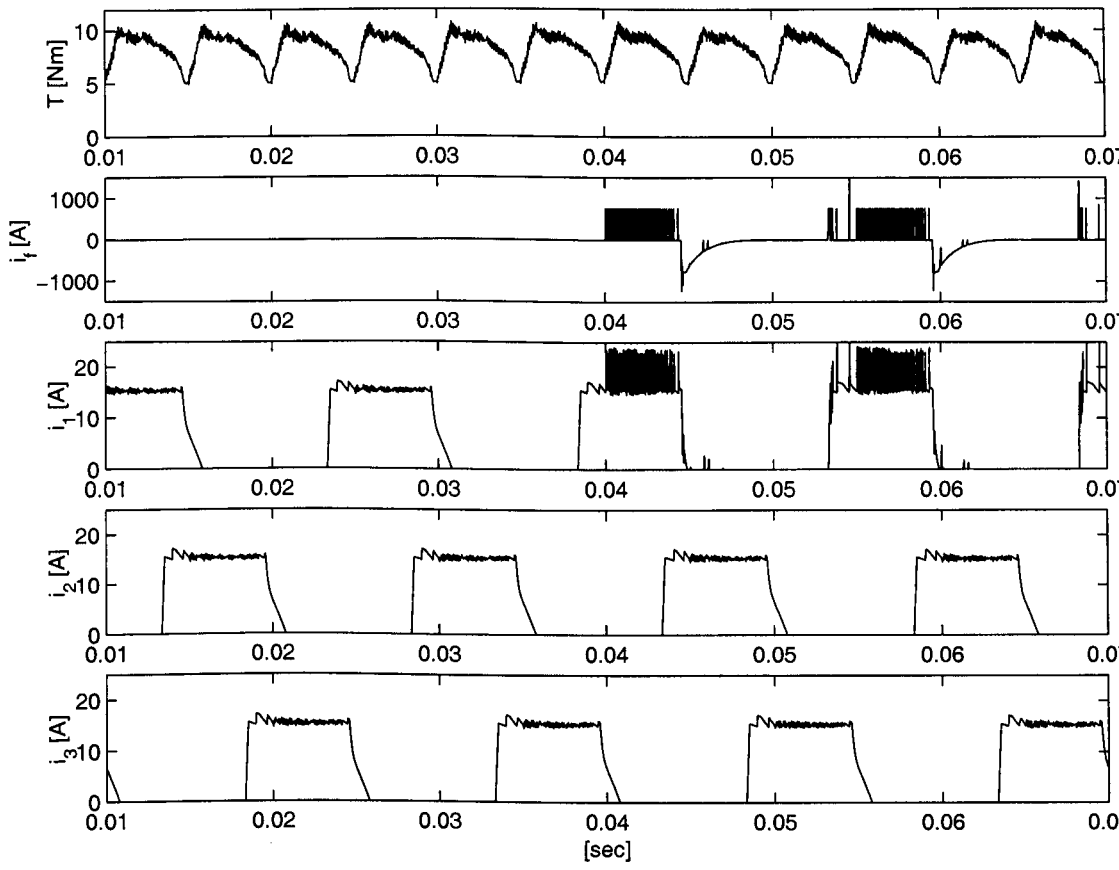

Figure 5.21: 1 turn short-circuit fault with parallel connection

When multiple turns are short-circuited, the phenomenon is very similar to that of the single-turn short-circuit fault. However, the increased MMF of the shorted turns could result in the fault current period extending into the phase 3 excitation period. As such, a braking torque with a peak value at least equal to normal motoring peak torque would be produced. As with the single-turn short, the magnetic circuit is not unbalanced and no unbalanced radial forces exist. Again, high di/dt on the faulty phase current could cause a threat to devices within the converter. The simulation results including the flux in the faulty pole $Flux_f$, the circulating current in the shorted turns i_f and the total torque are shown in Fig. 5.22 for the 1- and 20- turns shorted cases where the number of turns per coil is 98.

For full coil short-circuit fault, because the coils are connected in parallel, the coils are bypassed by the phase current thereby producing zero torque. The total average

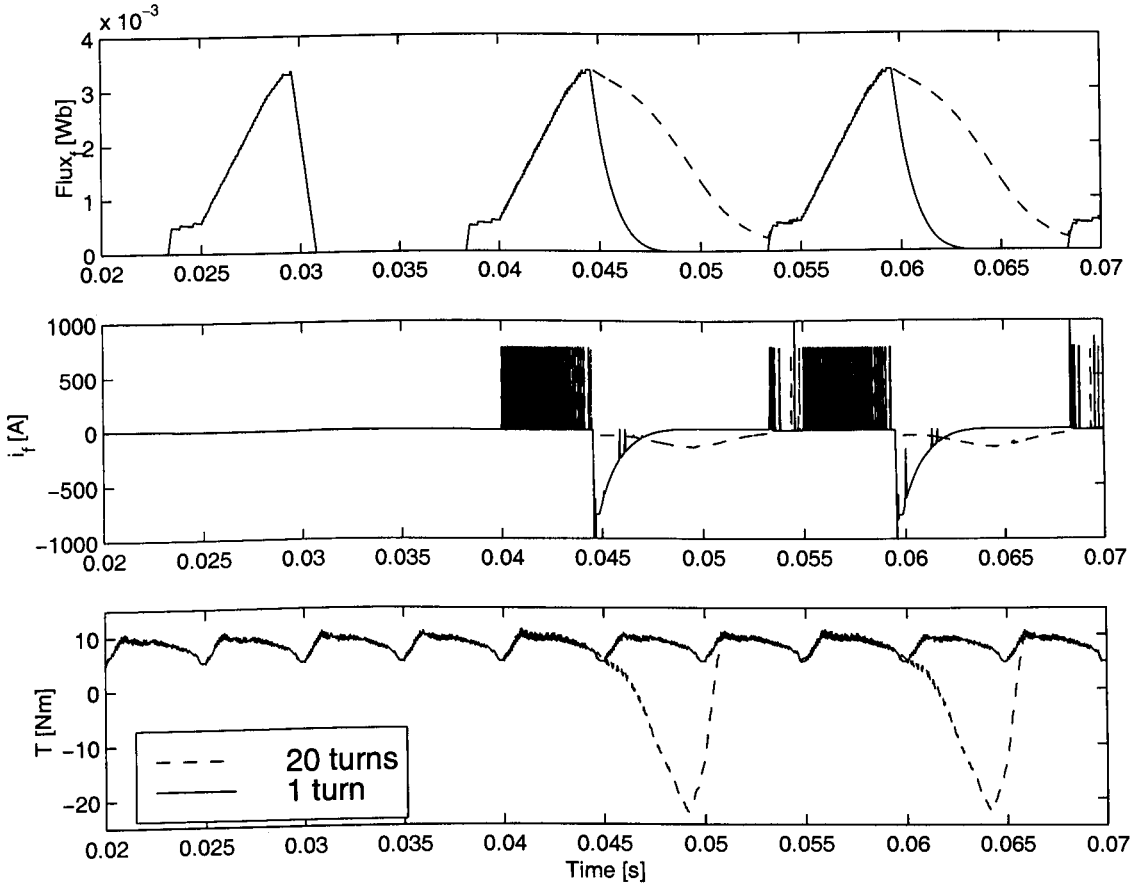

Figure 5.22: Turns short-circuit fault with parallel connection

torque becomes 1/3 of normal condition. The phase current in the faulty phase becomes very large and may cause device failure in the converter. No unbalanced radial forces are present.

5.7.3 Coil to coil short-circuit

The coil to coil fault between low terminal and low terminal with parallel connected coils results in slightly lower peak fault currents on account of a lower driving voltage in the phase 1 coils. With the low to high terminal fault, the fault current is quickly suppressed because the current is driving against a chopped voltage of $+V_s$ as compared with $+0.5V_s$ with the series connected coils.

5.7.4 Coil to ground fault

The impacts of the fault are similar to those with the series connected case. The excessive current in phase 1 could produce abnormal output torque and unbalanced radial forces.

5.8 Inverter faults

In this section, two converter faults are simulated including transistor short-circuit and DC-link short-circuit faults.

5.8.1 Transistor open-circuit fault

This fault is effectively the same as coil open circuit fault for the series connected phase. The total torque becomes one third of normal value and no radial forces are produced.

5.8.2 Transistor short-circuit fault

With this fault, the current freewheels through the lower leg diode $D1$, the coils and the faulty transistor $Q2$, which is a zero voltage loop. After the commutation, the flux in the faulty phase decreases very slowly and the current of the faulty phase may have a long tail. This produces large uncontrolled torque and possibly very large negative torque.

If the flux does not vanish before the next excitation, the current may oscillate at the commutation frequency and the amplitude may even increases with time. This causes imbalance in flux distribution among the phases and disturbs the operation of the healthy phases. This will result in a critical failure of the system. Therefore, the faulty phase must be shut off as soon as possible. Such a simulation result is shown in Fig. 5.23

To avoid the critical condition, the dwell angle may be limited for flux to vanish even with the zero voltage loop. However, in a real system where mutual coupling between phases exists, the mutual coupling may induce current in the faulty phase resulting in a similar condition. Furthermore, the critical condition is likely to occur in generating operation. Therefore, it might be useful to place fuses between the converter and motor or within the converter to shut off the excessive current for applications such

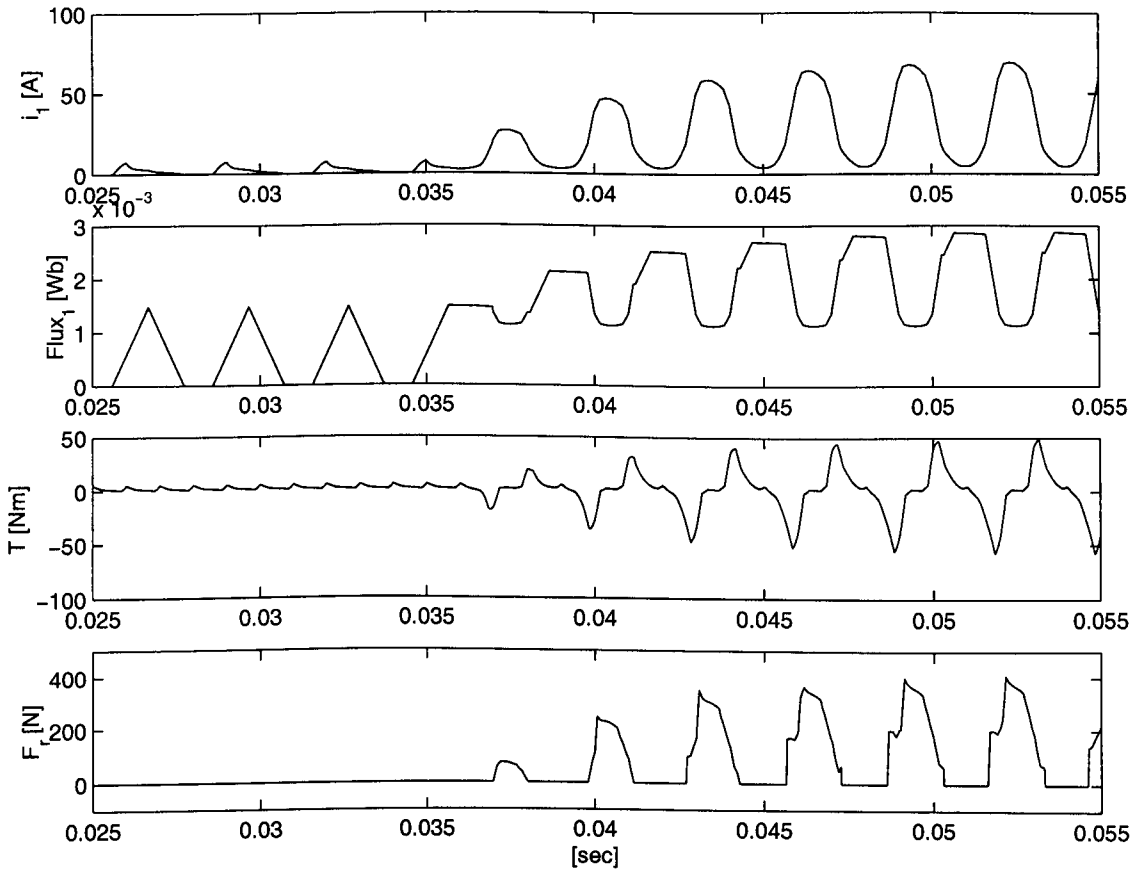

Figure 5.23: Transistor short-circuit fault

as aircraft starter/generator.

5.8.3 DC-link short-circuit fault

The DC-link voltage becomes zero after the fault occurs. For the phase whose flux-linkage is zero at the moment of the occurrence of the fault, the current is zero after the fault. While for the phase whose flux linkage is not zero, the flux decays slowly because of the lack of the reverse voltage after the turn-off angle. This may produce a current flowing even after the DC-link voltage becomes zero as a result of the fault. A large flux linkage at the moment of the fault may induce a current whose amplitude is much higher than normal value. The faulty current produces large torque ripples and impulsive radial forces. The flux-linkage, current, torque and the radial forces decrease

in time and vanish in a certain period.

5.9 Conclusions

In this chapter, analysis and classification of winding and inverter faults in the SRM, especially in the 3-ph 6/4 machine were presented. The new lumped parameter, magnetic equivalent circuit was used, which takes full account of the mutual coupling between phases. The SRM drive model was implemented in Saber™ simulation package. Results of the new method were compared with those of the time-stepping FEA and validated.

The simulation results are summarised in Tables 5.4 and 5.5. The main impacts of each fault are listed in Table 5.4. In Table 5.5, impacts of the faults on several factors are listed, which are torque reduction, unbalanced radial force F_r, possible heat rise in windings and possible risk of switching device failure. The severity is indicated by the number of *, where – shows no effect on the item by a fault, * shows that there is a slight, ** shows that the effect is large and *** shows that the effect is severe. For the case of torque reduction, * indicates torque reduction of less than 10 % by a fault, ** indicates that of 10 to 50 % and *** indicates that of more than 50 % including negative torque production. These Tables together with the analyses of faults described in the chapter give an overview of and detailed insight into the faults in the SRM.

Although the analysis was based upon the 3-ph 6/4 SRM, most of the impacts of faults are common for other configurations and the results shown will be applicable. It should be noted that although increasing the number of phases will reduce the impact of a fault in a phase on overall torque production, the risk of excessive unbalanced radial forces, heat rise by induced current, semiconductor switch failures etc. will not be reduced.

Categories	Faults	Main impacts
Series connected phase coils	Coil o/c	Torque reduction
	Full coil s/c	Radial force
	Partial coil s/c	Induced current in shorted turns
	Phase-phase s/c	Negative torque
	Coil-ground s/c	Radial force
Parallel connected phase coils	Coil o/c	Radial force
	Full coil s/c	Torque reduction
	Partial coil s/c	Induced current in shorted turns
	Phase-phase s/c	Negative torque
	Coil-ground s/c	Radial force
Inverter failure	Transistor s/c	Loss of negative V_{dc}
	Bus s/c	Serious for generating

Table 5.4: Main impacts of faults

Categories	Faults	T reduc.	F_r	Heat	SW at risk
Series connected phase coils	Coil o/c	**	–	–	–
	Full coil s/c	**	***	*	–
	Partial coil s/c	*	**	***	–
	Ph-Ph s/c L-L	***	–	*	**
	Ph-Ph s/c L-C	*	**	*	*
	Coil-ground s/c	**	**	**	**
Parallel connected phase coils	Coil o/c	–	***	**	**
	Full coil s/c	**	–	–	***
	Partial coil s/c	***	–	***	**
	Ph-Ph s/c L-L	***	**	*	**
	Ph-Ph s/c L-H	***	**	*	**
	Coil-ground s/c	**	**	**	**
Inverter failure	Transistor s/c	***	–	**	**
	Bus s/c	***	–	*	*

Table 5.5: Summary of impacts of faults

Chapter 6

Analysis of the multi-tooth per pole SRM

6.1 Introduction

In this chapter, the multi-tooth per pole switched reluctance motor (SRM) which is designed for low-speed high-torque direct-drive (DD) applications is discussed.

The DD configuration eliminates conventional transmission mechanisms between the motor and its load. This leads to advantages such as no backlash, low friction, high stiffness and so on. These features make DD motors suitable for high precision positioning and high speed trajectory control applications. The DD applications require large torque-producing capabilities, for high acceleration and deceleration. Both the permanent-magnet brushless dc motor (BLDCM) and the SRM have been studied and commercialised for the DD market [113, 114, 81, 16, 79]. The use of permanent magnets increases the cost of the BLDCM and there is a possibility of the demagnetisation. On the other hand, the SRM does not require any rotor magnets and has a simpler winding, which leads to low cost and high reliability. Low torque ripple controls of the SRM for DD applications were reported in [81, 16]. However, less has been reported on the design of the DD SRM itself[79, 78, 115].

The average torque T_{ave} of SRM is expressed by the following equation:

$$T_{ave} = N_\varepsilon \times W_\varepsilon. \tag{6.1}$$

where N_ε is the number of strokes per revolution and W_ε is the energy conversion per stroke. It is seen that there are two ways of increasing the average torque. One is to increase W_ε and the other is to increase N_ε. For the design of a normal SRM whose stator poles normally have no teeth, one may concentrate on increasing W_ε, hence increasing the inductance ratio in the aligned and unaligned positions. On the other hand, for the design of low-speed high-torque DD SRM, the multi-tooth per pole structure, which increases N_ε (in other words, the electrical gear ratio), may be considered to increase the torque. The number of teeth of the multi-tooth SRM can be determined for certain criteria such as torque, efficiency, switching frequency and so on. This is a different process of designing the stepping motor, where the number of teeth is determined by the number of steps per revolution which is a functional requirement for the motor.

It should be noted that increasing N_ε has drawbacks:

1. The increase in the switching frequency leads to higher iron and switching losses.
2. The decrease in the inductance ratio leads to a lower energy ratio resulting in higher copper losses and device ratings.

N_ε is increased with the increase in the number of teeth. However, W_ε is decreased at the same time mainly because of the increase in the unaligned inductance. It is expected that there is a certain number of teeth for an optimum combination of N_ε and W_ε which produces a maximum average torque. The objective of the present chapter is to investigate such a number.

Throughout the investigation finite element analysis (FEA) is used. Firstly, problems seen in the design of a commercial DD SRM are pointed out from measured data. Secondly, the tooth shape of the multi-tooth per pole motor is analysed for a maximum average torque. Thirdly, an optimum number of teeth per pole is analysed by

half-pole models. Finally, practical 3-phase models whose number of teeth are 5 and 8 are analysed.

6.2 Analysis of a commercial DD SRM (the Megatorque motor)

In this section, a commercial DD SRM *the Megatorque motor*, which is designed and manufactured by NSK Ltd., Tokyo, Japan [77], is analysed and problems seen in the design are pointed out.

6.2.1 Geometry of the Megatorque motor

The Megatorque motor is designed for DD applications where high-torque and low-speed characteristics are required [78, 77, 76]. Fig. 6.1 shows the cross-section of the motor together with the flux paths. The Megatorque motor is a 3-phase machine and has 2 stators outside and inside of a ring-type rotor. The number of teeth per stator poles is 8 and the number of poles in each stator is 18. Thus, the number of teeth on each stator is 144. There are 150 teeth on each side of the rotor ring. One electrical cycle corresponds to $360°/150 = 2.4$ mechanical degrees. The nominal value of the airgaps at both sides of the rotor is 0.127 mm. The double-stator and high-number of teeth configuration combined with the narrow airgaps exhibits low-speed and high-torque characteristics. For RS0608 type Megatorque motor whose outer diameter is 160 mm, the maximum torque is 40 Nm and the maximum speed is 3 rps. This corresponds to a TRV (the torque per unit rotor volume) of approximately 46 kNm/m^3. The TRV is comparable to high performance servomotors and machines for aerospace applications.

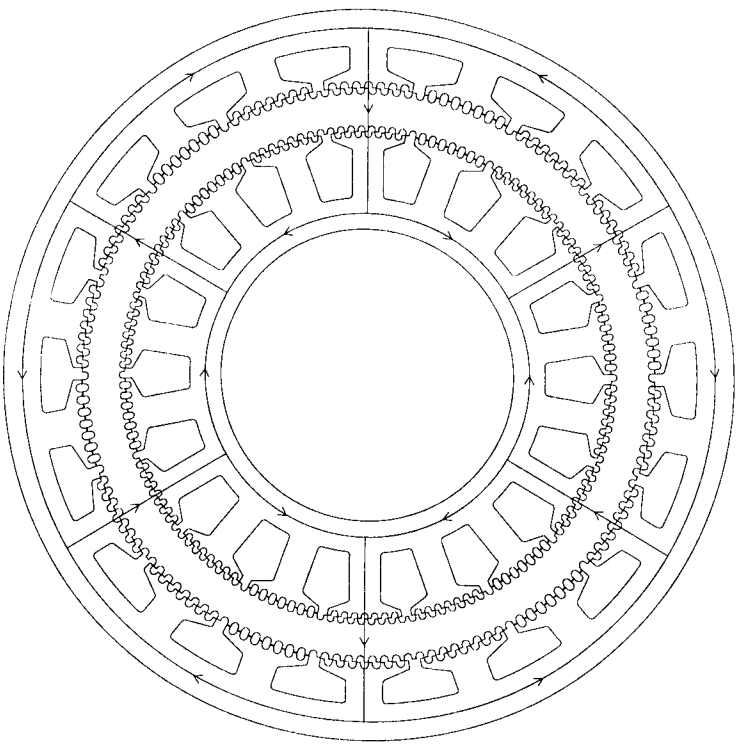

Figure 6.1: Cross-section of the Megatorque motor

6.2.2 Analysis of magnetisation curves

Fig. 6.2 shows an example of magnetisation curves of the SRM showing the curves in the aligned and unaligned positions. A reasonable design will give the inductance ratio of around 7-10 for small motors, increasing to 15-20 for motors up to 250 mm diameter [57].

Apart from the average torque, the energy ratio E is an important factor which characterises the SRM. E is defined as [2]:

$$E = \frac{W}{W+R} = \frac{W}{U}. \tag{6.2}$$

W is the enclosed area with o-a-b-o and R is the enclosed area with o-b-c-o in Fig. 6.2. $U = W + R$ corresponds to the total energy supplied to the machine. R is the reactive energy returned to the supply after W is converted into mechanical output. Lower in E may lead to poor utilisation of the device ratings and higher copper losses per

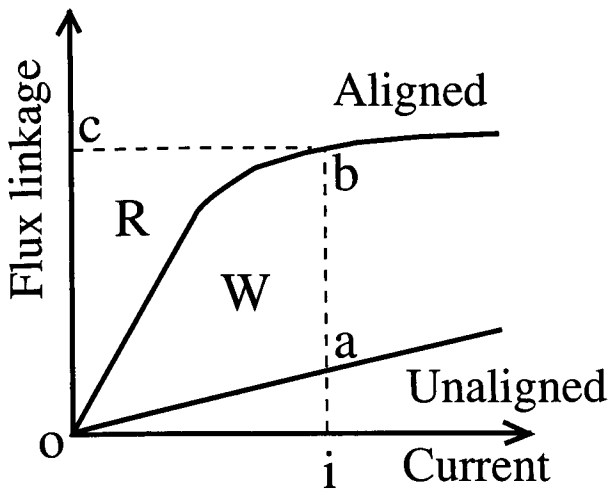

Figure 6.2: Example of magnetisation curves of SRM

output.

Measured magnetisation curves of the Megatorque motor are shown in Fig. 6.3. The curves were measured at every 10 electrical degrees, which corresponds to 0.067 mechanical degrees, from the aligned to unaligned positions. The rated current of the test motor is 6 A. The row measured curves contain irregularities due to the difficulties in precise positioning. The curves shown in Fig. 6.3 are fitted using polynomial functions.

Fig. 6.4 shows the static torque curves. The solid lines are ones reconstructed from the measured magnetisation curves and the dots are measured. The measured data was supplied by NSK Ltd. Both data match with each other reasonably although the constructed ones are slightly shifted to the unaligned position. This may be caused by inaccuracies in the measurement of the rotor position and/or the error in fitting the curves.

The following are observed in the magnetisation curves:

1. Inductance ratio is less than 2.

2. Low in W leading to a low energy ratio E.

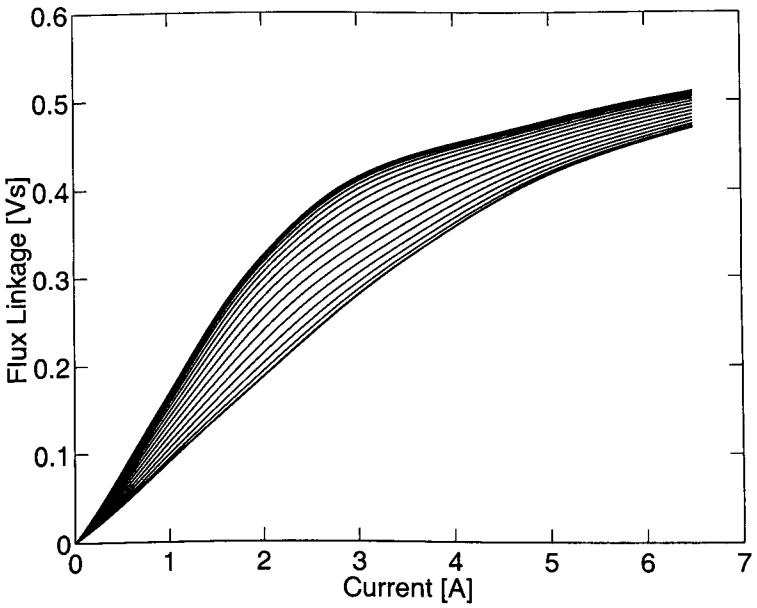

Figure 6.3: Measured magnetisation curves of the Megatorque motor

3. Unaligned curve is saturated as well as the aligned one.

It is seen that the high torque of the Megatorque motor relies on the higher value of $N_\varepsilon = 450$. However, obtaining higher average torque T_{ave} by increasing N_ε decreased the inductance ratio and the energy ratio E. There may be an optimum N_ε for higher torque for given rotor and stator sizes and current.

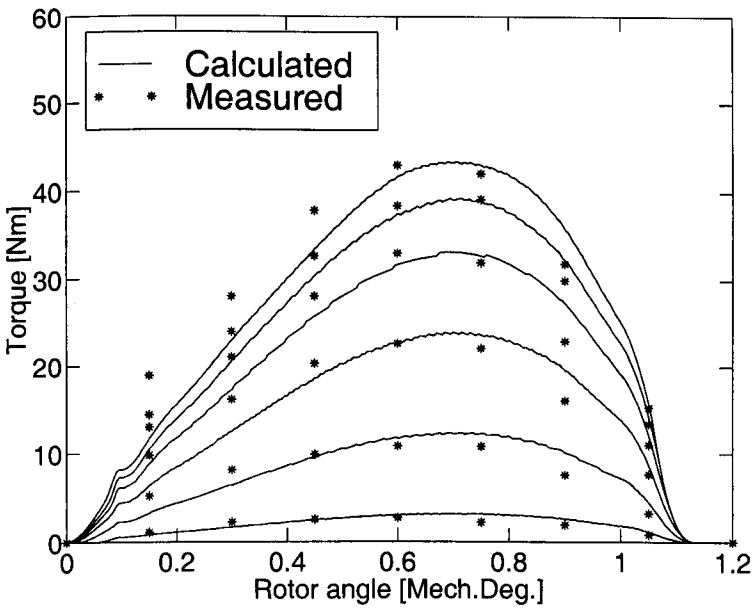

Figure 6.4: Static torque curves

6.3 Tooth model Analysis

The magnetic permeances of the doubly salient structures have been well studied and published [116, 117, 118, 119, 120]. It has been reported that the optimum ratio of t_w/λ is around 0.42 for a maximum force production [82, 116, 121], where t_w is the tooth width and λ is the tooth pitch. It has been also reported that the slot depth of half the tooth pitch $h = \lambda/2$ is sufficient and increasing h more than $h = \lambda/2$ is hardly beneficial for higher force production [121, 79]. The rounding of the slot bottoms has hardly any effect on force produced for a slot depth $h = 0.5$ [121, 79].

In this section, the influence of the ratio of tooth width to tooth pitch t_w/λ on the amount of energy conversion is analysed. The influence of the slot depth h is also analysed. The previously published results are validated by the analysis.

The stored energy W_m is calculated in the aligned and unaligned positions. The difference in W_m in the two positions is then calculated, which corresponds to the energy converted into the mechanical power. In order to find an optimum t_w/λ, λ is fixed and t_w is varied. For the analysis of the influence of h, t_w/λ is fixed and h/λ is varied.

6.3.1 Analytical models

Fig. 6.5 shows the analytical models used in the aligned and unaligned positions. Fig. 6.6 shows the finite element mesh for the model in the aligned position. It is assumed that the model is infinite in y-axis (horizontal axis in Fig. 6.5). Because of the symmetry, modelling of half tooth is sufficient.

6.3.2 Assignment of boundary conditions

Fixed values of the vector potential $\boldsymbol{A}$ are assigned to the horizontal lines at the top and bottom of the model which are parallel to y-axis. For the 2-D analysis, properties

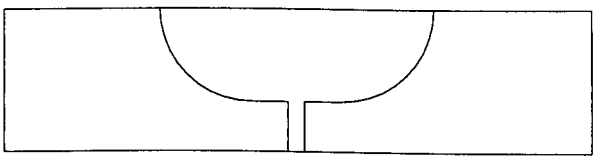

(a) aligned position

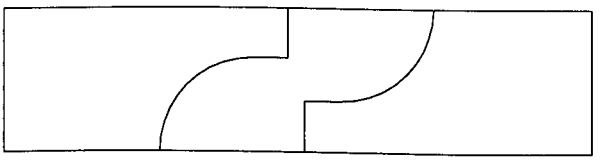

(b) unaligned position

Figure 6.5: Tooth models (↑:x-axis, ←:y-axis)

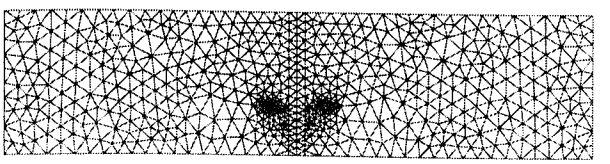

Figure 6.6: Finite element mesh (aligned position)

do not change in z-axis.

$$\boldsymbol{A_1} = A_1 \hat{\boldsymbol{z}} \tag{6.3}$$

$$\boldsymbol{A_2} = A_2 \hat{\boldsymbol{z}} \tag{6.4}$$

The flux density $\boldsymbol{B}$ is expressed as:

$$\boldsymbol{B} = \mathrm{rot}\boldsymbol{A} \tag{6.5}$$

$$= \begin{vmatrix} \hat{\boldsymbol{x}} & \hat{\boldsymbol{y}} & \hat{\boldsymbol{z}} \\ \frac{\partial}{\partial x} & \frac{\partial}{\partial y} & \frac{\partial}{\partial z} \\ A_x & A_y & A_z \end{vmatrix}. \tag{6.6}$$

Here, for 2-D finite element analysis, $A_x = A_y = 0$.

$$\boldsymbol{B} = \left(\frac{\partial}{\partial y} A_z\right) \hat{\boldsymbol{x}} - \left(\frac{\partial}{\partial x} A_z\right) \hat{\boldsymbol{y}} \tag{6.7}$$

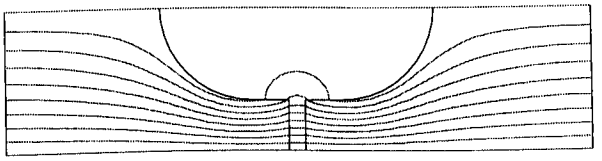

(a) aligned position

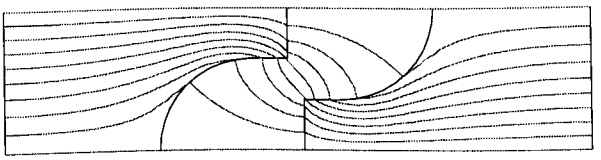

(b) unaligned position

Figure 6.7: Flux plots

The first term on the right hand side is zero since we assign a constant $\boldsymbol{A}$ along y-axis. Therefore,

$$\boldsymbol{B} = -\left(\frac{\partial}{\partial x} A_z\right) \hat{\boldsymbol{y}}. \tag{6.8}$$

The mean value of B across the model is

$$B = -\frac{A_1 - A_2}{x_1 - x_2} \tag{6.9}$$

where x_1 and x_2 are the coordinates of the positions where A_1 and A_2 are assigned respectively. Since the width of the model which corresponds to half the tooth pitch is fixed ($x_1 - x_2 =$ constant), a constant flux flow in the model is assigned.

6.3.3 Analytical results

Fig. 6.7 shows the calculated flux plots. The flux plots show the validity of the model. Fig. 6.8 shows the change in the coenergy dW_m with t_w/λ calculated. dW_m is normalised by dW_m with $t_w/\lambda = 0.40$. dW_m becomes maximum around $t_w/\lambda = 0.40$. The reduction in dW_m is less than 3% within the range of $t_w/\lambda = 0.35$ to 0.45. Therefore, t_w/λ can be chosen for secondary criteria within the range, such as flatter static torque curves and so on. Fig. 6.9 shows the change in dW_m with the change in the slot depth h. dW_m is normalised by dW_m with $h/\lambda = 0.45$. dW_m increases with increasing h

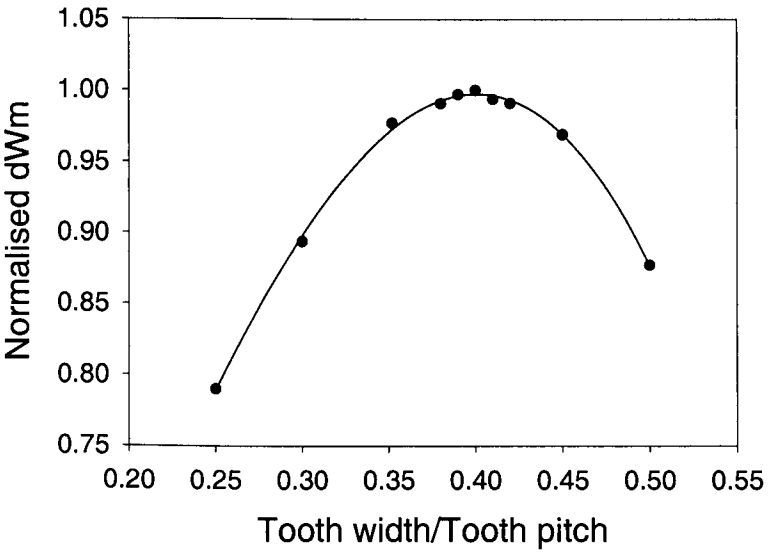

Figure 6.8: Change in dW_m with t_w/λ

when $h < 0.45$. However, for $h > 0.45$ there is little benefit in dW_m. These results agree with previously published results. The Megatorque motor has $t_w/\lambda = 0.35$ and $h/\lambda = 0.45$ and its tooth design is adequate.

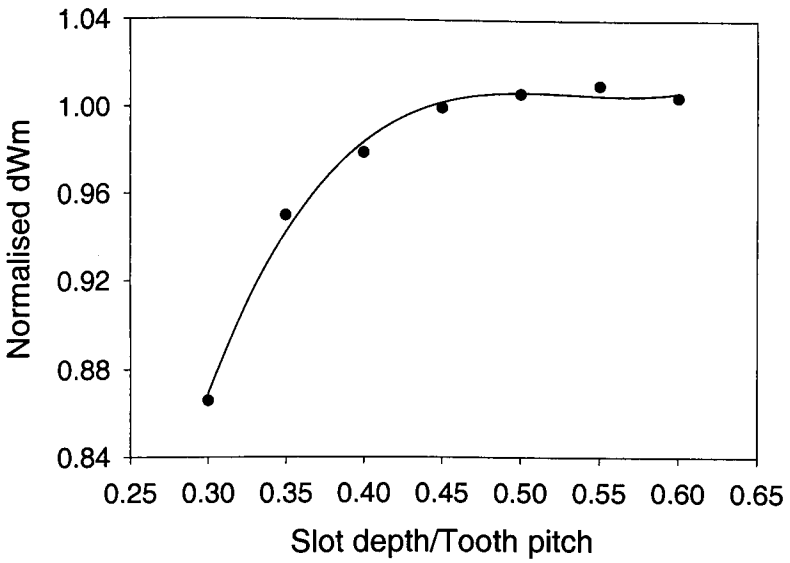

Figure 6.9: Change in dW_m with h/λ

6.4 Number of teeth per pole

In this section, the influence of the number of teeth per pole on the amount of the energy conversion is analysed with half-pole models.

6.4.1 Analytical model

Fig. 6.10 shows some of the models used for the analysis. The number of teeth per pole N_t is modelled from 2 to 12. The pole width, height and airgap length are fixed for all the models. The ratio of tooth width/tooth pitch t_w/λ is fixed at 0.352 and the ratio of slot depth/tooth pitch h/λ is set at 0.55. The rotor thickness is modelled as deep as 3 times the slot depth. It was confirmed that the difference in the rotor thickness modelled hardly affects the calculated results of the amount of energy conversion by comparing models with different rotor thickness. This is due to the saturation being much less in the rotor than that in the stator and the MMF drop in the rotor is negligible.

Constant values of the vector potential are assigned along y-axis at both ends of the model, as done for the tooth analysis in the previous section. The width of the models are slightly different to each other. This is because it models from the centre of a pole to half tooth pitch beyond the pole end. The difference in the width of the models is in the tooth pitch.

6.4.2 Analytical results

Fig. 6.11 shows the flux plots of the 8 teeth per pole model in the aligned and unaligned positions. Fig. 6.12 shows the magnetisation curves in the aligned and unaligned positions for different numbers of teeth calculated. The difference in the aligned curves including saturation is relatively small between models, while the difference in the unaligned curves is large. The aligned inductance of $N_t = 2$ is not larger than 1.2 times

that of $N_t = 12$. The unaligned inductance of $N_t = 2$ is approximately 4 times larger than that of $N_t = 12$.

The unaligned curves for models with higher numbers of teeth are saturated as well as the aligned curves. Finch pointed out in ref. [73] that *the normalised excitation MMF* can be increased by increasing the number of teeth per pole, where *the normalised excitation MMF* is the achievement of MMF to the *the critical MMF* at which the idealised unaligned tooth flux reaches the saturation value. Fig. 6.12 agrees with the statement above and shows that *the critical MMF* is decreased by increasing the number of teeth per pole.

Fig. 6.13 shows the energy conversion per stroke divided by the tooth pitch dW_m/λ for the number of teeth per pole N_t. The result is normalised for the value for $N_t = 8$. Three lines are shown: the solid line is for the normalised magnetic field $H_N = 1$ in Fig. 6.12, the dotted line is for $H_N = 0.8$ and the dashed line is for $H_N = 0.5$.

In the linear region, represented by the dashed line, a higher number of teeth per pole results in a larger average torque. As the effects of saturation increase and the number of teeth per pole also increases the average torque will begin to decrease as shown by the dotted line. This trend becomes more significant when both effects increase further and H_N increases.

It is found from the observation that an optimum number of teeth per pole varies with the excitation level. If the maximum excitation is chosen for the value at which the unaligned magnetisation curve starts saturating, it will lead to a maximum average torque.

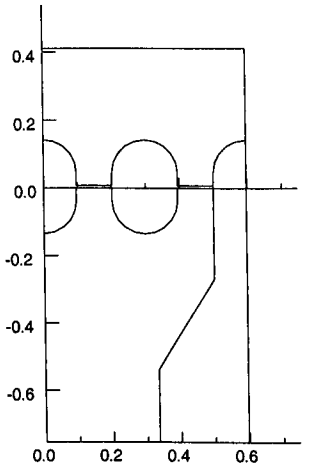

(a) $N_t = 4$

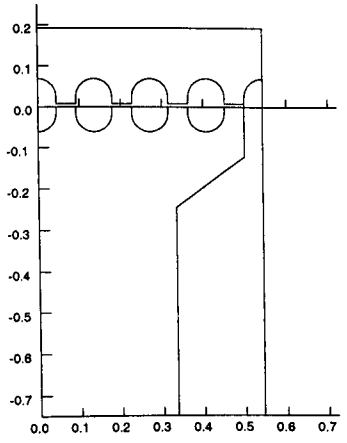

(b) $N_t = 8$

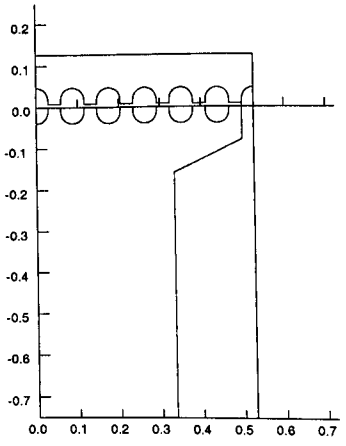

(c) $N_t = 12$

Figure 6.10: Pole models for different number of teeth (→:x-axis, ↑:y-axis)

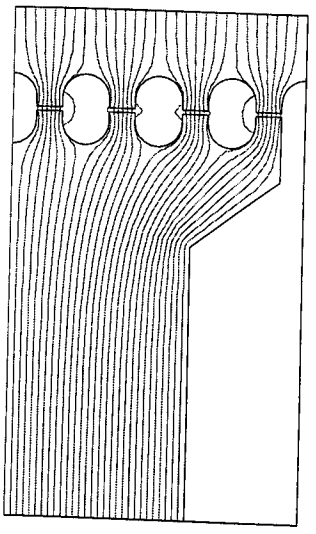

(a) Aligned position

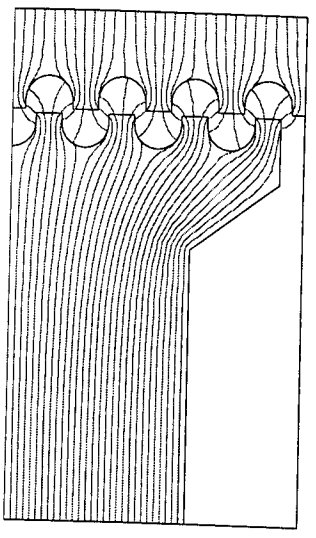

(b) Unaligned position

Figure 6.11: Flux plots of 8 teeth per pole model

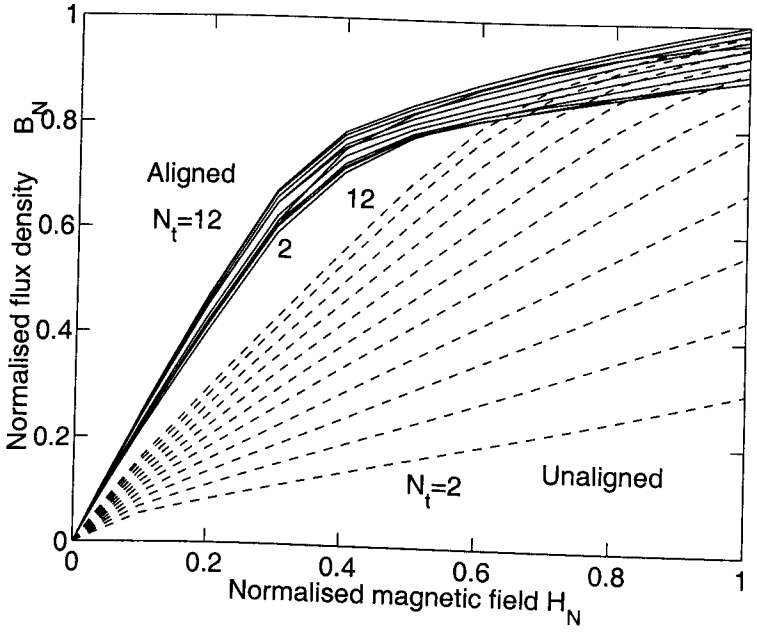

Figure 6.12: Magnetisation curves for different numbers of teeth

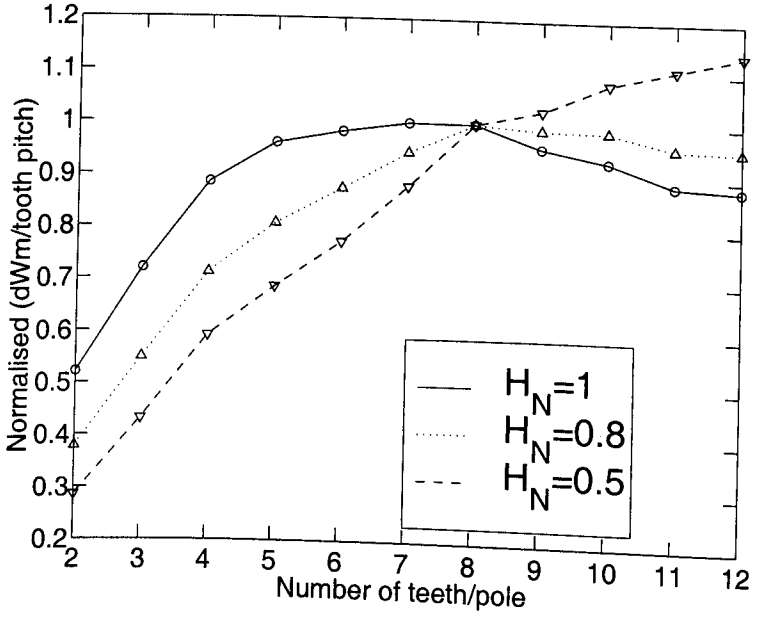

Figure 6.13: Change in dW_m with the number of teeth

6.5 Analysis of practical models

In the previous section, it has been shown that the optimum number of teeth per pole which maximise the average torque varies with the saturation level in the unaligned position. In this section, more practical models are analysed in order to investigate the effect of the number of teeth on the torque output.

6.5.1 Analytical models

Fig. 6.14 shows the models used. 5 and 8 teeth per pole motors are analysed. A *ring-type* rotor structure, which has a hollow space in the center, is chosen here. The hollow space is regarded as a preferable feature for DD applications and can be used for wiring and plumbing and so on [76]. This also contributes to increasing the rotor diameter leading to a higher torque.

Both models have identical dimensions except the tooth pitch λ. The design of teeth are chosen at $t_w/\lambda = 0.35$ and $h/\lambda = 0.55$. The stator outer radius is 80.0 mm, rotor outer radius is 53.3 mm and airgap length is 0.13 mm. The number of phases is chosen at 3. The tooth pitch of the stator and rotor is identical and the pole placement is shifted by 1/3 tooth pitch between phases (*equal pitch design* [122]). It is assumed that the number of poles is 18. It is sufficient to model 60 mechanical degrees because of symmetry. The number of turns per pole is assumed to be 60.

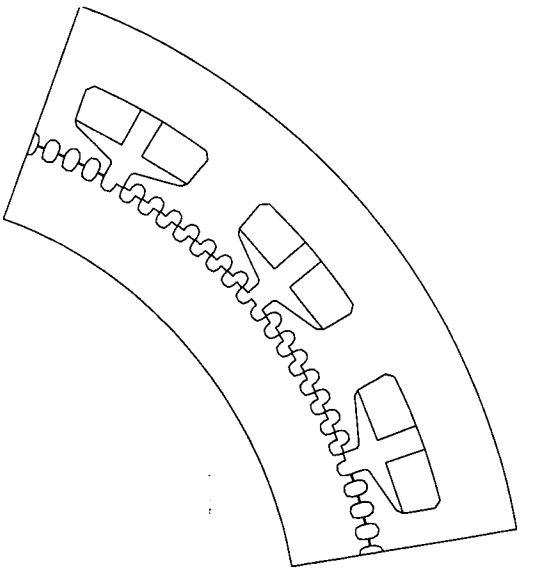

(a) 8-tooth model

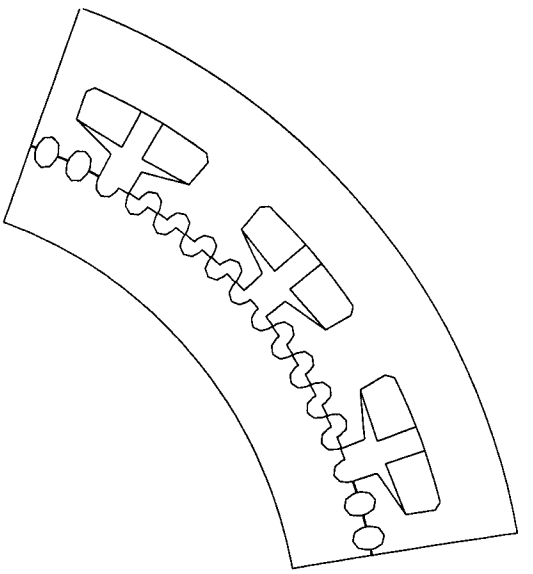

(b) 5-tooth model

Figure 6.14: Practical models

6.5.2 Analytical results

Figs. 6.15 and 6.16 show the flux plots for the 5- and 8-tooth models in the aligned and unaligned positions. The flux concentration in the stator yoke and the rotor is lower comparing to that in the stator poles for both models. The pole width could be designed wider, but with a penalty in the slot area [1]. The flux concentration is highest in the teeth in the aligned position, while the flux concentration is highest in the poles in the unaligned position. The mutual coupling between phases is small with the single-phase excitation.

The aligned and unaligned magnetisation curves of both models are shown in Fig. 6.17. MMF value was extended to unpractical value in order to show the effect of saturation in the unaligned position. It is seen that the curves in the aligned position are very close to each other. In these models, the pole pitch τ_s is chosen at 10° and τ_s is expressed as

$$\tau_s = \frac{N_t - 1}{2}\lambda + \frac{2}{3}\lambda. \tag{6.10}$$

The second term corresponds to the pole shift between phases. From the equation above, λ is expressed as a function of τ_s and N_t:

$$\lambda = \frac{\tau_s}{\frac{N_t-1}{2} + \frac{2}{3}}. \tag{6.11}$$

The total area of tooth surface per pole S_t is

$$\begin{aligned} S_t &= \lambda\left(\frac{t_w}{\lambda}\right) N_t L_{stk} \\ &= K\frac{2\tau_s}{1 + \frac{1}{N_t}} \end{aligned} \tag{6.12}$$

where L_{stk} is the stack length, (t_w/λ) is the ratio of tooth width to tooth pitch and $K = (t_w/\lambda)L_{stk}$. S_t of the 5-tooth model is approximately 6% smaller than that of the 8-tooth model. However, the difference in S_t does not seem to be affecting the aligned curves. On the other hand, the difference in the unaligned curves is significant. The

[1] The pole width of the analytical models was determined at a practical value by consulting the design of *the Megatorque motor*

unsaturated unaligned inductance of the 5-tooth model is about 80% of that of the 8-tooth model. This is due to the difference in the clearance in the unaligned position. The energy ratio E was calculated for a phase current of 6 A. E is 0.46 for the 8-tooth model and 0.52 for the 5-tooth model. The 8-tooth model is poorer in the utilisation of the device ratings.

Fig. 6.18 shows the energy conversion per stroke vs. MMF. The curve for the 5-tooth model is scaled to compensate for the difference in the tooth pitch by multiplying the factor of $N_{\varepsilon 5}/N_{\varepsilon 8}$, where $N_{\varepsilon 5}$ and $N_{\varepsilon 8}$ are the number of strokes per revolution for the 5- and 8-tooth models respectively. The average torque of the 8-tooth model is larger throughout the MMF level. The trend which is found in the half-pole model analysis is still seen in Fig. 6.18. When MMF level is lower, the difference in the average torque is larger. With increase in MMF level the difference becomes smaller. However, there is no crossover in the average torque. The average torque of the 5-tooth model is approximately 80% of that of the 8-tooth model for a phase current of 6 A, and it is 96 % for a phase current of 15 A.

Figs. 6.19 and 6.20 show the calculated magnetisation curves for the 8- and 5-tooth models respectively. The curves are shown in the aligned and unaligned positions including 5 intermediate positions. The static torque curves are calculated from the magnetisation curves and shown in Figs. 6.21 and 6.22. The average torque for the 8-tooth model is approximately 20 % higher for a range of MMF up to the highly saturated region. The curves of the 5-tooth model are flatter and this is advantageous for lower torque ripples with a constant current operation (see Fig. 6.23).

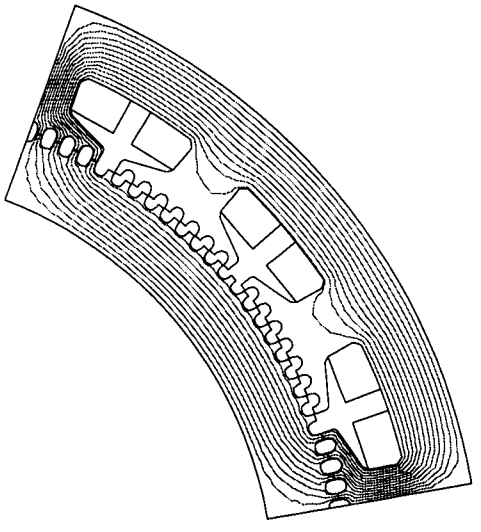

(a) Aligned position

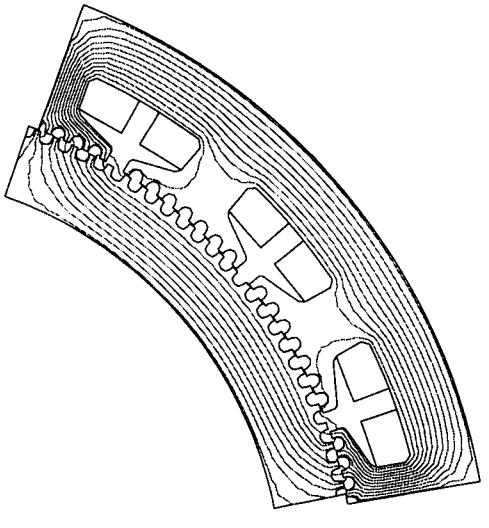

(b) Unaligned position

Figure 6.15: Flux plot (8-tooth model)

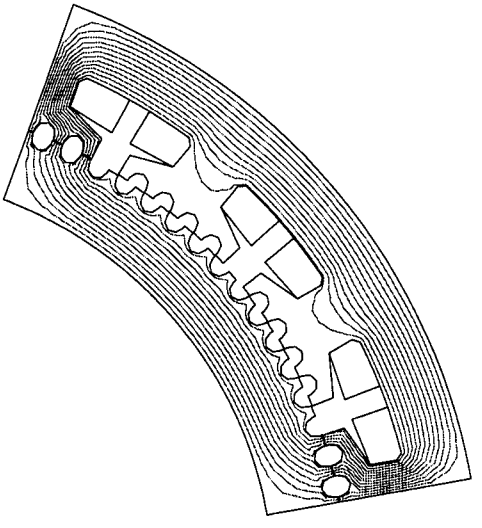

(a) Aligned position

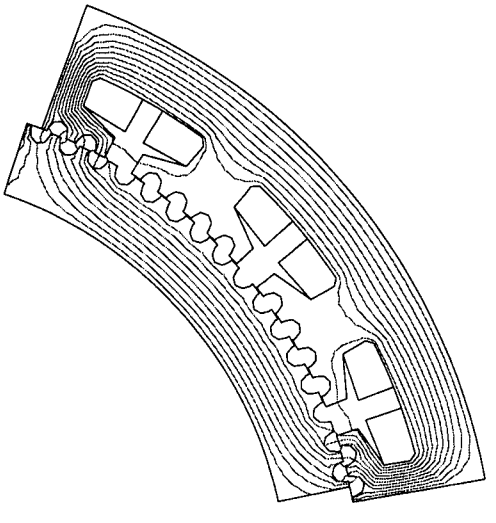

(b) Unaligned position

Figure 6.16: Flux plot (5-tooth model)

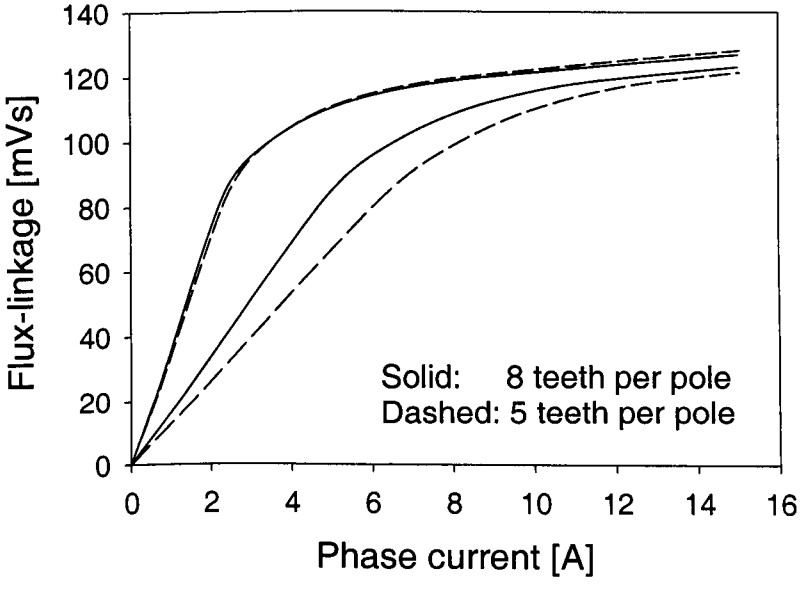

Figure 6.17: Magnetisation curves in aligned and unaligned positions

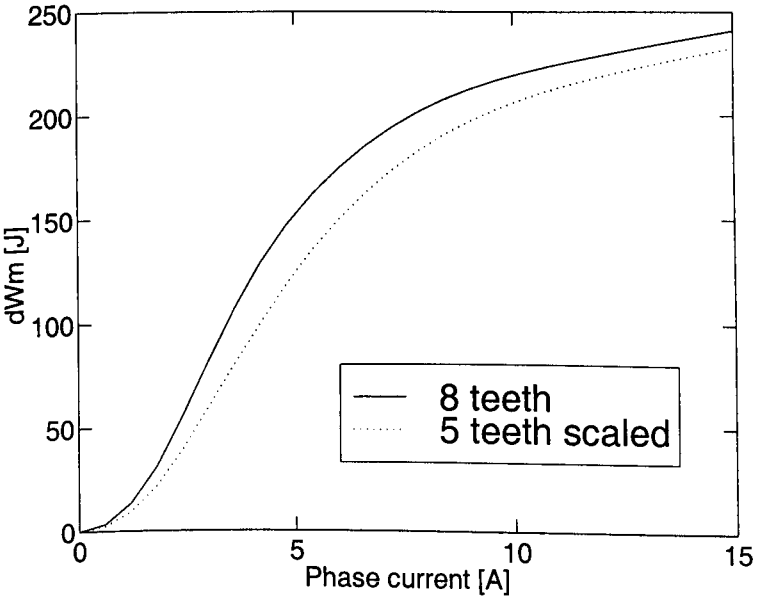

Figure 6.18: Energy conversion per stroke vs. MMF

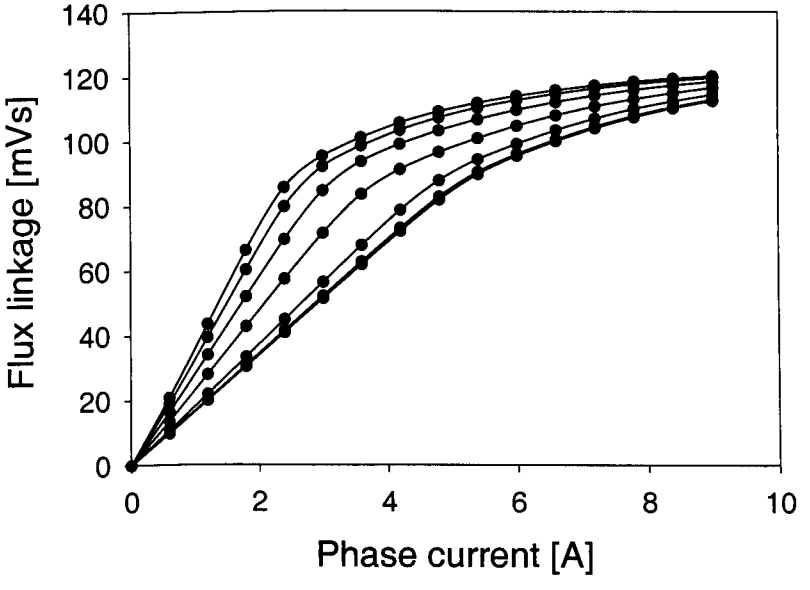

Figure 6.19: Magnetisation curves of 8 teeth per pole model

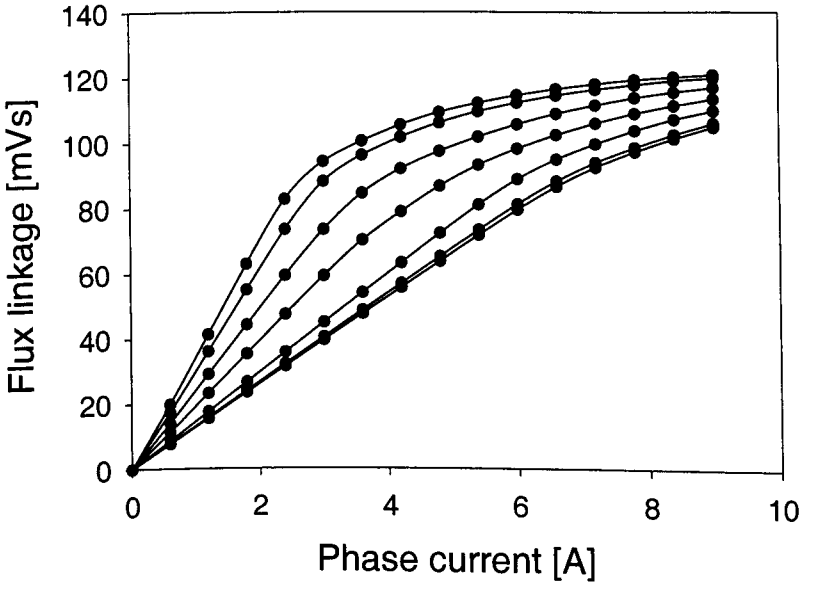

Figure 6.20: Magnetisation curves of 5 teeth per pole model

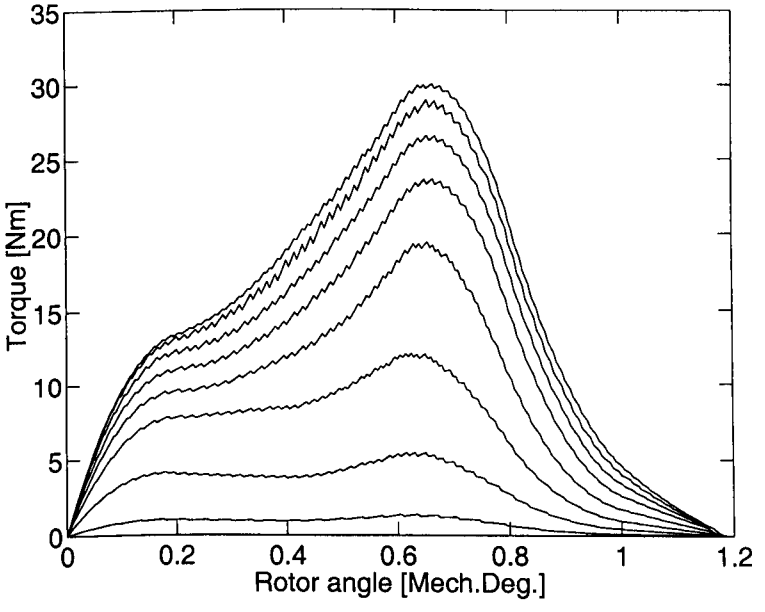

Figure 6.21: Static torque curves of 8 teeth per pole model

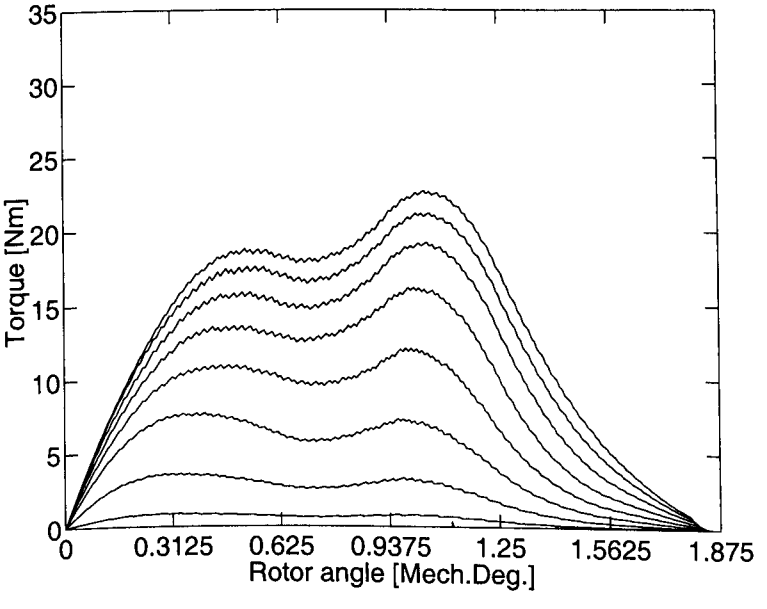

Figure 6.22: Static torque curves of 5 teeth per pole model

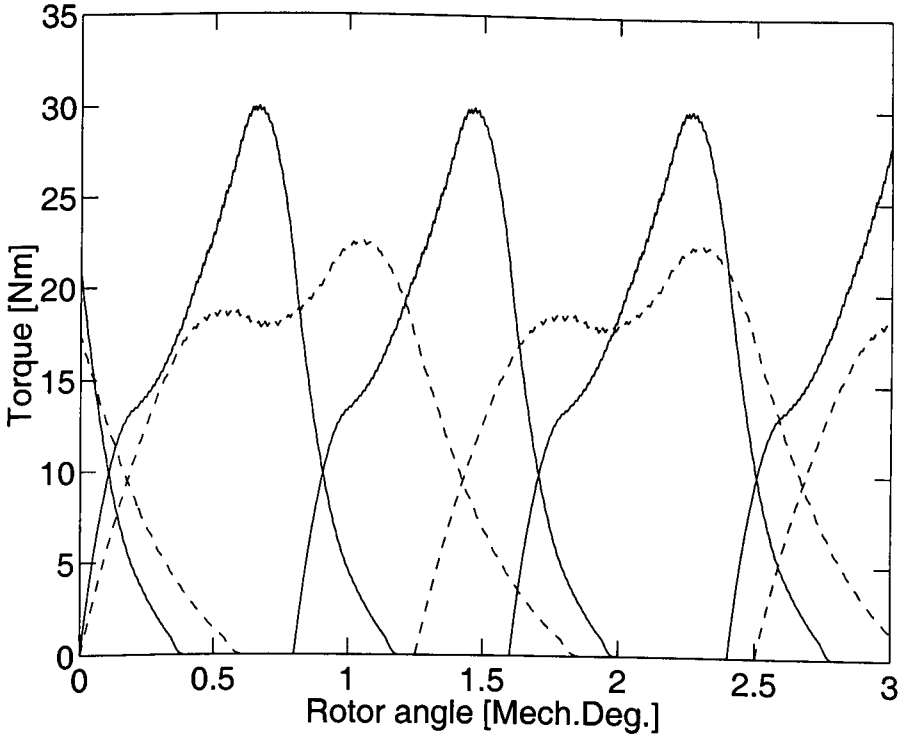

Figure 6.23: Torque waveforms with a constant current of 8 A (solid: 8-tooth, dashed: 5-tooth)

6.6 Conclusions

In this chapter, the optimisation of the tooth shape and the number of teeth per pole of the multi-tooth SRM for a maximum energy conversion were discussed.

Firstly, the tooth shape for a maximum energy conversion was studied. An optimum ratio of tooth width/tooth pitch and slot depth/tooth pitch were analysed. The results showed that an optimum ratio between tooth width and tooth pitch t_w/λ is around 0.4 and that the slot depth of $h = 0.5(t_w/\lambda)$ is sufficient. These results are of agreement with previously published ones.

Secondly, the number of teeth per pole for a maximum energy conversion was investigated. Half-pole models were employed for the analysis. It was found that an optimum number of teeth per pole for a maximum average torque varies with the saturation level. The number of teeth should be chosen such that the magnetisation curve in the unaligned position is about to start saturating for a given rated value of MMF.

Finally, practical models whose number of teeth are 5 and 8 were analysed. It was found that the average torque of the 8-tooth model was approximately 20% higher than that of the 5-tooth model. However, the energy ratio of the 5-tooth model was 5% higher. The static torque of the 5-tooth model was flatter than that of the 8-tooth model. This can be an advantage for a lower torque ripple with a constant current operation. However, the static torque curves of the 8-tooth model could also be changed by modifying the tooth geometry. It should be noted that many recent applications of the Megatorque motor such as silicon wafer positioning require low torque ripple rather than high torque, while high torque was the main requirement when the Megatorque motor was introduced about a decade ago. The 5-tooth model should be considered as a possible design for such new applications.

In summary, for the design of the multi-tooth SRM, increasing the number of teeth can be beneficial for a higher average torque, however, the cost of possible higher losses

and device ratings must be paid. Therefore, the number of teeth should be designed by taking in account overall characteristics of the system.

Chapter 7

Conclusions

This thesis has investigated the fault tolerant operation of the single-phase SR machine as a generator. It has also analysed coil and inverter faults in the poly-phase SR machine. Furthermore, the multi-tooth per pole SR motor has also been studied. In this chapter general conclusions of the present work and possible future work are presented.

7.1 Comparison of single- and poly-phase SR machines

In chapter 2 the advantages of the single-phase SR machine over poly-phase equivalents have been investigated.

The analysis demonstrated why the single-phase SR machine can be designed to achieve higher efficiency over poly-phase equivalents. The larger slot area, lower iron volume and shorter flux paths contribute to higher efficiency.

Finite element analysis showed that poly-phase equivalents require wider pole width for a comparable output with the single-phase machine, leading to higher copper losses.

Dynamic simulations using PC-SRD were performed in order to validate the analytical results. The simulation results and analytical results agreed. The overall efficiency of the single-phase 8/8-pole SR machine was 3 to 5% higher than that of a comparable 4-phase 8/6 SR machine.

Prototype single-phase 8/8-pole and 4-phase 8/6 SR machines with comparable geometry were built and dynamic and static tests were carried out. The test results validated the analysis and simulations.

In summary, the multi-pole single-phase SR machine could be designed for a higher efficiency over poly-phase equivalents and can be advantageous for certain applications where the lack of starting capability and the high torque ripple are not serious issues, like generator applications.

7.2 Maximisation of the energy conversion effectiveness in the SR generator

In chapter 3 maximisation of the energy conversion effectiveness of the SR generator was discussed. The effect of the DC-bus voltage and the rotor speed on the energy conversion effectiveness was highlighted by simulations.

The limitations of chopping control was discussed. Two limitations are that the generated current waveform can only be controlled at speed below the base speed where the back-EMF is smaller than the DC-bus voltage and that it is difficult to achieve a low excitation penalty.

An SR generator controller which regulates the DC-bus voltage in proportion to the speed was proposed. The controller maximises the energy conversion effectiveness by maintaining the current waveform close to the ideal "flat-top" shape even when the speed of the prime mover varies over a wide range. A converter topology which regulates the load voltage at a constant value with only one additional switch was

proposed. The simple additional circuit is sufficient if the load voltage is lower than the controlled DC-bus voltage over the operating speed range.

A nonlinear model of the proposed system was implemented in the SIMULINK® simulation package. Measured magnetisation curves of the prototype machine were used in the simulation model to take into account the nonlinearity. The simulation results confirmed that the "flat-top" current could be achieved by controlling the DC-bus voltage with rotor speed and it could be controlled dynamically. The load voltage was regulated at a constant value of 80 V for a speed range of 3,000 to 10,000 rpm independently of the DC-bus voltage by an addition of a simple step-down DC/DC converter.

The controller was implemented using a microcontroller for the single-phase 8/8-pole SR machine with power rating of 0.8 kW at 2,000 rpm. The validity of the proposed control method was confirmed by experiments. The proposed method may be suitable for applications where the speed of the prime mover varies widely, such as wind generators and jet turbine generators.

7.3 Fault-tolerant operation of the single-phase SR generator

In chapter 4 fault-tolerant operation of the single-phase SR generator was discussed. The split-winding converter which requires a few additional components for the single-phase 8/8-pole machine was proposed and the operation under open- and short-circuit coil faults were analysed.

The reduction in output power with loss of the coils was analysed for several winding configurations. It was found using the linear analysis and finite-element analysis that the SR generator was capable of generating half its normal power with 4 of the 8 coils open for the same coil current. The static torque measurement and generating tests confirmed this analysis. The winding configuration of NNSSNNSS magnetic polarity

may be the best configuration when the windings of the single-phase SR generator are split into two banks in parallel.

Transient state operation on disconnecting faulted coils with the proposed system was also studied. The circuit equations under faulted conditions were derived and computer simulations were performed. A fault in one of the 8 coils affects all healthy coils significantly if the magnetic unbalance is not removed. It was shown that the proposed SR generator system could separate faulty coils dynamically and keep generating half the normal power after coil faults. It demonstrated that the output power after faults with the fixed-angle single-pulse control depends on the winding configuration and will be either its normal value or half its normal value.

The analytical and simulation results were validated by experiments using the SR generator system developed in chapter 3. The experimental results proved stable operation of the SR generator under the coil faults.

7.4 Analysis and classification of faults in SR motors

In chapter 5 analysis and classification of winding and inverter faults in the SR motor were presented. The new lumped parameter magnetic equivalent circuit was used taking full account of nonlinearity and the mutual coupling between phases. The 3-phase 6/4-pole SR drive model was implemented in the Saber™ simulation package. The model was validated with time-stepping finite element analysis.

Many potential winding and inverter faults were analysed. The simulated coil faults include coil open-circuit, full coil short-circuit, partial coil short-circuit, phase to phase short-circuit, and coil to ground short-circuit faults. The simulated inverter faults include transistor short-circuit and bus short-circuit faults. All faults were simulated for series and parallel connected phase coils, two pole magnetic configurations of NNNSSS and NSNNSN and with single-pulse and current chopping control modes.

A detailed analysis of the simulated results were described in chapter 5 and are summarised below. With the series connected phase coils the main effects of the coil faults on the performance are:

- torque reduction for coil open-circuit fault
- unbalanced radial force production for full coil short-circuit and coil to ground short-circuit faults
- induced current in shorted turns for partial coil short-circuit fault
- negative torque production for phase to phase short-circuit fault.

The main impact is the same for the parallel connected phase coils except for coil open-circuit and full coil short-circuit faults, the main effects of these faults being torque reduction and unbalanced radial force production respectively.

For the inverter faults the main impact of the transistor short-circuit fault is the loss of the negative voltage loop which results in abnormal flux linkage and current. The bus short fault is serious for generating operation because generated current may become excessive with the loss of applied negative voltage.

It should be noted that only the main effects of the faults on the system are highlighted above. A more detailed discussion of the full impact of faults on the system is given in chapter 5.

Although the analysis was based upon the 3-ph 6/4 SR motor, most of the results are considered to be common for other configurations. It should be noted that although increasing the number of phases will reduce the impact of a fault in a phase on overall torque production the risk of excessive unbalanced radial forces, heat rise by induced current, semiconductor switch failures etc. will not be reduced.

7.5 The multi-tooth per pole SR motor

In chapter 6, the analysis of the multi-tooth SR motor was presented.

Optimum ratios of tooth width/tooth pitch and slot depth/tooth pitch were analysed by finite element analysis for a maximum energy conversion. An optimum ratio of tooth width/tooth pitch was found to be around 0.4 and a ratio of slot depth/tooth pitch of 0.5 was found to be sufficient. This confirms previously published results.

An optimum number of teeth per pole for a maximum energy conversion was also investigated. It was found that an optimum number of teeth per pole varied with the saturation level and the number of teeth should be chosen such that the magnetisation curve in the unaligned position was about to start saturating for a given rated value of MMF.

Practical 5 and 8 teeth per pole models were analysed. The 8-tooth model was 20 % higher in average torque and 5 % lower in the energy ratio than the 5-tooth model. The static torque curves of the 5-tooth model were flatter than those of the 8-tooth model which may result in a lower torque ripple with current control operation. The static torque curves of the 8-tooth model could be changed by modifying the geometry.

In summary, increasing the number of teeth in the design of the multi-tooth SRM may increase the average torque but decrease the energy ratio at the same time which in turn may lead to higher losses and higher device ratings. Therefore the number of teeth should be determined from desired overall system characteristics.

7.6 Future work

- Although the single-phase SR machine can be higher in efficiency, application is limited because of the lack of starting capability and high torque ripple. Identification of the applications where the single-phase SR machine has clear advantages is required.

- In the SR generator system studied in chapter 3, the single-pulse control in which the switching angles were determined by a linear model was used. Although this was sufficient for the validation of the proposed DC-bus voltage control system, further investigation of the control laws of the SR generator is required for optimum performance. Analysis of the dynamic response of the proposed scheme is also required.

- The single-phase SR generator system discussed in chapter 4 offers an option for low-cost implementation of a fault-tolerant system. However relative assessment of fault-tolerant systems including poly-phase system is required.

- Though many possible faults in the SR motor were analysed in chapter 5 there still remain faults uncovered. Investigation of probability of the occurrence of faults is necessary for the determination of fault detection and protection required. Validation of the simulation model by experiment would be ideal although only validation by the time-stepping finite element analysis was carried out.

- Although studied by finite element analysis in chapter 6, the design of the multi-teeth per pole SR machine is still difficult and as yet unclear. This issue is left for further investigation.

Appendix A

Data for prototype machines

In the following, drawings of laminations, measured magnetisation curves and measured static torque curves of the prototype single-phase 8/8-pole and 4-phase 8/6 SR machines are presented.

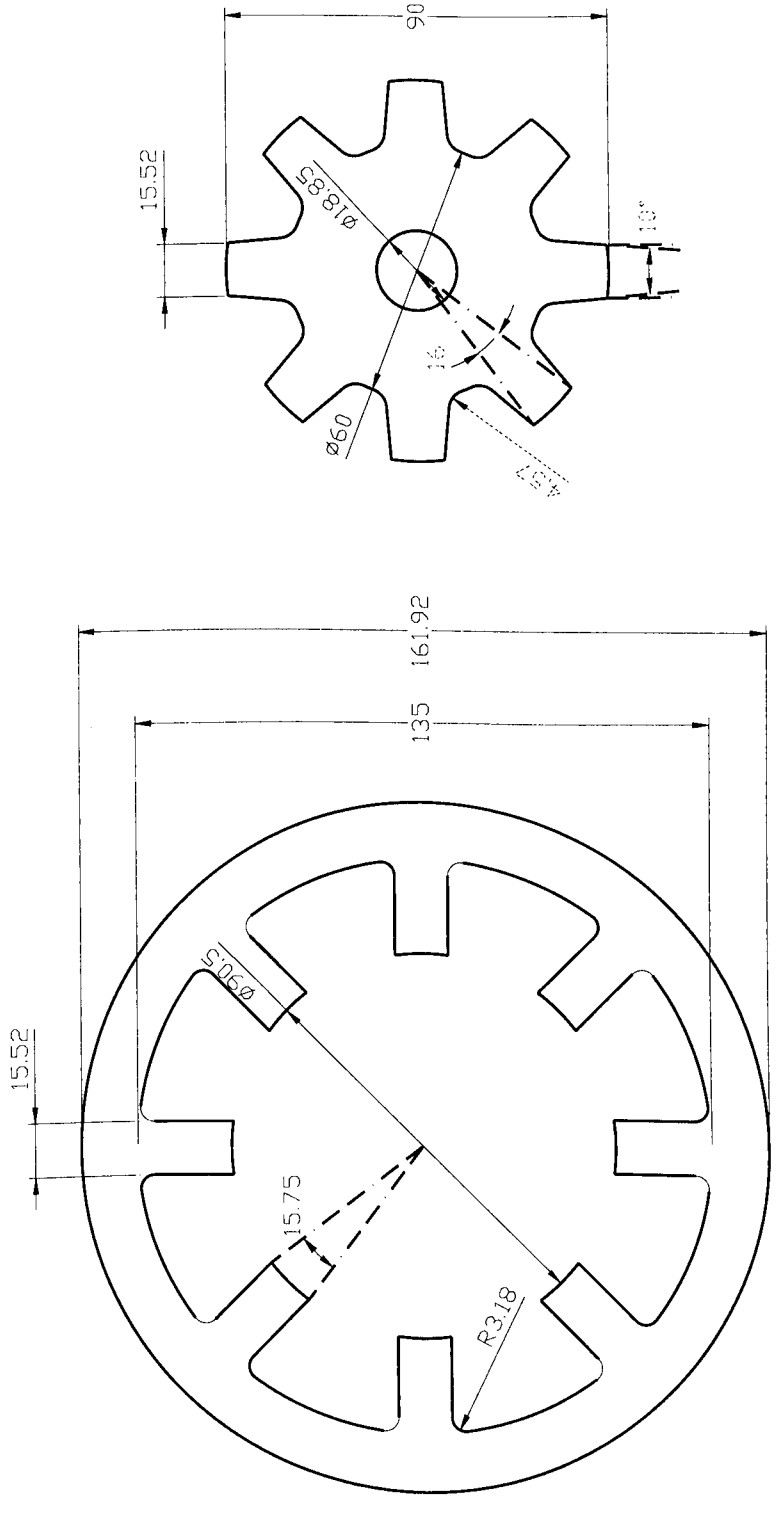

Figure A.1: Drawings of lamination of prototype 1-ph 8/8 SR machine

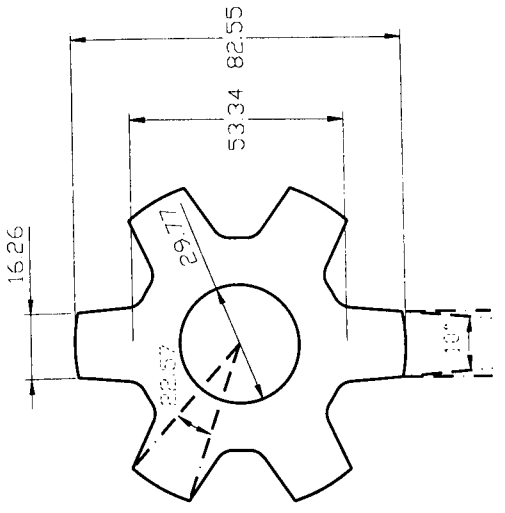

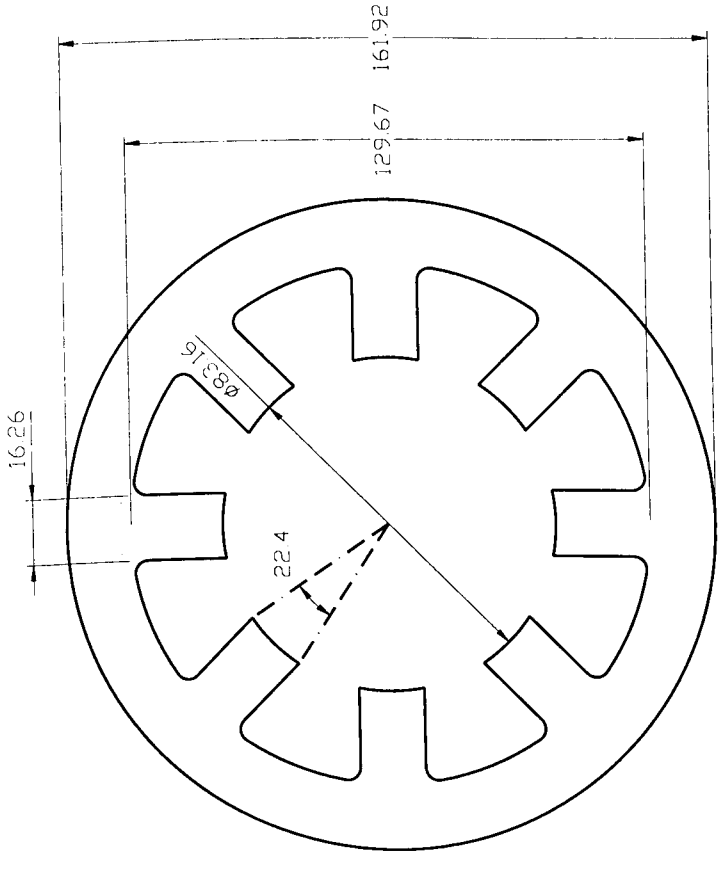

Figure A.2: Drawings of lamination of prototype 4-ph 8/6 SR machine

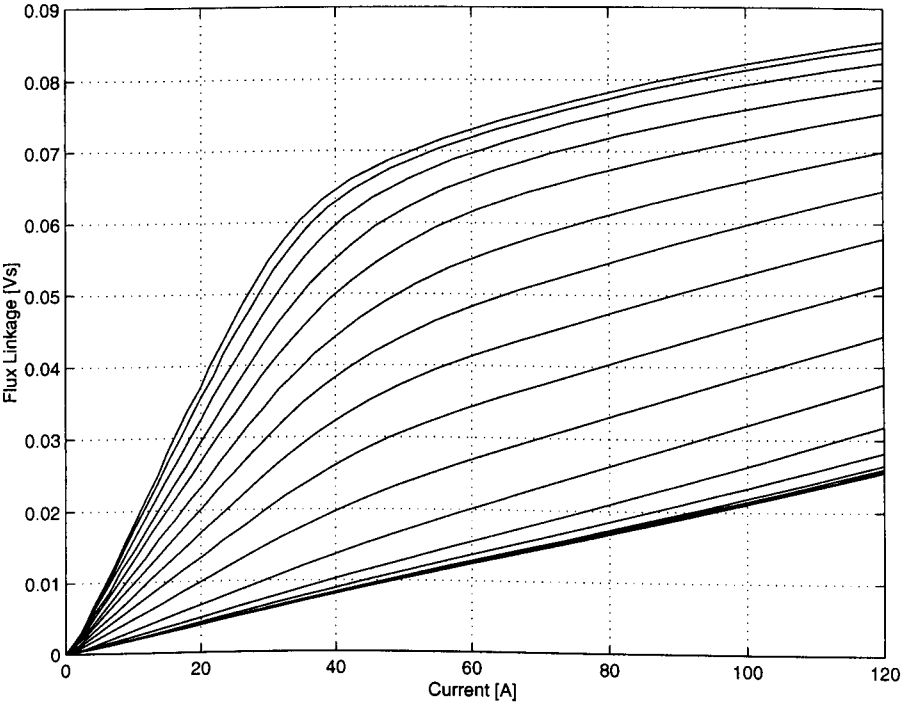

Figure A.3: Measured magnetisation curves of prototype 1-ph 8/8 SR machine

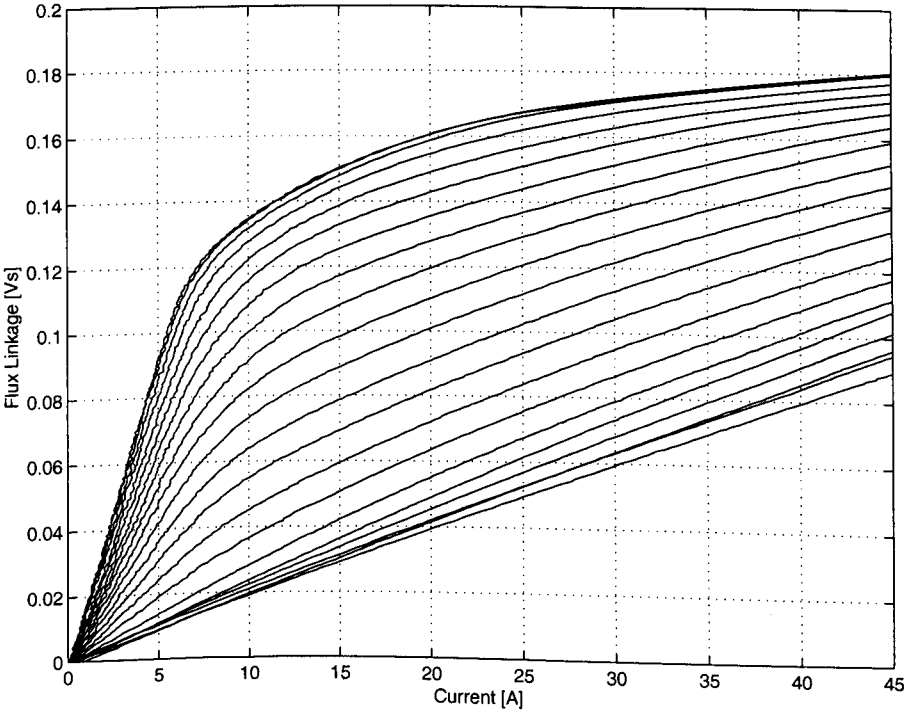

Figure A.4: Measured magnetisation curves of prototype 4-ph 8/6 SR machine

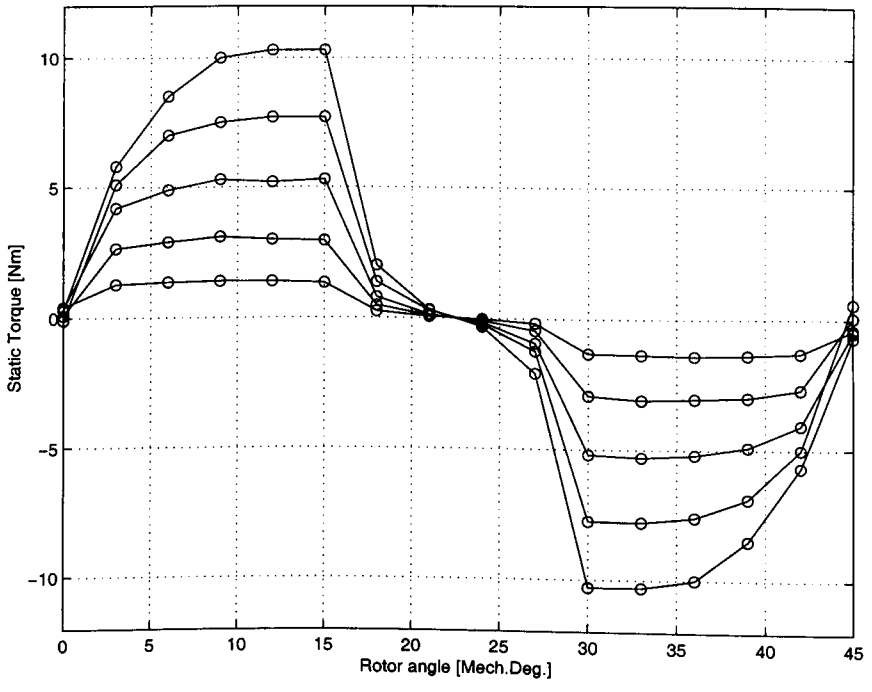

Figure A.5: Measured static torque curves of prototype 1-ph 8/8 SR machine (20, 30, 40, 50, 60A)

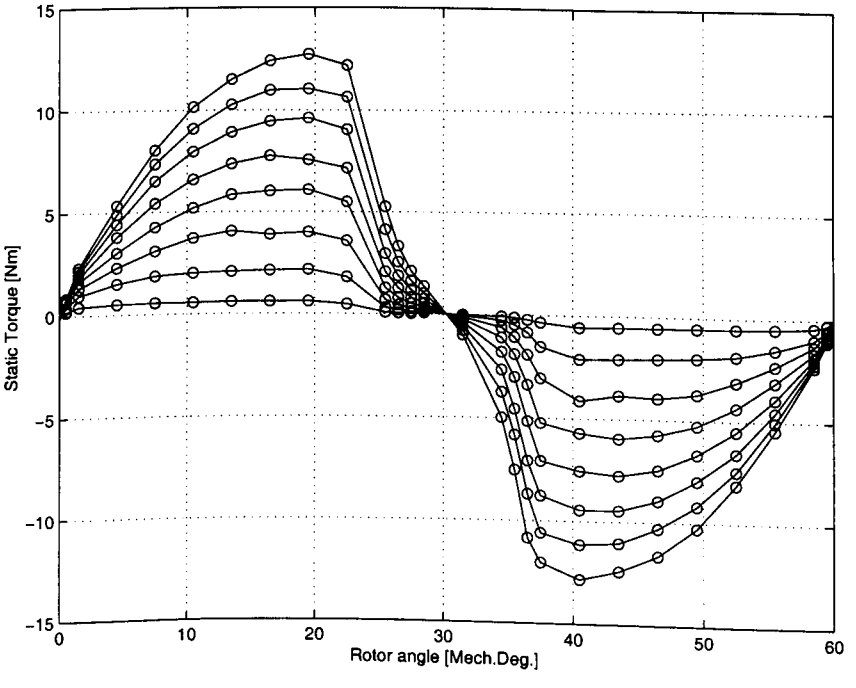

Figure A.6: Measured static torque curves of prototype 4-ph 8/6 SR machine (5, 10, 15, 20, 25, 30, 35, 40A)

Appendix B

Circuit diagrams

In the following, circuit diagrams of the SRG controller, isolation amplifier and power electronic inverter are presented. Most of the commutation board circuits are programmed in a XILINX XC3064A FPGA.

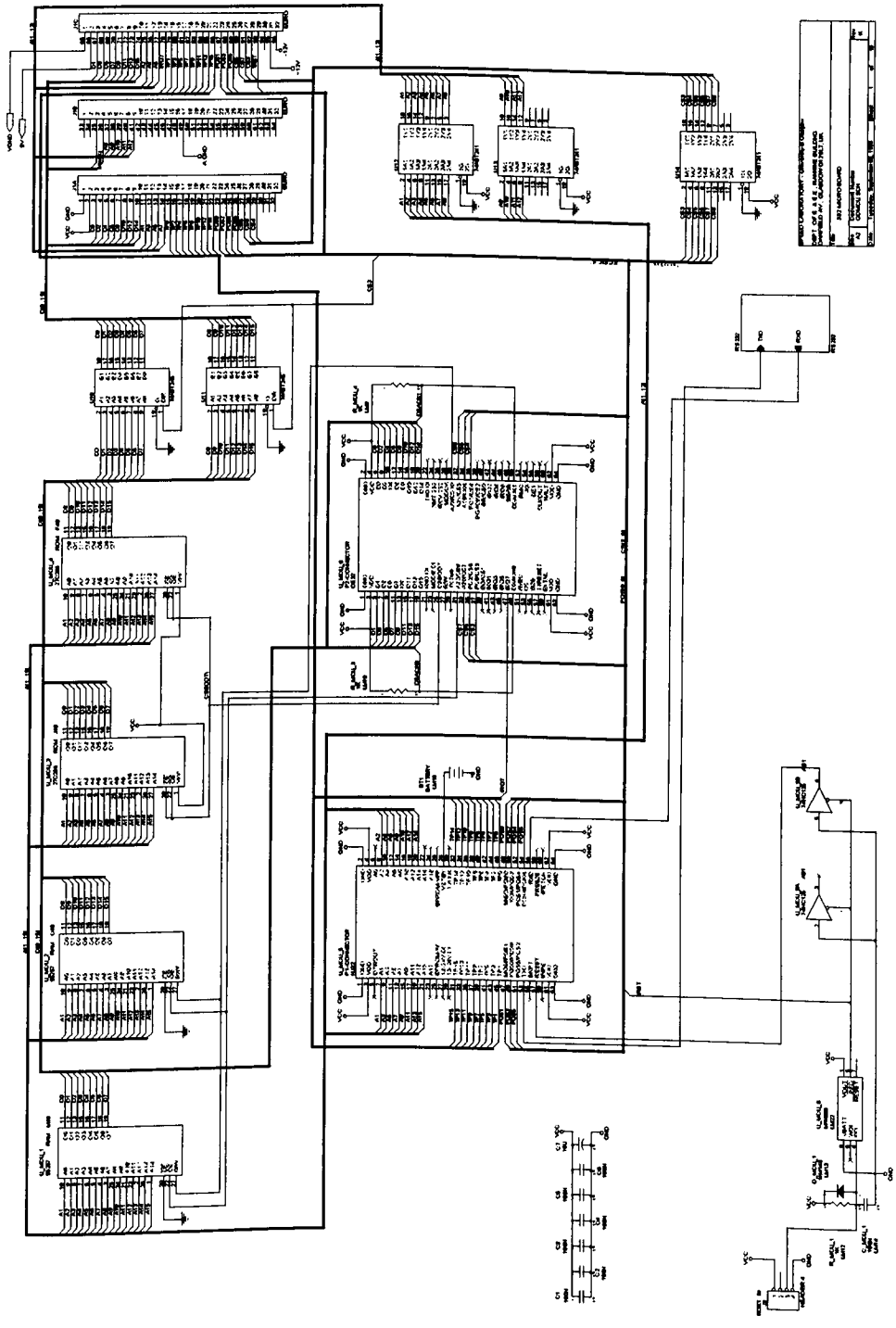

Figure B.1: Circuit diagram of MC68332 microcontroller board

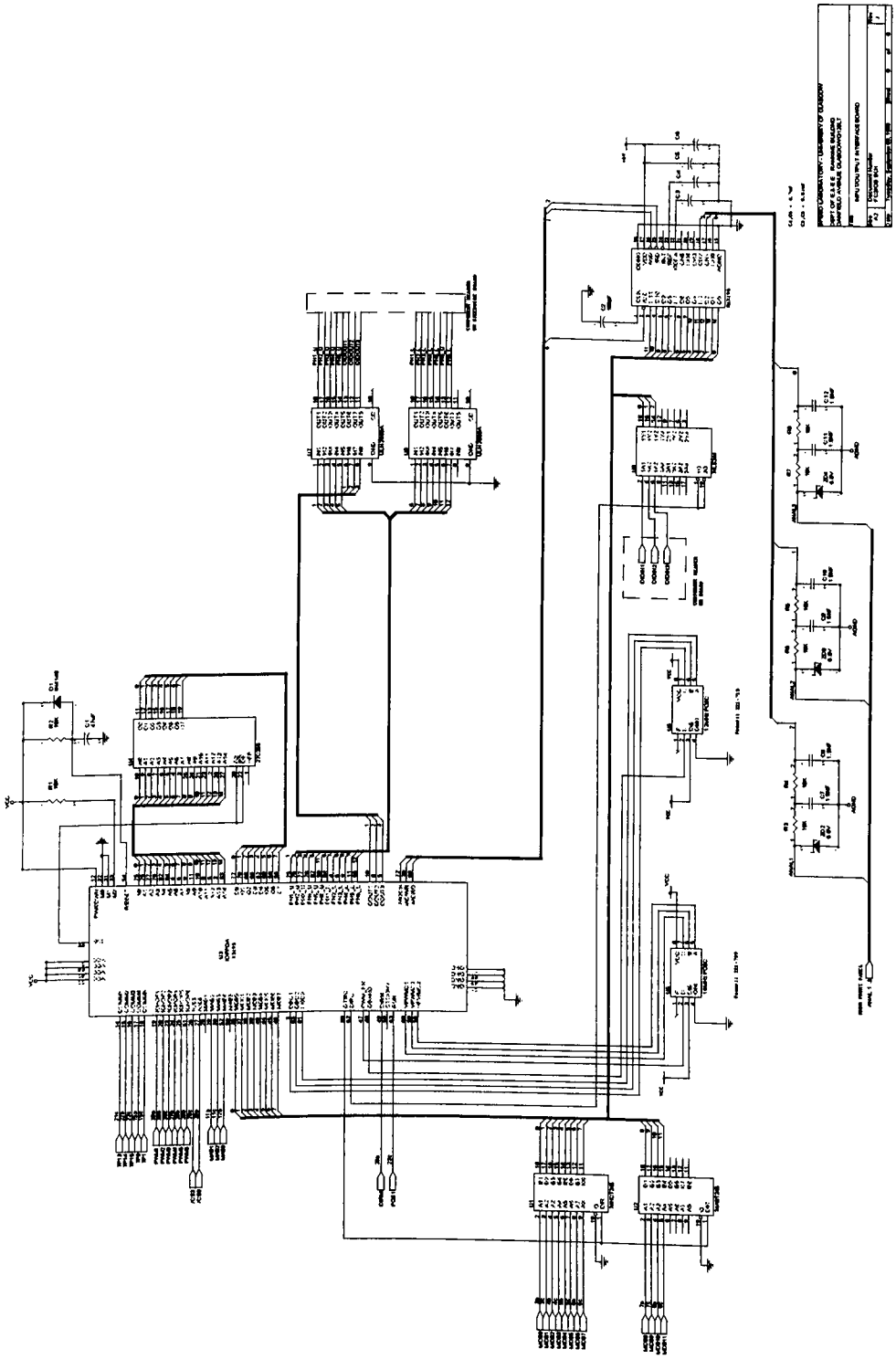

Figure B.2: Circuit diagram of I/O board

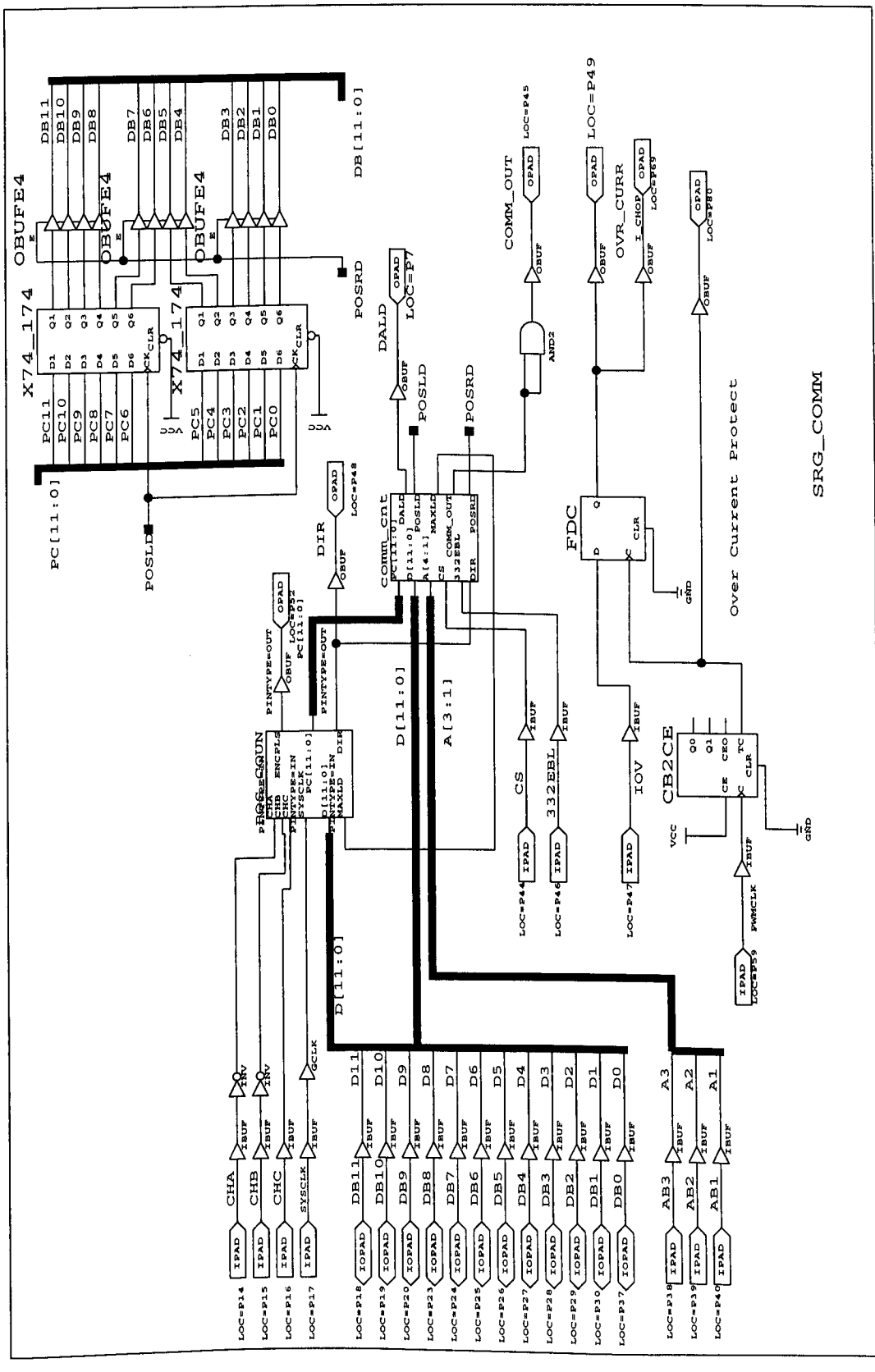

Figure B.3: Circuit diagram of commutation board: top level

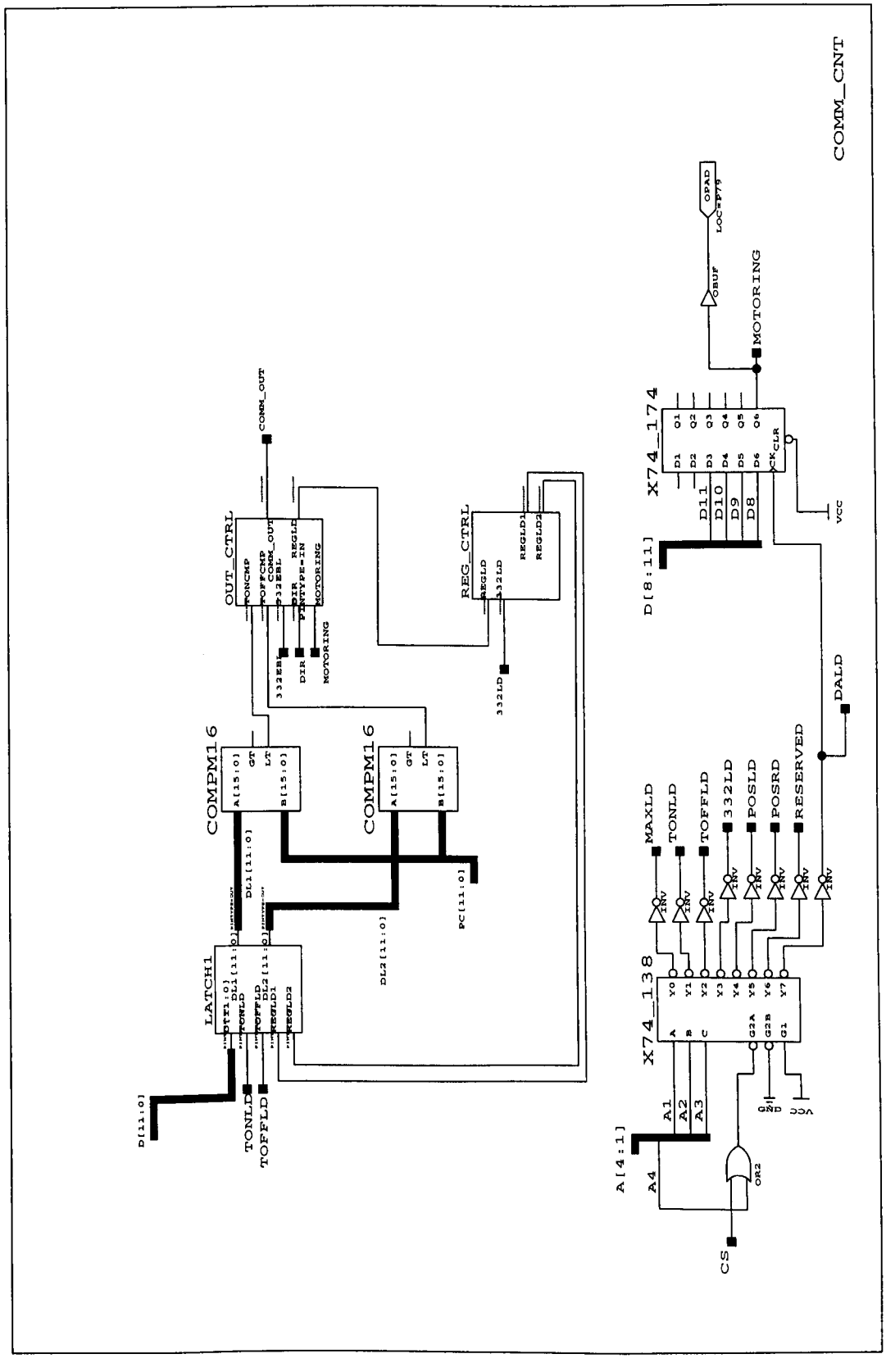

Figure B.4: Circuit diagram of commutation control block in commutation board

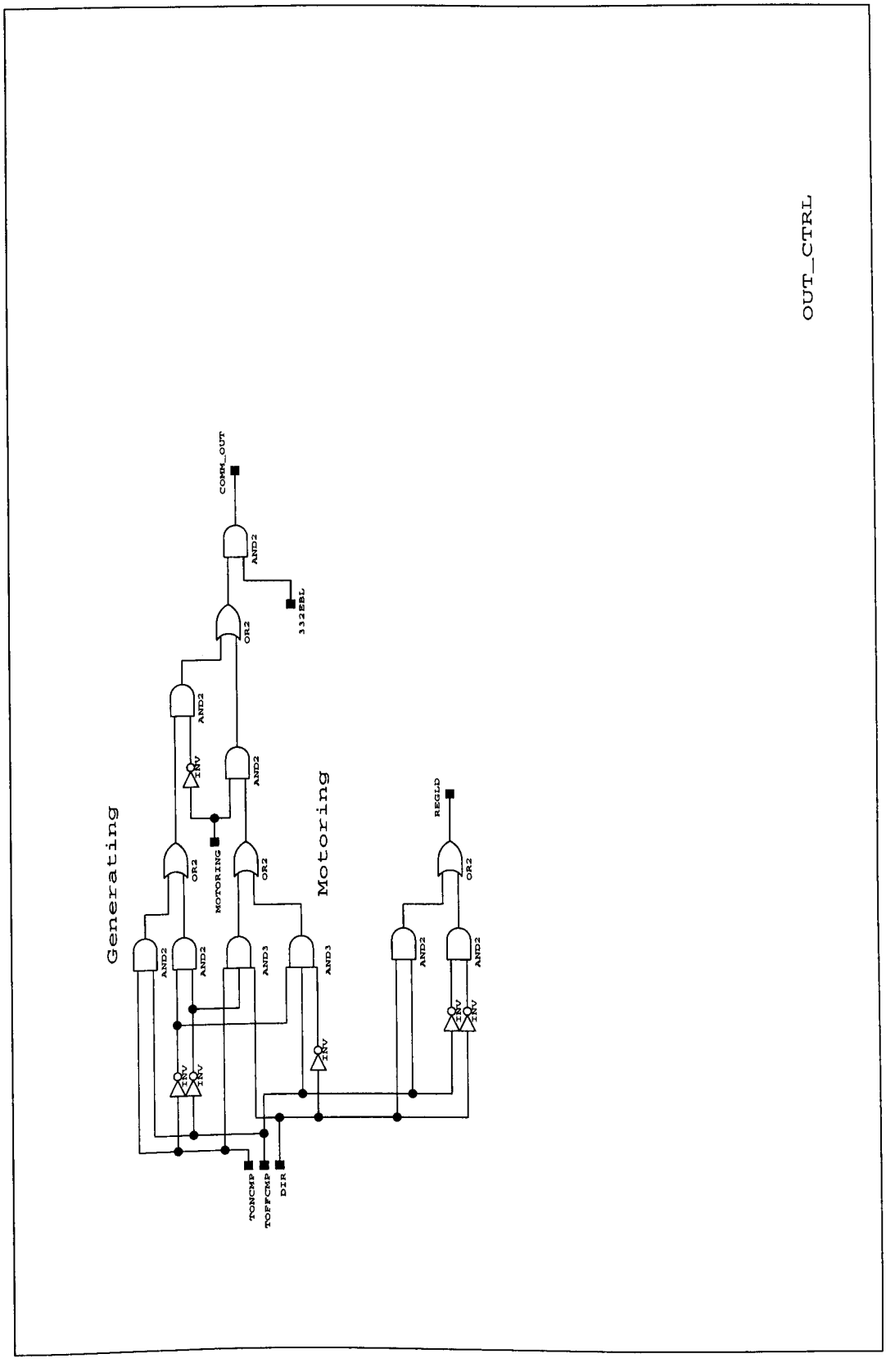

Figure B.5: Circuit diagram of output control block in commutation board

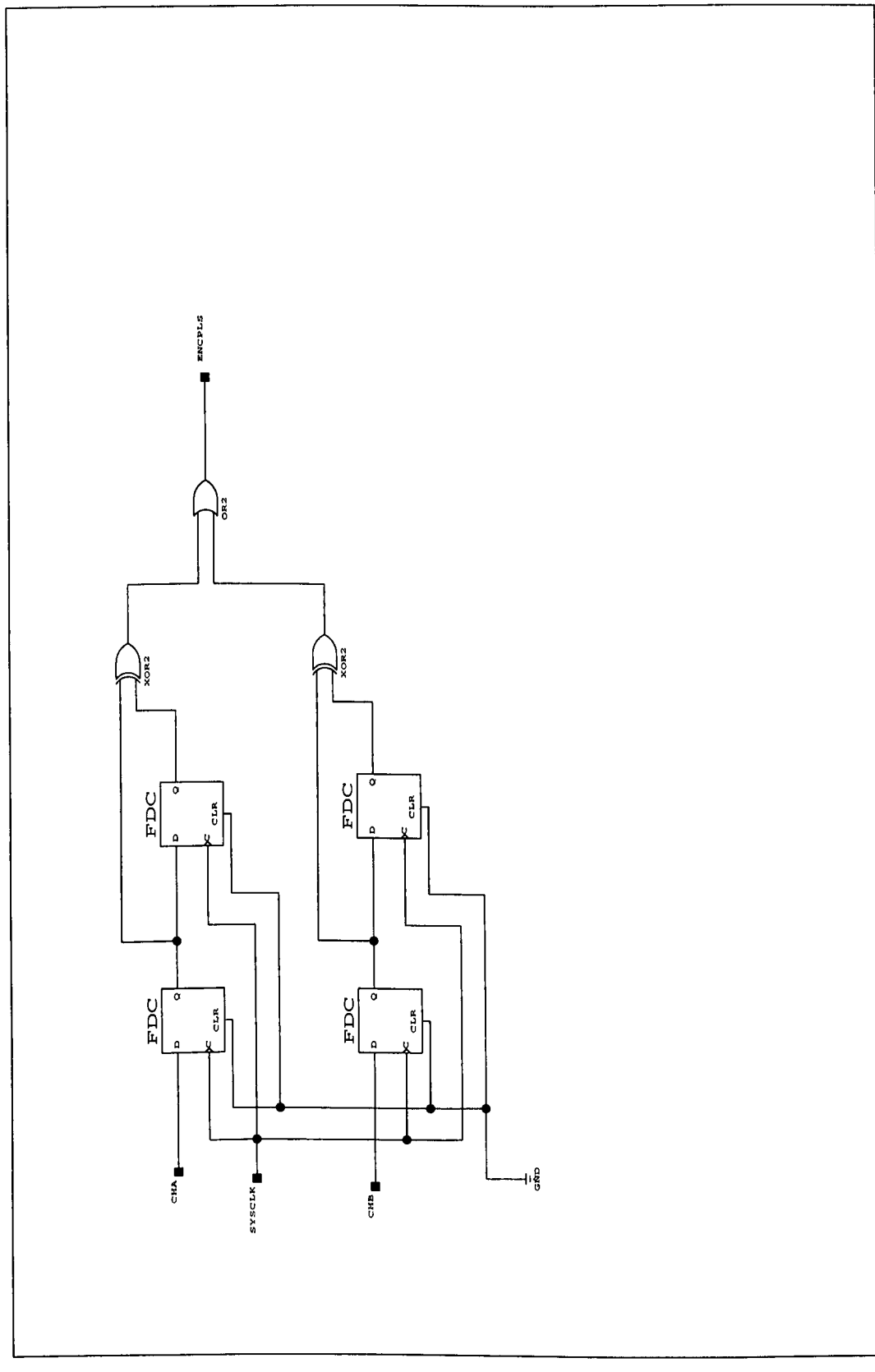

Figure B.6: Circuit diagram of encoder signal edge detection block in commutation board

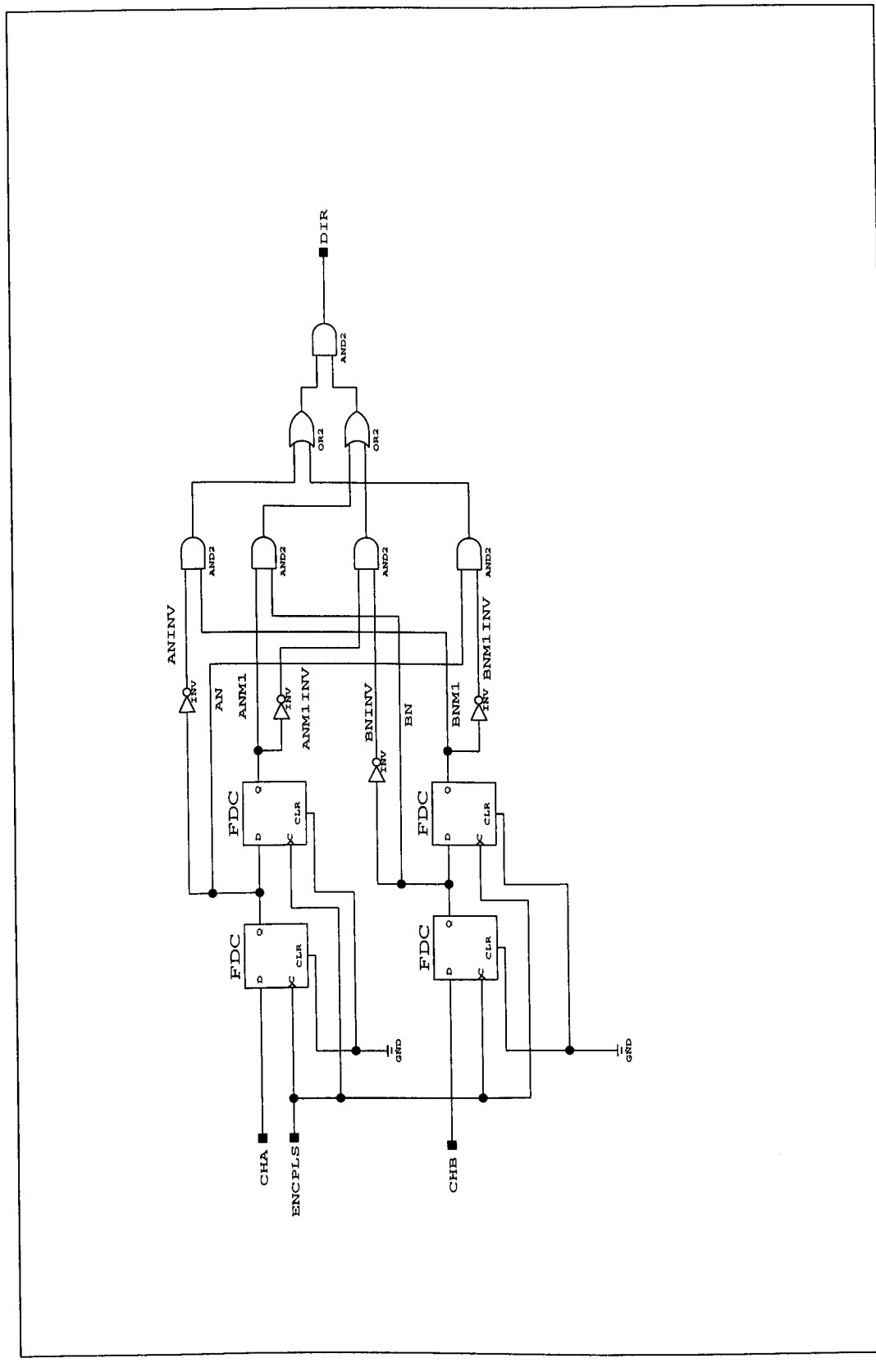

Figure B.7: Circuit diagram of rotation direction detection block in commutation board

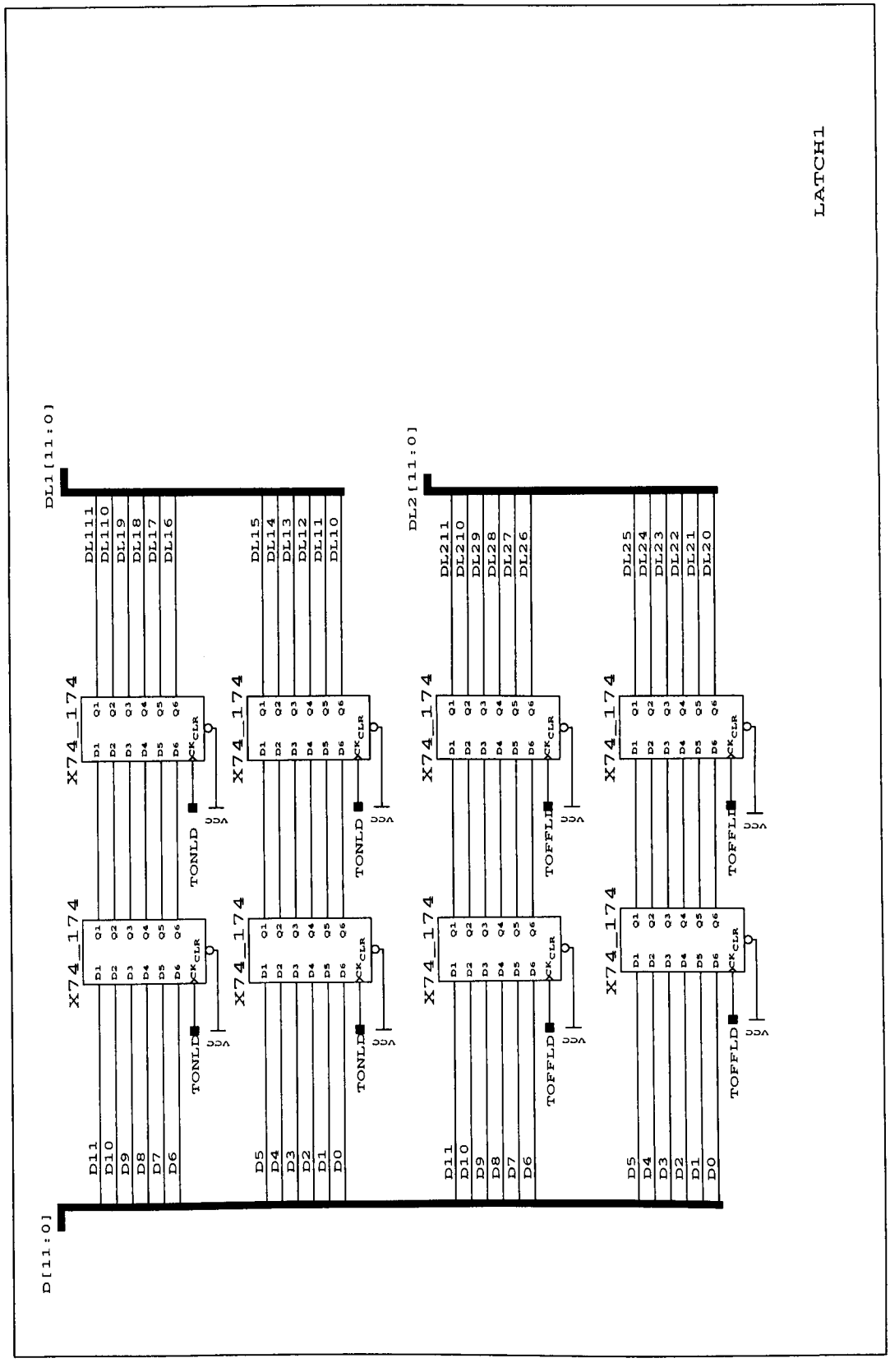

Figure B.8: Circuit diagram of latch array block in commutation board

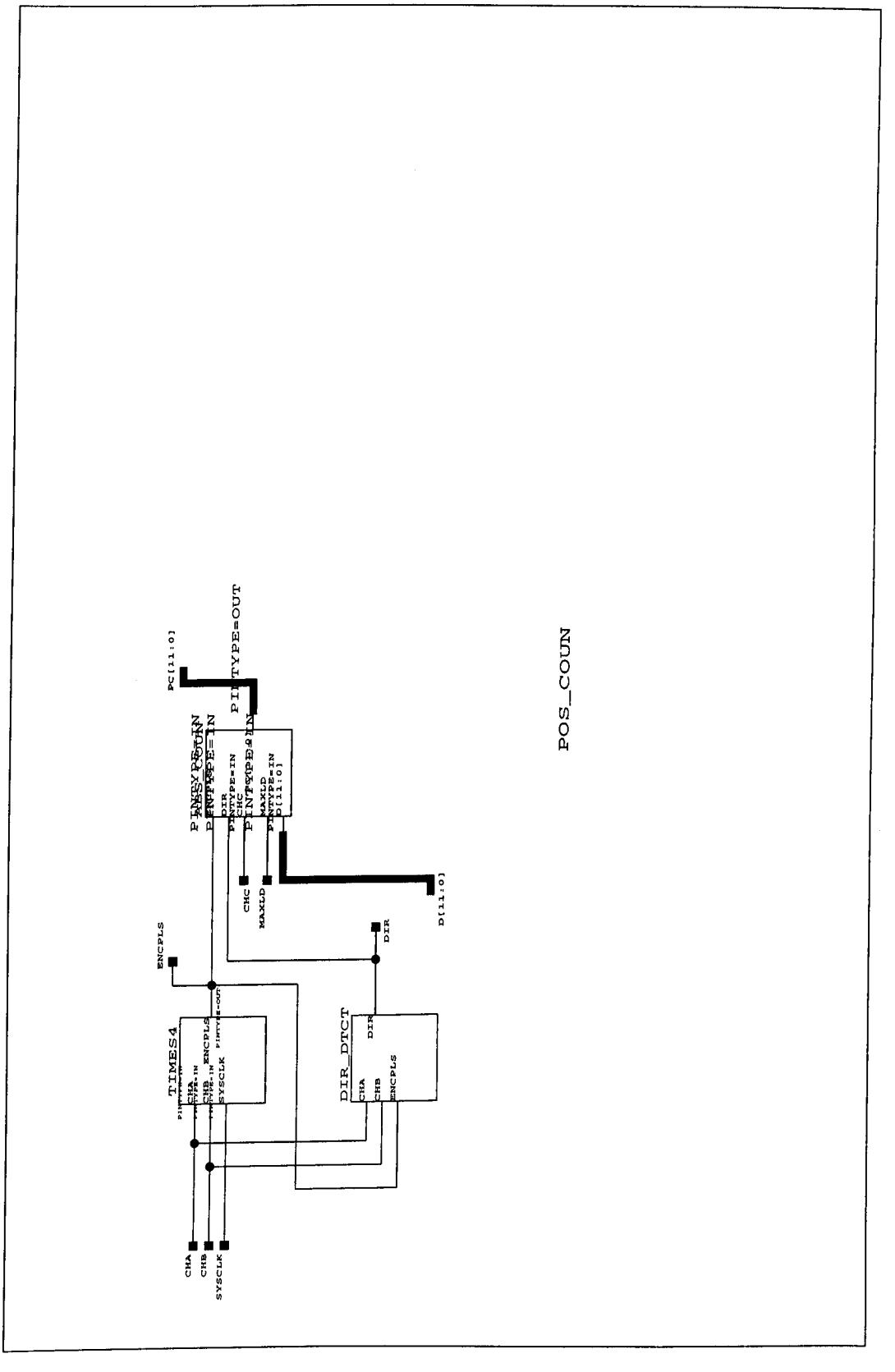

Figure B.9: Circuit diagram of position counter block in commutation board

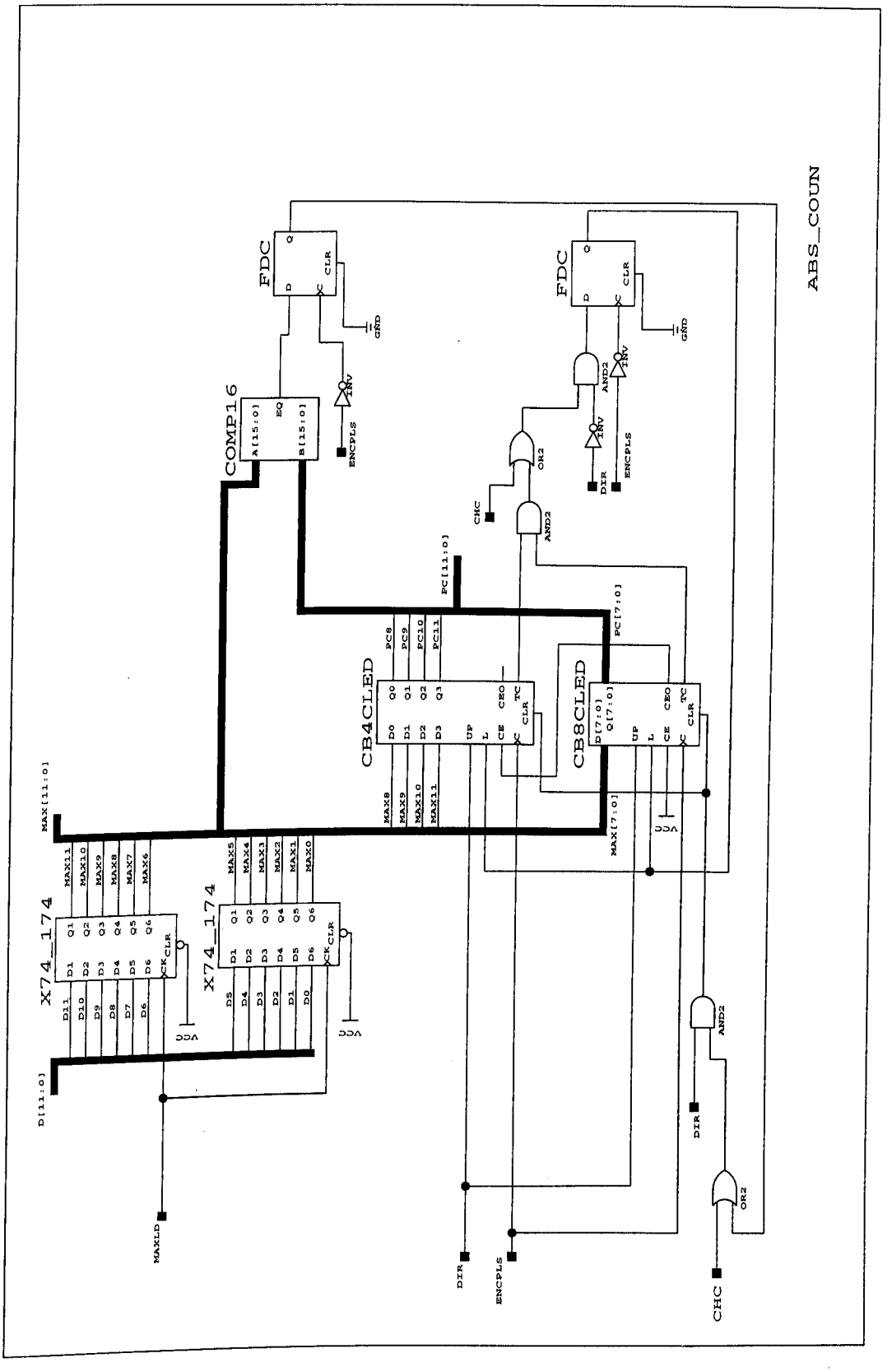

Figure B.10: Circuit diagram of absolute position counter block in commutation board

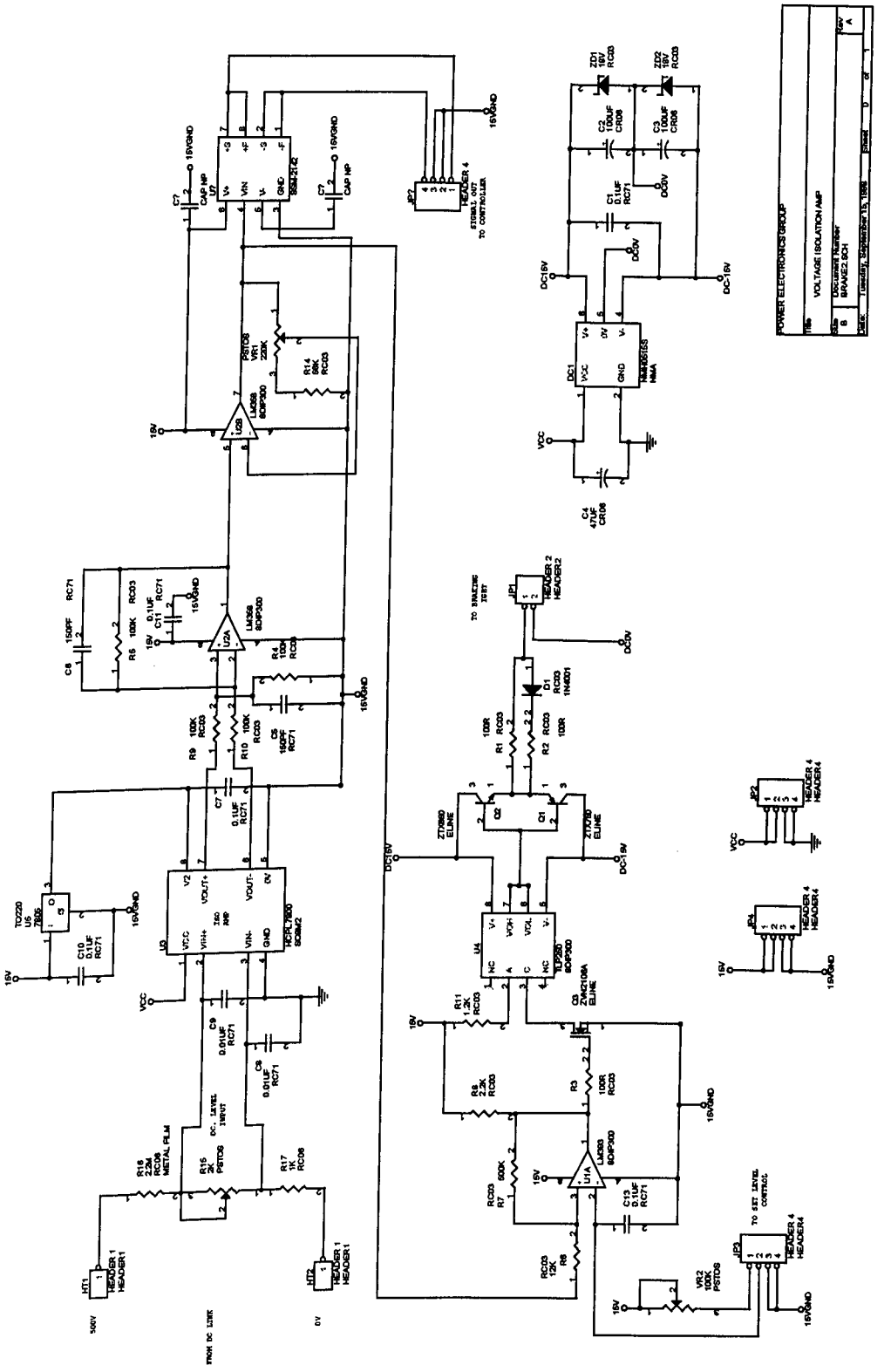

Figure B.11: Circuit diagram of isolation amplifier

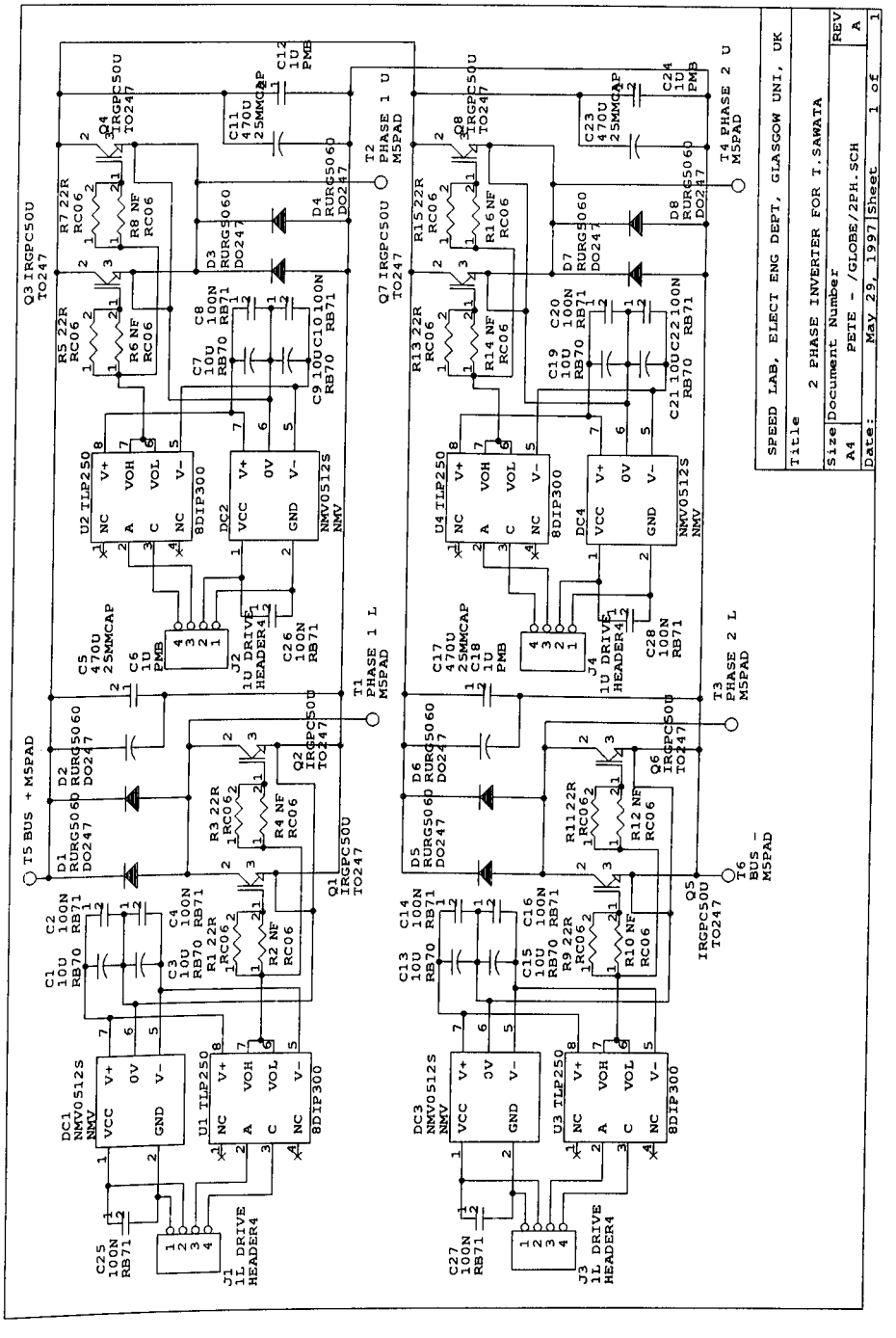

Figure B.12: Circuit diagram of power electronic inverter

Appendix C

Magnetisation curve measurement of Megatorque motor

C.1 Positioning of the rotor

Measurement of magnetisation curves of Megatorque motor requires very precise positioning of the rotor since one electrical cycle corresponds to 2.4 mechanical degrees. When the magnetisation curves are measured for the rotor position of every 10 electrical degrees, the rotor has to be positioned and locked at every 0.0667 mechanical degrees.

For magnetisation curve measurement of a normal SR machine, the rotor may be positioned and locked by a dividing head. However, the dividing head available in the SPEED laboratory has a resolution of 0.2 mechanical degrees which is not enough for the measurement for Megatorque motor.

A rig which locks the rotor of Megatorque motor in desired positions was constructed and is shown in Fig. C.1. The stator is fixed to the back plate and the rotor is fixed to the front plate of the rig. The front plate has holes which have enough clearance to allow the rotor to rotate more than one electrical cycle. The rotor can be rotated by loosing the 6 screws which lock the rotor.

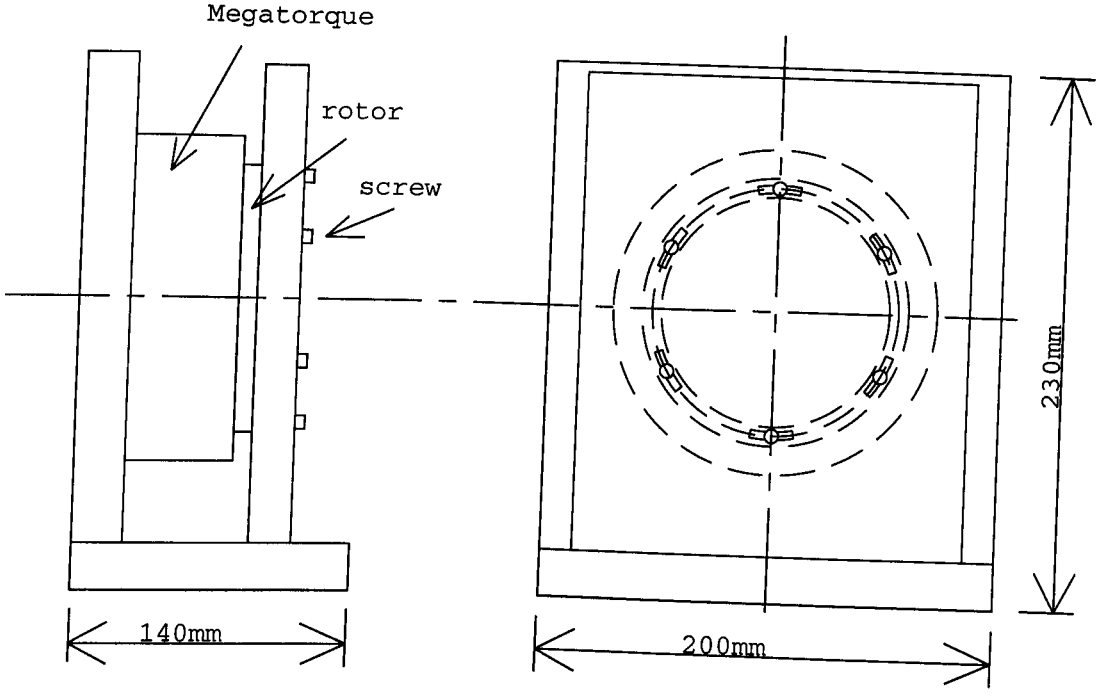

Figure C.1: The rig for magnetisation curve measurement of Megatorque motor

For the positioning of the rotor, the resolver and position servo controller of the Megatorque motor driver/controller were used. The controller provides the positioning resolution of 614,400/revolution. To obtain a position required:

1. Loosen the screws to allow the rotor to rotate.
2. Energise the motor and get the position by the Megatorque position servo controller.
3. Assuring the position error is zero, tighten the screws to lock the rotor.
4. Disconnect the Megatorque controller from the motor.
5. Connect the magnetisation curve measurement setup to the motor and conduct the measurement (described below).
6. Repeat 1 to 5.

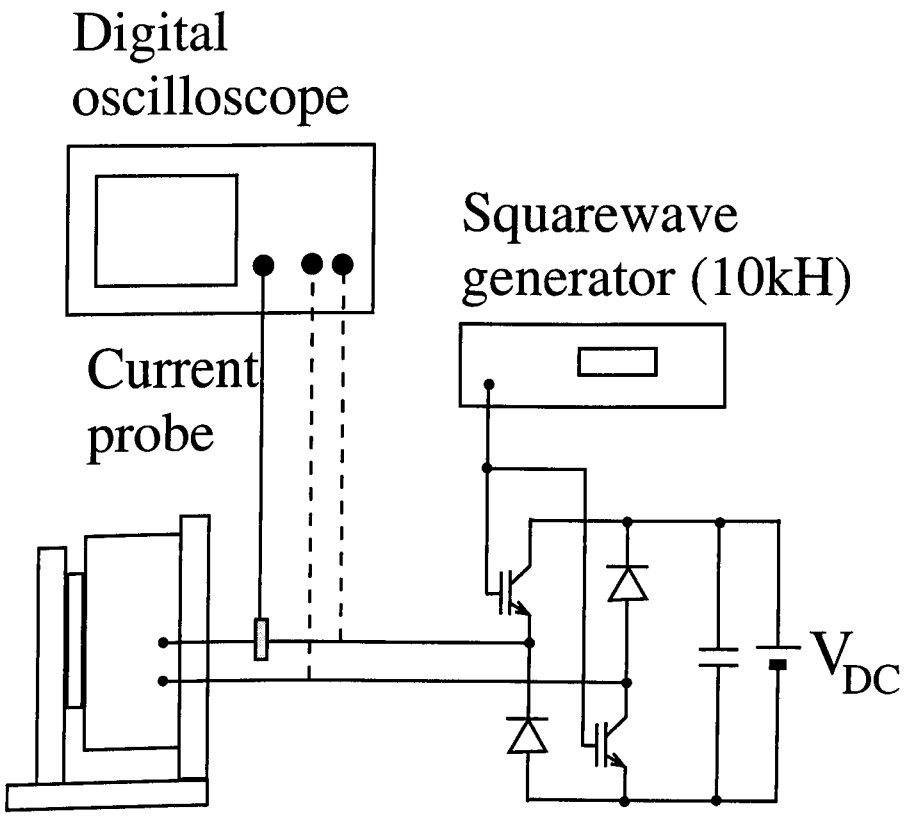

Figure C.2: Experimental setup for measurement of magnetisation curves

C.2 Measurement

Fig. C.2 shows the experimental setup for the measurement of magnetisation curves. One phase winding is connected to a power phase-leg. The output signal of a square-wave generator is used as the switching gate signal for the power transistors. The duty cycle of the squarewave is set less than 50 % for flux linkage to reach zero before the next cycle. The DC voltage and frequency of the squarewave are determined for a desired peak value of the current. The frequency is typically around 10 kHz. A higher value of the DC voltage is desirable to reduce the effect of voltage drop in winding resistance. The voltage and current are measured by and stored in a digital oscilloscope. In practice, the waveforms of voltage and current are averaged over 20-30 cycles to minimise measurement errors. Fig. C.3 shows examples of the voltage and current waveforms.

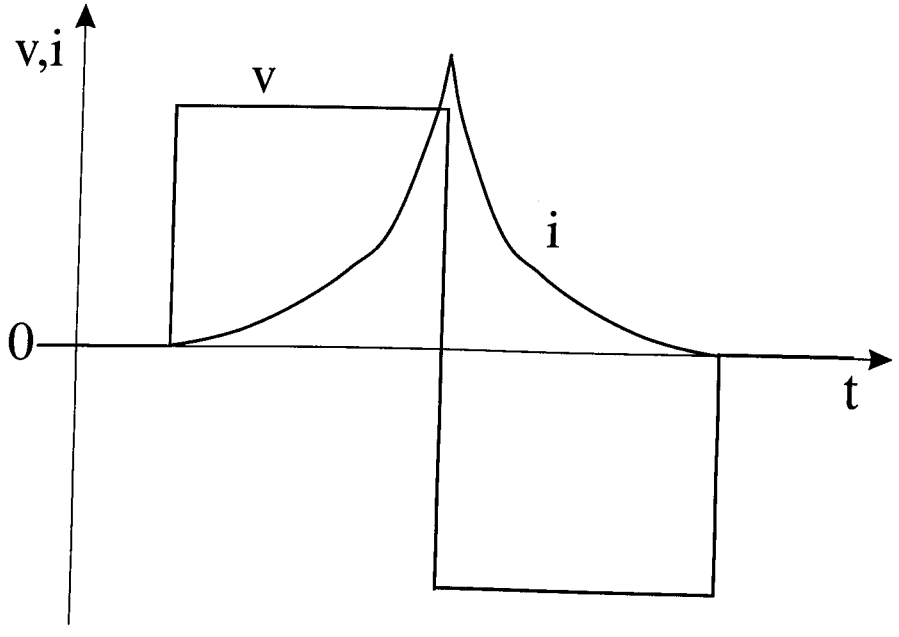

Figure C.3: Example of the voltage and current waveforms

From measured waveforms, the flux linkage ψ is calculated by following equation:

$$\psi = \int \{v(t) - R \cdot i(t)\}\, dt \tag{C.1}$$

where R is winding resistance and may be measured by a multi-meter. Plotting ψ versus i gives a magnetisation curve for a corresponding rotor position.

C.3 Measured magnetisation data

Measured magnetisation curves are shown in Figs. C.4, C.5 and C.6. The curves were measured at every 10 electrical degrees from the aligned position to unaligned position. Fig. C.4 shows the curves when the motor is being magnetised and this corresponds to the data while the current is rising in Fig. C.3. Fig. C.5 shows the curves when the motor is being demagnetised and this corresponds to the data while the current is decreasing. The curves during the magnetisation and demagnetisation differ from each other slightly and the average of them were taken. The averaged curves are shown in Fig. C.6.

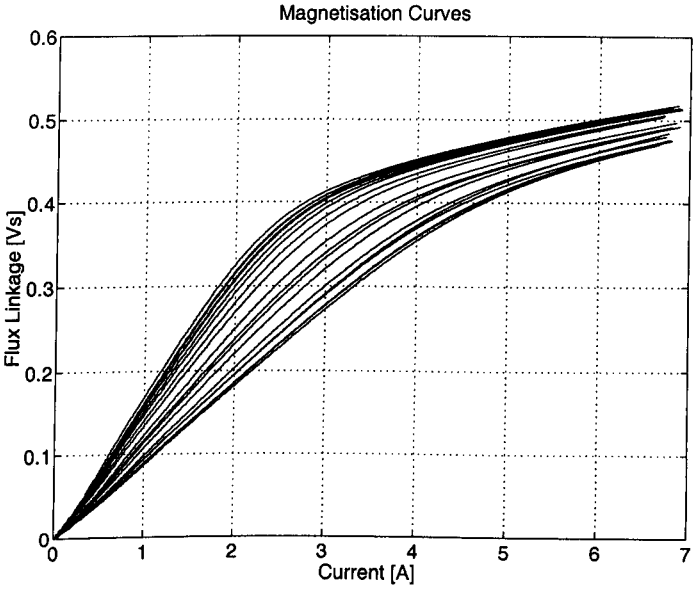

Figure C.4: Measured magnetisation curves (magnetisation)

The magnetisation curves in Fig. C.6 are not uniformly distributed for the rotor positions. Possible causes for this are:

- Inaccuracy in the rotor position (The movement of the rotor position was being observed during the measurement. The maximum displacement was less than 0.8 electrical degrees.).
- Effect of high resistance of the winding (approximately 8 Ω) on calculation of ψ by equation (C.1).
- Effects of hysteresis and induced currents.

The irregularity of the magnetisation curves results in large ripples in torque calculated from them. In the next section, a smoothing technique to compensate the irregularity is discussed.

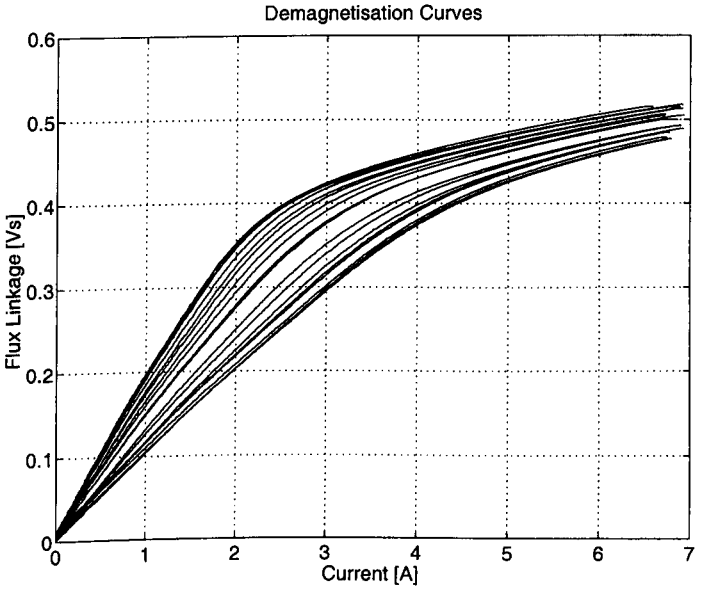

Figure C.5: Measured magnetisation curves (demagnetisation)

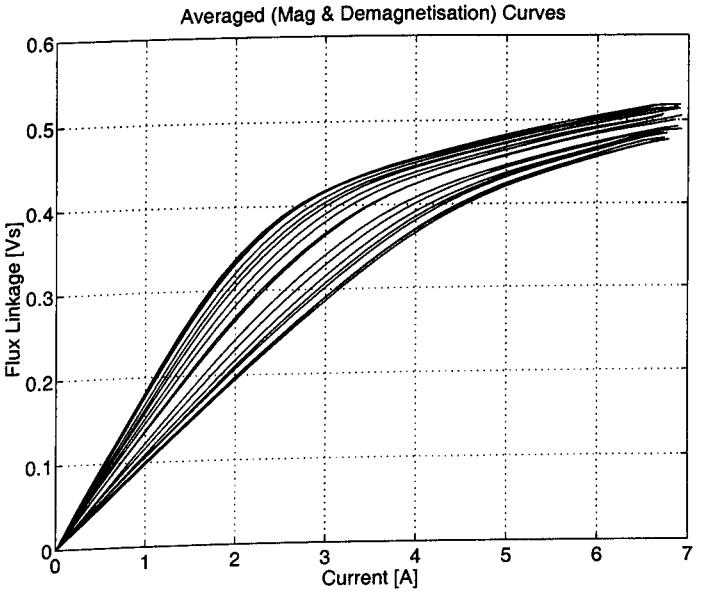

Figure C.6: Average of magnetisation and demagnetisation curves

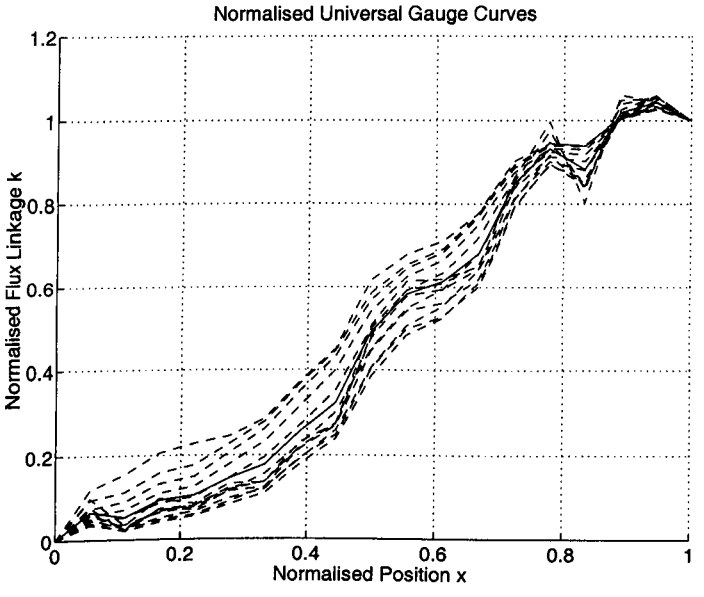

Figure C.7: Normalised gauge curves

C.4 Process of measured data

The gauge curve model, which represents the flux linkage as a function of rotor position with a constant current, was proposed by Miller and McGlip in [45]. Here, the gauge curve is used to make the measured magnetisation curves uniform.

Fig. C.7 shows the normalised gauge curves calculated from the measured magnetisation curves. The dotted lines show the gauge curves for currents from 0.5 to 6.5 A for every 0.5 A. The solid line is the average of the dotted lines.

Fig. C.8 shows the averaged gauge curve fitted with a polynomial function. The model proposed in [45] can be used instead of the polynomial function. Fig. C.9 shows reconstructed magnetisation curves by using the gauge curve in Fig. C.8 and measured magnetisation curves in aligned and unaligned positions in Fig. C.6. The magnetisation curves in Fig. C.9 are uniformly distributed and the torque calculated from the curves are expected to be smooth. The static torque curves calculated from the reconstructed magnetisation curves were compared with measured ones and are shown in chapter 6.

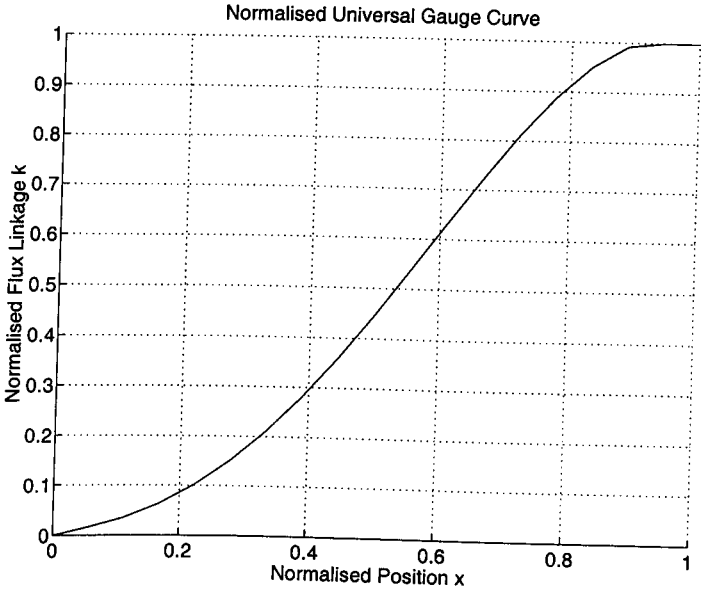

Figure C.8: Normalised gauge curve fitted with a polynomial function

The comparison gave a reasonable agreement and the process of the magnetisation curves discussed here appears to be validated.

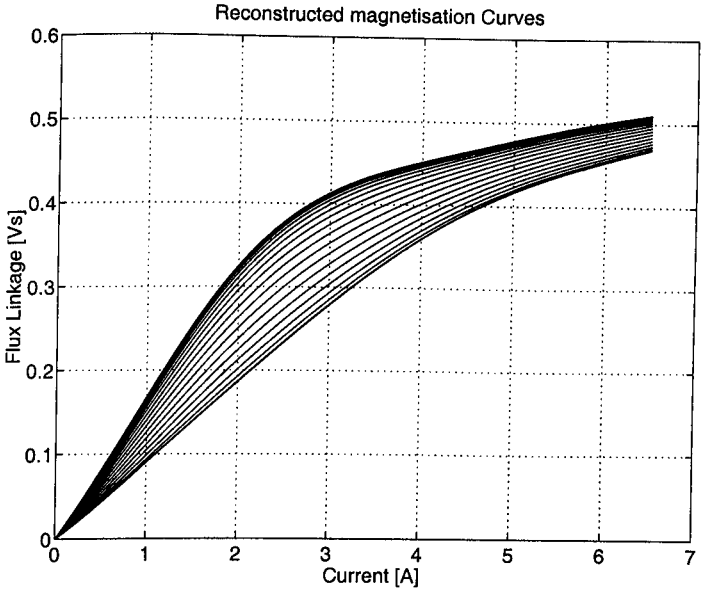

Figure C.9: Reconstructed magnetisation curves from the fitted gauge curve

Appendix D

Author's publications

The author's publications resulting from the research in the thesis are listed below.

1. T. Sawata, P. C. Kjær, C. Cossar, T. J. E. Miller and Y. Hayashi, "Fault-tolerant operation of single-phase switched reluctance generators", 12th Annual 1997 Applied Power Electronics Conference and Exposition (APEC'97), pp. 553-558, Atlanta, Georgia, USA, February 23-27, 1997

2. T. Sawata, P. C. Kjær, C. Cossar and T. J. E. Miller, "A study on operation under faults with the single-phase SR generator", 13th Annual 1998 Applied Power Electronics Conference and Exposition (APEC'98), pp. 1040-1046, Anaheim, California, USA, February 15-19, 1998

3. T. Sawata, P. C. Kjær, C. Cossar and T. J. E. Miller, "A control strategy for the switched reluctance generator", International Conference on Electrical Machines (ICEM'98), pp. 2131-2136, Istanbul, Turkey, September, 1998

4. T. Sawata, P. C. Kjær, J. J. Bremner, T. J. E. Miller, J. R. Coles and G. White, "Multi-dimensional, non-linear, lumped magnetic parameter circuit for dynamic modelling of mutual coupling and faults in switched reluctance motors", Submitted to 8th European Conference on Power Electronics and Applications (EPE'99), Lausanne, Switzerland, September, 1999

5. T. Sawata, P. C. Kjær, C. Cossar, T. J. E. Miller and Y. Hayashi, "Fault-tolerant operation of single-phase switched reluctance generators", IEEE Transactions on Industry Applications, (tentatively accepted)

Bibliography

[1] J. V. Byrne and J. G. Lacy. Characteristics of saturable stepper and reluctance motors. *IEE conference publication No. 136, small electrical machines*, pages 93–96, March 1976.

[2] P. J. Lawrenson, J. M. Stephenson, P. T. Blenkinsop, J. Corda, and N. N. Fulton. Variable-speed switched reluctance motors. *IEE Proceedings, Part B*, 127(4):253–265, July 1980.

[3] X. Wu, S. Haramura, and J. Ueda. Development of switched reluctance motor for electric vehicle -acoustic noise reduction. *Drives and Controls exhibition and conference*, pages 1–5, March 1996.

[4] H. Bausch, A. Greif, and A.B.A. Nickel. A 30 kW/9000 rpm switched reluctance drive for traction applications. *International Conference on Electrical Machines*, 3:2149–2154, September 1998.

[5] C. A. Ferreira, S. R. Jones, W. S. Heglund, and W. D. Jones. Detailed design of a 30-kW switched reluctance starter/generator system for a gas turbine engine application. *IEEE Transactions on Industry Applications*, 31(3):553–561, May/June 1995.

[6] P. St.-J. R. French. Switched reluctance motor drives for rail traction: relative assessment. *IEE Proceedings, Pt. B*, 131(5):209–219, September 1984.

[7] W. F. Ray, R. M. Davis, P. J. Lawrenson, J. M. Stephenson, N. N. Fulton, and B. J. Blake. Switched reluctance motor drives for rail traction: a second view. *IEE Proceedings, Pt. B*, 131(5):220–225, September 1984.

[8] M. R. Harris, J. W. Finch, J. A. Mallick, and T. J. E. Miller. A review of the integral-horsepower switched reluctance drive. *IEEE Transactions on Industry Applications*, IA-22(4):716–721, July/August 1986.

[9] T. J. E. Miller. Converter volt-ampere requirements of the switched reluctance motor drive. *IEEE Transactions on Industry Applications*, IA-21(5):1136–1144, September/October 1985.

[10] N. N. Fulton and J. M. Stephenson. A review of switched reluctance machine design. In *International conference on electric machines*, 1988.

[11] J. Faiz. A review of the performance prediction and design techniques for switched reluctance motors. *Journal of Electrical and Electronics Engineering, Australia*, 12(3):258–266, September 1992.

[12] T. J. E. Miller. *Switched reluctance motor drives, a reference book of collected papers.* Intertec communications inc., Ventura, CA, USA, October 1988.

[13] M. Ilic-Spong, T. J. E. Miller, S. R. MacMinn, and J. S. Thorp. Instantaneous torque control of electric motor drives. *IEEE Transactions on Power Electronics*, 2:55–61, January 1987.

[14] I. Husain and M. Ehsani. Torque ripple minimization in switched reluctance motor drives by PWM current control. *IEEE Transactions on Power Electronics*, 11(1):83–88, January 1996.

[15] A. M. Stankovic, G. Tadmor, and Z. J. Coric. Low torque ripple control of current-fed switched reluctance motors. In *Conf. Record of IEEE Industry Applications Society Annual Meeting*, volume 1, pages 84–91, 1996.

[16] R. S. Wallace and D. G. Taylor. Low-torque ripple switched reluctance motors for direct-drive robotics. *IEEE Transactions on Robotics and Automation*, 7(6):733–742, December 1991.

[17] R. S. Wallace and D. G. Taylor. A balanced commutator for switched reluctance motors to reduce torque ripple. *IEEE Transactions on Power Electronics*, 7(4):617–626, October 1992.

[18] P. C. Kjaer, J. J. Gribble, and T.J.E. Miller. High-grade control of switched reluctance machines. *IEEE Transactions on Industry Applications*, 33(6):1585–1593, November/December 1997.

[19] D. E. Cameron, J. H. Lang, and S. D. Umans. The origin and reduction of acoustic noise in doubly salient valiable-reluctance motors. *IEEE Transactions on Industry Applications*, 28(6):1250–1255, November/December 1992.

[20] R. S. Colby, F. M. Mottier, and T. J. E. Miller. Vibration modes and acoustic noise in a four-phase switched reluctance motor. *IEEE Transactions on Industry Applications*, 32(6):1357–1364, November/December 1996.

[21] C. Y. Wu and C. Pollock. Time domain analysis of vibration and acoustic noise in the switched reluctance drive. *Conf. Record. of 6th Int. Conf. on Electrical Machines and Drives, IEE*, pages 558–563, 1993.

[22] C. Y. Wu and C. Pollock. Analysis and reduction of vibration and acoustic noise in the switched reluctance drive. *IEEE Transactions on Industry Applications*, 31(1):91–98, January/February 1995.

[23] C. Pollock and C. Y. Wu. Acoustic noise cancellation techniques for switched reluctance drives. *Conf. Record. of IEEE Industry Application Society Annual Meeting*, 1:448–455, 1995.

[24] A. Michaelides and C. Pollock. Reduction of noise and vibration in switched reluctance motors: new aspects. *Conf. Record. of IEEE Industry Application Society Annual Meeting*, 2:771–778, 1996.

[25] J. T. Bass, M. Ehsani, and T. J. E. Miller. Robust torque control of switched-reluctance motors without a shaft-position sensor. *IEEE Transactions on Industrial Electronics*, IE-33(3):212–216, August 1986.

[26] J. T. Bass, M. Ehsani, and T. J. E. Miller. Simplified electronics for torque control of sensorless switched reluctance motor. *IEEE Transactions on Industrial Electronics*, IE-34(2):234–239, May 1987.

[27] G. Gallegos-Lopez, P. C. Kjaer, and T. J. E. Miller. A new sensorless method for switched reluctance motor drives. *IEEE Industry Applications Society Annual Meeting*, pages 564–570, October 1997.

[28] P. P. Acarnley, R. J. Hill, and C. W. Hooper. Detection of rotor position in stepping and switched reluctance motors by monitoring of current waveforms. *IEEE Transactions on Industrial Electronics*, IE-32(3):215–222, August 1985.

[29] W. D. Harris and J. H. Lang. A simple motion estimator for variable-reluctance motors. *IEEE Transactions on Industry Applications*, 26(2):237–243, March/April 1990.

[30] M. Ehsani, I. Husain, and A. B. Kulkarni. Elimination of discrete position sensor and current sensor in switched reluctance motor drives. *IEEE Transactions on Industry Applications*, 28(1):128–135, January/February 1992.

[31] A. Lumsdaine and J. H. Lang. State observers for variable-reluctance motors. *IEEE Transactions on Industrial Electronics*, 37(2):133–142, April 1990.

[32] G. Gallegos-Lopez, P. C. Kjaer, and T. J. E. Miller. High-grade position estimation for SRM drives using flux linkage/current correction model. *To be presented IEEE Industry Applications Society Annual Meeting*, 1998.

[33] K. Konecny. Analysis of variable reluctance motor parameters through magnetic field simulations. *MOTOR-CON proceedings*, pages 2A2.1–11, 1981.

[34] G. E. Dawson, A. R. Eastham, and J. Mizia. Switched reluctance motor torque characteristics: finite element analysis and test results. *IEEE Transactions on Industry Applications*, 23(3):532–537, May/June 1987.

[35] Y. Tang. Characterisation, numerical analysis and design of switched reluctance motor for improved material productivity and reduced noise. *Conf. Record. of IEEE Industry Application Society Annual Meeting*, 2:715–722, 1996.

[36] M. Moallem, C. Ong, and L. E. Unnewehr. Effect of rotor profiles on the torque of a switched-reluctance motor. *IEEE Transactions on Industry Applications*, 28(2):364–369, March/April 1992.

[37] A. G. Jack, J. W. Finch, and J. P. Wright. Adaptive mesh generation applied to switched-reluctance motor design. *IEEE Transactions on Industry Applications*, 28(2):370–375, March/April 1992.

[38] S. Williamson and A. A. Shaikh. Three dimensional effects in λ/i diagrams for switched reluctance motors. *Proceedings of International Conference on Electrical Machines*, pages 489–493, 1992.

[39] A. M. Michaelides and C. Pollock. Effect of end core flux on the performance of the switched reluctance motor. *IEE Proc.-Electr. Power Appl.*, 141(6):308–316, November 1994.

[40] J. V. Byrne and J. B. O'Dwyer. Saturable variable reluctance machine simulation using exponential functions. *Proceedings of the International Conference on Stepping Motors and Systems*, pages 11–16, July 1976.

[41] D. A. Torrey and L. H. Lang. Modelling a nonlinear variable-reluctance motor drive. *IEE Proceedings, Pt. B*, 137(5):314–326, September 1990.

[42] J. M. Stephenson and J. Corda. Computation of torque and current in doubly-salient reluctance motors from nonlinear magnetisation data. *Proceedings IEE*, 126(5):393–396, May 1979.

[43] N. N. Fulton. The application of CAD to switched reluctance drives. *Electric Machines and Drives Conference, IEE Conference Publication No. 282*, pages 275–279, December 1987.

[44] D. W. J. Pulle. New data base for switched reluctance drive simulation. *IEE Proceedings-B*, 138(6):331–337, November 1991.

[45] T. J. E. Miller and M.I. McGilp. Nonlinear theory of the switched reluctance motor for rapid computer-aided design. *IEE Proceedings, Part B*, 137(6):337–347, November 1990.

[46] S. A. Nasar. D.C.-switched reluctance motor. *Proceedings IEE*, 116(6):1048–1049, June 1969.

[47] H. R. Bolton and D. A. G. Pedder. Low-cost reluctance drive system for low power, low speed application. *IEE Conference Publications No. 179*, pages 88–92, 1979.

[48] S. Chatratana, H. R. Bolton, and D. A. G. Pedder. Investigations into small single-phase switched reluctance motors. *Proceedings IEE Conference on Small & Special Electric Machines*, pages 99–102, September 1981.

[49] C. C. Chan. Single-phase switched reluctance motors. *IEE Proceedings, Part B*, 134(1):53–56, January 1987.

[50] C. Chan and H. R. Bolton. Development of sub-kW single-phase switched reluctance motor drives. *Proceedings of international conference on electrical machines*, 2:527–531, September 1992.

[51] J. C. Compter. Microprocessor-controlled single-phase reluctance motor. *Proceedings of Drives/Motors/Controls*, pages 64–68, October 1984.

[52] G. Horst. Hybrid single-phase variable reluctance motor. U.S. patent, 1992. 5122697.

[53] C. Chan and H. R. Bolton. Performance enhancement of single-phase switched-reluctance motor by DC link voltage boosting. *IEE Proceedings-B*, 140(5):316–322, September 1993.

[54] J. D. Lewis, H. R. Bolton, and N. W. Phillips. Performance enhancement of single and two phase SR drives using capacitor boost circuit. *European Conference on Power Electronics and Applications*, 3:3.229–3.232, 1995.

[55] M. Barnes and C. Pollock. Power converter for single phase switched reluctance motors. *Electronics Letters*, 31(25):2137–2138, 7th December 1995.

[56] Y. Hayashi and T. J. E. Miller. Single-phase multi-pole SRM for solar-powered vehicle. *Conf. Record, IPEC-Yokohama '95*, pages 575–579, 1995.

[57] T. J. E. Miller and M.I. McGilp. *PC-SRD 6.2 manual. SPEED* Laboratory, University of Glasgow, April 1995.

[58] R. R. Secunde, R. P. Macosko, and D. S. Repas. Integrated engine-generator concept for aircraft electric secondary power. *NASA TM X-2579*, June 1972.

[59] R. I. Jones. Considerations of the all electric (accessory) engine concept. *Proceedings of the Institution of Mechanical Engineers, Pt.G,Journal of Aerospace Engineering*, 209(G4), 1995.

[60] M. E. Elbuluk and M. D. Kankam. Motor drive technologies for the power-by-wire (PBW) program: options, trends and tradeoffs. *NASA TM-106885*, March 1995.

[61] S. R. MacMinn. Control of a switched reluctance aircraft engine starter-generator over a very wide speed range. *Proceedings IECEC*, pages 631–638, August 1981.

[62] E. Richter. High temperature, lightweight, switched reluctance motors and generators for future aircraft engine applications. *Proceedings of the American Control Conference*, pages 1846–1851, 1988.

[63] S.R. MacMinn. A very high speed switched reluctance starter-generator for aircraft engine applications. *Proceedings of NAECON '89*, May 1989.

[64] E. Richter and C. Ferreira. Performance evaluation of a 250 kW switched reluctance starter generator. *Conf. Record, IEEE IAS Annual Meeting*, pages 434–440, 1995.

[65] A. V. Radun, C. A. Ferreira, and E. Richter. Two channel switched reluctance starter/generator results. *Conf. Proceedings, APEC '97*, pages 546–552, February 1997.

[66] C. M. Stephens. Fault detection and management system for fault-tolerant switched reluctance motor drives. *IEEE Transactions on Industry Applications*, 27(6):1098–1102, November/December 1991.

[67] C. A. Ferreira and E. Richter. About channel independence for multi channel switched reluctance generator systems. *Conf. Record, IEEE IAS Annual Meeting*, pages 816–822, 1996.

[68] D. F. Warne and P. G. Calnan. Generation of electricity from the wind. *Proceedings IEE*, 124(11R):963–985, November 1977.

[69] I. K. Buehring and L. L. Freris. Control policies for wind-energy conversion systems. *IEE Proceedings, Part C*, 128(5):253–261, September 1981.

[70] N. Ammasaigounden and M. Subbiah. Microprocessor-based voltage controller for wind-driven induction generators. *IEEE Transactions on Industrial Electronics*, 37(6):531–537, December 1990.

[71] N. N. Fulton and S. P. Randall. Switched reluctance generators for wind energy applications. *Proceedings of the 8th BWEA Wind Energy Conference (British Wind Energy Association)*, pages 211–218, 1986.

[72] D. A. Torrey and M. Hassanin. The design of low-speed variable-reluctance generators. *Conf. Record, IEEE IAS Annual Meeting*, 1:427–433, 1995.

[73] J. W. Finch, M. R. Harris, A. Musoke, and H. M. B. Metwally. Variable-speed drives using multi-tooth per pole switched reluctance motors. *13th Incremental Motion Control Systems Symposium*, pages 293–302, 1984.

[74] J. F. Lindsay, R. Arumugam, and R. Krishnan. Finite-element analysis characterisation of a switched reluctance motor with multitooth per stator pole. *IEE Proceedings, Part B*, 133(6):347–353, November 1986.

[75] G. Hedlund. D. C. motor with multi-tooth poles. *United States Patent, 4,748,362*, May 31 1988.

[76] NSK Ltd. *Mechatronic actuators*, 1994.

[77] NSK Ltd. *Megatorque motor system user's manual*, 3rd edition, September 1993.

[78] R. Welburn. Ultra-high torque motor system for direct drive robotics. *MOTORCON Proceedings*, pages 17–24, April 1984.

[79] J. Wagner, D. Maga, and R. Ort-Snep. Magnetic field of hightorque stepping motor. *Proceedings of the International PCIM'95 Conference*, pages 243–249, June 1995.

[80] J. Wagner and D. Maga. Analysis and design of the high-torque low-speed step motor. *ElectroMotion*, 4(3):121–128, 1997. ISSN 1223-057X.

[81] F. Filicori, C. G. Lo Bianco, and A. Tonielli. Modeling and control strategies for a variable reluctance direct-drive motors. *IEEE Transactions on Industrial Electronics*, 40(1):105–115, February 1993.

[82] M. R. Harris, A. Hughes, and P. J. Lawrenson. Static torque production in saturated doubly-salient machines. *Proceedings IEE*, 122(10):1121–1127, October 1975.

[83] T. J. E. Miller. *Switched reluctance motors and their control.* Oxford University Press/Magna Physics Publications, 1993. ISBN 0-19-859387-2.

[84] O. Materu and R. Krishnan. Estimation of switched reluctance motor losses. *IEEE Transactions on Industry Applications*, 28(3):668–679, May/June 1992.

[85] Y. Hayashi and T. J. E. Miller. A new approach to calculation core losses in the SRM. *IEEE Transactions on Industry Applications*, 31(5):1039–1049, September/October 1995.

[86] A. Michaelides and C. Pollock. Short flux paths optimise the efficiency of a 5-phase switched reluctance drive. *Conf. Record, IEEE IAS Annual Meeting*, pages 286–293, 1995.

[87] A.V. Radun. Generating with the switched reluctance motor. *Proceedings of APEC 1994*, pages 41–46, 1994.

[88] C. M. Stephens and A. V. Radun. Current chopping strategy for generating action in switched reluctance machines. U.S. patent, November 24 1992. 5166591.

[89] D. E. Cameron and J.H. Lang. The control of high-speed variable-reluctance generators in electric power systems. *IEEE Transactions on Industry Applications*, 29(6):1106–1109, November/December 1993.

[90] A.V. Radun. Linearizer for a switched reluctance generator. U.S. patent, April 20 1993. 5204604.

[91] P. C. Kjaer, C. Cossar, J. J. Gribble, Y. Li, and T. J. E. Miller. Switched reluctance generator control using an inverse machine model. *Proceedings of ICEM '94*, pages 380–385, 1994.

[92] P. C. Kjaer, C. Cossar, J. J. Gribble, T. J. E. Miller, and Y. Li. Minimisation of reactive power flow in switched reluctance generators. *Conf. Record, IPEC-Yokohama '95*, pages 1022–1026, 1995.

[93] Y. A. Kwon. Computation of optimal excitation of a switched reluctance motor using variable voltage. *IEEE Transactions on Industrial Electronics*, 45(1):177–180, February 1998.

[94] The MathWorks Inc. *SIMULINK user's guide.* The MathWorks Inc., 1992.

[95] Motorola. *CPU32 reference manual.* Motorola Inc., 1990.

[96] H. C. Lovatt and J. M. Stephenson. Influence of number of poles per phase in switched reluctance motors. *IEE Proceedings, Part B*, 139(4):307–314, July 1992.

[97] T. J. E. Miller. Faults and unbalance forces in the switched reluctance machine. *IEEE Transactions on Industry Applications*, 31(2):319–328, March/April 1995.

[98] The MathWorks Inc. *The MATLAB user's guide.* Prentice-Hall Inc., 1995.

[99] C. M. Stephens. Fault detection and management system for fault tolerant switched reluctance motor drives. *Conf. Record, IEEE IAS Annual Meeting*, pages 574–578, September 1989.

[100] A. A. Arkadan and B. W. Kielgas. Switched reluctance motor drive systems dynamic performance prediction under internal and external fault conditions. *IEEE Transactions on Energy Conversion*, 9(1):45–51, March 1994.

[101] L. A. Belfore and A. A. Arkadan. Modeling faulted switched reluctance motors using evolutionary neural networks. *IEEE Transactions on Industrial Electronics*, 44(2):226–223, April 1997.

[102] A. G. Jack, B. C. Mecrow, and J. A. Haylock. A comparative study of permanent magnet and switched reluctance motors for high-performance fault-tolerant applications. *IEEE Transactions on Industry Applications*, 32(4):889–895, July/August 1996.

[103] B. C. Mecrow, A. G. Jack, D. J. Atkinson, and J. A. Haylock. Fault tolerant drives for safety critical applications. *IEE Colloquium on New Topologies for Permanent Magnet Motors*, pages 5/1–5/7, June 1997.

[104] T. Sawata, P. C. Kjaer, T. J. E. Miller, J. J. Bremner, J. R. Coles, J. Rogers, and G. White. Multi-dimensional, non-linear, lumped magnetic parameter circuit for dynamic modelling of mutual coupling and faults in switched reluctance motors. *Submitted to APEC '99*, 1999.

[105] J. C. Moreira and T. A. Lipo. Simulation of a four phase switched reluctance motor including the effects of mutual coupling. *Electric Machines and Power Systems*, 16:281–299, 1989.

[106] R. M. Davis and I. Al-Bahadly. Experimental evaluation of mutual inductances in a switched reluctance motor. *IEE Conference Publication No.324*, pages 243–248, 1990.

[107] M. A. Preston and J. P. Lyons. A switched reluctance motor model with mutual coupling and multi-phase excitation. *IEEE Transactions on Magnetics*, 27(6):5423–5425, November 1991.

[108] A. M. Michaelides and C. Pollock. Modelling and design of switched reluctance motors with two phases simultaneously excited. *IEE Proceedings Electric Power Applications*, 143(5):361–370, September 1996.

[109] P. Pillay, Y. Liu, W. Cai, and T. Sebastian. Multiphase operation of switched reluctance motor drives. *Conf. Record, IEEE IAS Annual Meeting*, pages 310–317, 1997.

[110] N. Allen, H. C. Lai, P. J. Leonard, and D. Rodger. External circuit, movement, and periodicity considerations in the design of electrical machines using finite elements. *IEE Conference Publication No.412*, pages 126–130, 1995.

[111] Analogy Inc. *SaberDesigner Reference release 4.1.* Analogy Inc., December 1996.

[112] B. C. Mecrow. New winding configurations for doubly salient reluctance machines. *IEEE Transactions on Industry Applications*, 32(6):1348–1356, November/December 1996.

[113] H. Asada and K. Youcef-Toumi. *Direct Drive Robots: Theory and Practice.* The MIT Press, Cambridge, Massachusetts, 1987. ISBN 0-262-01088-7.

[114] N. Hemati, J. S. Thorp, and M. C. Leu. Robust nonlinear control of brushless dc motors for direct-drive robotic applications. *IEEE Transactions on Inductrial Electronics*, 37(6):460–468, December 1990.

[115] K. R. Rajagopal, M. Krishnaswamy, B. Singh, and B. P. Singh. An improved high resolution hybrid stepper motor for solar array drive of indian remote sensing satellite. *Proceedings of the International Conference on Power Electronics and Drive Systems*, 2:610–615, 1995.

[116] P. A. Ward and P. J. Lawrenson. Magnetic permeance of doubly-salient airgaps. *Proceedings IEE*, 124(6):542–544, June 1977.

[117] J. W. Finch. Magnetic permeance of aligned doubly salient structures. *IEE Proceedings, Part B*, 133(6):365–366, November 1986.

[118] K. C. Mukherji and S. Neville. Magnetic permeance of identical double slotting (deductions from analysis by F. W. Carter). *Proceedings IEE*, 118(9):1257–1268, September 1971.

[119] J. V. Byrne. Tangential forces in overlapped pole geometries. *IEEE Transactions on Magnetics*, MAG-8(1):2–9, March 1972.

[120] H. D. Chai. Technique for finding permeance of toothed structure of arbitrary geometry. *Proc. of the International Conf. on Stepping motors and systems*, pages 31–37, July 1976.

[121] A. J. C. Bakhuizen and R. de Boer. *On the calculation of permeances and forces between doubly slotted structures.* Eindhoven university of technology, The Netherlands, September 1976. ISBN 90-6144-065-3.

[122] C. W. de Silva. Design equations for the tooth distribution of stepping motors. *IEEE Transactions on Industrial Electronics*, 37(2):184–186, April 1990.

GLASGOW UNIVERSITY LIBRARY